Terahertz Ultrafast Spectroscopy: A Paradigm for Material Characterization and Light Interaction

Yuezhen Lu

School of Engineering

Lancaster University

A thesis submitted for the degree of

Doctor of Philosophy

Declaration

This dissertation is the result of work carried out in the Terahertz Photonic Group at Lancaster University from May 2020 to May 2023. This dissertation is the result of my own work and includes nothing which is the outcome of work done in collaboration except where specifically stated in the text. This work is not the same as any I have already submitted, or I am in the process of submitting, for any degree at this, or any other university. This dissertation contains fewer than 50,000 words including appendices, bibliography, footnotes, tables, and equations.

Yuezhen Lu

Acknowledgements

I express my deepest gratitude to my primary supervisor, Dr. Riccardo Degl'Innocenti, for his invaluable insights, unwavering support, and sagacious guidance throughout my PhD journey. His faith in my abilities and his consistent encouragement played a pivotal role in shaping my academic pursuits.

My heartfelt thanks also go to my second supervisor, Dr. Hungyen Lin, and my appraisal committee, Dr Rosa Latizia, who have been a pillar of support. Their continuous encouragement has been instrumental in my research endeavors.

I would like to extend my special gratitude to Dr. Abdullah M. Zaman and Dr. Xavier Romain for their invaluable insights and stimulating discussions throughout my PhD journey. Additionally, my heartfelt thanks go to Dr. Lucy Hale, with whom I collaborated on the near-field experiments elucidated in Chapter 6. I am also deeply indebted to Dr. Avinash Pai and Dr. Haitao Zhu for their commendable contributions in providing advanced materials, as discussed in Chapter 3. Moreover, I would be grateful to acknowledge the collective contributions of numerous collaborators I have worked with over the years, including but not limited to Prof. Oleg Mitrofanov, Dr. Nikita Almond, Dr. Harvey Beere, Prof. David Ritchie, Dr. Jack Alexander-Webber, Prof. Stephan Hofmann, and Prof. Allan EW Rennie.

I want to thank Mr Garry Vernon, Dr Kunal Lulla, Mr Xiuxin Xia, Mr Sam Jones, Mr Jonathan Hall, and Dr Farhan Hasan for their continuous help in the cleanroom work. I am thankful to all the School of Engineering staff members and technicians who have helped in one way or another. I would also like to appreciate all my friends met in Lancaster, including but limited to Ziran Zuo, Pu Tan, Yueqi Wu, Yue Chen, Li Zhang, and George Ludlam, for their support in my daily life.

I wish to express my boundless gratitude to my parents, Dongsheng Lyu and Yixiang Liu, whose unwavering support and encouragement throughout my life. Their infinite love and immeasurable sacrifices have laid the foundation for all my accomplishments and made the journey feasible. Lastly, a special note of deep appreciation is extended to my girlfriend, Dongni Zhao. Her steadfast presence, constant support, and enduring love through times of triumph and tribulation have been invaluable.

Publications

1. Lu, Yuezhen, Lucy L. Hale, Abdullah M. Zaman, Sadhvikas J. Addamane, Igal Brener, Oleg Mitrofanov, and Riccardo Degl'Innocenti. "Near-Field Spectroscopy of Individual Asymmetric Split-Ring Terahertz Resonators." *ACS photonics* 10, no. 8 (2023): 2832-2838.

2. Lu, Yuezhen, Haitao Zhu, Abdullah M. Zaman, Allan EW Rennie, Hungyen Lin, Yingtao Tian, and Riccardo Degl'Innocenti. "Contactless 3D surface characterization of additive manufactured metallic components using terahertz time-domain spectroscopy." Optical Materials Express 13, no. 9 (2023): 2513-2525.

3. Pai, Avinash R., **Yuezhen Lu**, Saju Joseph, Neelakandan M. Santhosh, Riccardo Degl'Innocenti, Hungyen Lin, Rosa Letizia, Claudio Paoloni, and Sabu Thomas. "Ultra-broadband shielding of cellulose nanofiber commingled biocarbon functional constructs: a paradigm shift towards sustainable terahertz absorbers." Chemical Engineering Journal 467 (2023): 143213.

4. Zaman, Abdullah M., **Yuezhen Lu**, Xavier Romain, Nikita W. Almond, Oliver J. Burton, Jack Alexander-Webber, Stephan Hofmann et al. "Terahertz metamaterial optoelectronic modulators with GHz reconfiguration speed." IEEE Transactions on Terahertz Science and Technology 12, no. 5 (2022): 520-526.

5.Zaman, Abdullah M., **Yuezhen Lu**, Nikita W. Almond, Oliver J. Burton, Jack Alexander-Webber, Stephan Hofmann, Thomas Mitchell et al. "Versatile and active THz wave polarization modulators using metamaterial/graphene resonators." *Frontiers in Nanotechnology* 5 (2023): 1057422.

6. Zaman, Abdullah M., Yuichi Saito, **Yuezhen Lu**, Farhan Nur Kholid, Nikita W. Almond, Oliver J. Burton, Jack Alexander-Webber et al. "Ultrafast modulation of a THz metamaterial/graphene array integrated device." Applied Physics Letters 121, no. 9 (2022).

7. Xia, R., Almond, N.W., Kindness, S.J., Mikhailov, S.A., Tadbier, W., Degl'Innocenti, R., **Lu, Y.**, Lowe, A., Ramsay, B., Jakob, L.A. and Dann, J., 2023. Achieving 100% amplitude modulation depth in a graphene-based tuneable capacitance metamaterial. arXiv preprint arXiv:2312.16330.

Peer-Reviewed Conference Proceedings

1. Lu, Yuezhen, Haitao Zhu, Abdullah M. Zaman, Hungyen Lin, Riccardo Degl'Innocenti, and Yingtao Tian. "Surface Roughness Measurement of 3D-Printed 316L Stainless Steel Surface using Terahertz Time-Domain Spectroscopy." In 2022 47th International Conference on Infrared, Millimeter and Terahertz Waves (IRMMW-THz), pp. 1-2. IEEE, 2022.

2. Lucy Hale, **Yuezhen Lu**, Abdullah Zaman, Sadhvikas Addamane, Igal Brener, Oleg Mitrofanov, Riccardo Degl'Innocenti (2023). "Near Field Analysis of Individual High Quality Factor THz Resonators". Submitted to the 2023 48th International Conference on Infrared, Millimeter, and Terahertz Waves (IRMMW-THz).

3.Zaman, Abdullah M., **Yuezhen Lu**, Nikita W. Almond, Oliver J. Burton, Jack Alexander-Webber, Stephan Hofmann, Thomas Mitchell et al. "Active Polarization Modulation of Terahertz Radiation Using Metamaterial/Graphene-Based Optoelectronic Devices." In 2022 47th International Conference on Infrared, Millimeter and Terahertz Waves (IRMMW-THz), pp. 1-3. IEEE, 2022.

4. Zaman, Abdullah, Nikita Almond, **Yuezhen Lu**, Xavier Romain, Decio Alves De Lima, Hungyen Lin, Oliver Burton et al. "Graphene-based external optoelectronic terahertz modulators for high speed wireless communications." (2021).

Abstract

Recent advancements in terahertz (THz) technology have heralded the development of cutting-edge sources, detectors, and modulators, catalyzing progress in fields such as molecular spectroscopy, 6G wireless communication, and biomedical imaging. Central to these innovations is terahertz time-domain spectroscopy (THz-TDS), which has garnered significant attention in both foundational and applied research. THz-TDS's unique capability to concurrently obtain time-domain and frequency-domain spectral data, along with its non-destructive nature, positions it as an indispensable tool for elucidating the physical and chemical properties of various materials without causing damage. This technique provides profound insights into diverse fields, such as molecular dynamics and vibrational modes of crystal lattices.

Leveraging the state-of-the-art measurements enabled by THz-TDS, this thesis delves into the characterization of advanced materials and the examination of light interactions within artificial photonic structures. It showcases a variety of innovative THz-TDS applications aimed at propelling research in diverse areas:

Initially, the thesis presents material characterization applications utilizing a standard THz-TDS system configured for both transmission and reflection measurements. Through the analysis of different transmission characteristics of samples, it highlights two exemplary methods: evaluating the surface roughness of 3D-printed metals to within micrometer accuracy, and determining the shielding effectiveness of bio-degradable THz absorbers up to 99.99999%. These methodologies underscore the pivotal role of THz-TDS in advancing next-generation manufacturing technologies.

Furthermore, the thesis explores the investigation of artificial photonic structures using a general THz-TDS system. It details the initial measurements of two types of metamaterials—each designed for high Q-factor enhancement and increased light absorption—using both standard and cryogenic THz-TDS. The photonic samples, meticulously engineered through finite element simulations and crafted with cutting-edge microfabrication techniques,

demonstrate a seamless correlation between THz-TDS results and simulation predictions, establishing a robust framework for future THz photonic development.

In the concluding chapters, specialized THz-TDS techniques, such as aperture near-field scanning microscope (a-SNOM) THz-TDS and high-field THz-TDS, are introduced for detailed analysis of localized light interactions in high Q-factor resonators and high harmonic generation in integrated graphene metamaterials, respectively. The a-SNOM THz-TDS, with its sub-micron spatial resolution and comprehensive time-domain investigation capabilities, facilitates the mapping and quantitative analysis of tightly confined modes, including weakly radiative modes through a cross-polarized configuration. This insight is invaluable for advancing metamaterial-based optoelectronic platforms in THz photonics.

High-field THz-TDS is employed to generate tunable, high-power pulses, intensifying the nonlinear effects in materials. Graphene, with its massless electron dynamics and linear band characteristics, emerges as the most effective material for generating high-order harmonic generation in the THz range. The coherent measurement capabilities of high-field THz-TDS unveil distinct high-harmonic trends in graphene-based opto-electronics, showcasing the potential for the development of future THz components.

Table of Content

List of Figures

List of Tables

Chapter 1 Introduction

Terahertz (THz) is a portion of the electromagnetic spectrum which finds applications in various research, including investigating fundamental science, characterizing different materials, and improving industrial quality control. This chapter will briefly introduce THz radiation and the THz applications used for imaging, spectroscopic analysis, and communication in detail. The summary for discussing the challenges in advancing THz technology and the overview of this thesis will be presented at the end of this chapter.

1.1 Overview of terahertz wave

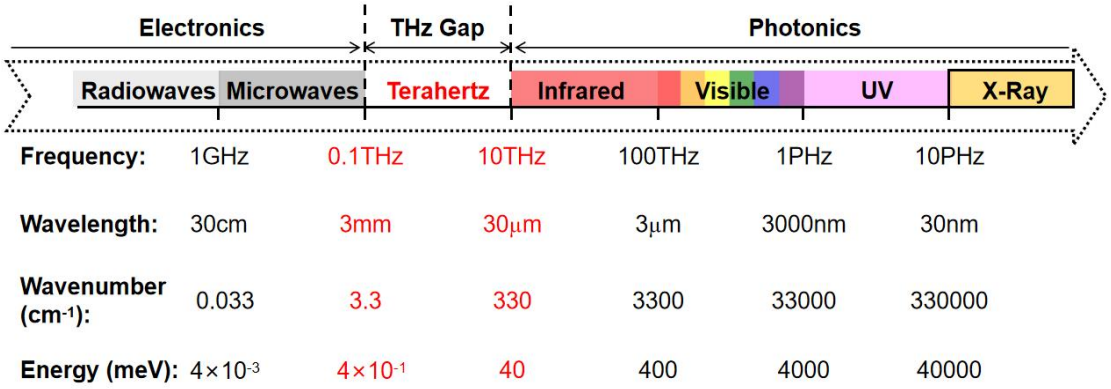

Figure 1.1 The electromagnetic spectrum.

THz wave generally refers to electromagnetic waves with frequencies of 0.1THz-10THz, corresponding to a wavelength range of 3000 μm-30 μm, as shown in Figure 1.1. THz waves are located between the microwave and infrared bands within the electromagnetic spectrum. In the late 1980s, limited by the lack of efficient THz sources and detectors, the versatile research based on THz wave was significantly less developed than other electromagnetic waves, thus also being called the "THz gap" [1]. Nowadays, the rapid development of semiconductor technologies, such as photoconductive antenna [2], and ultrafast optical techniques, such as optical rectification [3], have enabled the generation and detection of THz waves as routine approaches.

As THz wave situates at a distinct position within the electromagnetic spectrum, exhibits several remarkable characteristics that distinguish it from other electromagnetic waves. This section outlines the key features of THz waves as follows:

1. Good penetrability: THz waves possess exceptional penetrability, allowing it to propagate through most non-polar and non-metallic materials, including cloth [4], plastic [5], ceramics [6], paper [7], and leather [8]. This unique property enables the investigation of diverse physical properties, such as conductivity, below the material's surface.

2. Low ionization: The low photon energy of THz waves, approximately 0.41-41.4meV, ensures that they do not induce ionization within materials. This feature offers THz wave as a safer alternative to X-ray waves for biomedical diagnosis without inflicting damage, such as skin cancer detection [9].

3. Ultra-large bandwidth: THz waves, with higher frequencies than microwaves, enable communication transmission with higher bandwidth and larger capacity. Moreover, due to their shorter wavelengths, it is possible to design more compact THz communication systems compared to current technologies [10].

4. 'Fingerprint' absorption spectrum: Within the THz band, molecules display characteristic absorption peaks in the THz absorption spectrum owing to their vibration and rotational energy. This phenomenon is particularly significant for gases, such as greenhouse gases or poisonous substances [11]. The unique 'fingerprint' absorption spectrum of THz waves plays a pivotal role in diverse applications, including biological sensing [12] and explosives imaging detection [13].

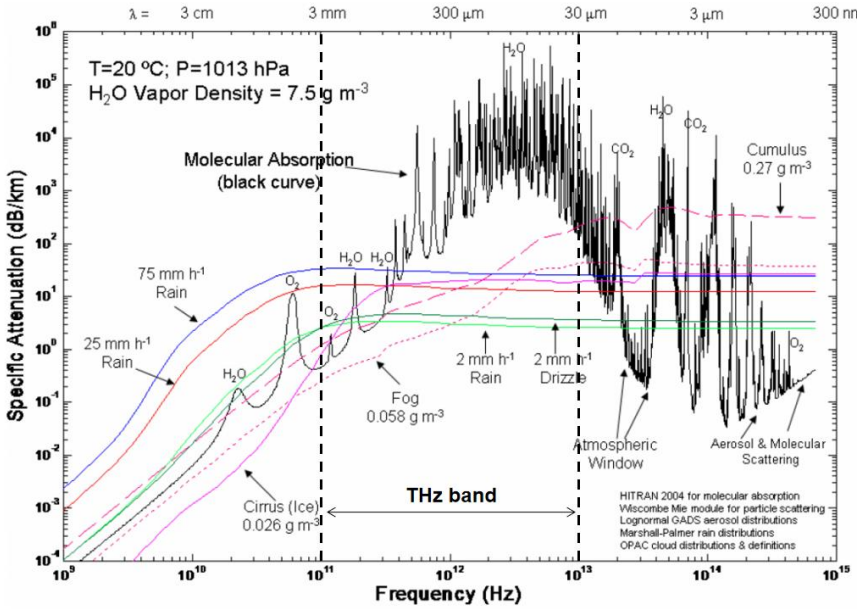

Figure 1.2 Atmospheric attenuation of electromagnetic radiation [15].

These distinctive properties of THz waves underscore their potential as a valuable tool in various research areas, promising advances in communication, materials analysis, and detection techniques.

However, the utilization of THz waves also comes with certain hurdles. As mentioned earlier, THz waves are sensitive to absorption by multiple molecules, including gases in the air, such as H_2O, O_2, and CO_2 [14]. Consequently, the practical applications of THz technology are highly influenced by the surrounding environment. Figure 1.2 illustrates the specific atmospheric attenuation rate of electromagnetic waves with frequencies ranging from 0.01 to 1000 THz, with the THz band range highlighted by two black dashed lines [15]. It is evident that the air, particularly water molecules, significantly attenuates THz wave propagation. Besides molecular absorption, THz light is also sensitive to the morphology of materials it passes through, which can lead to severe scattering of THz waves. As a result, THz applications are not well-suited for long-distance transmission in general conditions.

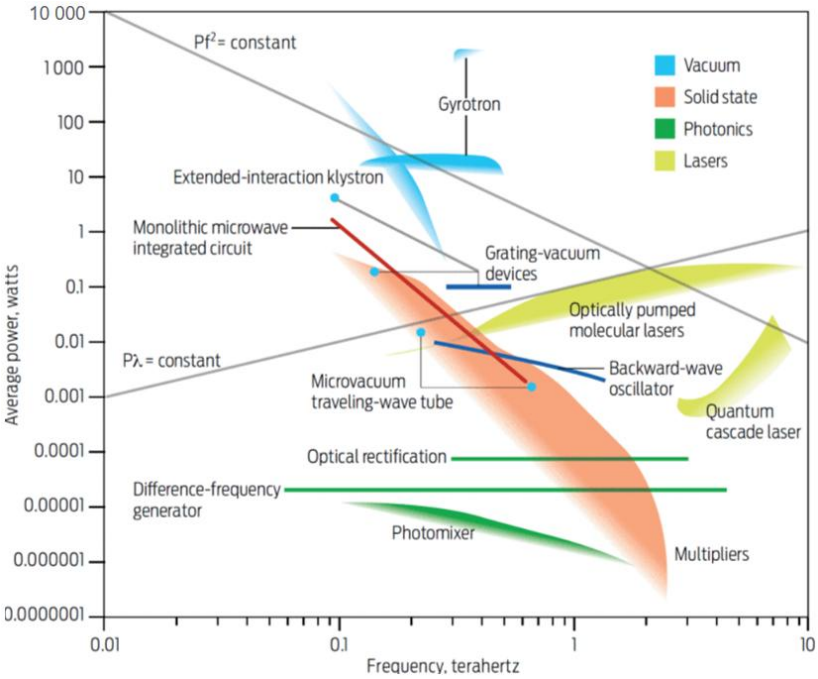

Figure 1.3 Power levels of different THz sources [16].

In the realm of hardware advancement, the progression of ultrafast THz communication or imaging systems encounters impediments due to insufficient efficient THz components for optimal radiation and wavefront modulation. The effective generation and manipulation of

THz radiation necessitates reliable and handy components, a deficiency that curtails such systems' evolutionary trajectory. Diverse methodologies are employed to achieve THz radiation, encompassing vacuum-based, solid-state, photonics-based, and laser-based techniques, as illustrated in Figure 1.3 [16]. It is pertinent to note that certain approaches, such as free electron lasers and spintronics, while noteworthy, are omitted from the figure owing to their typical requisites of a synchrotron radiator [17] or an ultra-low temperature environment [18]. It is worth highlighting that the availability of emitters that facilitate the generation of THz waves characterized by broadband frequencies and power levels surpassing the threshold of 1W remains constrained.

Notwithstanding the constraints that hinder the widespread application of THz technologies, substantial research efforts have yielded diverse applications based on THz waves' distinctive attributes within laboratory settings. The subsequent section provides a succinct overview of the emergent THz applications dedicated to imaging, spectroscopy, and communication domains.

1.2 THz applications

1.2.1 THz communication

As the communication capacity C_a (also called as “maximum data transfer rate”) is determined by the equation [19]:

$$C_a = W * \log_2(1 + SNR) \tag{1.1}$$

W is the bandwidth and SNR is the signal-to-noise ratio of the transmitted signal. Indeed, the intrinsic higher bandwidth of THz waves has the potential to linearly increase the communication capacity compared to current 5G techniques that use millimeter waves. As discussed in section 1.1, THz waves are not well-suited for long-distance communication due to their higher attenuation in the atmosphere. However, for short-range communication, THz waves offer significant data transmission rates and capacity advantages.

1.2.2 THz spectroscopy

Benefiting from the penetrability and low ionization characteristics introduced above, THz spectroscopy has found numerous compelling applications in industrial and scientific domains. Based on the unique interactions between THz waves and various media types (including gases, liquids, and solids), distinct phenomena like absorption, phase shifts, and scattering occur when THz waves pass through these mediums [20].

For example, by precisely measuring changes in both amplitude and phase, it becomes possible to discern the fundamental characteristics of dielectric materials—ranging from electronic behavior [21], lattice vibrations [22] to chemical compositions [23]. Consequently, this technique facilitates the accurate assessment of material properties such as absorption coefficients, refractive indices, dielectric constants, frequency shifts, and other relevant traits [20]. Moreover, this approach with time-resolved measurement enables the probing of ultra-fast internal attributes within substances [24]. For instance, when THz waves interact with conductors or semiconductors possessing significant free-carrier concentrations, it becomes feasible to analyze parameters such as carrier densities [25] and electron scattering time [26], within the THz frequency range of these materials.

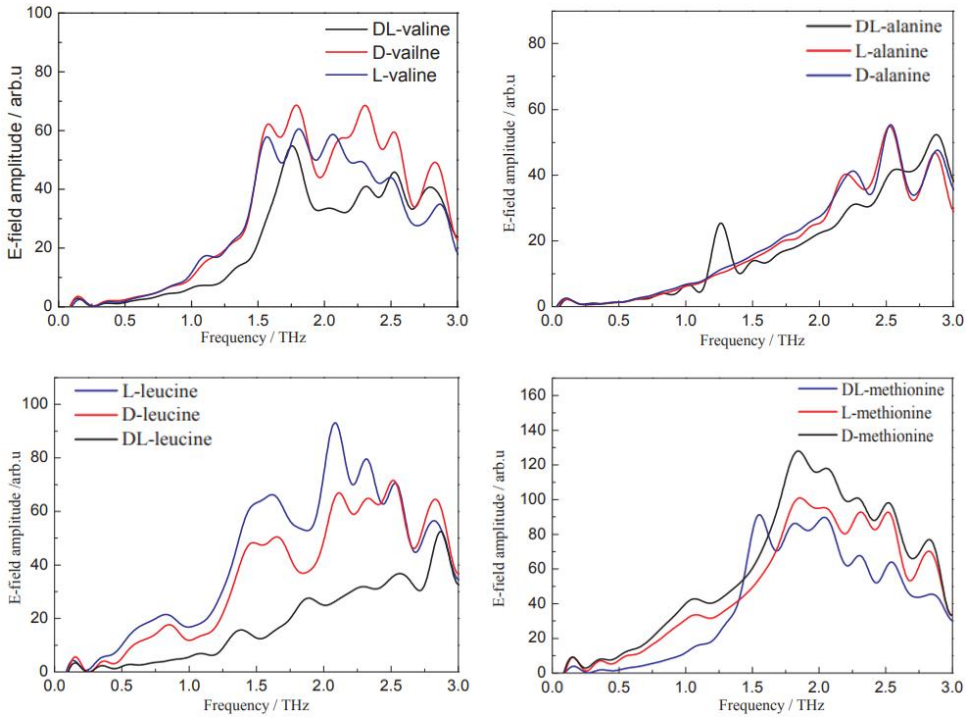

Figure 1.4 THz transmission spectra of different types of DNA molecules [27].

Moreover, the distinctive 'fingerprint' interaction exhibited by THz waves when interacting with specific media provides a valuable approach for exploring energy-level structures, discerning resonance structures, and investigating molecular rotational and vibrational energies. This inherent characteristic bestows THz spectroscopy's remarkable capacity to function as a productive tool, facilitating the precise differentiation and quantification of intricate molecules or complex composite materials. Notably, THz spectroscopy's aptitude stems from its ability to isolate transition levels with a higher granularity than the infrared spectrum [20].

For instance, THz waves directly correlate with the energy absorption characteristics of amino acids and polypeptides. Leveraging the distinct attributes of the THz band, it becomes possible to assess the energy absorption profiles of these biomolecules directly. For example, Liu et al. [27] harnessed the THz-TDS system to compile a diverse array of amplitude spectra encompassing various amino acids, such as alanine, methionine, leucine, and valine, spanning the spectral region of 0.1 to 3 THz, as visually depicted in Figure 1.4. The measured spectral data from this study underscores that despite exhibiting structural resemblances, which are difficult to distinguish in other characterization methods, discernible dissimilarities manifest in the THz absorption spectra of these amino acids. As evident in Figure 1.4, distinct peaks emerge in the absorption spectra of individual amino acids, concurrently accompanied by divergent absorption patterns and associated energy levels.

Importantly, most THz spectroscopic measurements rely on detecting analogue signals proportional to the waves' propagation after interacting with the materials under evaluation, which is an indirect form of measurement. This indirect measurement is susceptible to the influence of the propagation environment. It has the potential for misleading outcomes arising from extraneous materials or unrelated optical interactions within the measurement spot.

1.2.3 THz imaging

As introduced above, the inspiring functionalities of THz wave enable numerous compelling applications of THz imaging in industrial and scientific domains via raster scanning or multi-pixel detection methods [28]. One notable application lies in biomedical inspections, where THz imaging holds promising prospects. By detecting the resonance

modes of proteins and water molecules, it becomes possible to examine the occurrence of pathological changes in tissues [21,22], particularly enabling in-vivo measurements of cancerous cells [29]. Figure 1.5 (a) illustrates a classic biomedical application, showcasing cancer tissue characterization beneath the skin based on its extraordinary water molecular THz absorption within reflection-type imaging.

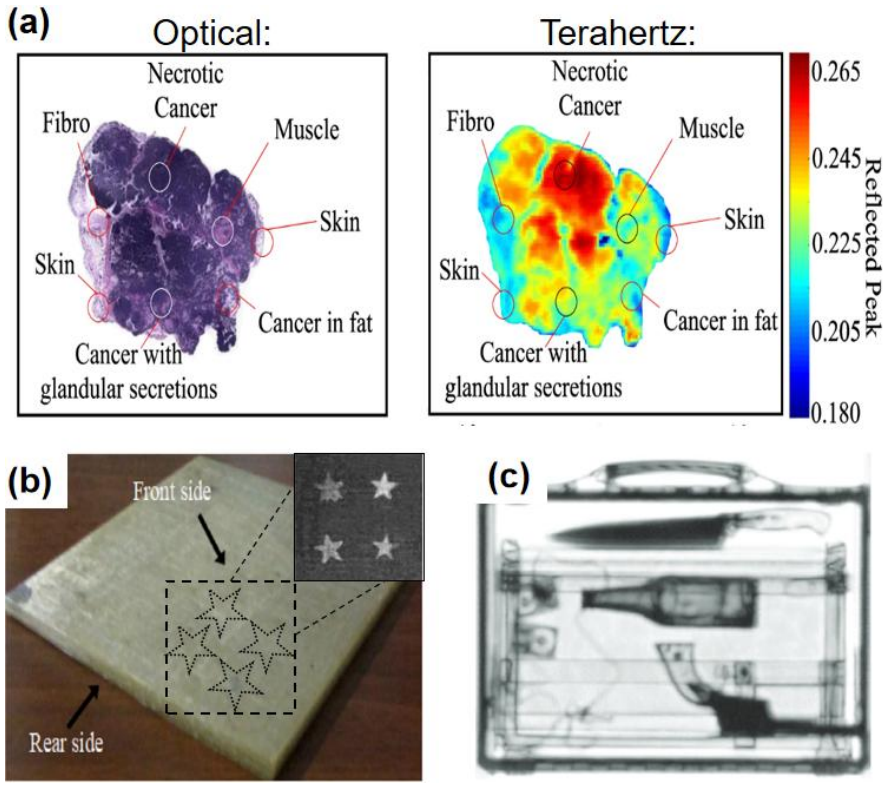

Figure 1.5 THz imaging applications of (a) optical image and THz image of cancer tissue [29]; (b) inspection of thin and multi-depth delamination and foreign inclusion defects inside glass fiber-reinforced polymer [31]; (c) THz transmission image through a case. A gun, a knife and a bottle are clearly identified [32].

Non-destructive testing (NDT) using THz imaging also has emerged as an attractive technology in recent years. As stated previously, many materials, including semiconductors, polymers, and ceramics, are semi-transparent to THz radiation, making THz imaging increasingly popular for investigating internal defects and intermolecular interactions within these materials. It proves particularly valuable for detecting damages in rubbers, coatings, glass fiber-reinforced composites, and other materials widely employed in aviation, aerospace, and high-speed rail applications [30]. Figure 1.5 (b) presents an example of inspecting thin

and multi-depth delamination and foreign inclusion defects inside a glass fiber-reinforced polymer through amplitude and phase analysis via transmission-type THz imaging [31].

Moreover, the 'fingerprint' absorption spectrum and the high reflection from metallic materials of THz radiation render THz imaging an effective security tool for accurately detecting hidden drugs, explosives, and weapons concealed within enclosed objects. Figure 1.5 (c) demonstrates an example of THz transmission imaging for security checks, clearly identifying a gun, a knife, and a bottle due to their low transmission caused by the presence of metal and multi-layer structures [32].

1.3 Challenges and advancements in THz techniques

1.3.1 Challenges in THz techniques

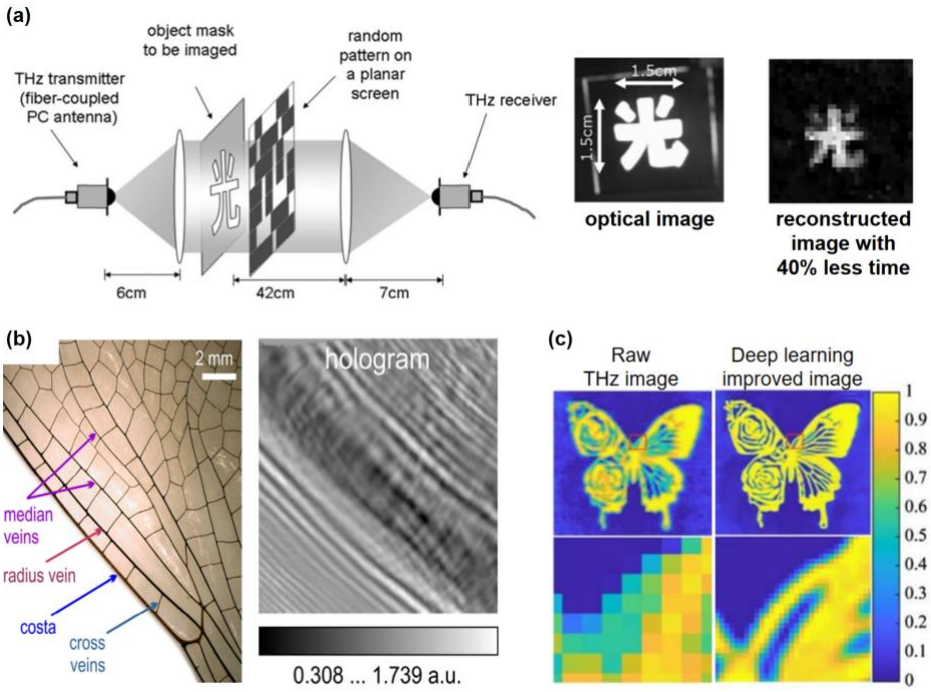

Figure 1.6 THz computational images of (a) schematic of the THz CS imaging and its reconstructed THz image with 40% less time [35]; (b) THz hologram of the dragonfly's hind wing based on phase iterative retrieval method [36]; (c) THz image with better resolution by Resnet deep learning network [37].

As demonstrated previously, THz spectroscopy and imaging have broad applicability spanning various domains, rendering them a pivotal subject of contemporary scientific inquiry.

Notwithstanding their increasing prominence, the realm of THz applications encounters specific challenges rooted in the preliminary phases of THz device development, thus giving rise to the subsequent conflicts:

1. Slow spatial sampling speed versus phase information retrieval: the current widely used versatile THz imaging method can acquire amplitude and phase information based on THz time-domain spectroscopy through raster scanning. Nonetheless, the inherently slow stage motion speed and the unstable THz radiation often hamper dynamic detection and real-time spatial evaluation. In contrast, real-time THz sampling can be achieved using multi-pixel detectors, which only rely on measuring the amplitude of the THz wave, losing the phase information during the data acquisition.

2. Low imaging resolution versus broadband spectral information: the imaging resolution of prevalent THz imaging techniques, such as confocal imaging, encounters inherent limitations dictated by the spatial extent of the THz wave's focal spot. This limitation primarily arises from the diffraction limit, which is a consequence of the extended wavelength of THz waves. The minimum diameter $\boldsymbol{d}$ of the spot can be mathematically expressed as: $\boldsymbol{d}=1.22\lambda/NA$(where λ is the wavelength of the THz waves, as shown in Figure 1.1; NA is the numerical aperture, dependent on the focusing components, typically less than 1). Consequently, the spot size is restricted to the millimeter scale due to the relatively long wavelength of THz waves. Although more sophisticated methodologies, exemplified by four-wave mixing [33] or two-photon absorption mechanisms [34], hold promise in augmenting image contrast through specific optical phenomena, a noteworthy proportion of these techniques necessitate the utilization of narrowband radiation. This employed narrowband radiation engenders a trade-off whereby the acquisition of essential comprehensive broadband spectral information, imperative for characterizing intrinsic physical attributes of materials, such as conductivity or scattering time, is compromised.

To contend with the challenges outlined above, numerous computational methodologies have been proposed by researchers, aimed at curtailing imaging time [35], extracting phase information [36], and augmenting imaging resolution [37]. The visual representation in Figure 1.6 (a-c) delineates the typical applications employed in each respective domain.

However, these computational techniques exhibit conspicuous limitations. For instance, the reconstructed THz image portrayed in Figure 1.6 (a) is accomplished through compressed

sensing (CS) theory [35]. CS entails a numerical paradigm wherein image data is sampled using a bi-dimensional matrix in contrast to the conventional unidimensional sequential methodology. This facilitates real-time imaging via a THz time-domain spectrometer. Nonetheless, owing to the constrained advancement of fast spatial light modulators capable of encoding the spatial matrix, the present timeframe for THz CS imaging still hovers within the second's range. At the same time, strategies geared toward phase retrieval or resolution enhancement hinge on iterative computations or machine-learning based techniques, which may inadequately represent the intricate characteristics inherent to actual propagating THz radiation.

1.3.2 Advancements in THz techniques

The preceding section meticulously elucidated the hurdles encountered in the progression of THz techniques. This section aims to provide a concise yet comprehensive overview of two up-and-coming advanced techniques: THz scanning near-field optical microscope (THz SNOM) and active THz metamaterials-based device. THz SNOM is a novel technique for improving the spatial resolution of THz spectroscopic and imaging applications without losing phase information. At the same time, the THz metamaterials-based device provides a versatile approach for tailoring THz components with different extraordinary performances, suggesting an effective way to overcome the abovementioned challenges.

1.3.2.1 THz SNOM

Considering the THz band encompasses wavelengths ranging from 30 to 1000μm, the minimum resolution of THz wave determined by the diffraction limit typically remains within the millimeter range [38]. This limitation underscores the pressing need to advance THz applications capable of attaining high spatiotemporal resolutions, thereby facilitating investigations at the micro-nano scale.

THz SNOM adeptly overcomes the diffraction limit inherent in conventional THz techniques and provides a paradigm for directly measuring the optical interaction proximate sample. THz SNOM is achieved by measuring evanescent waves rather than relying on only propagating waves, as in traditional THz spectroscopy.

The distinction between propagating and evanescent waves lies in their fundamental

characteristics. The propagating wave, whose amplitude decreases in an inverse relationship with the distance from the emission source, carries energy and propagates through space but lacks detailed field information on the sample under investigation. Conversely, the evanescent waves, confined to the proximity of the electric field source (typically, it's the sample surface being illuminated in the measurement), do not propagate with energy flow but contains intricate field information about the sample. The nonradiative field $U(x, y, z, t)$ composed of evanescent waves can generally be written in the following form [39-41]:

$$U(x, y, z, t) = A(x, y, z)\, e^{-i(k_x x + k_y y)} \cdot e^{-\frac{z}{d}} \cdot e^{i\omega t} \tag{1.2}$$

Where $A(x, y, z)$ denotes the amplitude of the field at the specified spatial coordinates (x, y, z). The first exponential term $e^{-i(k_x x + k_y y)}$ encapsulates the propagation dynamics of the evanescent wave within the x-y plane, corresponding to the sample surface. Subsequently, the second exponential term $e^{-\frac{z}{d}}$ describes the evanescent wave's behavior along the z-direction, delineating its attenuation as it progresses from the sample surface. The attenuation parameter, ***d***, is intrinsically tied to the sample's unique properties and structural configuration. Lastly, the third exponential term $e^{i\omega t}$ elucidates the temporal relationship of the evanescent field.

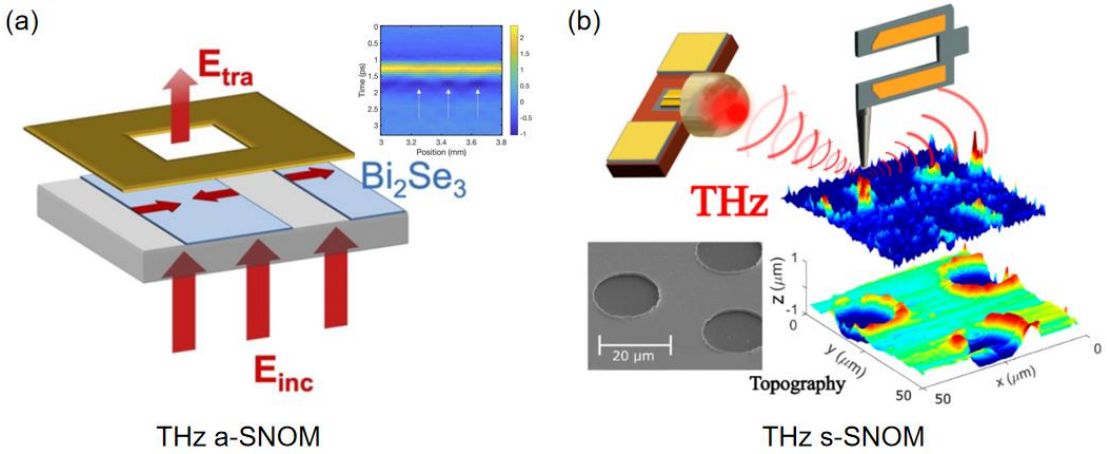

Figure 1.7 Schematics of operating THz SNOM of (a) THz a-SNOM [42], (b) THz s-SNOM [43] in probing sample within μm size.

The advancement of THz SNOM is intricately tied to the generation, detection, and manipulation of evanescent waves in the near field. Figures 1.7 (a-b) delineate the principal

technological avenues and their acquired images for THz SNOM, encompassing THz aperture SNOM (THz a-SNOM) [42] and THz scattering SNOM (THz s-SNOM) [43].

Typically, THz a-SNOM [42,44-46] employs subwavelength apertures at the THz wave transmission terminus to confine and amplify the optical interaction before it engages with the sample surface. The spatial resolution facilitated by this technique spans from a few micrometers up to 100 μm. This modality offers an array of aperture near-field probe alternatives, including physical apertures [42], dynamic apertures [44] and metamaterial configurations [45]. Fundamentally, the accuracy of THz a-SNOM derives from the resolution capabilities linked to the spatial proportions of the aperture. Apertures with diminished dimensions yield superior localized probing attributes, augmenting resolution capabilities.

Nonetheless, a caveat emerges that reducing the aperture size inversely affects THz transmittance, leading to a concomitant decline. This decrement in transmittance subsequently limits the attainable resolution. Hence, achieving optimal imaging fidelity and spatial resolution demands a reasonable balance among the aperture's size, the employed spectral bandwidth, and the efficiency of near-field coupling.

Unlike THz a-SNOM, where the THz wave directly couples to the near-field surface via the aperture, THz s-SNOM [43, 47-50] relies on the incident THz wave. Capitalizing on the subwavelength spatial scale between the probe and the sample, this method harnesses scattering to capture and characterize the subwavelength-scale intricacies of the sample's surface. The main mechanism of operating THz s-SNOM can be viewed as below [47]:

In the near field implementing THz s-SNOM, the interplay between the irradiated tip and the sample surface within the proximity of the tip is described by a net dipole moment, $\boldsymbol{p}$, oriented vertically. Specifically, the $\boldsymbol{p}$ value arises from the synergy of the dipole moment $\boldsymbol{p_0}$—induced by the incident electric field—and the dipole moment $\boldsymbol{P_{nf}}$, resulting from near-field effects. The intensity of the near-field scattering signal, $\boldsymbol{E_{sca}}$, is proportional to the magnitude of $\boldsymbol{p}$. In addition, given a constant intensity of the incident electric field, the magnitude of $\boldsymbol{E_{scat}}$ is intimately tied to the distance $\boldsymbol{h}$ between the tip and the sample surface. The near-field effects become negligible if the $\boldsymbol{h}$ exceeds the tip's radius $\boldsymbol{R}$ substantially, rendering themselves nearly imperceptible. Conversely, as the $\boldsymbol{h}$ narrows and approaches zero, the near-field interaction amplifies, leading to a corresponding surge in the $\boldsymbol{E_{sc}}$ intensity.

Achieving imaging of the sample surface entails a meticulous scanning process,

capturing the near-field scattering signal $\boldsymbol{E_{scat}}$ at each point. However, a pivotal challenge arises from the relative weakness of the $\boldsymbol{E_{scat}}$ signal compared to background noise, harnessing THz s-SNOM for high-resolution imaging.

1.3.2.2 Active THz metamaterial-based devices

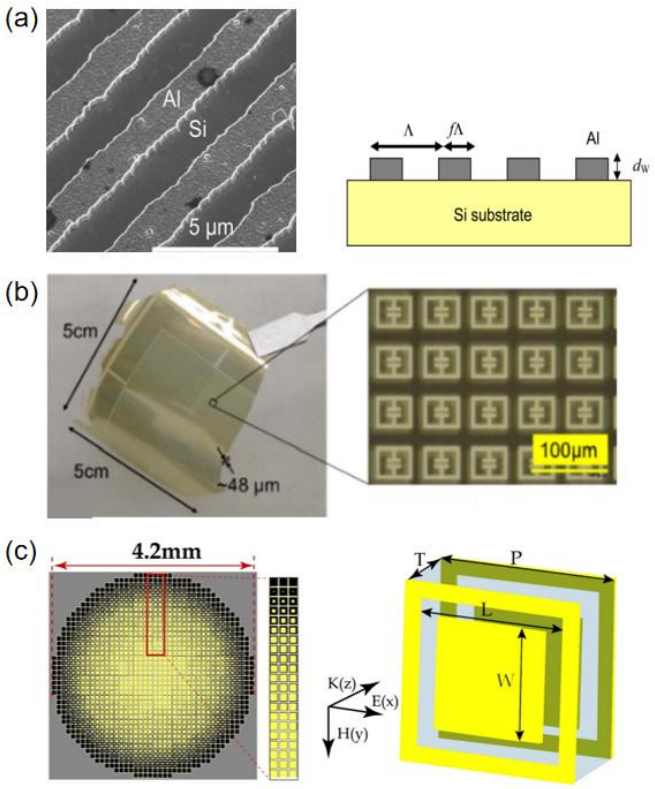

Figure 1.8 Various THz metamaterial schematics with different functions of (a) THz polarizer [64]; (b) THz quarter-wave plate [65]; and (c) THz lens [66].

Metamaterial is a kind of artificial composite consisting of macroscopic ensembles of periodically arranged structures, which act as effective media with the size of approximately one-tenth of the impinging electromagnetic wavelength. Notably, electromagnetic characteristics of metamaterial can be altered merely by adjusting the dimensions or geometries of its periodic structures, offering design flexibility across vast segments of the electromagnetic spectrum.

Metamaterials have emerged as a pivotal area of contemporary research following the seminal demonstration of negative refraction through a three-dimensional composite structure consisting of split-ring resonators (SRRs), a feat unattainable with natural materials. This

groundbreaking development underscores the unique potential of metamaterials to manipulate electromagnetic waves in ways that extend beyond the capabilities of conventional materials, thereby opening new avenues for innovation in various technological fields. The advanced metamaterials promise a more streamlined and integrative approach to photonics, catering to a broad spectrum of applications. Key areas of exploration include metalenses [52-55], perfect absorbers [56-59], and invisibility cloaks [60-63], to name a few.

Particularly in the THz domain, the absence of natural materials exhibiting extraordinary responsiveness to THz waves makes metamaterials invaluable. The flexibility provided by adjusting the periodic structures scale to tailor metamaterials to resonate within the THz spectrum precisely brings significant convenience in the THz applications. In addition, because the unit cell periodicity of THz metamaterials typically ranges from a few to several hundred micrometers, the fabrication and processing of metamaterial, such as optical lithography, is much easier to be implemented compared to higher frequency electromagnetic bands. Therefore, various THz optical components based on metamaterials with diverse functionalities, including THz polarizer [64], THz quarter-wave plate [65] and THz lens [66], are developed, as shown in Figure 1.8.

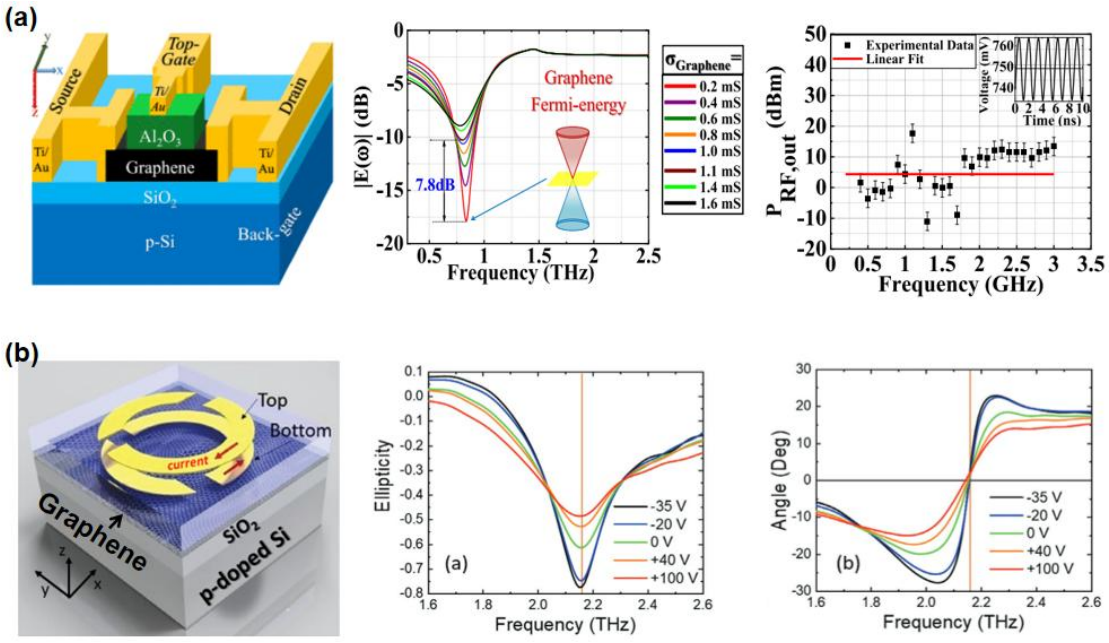

Figure 1.9 The schematics and performance of two graphene-metamaterial structured THz devices: (a) ultrafast modulator [71], (b) chirality controller [72].

In the early stages of metamaterial research, the primary emphasis was passive metamaterials, characterized by specific periodic structures that dictate distinct relative permittivities and magnetic permeabilities, engendering predetermined resonance responses. Even though passive metamaterials allow researchers to customize overall material properties through deliberate design, they fall short when dynamic adaptability and flexibility are requisite in the designs. Consequently, myriad methodologies have been proposed and developed to achieve dynamic control of active metamaterials.

At its core, the control mechanisms for active metamaterials can be categorized as optical, electrical, thermal, or mechanical, each contingent upon the specific design parameters. Disregarding the mechanical method, which typically alters the metamaterial's geometry, the optical, electrical, and thermal approaches dynamically modulate optical properties, encompassing refractive index, damping loss, or conductivity, inherent to the materials employed within the metamaterial configurations. In the realm of THz technology, various tunable materials such as VO_2 (modulated thermally) [67-68], liquid crystal (modulated electrically) [69-70], graphene (modulated electrically and optically) [71-75], 2DEG (modulated electrically and optically) [76-77], and superconductors (modulated thermally) [78-79] are predominantly employed in the construction of active metamaterials.

Graphene has emerged as a promising material due to its unique attributes. This includes its capability for broadband tunability within the THz range, ultra-rapid electron transport, and linear bandgap absorption. A comprehensive elucidation of graphene is later presented in Chapter 4. Capitalizing on these characteristics, a myriad of graphene-based metamaterials has been developed, targeting diverse THz applications, encompassing ultrafast modulators [71], chirality controllers [72], swift detectors [74], and perfect absorbers [75]. Figures 1.9 (a-b) delineate the schematics of two electrically controlled devices founded on the graphene-metamaterial structure. Specifically, Figure 1.9 (a) portrays a THz ultrafast modulator adept at achieving an electrical modulation speed reaching 3 GHz, coupled with a modulation depth of 7.8 dB [71], and Figure 1.9 (b) exemplifies a chirality controller designed to modulate chirality actively [72].

1.4 Thesis overview

This thesis delves into various configurations of ultrafast THz TDS techniques, focusing on probing the optical interactions of advanced natural materials and sophisticated photonic structures. The intent of this exploration is twofold: to establish a framework for expanding THz applications in industrial applications, and to introduce advancement of various materials and metamaterials within the THz domain to address the previously mentioned challenges.

This thesis is divided into 7 Chapters, and the details of each chapter are explained below:

In Chapter 1, the foundational principles of THz wave are briefly presented, followed by an exposition of the various techniques for THz radiation generation. The ensuing discourse outlines the myriad applications utilizing THz waves and emphasizes the attendant challenges in communication, spectroscopy, and imaging. In the quest to advance THz technologies, the chapter thoroughly discusses advanced methodologies, specifically scanning near-field spectroscopy and utilizing active metamaterials.

Chapter 2 embarks on a comprehensive discussion of THz TDS, emphasizing its analytical capabilities in characterizing a range of materials. The discussion delineates prevalent radiation and detection techniques, spotlighting configurations such as the photoconductive antenna and nonlinear crystals. The chapter further articulates the standard data analysis procedure in deducing specific optical parameters. It also elaborates on the advanced functionalities of the Menlo THz TDS.

Chapter 3 presents two investigative studies leveraging different configurations of the Menlo THz TDS to explore the forefront of materials manufacturing—these practical endeavors aimed to promote bio-based nanofiber composites and additive metal manufacturing advancements. The evaluated results validate the potential of a sustainable nanofiber-based THz absorber with an impressive absorption rate, and propose a novel method for discerningly appraising the surface roughness in industrial additive manufacturing.

Chapters 4 and 5 are dedicated to realizing the capabilities of THz-TDS in the assessment of photonic structures, with a specific emphasis on metamaterials. Chapter 4 provided an exhaustive discourse on the foundational design principles of various metamaterials, highlighting functionalities like enhanced Q-factors and improved absorption.

This was complemented by a series of rigorous Finite Element Method (FEM) simulations, facilitated via the COMSOL software, to optimize the optical responses of the proposed metamaterial designs. The simulation delved deep into aspects of geometry, unit cell delineation, meshing paradigms, and the resultant outcomes.

In Chapter 5, the narrative explores the sophisticated micro-fabrication techniques requisite for metamaterial realization from rudimentary materials. The discourse thoroughly examines the principles and detailed protocols underpinning techniques such as standard photolithography, laser writing, reactive ion etching (RIE), atomic layer deposition (ALD), and the deposition and transfer of graphene. The chapter culminates with exemplary processes and resultant structures, explicitly focusing on fabricating asymmetric split-ring resonators (ASDR) composed of Au or NbN, and graphene-based active modulators.

Chapter 6 unveils an innovative methodological approach, applying a broadband TDS analysis to the individual ASDR designed and fabricated from Chapters 4 and 5, through a THz aperture scanning near-field optical microscope (a-SNOM). The insights from the THz a-SNOM are juxtaposed against data from far-field Menlo THz-TDS measurements. The chapter underscores the pioneering capabilities of the THz a-SNOM, enabling detailed mapping and quantitative evaluation of localized resonator modes with a few μms spatial resolution surpassing the limit of aperture size.

Chapter 7 culminates the discussions and findings in Chapters 1 through 6 and introduces two subsequent research endeavors aligned with the thesis's objectives. The initial investigation delves into the cryogenic THz a-SNOM/s-SNOM analysis on superconductor metamaterials. The metamaterials have been meticulously characterized using the cryogenic Menlo THz TDS, showcasing a commendable high Q-factor matched with simulation predictions. The further establishment of this study aims to develop precise single resonator applications in the THz field. This investigation centers on graphene THz high harmonic generation. This study was initially executed leveraging the capabilities of high-field THz TDS in tandem with the expertly fabricated active graphene-metamaterial modulators. Preliminary outcomes and envisaged enhancements to the experimental procedures undertaken at Warwick University are expounded upon.

Chapter 2 Terahertz Time-domain Spectroscopy

A highly efficient THz testing system, characterized by a high signal-to-noise ratio (SNR), broad spectral coverage, and rapid coherent measurement capabilities, is indispensable for comprehensively evaluating materials' spectral properties within the THz frequency range. Successful THz testing systems hinge on the effective generation and sensitive detection of THz waves. The generation and detection of THz waves in the time domain are primarily achieved through two main techniques: semiconductor-based electronic methods and ultrafast optical technologies [80-81].

Ultrafast optical methods are particularly noteworthy for their capacity to produce and detect THz waves with substantial bandwidth and impressive SNR [81]. The preferred approaches for evaluating materials using THz waves typically involve ultrafast spectroscopy techniques like THz-TDS [80-81] or Fourier Transform Far-infrared Spectroscopy (FTFIR) [82]. These methodologies offer the distinct advantage of measuring both the amplitude and phase information of transmitted or reflected THz waves, thus providing direct insights into parameters such as complex permittivity and transmission coefficients. It's important to note that while FTFIR boasts a broader spectral range compared to THz-TDS, it has seen somewhat limited adoption due to inherent drawbacks such as operational complexity, lower SNR, and incoherent phase measurement [82]. Consequently, the spectroscopic measurements referenced in this thesis primarily use THz-TDS for its operational efficiency and superior performance.

This chapter provides an overview of THz-TDS, which encompasses key information about the various THz emitters and detectors based on different mechanisms, the typical setup, and the underlying principles of coherent measurement. Following this, the specific THz-TDS system employed in this thesis is demonstrated. In addition, the exploration of its extended capabilities, including integrated cryogenic functionality operating at temperatures as low as 4 K, and 2D imaging systems capable of both transmission and reflection mode operation. These enhancements and functionalities are central to the research conducted within this thesis.

2.1 THz radiation and detection based on photoconductive antenna and nonlinear crystal

In general, the generation of THz pulses in THz-TDS systems relies on the utilization of either the transient current in a photoconductive antenna (PCA) [83,85-89] or the optical rectification effect in nonlinear crystals [84,89-91]. Conversely, the detection of THz fields is also achieved using either a photoconductive antenna or a nonlinear crystal, but with reverse operations. The following sections discuss the mechanisms of applying PCA or nonlinear crystal for pulse generation and detection.

2.1.1 PCA THz radiation

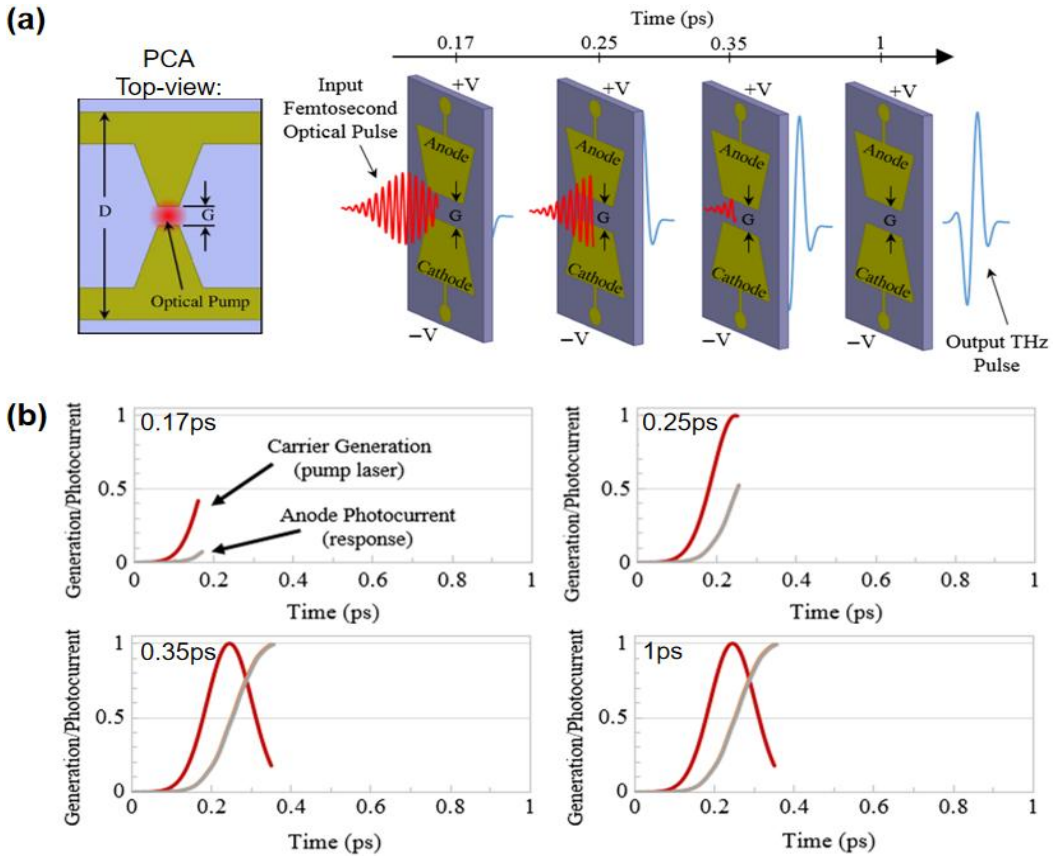

Figure 2.1 (a) Schematic diagram of PCA generating terahertz pulses and (b) the simulated photocurrent change curve with time [83].

A PCA is an electronic switch that exploits the increase in electrical conductivity of semiconductors when exposed to a pumping laser. This phenomenon, photoconductivity, is driven by generating free charge carriers (electrons and holes) in the semiconductor due to

incident photons. These carriers must be numerous enough to initiate THz radiation.

Figure 2.1 (a) provides a schematic diagram of a PCA configuration and outlines the process of generating THz pulses using a PCA [83]. The figure shows that a PCA typically consists of a semiconductor substrate and two metal electrodes affixed to the substrate. THz pulse generation begins with the exposure of a powerful pumping femtosecond laser (FSL) to the semiconductor region between the two electrodes.

Before laser exposure, a DC bias voltage is applied between the two electrodes. When the laser irradiates the semiconductor, it generates many photo-induced carriers within the substrate. These excited photo-carriers are accelerated by the existing electric field created by the DC bias, resulting in a subpicosecond current that radiates outward as a single-cycle coherent THz pulse, resembling a dipole function. The time-varying electric field intensity of the THz pulse generated by the PCA is determined by the derivative of the transient photocurrent concerning time [83, 85]:

$$E_{THz} \approx \frac{1}{4\pi\epsilon_0 c^2 r}\frac{dJ_t}{dt} \tag{2.1}$$

ε_0 is the vacuum dielectric constant, r is the distance between the far-field point and the antenna, c is the speed of light, and J_T is the instantaneous current density between the two electrodes of the antenna.

As shown in Figure 2.1 (b) [83], the rise time of the transient photocurrent is directly proportional to the rise time of the pumping laser pulse. However, when the photocurrent reaches its peak value, its decay time is determined by the lifetime of the photo-induced carriers in the semiconductor. In other words, it's the carrier lifetime that mainly influences the duration of the photocurrent. Semiconductors with short carrier lifetimes, typically on the order of sub-picoseconds, are preferred for THz pulse generation because they can produce shorter and wider bandwidth THz pulses. Examples of such materials include LT-GaAs (low-temperature grown gallium arsenide) [86], RD-SOS (radiation-damaged silicon-on-sapphire) [87], and InP (indium phosphide) [88].

2.1.2 PCA THz detection

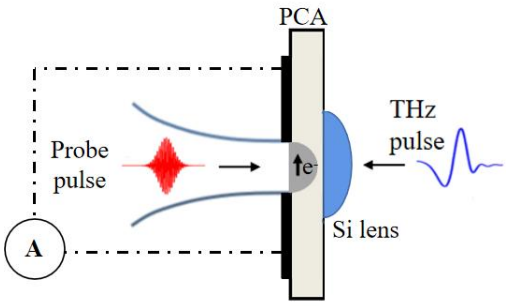

Figure 2.2 Schematic representation of THz pulse detection with a PCA

The PCA detection method is like its transmitter approach, but the DC bias is replaced by a sensitive galvanometer, as shown in Figure 2.2. At the beginning of detection, the probe laser is incident on the substrate to generate free carriers, reducing the resistance between the two electrodes [89]. The THz pulse incidence onto the PCA can generate transient bias voltage among the electrodes, raising a time-dependent detectable current whose magnitude is proportional to the intensity of the incident terahertz electric field and the free carriers' concentration within the substrate as [83]:

$$J(t) \propto N(t) * E_{THz}(t) \tag{2.2}$$

2.1.3 Terahertz radiation based on optical rectification effect

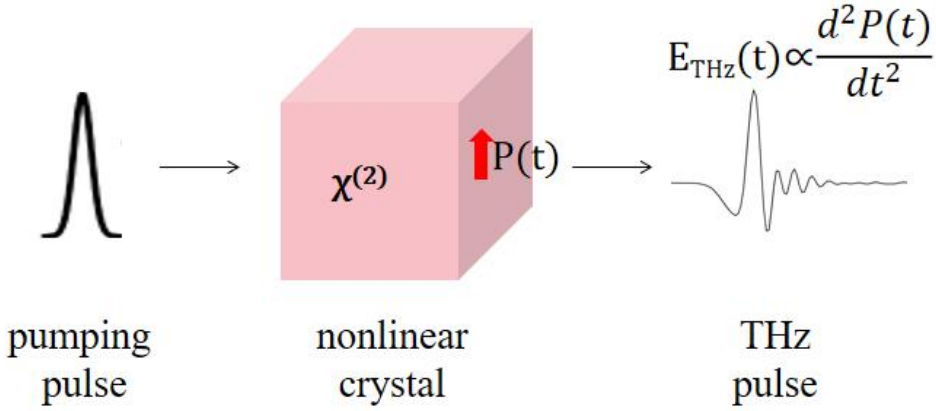

Figure 2.3 Schematic diagram of terahertz pulse generated by optical rectification effect with second-order nonlinear material.

The optical rectification (OR) effect in nonlinear crystals is another common method for generating THz pulses using ultrafast optical techniques. Unlike the PCA method, OR relies solely on the power of the pumping light to generate the THz pulse and does not require the application of a DC bias. Several parameters, such as the orientation of the nonlinear crystal with respect to the incoming electric field, the length of the crystal, and the crystal's temperature, also influence the THz pulse generation in OR [90,91].

OR is a second-order nonlinear phenomenon that involves the nonlinear interaction between a material and two photons, denoted as ω_1 and ω_2, provided by a powerful incident pumping laser. The wavelengths of these photons are characteristic and dependent on the phase-matching condition specific to the nonlinear crystal with a certain thickness in use. This interaction leads to the induced polarizations of the mixed frequency ($\omega_1+\omega_2$) and the beat frequency ($\omega_1-\omega_2$) within the nonlinear material. When ω_1 equals ω_2, the beat frequency produces a "DC" polarization that is proportional to the intensity of the pumping light. If the bandwidth of the pumping laser spans the THz range and its intensity varies over time, it can induce an oscillation in the "DC polarization," resulting in the generation of a terahertz pulse, as illustrated in Figure 2.3.

The electric field strength $E_{THz}(t)$ of the radiated THz pulse is proportional to the second-order differential of the induced polarization P(t) with respect to time. This relationship is further explained by the second-order nonlinear susceptibility, $\chi^{(2)}$, of the nonlinear material and the time-varying intensity of the pumping laser, $I(t)$ [89-90]:

$$E_{THz}(t) = \frac{d^2P(t)}{dt^2} = \chi^{(2)} \frac{d^2I(t)}{dt^2} \tag{2.3}$$

As mentioned above, the realization of the efficient OR THz radiation is also dependent on the phase-matching condition of the material, which requires the group velocities of the pumping laser and the generated THz pulse to be the same. Materials such as $LiNbO_3$ (Lithium niobate) [92], ZnTe (zinc telluride) [93], GaAs (gallium arsenide) [94] and GaSe (gallium selenide) [95] with precisely prepared sample thickness are found to be the proper materials meeting the above requirements.

2.1.4 Terahertz detection based on free-space electro-optic sampling

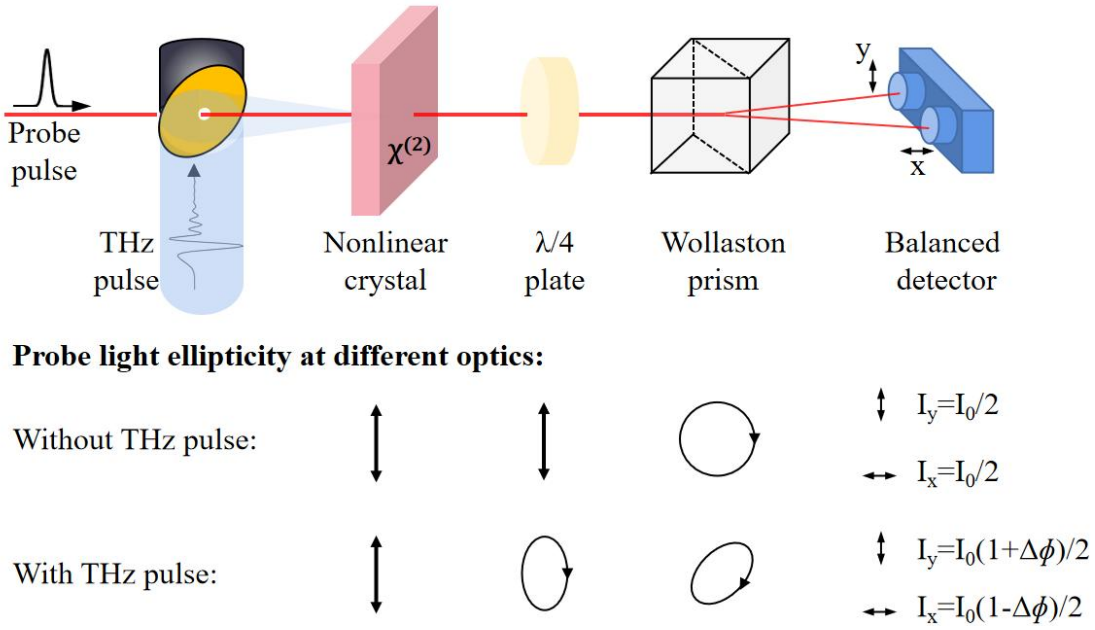

Figure 2.4 Schematic of applying FES for THz wave detection.

Free-space electro-optic sampling (FES) is a THz wave detection method based on a second-order nonlinear process [89,96]. This detection process relies on the refractive index change of a nonlinear material within the near-infrared band induced by the incidence of a THz pulse. This change in refractive index alters the circular-polarized detecting light's ellipticity, which a balanced detector can then detect. Here's how the FES detection procedure works, as shown in Figure 2.4:

1. When the THz pulse interacts with the nonlinear material, it causes a change in the refractive index of the material. This change is proportional to the strength of the THz pulse; 2. The altered refractive index affects the ellipticity of circularly polarized detecting light that passes through the nonlinear material.; 3. The probe light, which has changed ellipticity due to the THz pulse, is passed through a Wollaston prism. This prism splits the circular-polarized beam into two linear-polarized beams with orthogonal polarizations; 4. The two split beams are then detected by a balanced detector. The detector measures the intensity difference between the two converted beams, denoted as Is = Iy-Ix, to obtain the relative electric field strength. The ZnTe crystal is commonly used as the nonlinear material in THz FES detection because of its similar refractive index in the far-infrared and visible light bands, which results

in a high signal-to-noise ratio.

2.2 Principles and experimental setup of THz-TDS measurement

2.2.1 Principles of operating THz-TDS

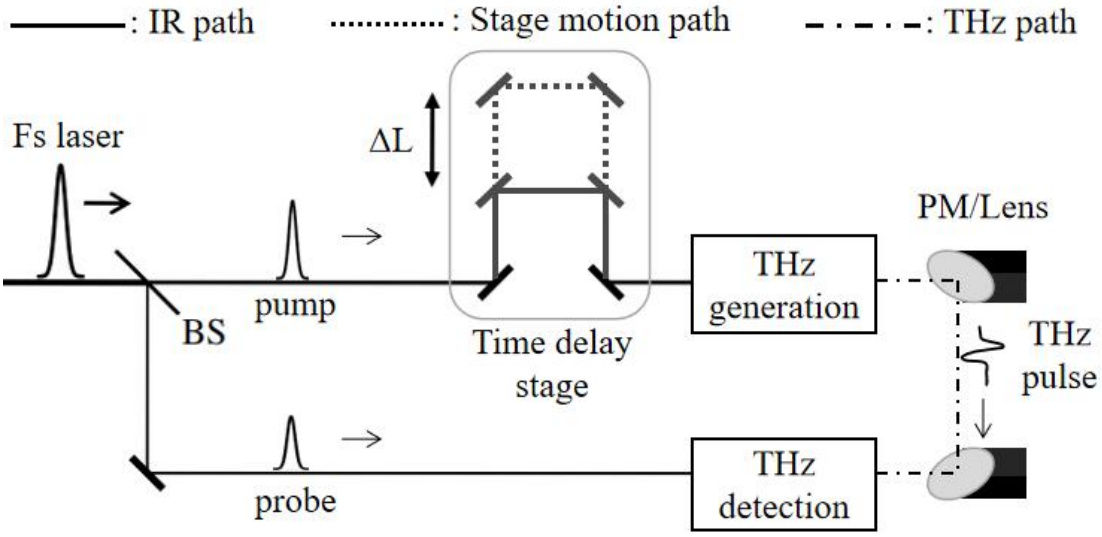

Figure 2.5 Schematic of a typical setup for generation and detection of THz pulses using femtosecond optical pulse; BS: beam splitter, PM: parabolic mirror, ΔL: motion distance of the time delay stage.

The origins of THz-TDS techniques can be traced back to the 1980s, with early research conducted at Bell Labs [97]. THz-TDS operates by employing a femtosecond laser to generate broadband THz pulses and then measures both the amplitude and phase changes of these pulses using a coherent detection method [98]. The resulting digitized pulse signal is transient, discrete, and energy-limited, representing an aperiodic temporal signal. Through Fourier transform, THz-TDS can provide frequency domain information. Therefore, it enables the extraction of a material's physical properties and spectral characteristics, including parameters like thickness and dielectric constant, directly from both the time domain and frequency domain data, without the need for complex techniques like Kramers-Kronig transform [99].

Conventional THz-TDS systems operating in free space necessitate several key components, including a FSL, a THz emitter, a THz detector, a time delay stage, and various

optical elements for collimation and focusing. Depending on the arrangement of these components relative to one another and the measured sample, THz-TDS can be categorized into either transmission or reflection modes. Figure 2.5 provides a schematic of a transmission-type THz-TDS setup and illustrates its working principle.

In both transmission and reflection modes, the underlying principles remain the same [89,99]: THz-TDS emitters and detectors require the incident FSL to initiate their operation (detailed introductions of the emitters and detectors are presented in subsequent sections of this thesis). Consequently, the FSL is divided into two beams using a beam splitter. One of these beams is the pumping laser to activate the THz emitter, while the other is the detecting laser to activate the THz detector.

The pumping laser is first adjusted using the time delay stage, generating a short THz pulse when it impinges on the THz emitter. The time delay stage typically comprises an electrically controlled moving stage with micrometer precision featuring two mirrors. The delayed time, denoted as Δt, can be described by the equation: $\Delta t = 2\Delta L/c$, where ΔL represents the motion distance of the stage, and c represents the speed of light (factor 2 arises from the fact that the optical path is double the translational stage movement). Subsequently, the emitted THz pulse propagates through free space for a certain distance, undergoing two rounds of focusing and collimation via sets of off-axis parabolic mirrors or lenses before reaching the THz detector.

The pulse-induced transients within the THz detector are measured simultaneously with the incidence of the detecting laser. The THz pulse waveform is reconstructed by collecting digitalized signals acquired from the detector at various delayed times. During the experiment, signal collection can be conducted both with and without a sample, ideally positioned at the focus point of the THz beam to maximize interaction.

The implementation of the time-delay stage in the measurement, which is the characteristic feature of THz-TDS, is due to the frequency of THz waves exceeding the maximum frequency response range of conventional electrical sampling instruments (tens of GHzs) [89]. It is inevitable to reconstruct the THz time-domain waveform by successive data collection with different relative times in multiple laser cycles.

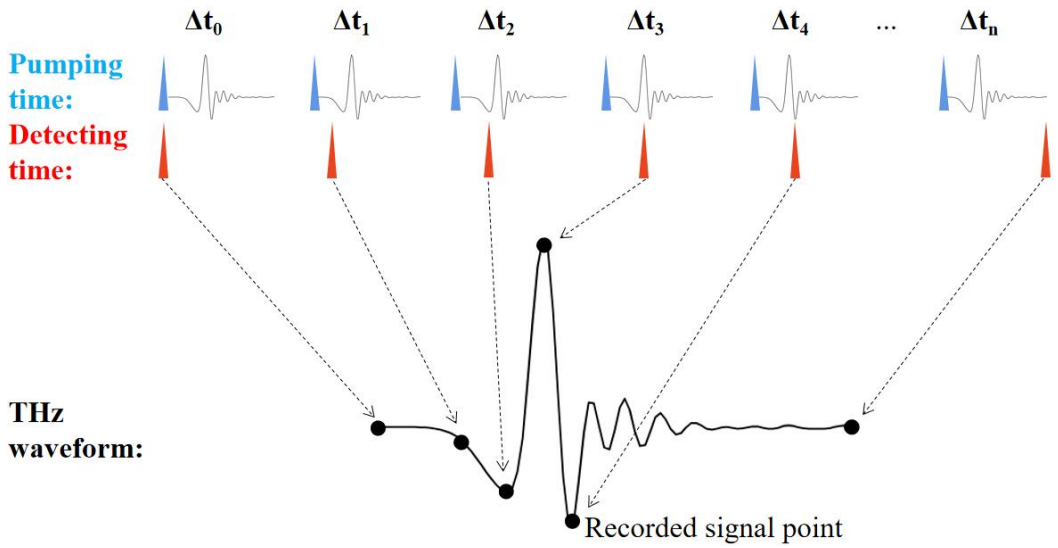

Figure 2.6 THz time domain waveform reconstruction based on equivalent time method.

Figure 2.6 illustrates the principle of data reconstruction in THz-TDS. It begins with the assumption that the total optical path travelled by the pumping light and the THz wave is equivalent to the path of the detecting laser. In this scenario, the detected THz pulse and the detecting laser can simultaneously reach the detector, registering a data point at a specific time delay, denoted as Δt_0. Since the emitted and detected THz pulses originate from the same FSL source and have the same repetition rate, there are no synchronization issues.

In the subsequent pulse cycle, the time delay stage moves a certain distance, resulting in a time difference of Δt_1. THz-TDS captures a new data point representing the THz waveform during this new cycle. This process continues, with the time difference increasing in successive cycles, until it reaches the specified value of Δt_n. As a result, a continuous series of data points is acquired, describing the changes in the detector signal over time. Therefore, the waveform generated by THz-TDS is directly proportional to the THz pulse's relative intensity as a time function. Collecting more data points within a given time range allows a more precise description of the intrinsic THz pulse profile.

2.2.2 Menlo K15 THz-TDS

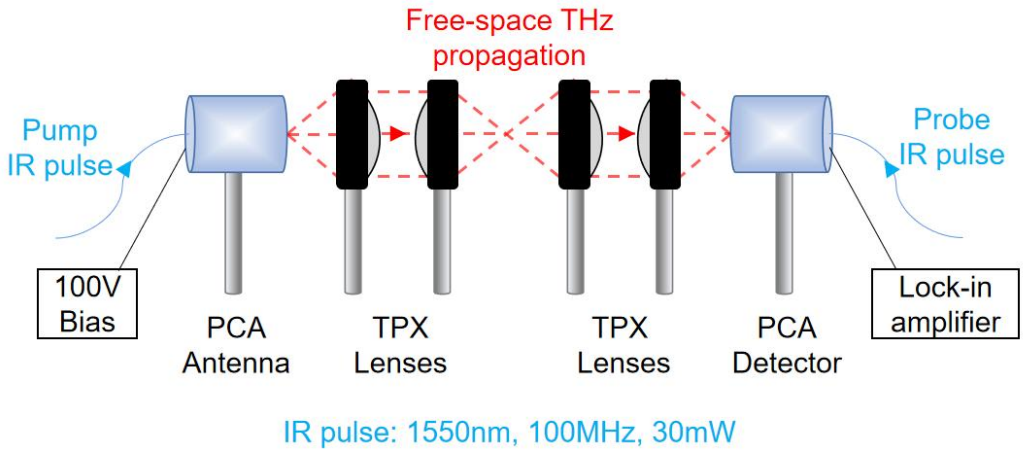

Figure 2.7 Transmission mode set-up of Menlo K15 THz-TDS system.

The THz-TDS system used in this thesis is based on the commercial system Menlo Systems Tera K15 (referred to as "Menlo"). In the transmission configuration, Menlo employs a 1550nm infrared ultrafast laser with a fixed repetition rate of 100 MHz and a maximum power of 30mW at the antenna end, serving as the femtosecond pulse source. The Menlo system's emitter and detector are designed based on the PCA concept and fabricated on LT-InGaAs/InAlAs substrates. The PCA emitter is biased with an additional 100V power supply, while the PCA detector is connected to a lock-in amplifier to enhance its SNR.

The THz light is collimated and focused twice using two sets of TPX50 lenses (made of TPX material with a focus length of 50mm) before being incident on the detector. This setup has a minimum beam diameter of approximately 1-1.2 mm at the focal point. The time domain sampling is accomplished using a fast delay shaker, although it is not shown in Figure 2.7. This delay shaker can achieve a maximum delay time of 800ps with a fixed sampling step of 0.033 ps. This setup allows for collecting 3000 data points for the detected current in a standard raw data file, with each data point corresponding to a 100ps delay time.

Figure 2.8 (a) illustrates the additional functionalities integrated into the Menlo system: two sets of Keithley 2400 Graphical source meters (the electrical connectors are displayed in the picture, and one of the control panels is shown in the inset), an acrylic box for the enclosed N_2 purging and a translation stage.

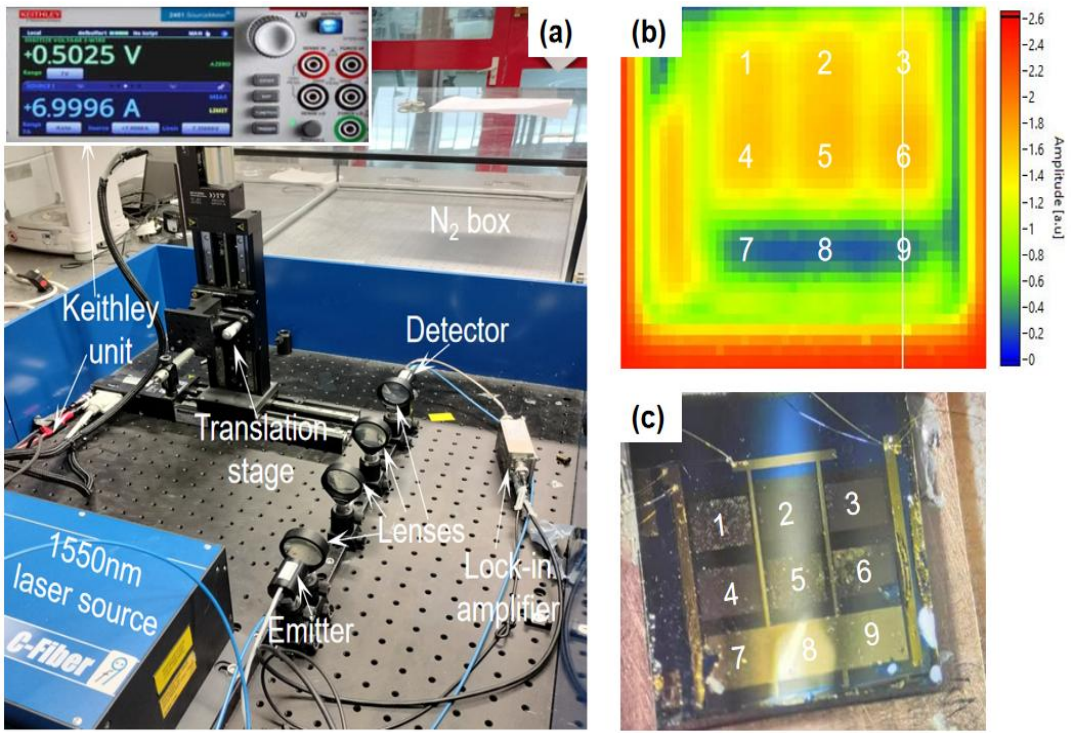

Figure 2.8 (a) The optical picture of Menlo; (b) intensity mapping acquired by Menlo, and (c) optical picture of the fabricated sample. Numbers 1-9 represent the relative positions of nine individual arrays.

The Menlo system has a translation stage that enables sample mapping through continuous data sampling via planar raster scanning. Each pixel point recorded in the mapping result contains complete time domain information relative to its position. This mapping function efficiently identifies and aligns samples based on their distinct spatial intensity distribution. Additionally, it can be used to retrieve various physical properties distributions, such as conductivity, scattering time, etc., from the frequency domain information obtained through Fourier transformation of the time domain waveform.

In the THz TDS experiments assessing the optical interactions of various materials, as illustrated in Chapters 4, 6, and 7, the parameters evaluated are contingent upon their relative positioning. Consequently, a THz map that delineates the spatial intensity distribution proves invaluable for preliminary alignment and sample identification. Figure 2.8 (b) illustrates a map of a typical fabricated sample introduced in this thesis acquired by Menlo system in the transmission configuration, with a raster step of 0.2 mm. In this map, the color bar represents the transmitted electric field intensity. Figure 2.8 (c) shows an optical image of the measured

sample. This sample consists of nine identical arrays, each measuring 1.2x1.2 mm^2, and is uniformly distributed on a 300 nm SiO_2-coated 500 μm Si substrate. These arrays are labelled with numbers 1-9 to indicate their positions in the mapping and the optical image.

Among these arrays, arrays 1-6 are metamaterials designed for high transmission, while arrays 7-9 are patterned for high reflection. This design is reflected in the map, with low transmissive amplitude in areas mostly covered by gold (such as arrays 7-9 and the vertical gold connection bars separating arrays 1-6) and high transmissive amplitude in arrays 1-6. This mapping effectively displays the relative positions of each array. It's important to note that the high transmission shown in the edge area within the mapping corresponds to the free-space area and not the copper holder, as indicated in the optical image.

The other two components, the Keithley source meter and the acrylic box, can enable the simultaneous electrical control of the active samples and provides a closed environment filled by N_2 to remove water absorption lines in the air during the measurement, as discussed in more detail in the next section), respectively.

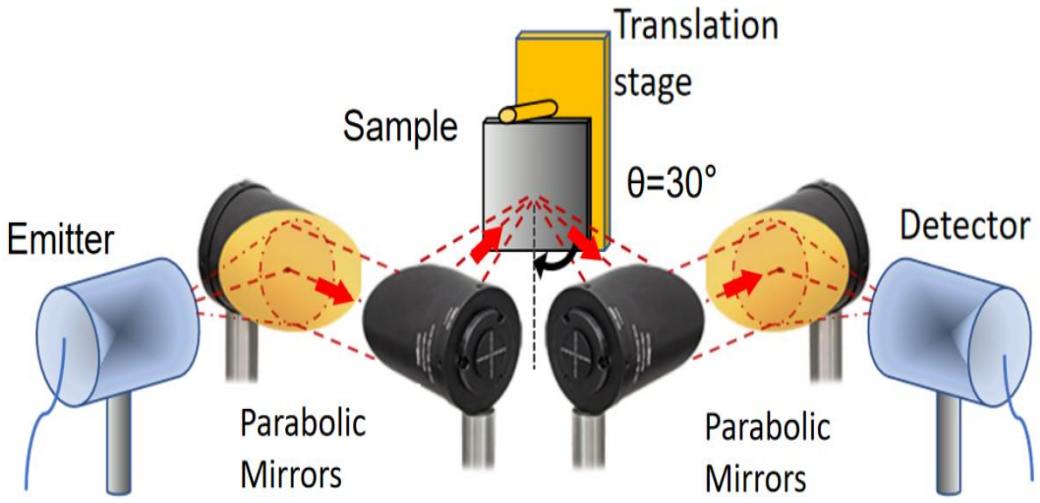

Figure 2.9 Reflection mode set-up of Menlo spectrometer.

Inherent to the fiber couple configuration of the system as a high degree of flexibility, Menlo can also be into the reflection configuration. Figure 2.9 shows the schematic of the Menlo set in reflection configuration for evaluating samples discussed in this thesis. The basic principle of implementing reflection THz TDS is the same as the transmission, excluding the detector measures the wave reflected from the sample surface instead of waves going through

the sample. During the measurement, THz radiation is focused and collected using four 5cm-focal-length gold-coated parabolic mirrors, showing a spot size of 1.5 mm^2 at the focal point onto the sample. The incident angle is kept fixed at approximately 30 deg. With the help of the translation stage, Menlo can also realize spatial mapping in reflection configuration.

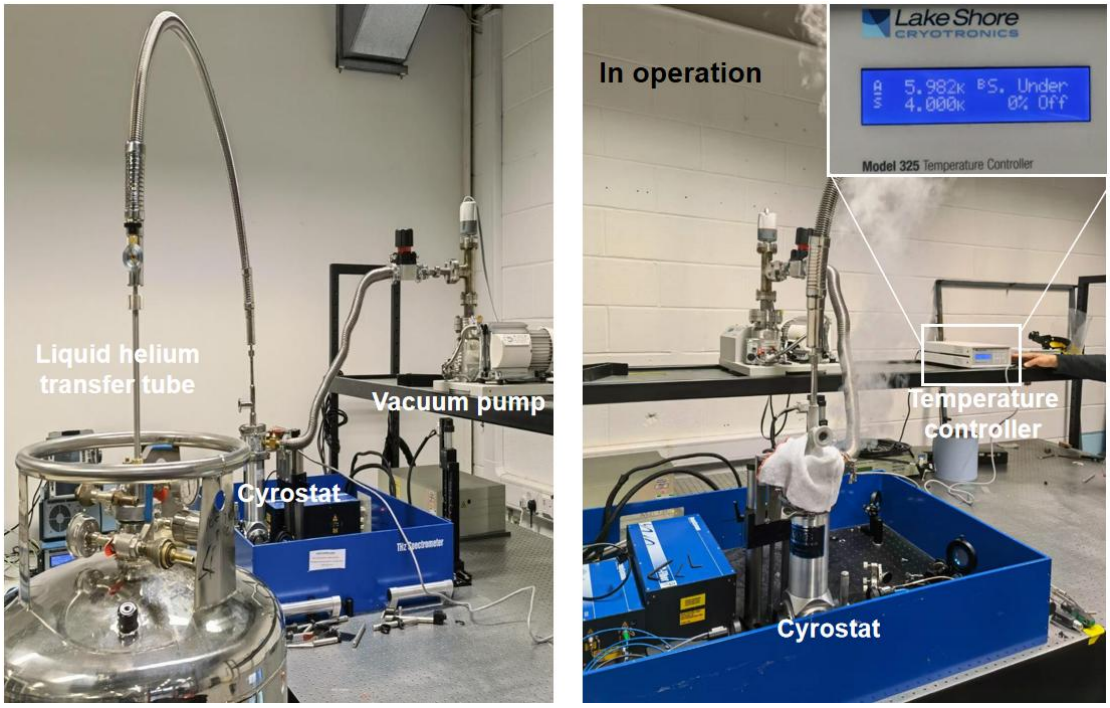

Figure 2.10 Schematic of the cold finger Liquid He cryostat from *Janis*, allowing measurements up to 4 K, integrated in the Menlo system.

To facilitate measurements of superconductor samples operating below their critical temperature (in the case of NbN, at or below 15 K) [100], our experimental setup incorporates a commercial cryostat provided by *Janis*. Figure 2.10 presents a series of optical representations that detail the practical execution of cryogenic THz-TDS investigations, specifically within a transmission configuration.

The specimens under scrutiny are housed within the cryostat chamber, equipped with THz-transparent polyethene windows to facilitate the unimpeded passage of THz waves. These samples are affixed to specialized holders featuring a central 2x2 mm^2 aperture, requiring precise positioning due to the aperture's diminutive dimensions.

The cryostat, mounted to a custom-designed mobile bracket, is strategically positioned midway between two sets of lenses to enable optimal focusing of light onto the sample

surface, thereby optimizing intensity through the sample and aperture.

To allow the transfer of liquid helium and prevent condensation, it is imperative to maintain the cryostat's internal pressure below 10^{-4} Bar, a process facilitated by a vacuum pump. Liquid helium, drawn from an L-He Dewar, is manually regulated via a valve integrated into the transfer tube.

A temperature sensor and electrical heater are affixed to the cryostat's extremity for precise temperature control, linked to a temperature controller supplied by *Lakeshore*. This programmable controller ensures temperature stability with a closed-loop system within a narrow margin of 0.1 K, down to a nominal temperature of 4 K.

2.3 THz TDS data analysis

This section provides a succinct overview of the customary time-domain waveforms and their Fourier-transformed spectrum obtained from the Menlo system across various configurations introduced in the preceding section. Subsequently, the fundamental principle underlying the assessment of material properties through the measured THz signal is elucidated.

2.3.1 Time domain waveforms and Fourier transformation

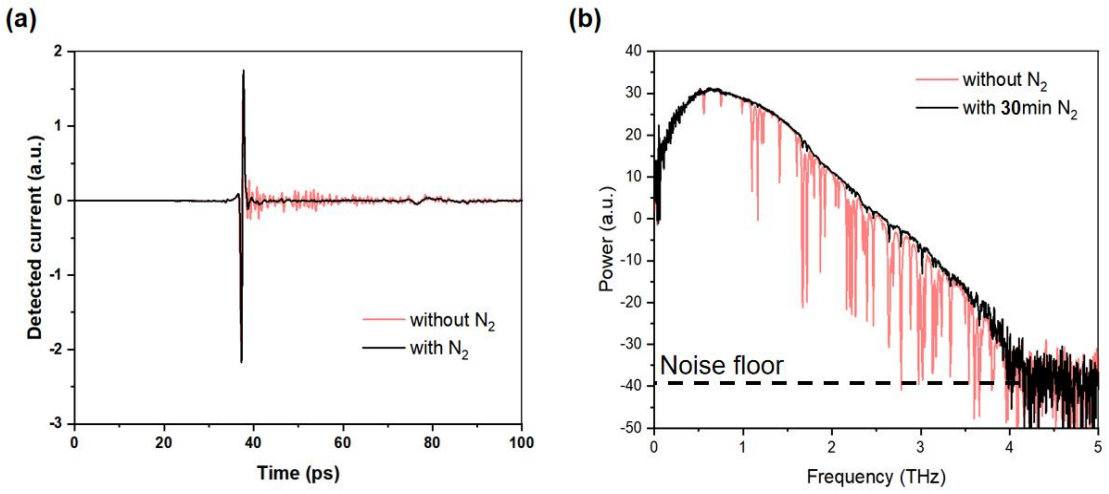

Figure 2.11 (a) Detected time domain currents of THz pulse in transmission type Menlo from without (red) and with (black) N_2 purging. (b) Spectral power content of the measured pulses converted by applying a Fourier transformation. The red and black lines indicate measurements with and without N_2 purging, respectively.

One of the advantages of using THz-TDS is that it can provide sensitive broadband phase and amplitude information simultaneously, which are based on the polarization of the induced current within the detector. This information is crucial for quantitatively evaluating the spectral complex material properties, such as conductivity, refractive index, and permittivity. After Fourier transformation, the acquired time domain waveform retrieves the broadband material's information. The frequency resolution in the Fourier transformation is mainly determined by the total time length T of the processed wavelength as 1/T [101]. However, the sampling rate also determines the spectral amplitude and maximum mathematical supported frequency (the number of the processed data points×step resolution).

For example, Figures 2.11 (a-b) display the time domain waveform in free space and its converted frequency domain information in the range of 0.2-5 THz acquired by transmission type Menlo with and without N_2 purging. The time domain data is obtained within 100 ps and averaged for 30 minutes to improve the SNR, resulting in a frequency resolution of 10 GHz (0.01THz). As shown in Figure 2.11 (b), the valid spectral bandwidth is in the range of 0.2- 4 THz, yielding a good signal-to-noise ratio in power up to 70 dB around 0.6 THz.

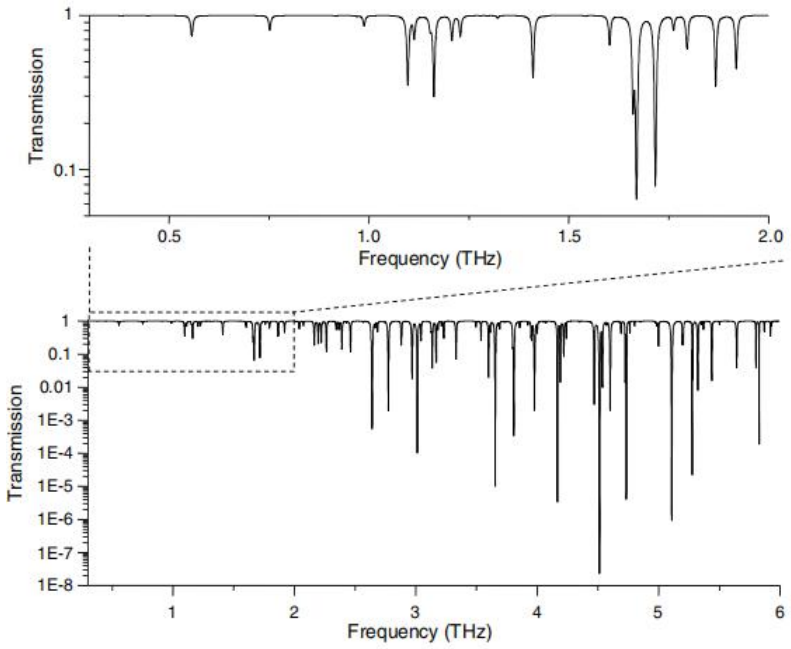

Figure 2.12 Water vapor transmission spectrum from 0.3 to 6THz [89].

In the context of THz TDS applications for molecule sensing or high Q-factor mode

characterization, achieving a clear spectrum devoid of undesired absorption states is imperative. As the energy of THz waves corresponds to the vibrational and rotational energy transitions of various gas molecules, such as H_2O [89,102], CO_2 [103], and CO [104], the resulting spectra often contain multiple absorption lines. These absorption lines can significantly diminish the signal-to-noise ratio at their respective frequencies. Figure 2.12 illustrates the conventional water vapor absorption spectrum within the 0.1-6 THz range [89], featuring various absorption lines evident in the recorded spectrum without N_2 purging.

In contrast, the spectrum obtained after a 30-minute exposure to N_2 within the acrylic box (black line in Figure 2.11(b)) effectively mitigates the water vapor effects absorption lines, such as those observed at 1.1, 1.6, and 1.7 THz (the red line in Figure 2.11(a)) within the range preceding 3 THz. Further improvement in the measured spectrum can be attained through extended N_2 purging periods. However, it's worth noting that such approaches are often time-consuming and operationally challenging. Consequently, all TDS results presented in this thesis, acquired in the transmission configuration, are generally conducted within an environment after 30 minutes N_2 purging unless specified otherwise.

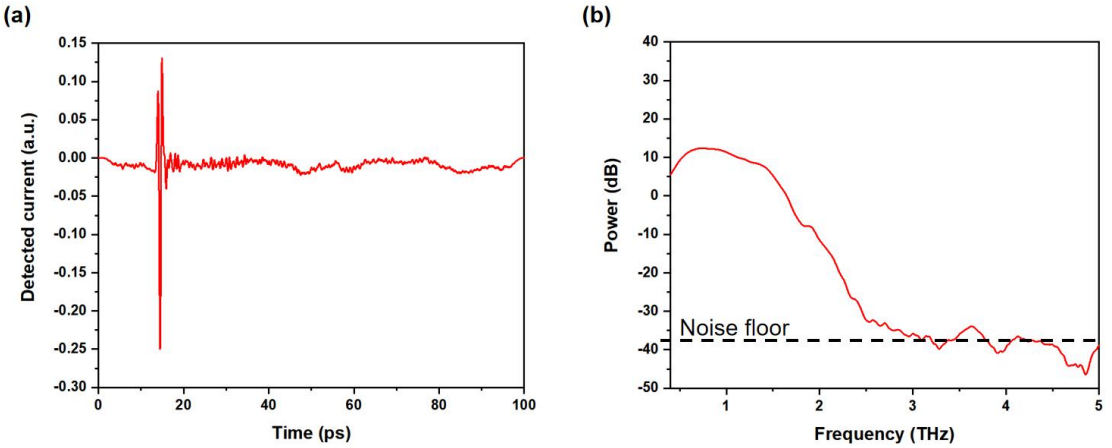

Figure 2.13 (a) Detected time domain current of THz pulse in reflection configuration Menlo. (b) Spectral power content of the pulse converted by applying a Fourier transformation.

Figure 2.13 presents the characteristic free-space time-domain waveform and its corresponding THz spectrum, as measured by the Menlo system in the reflection configuration. A 200 nm evaporated gold mirror is utilized in this setup, demonstrating reflection reference.

In reflection measurements, it is highly advisable to conduct extended N_2 purging. This precaution is essential because the absolute value of the detected current in the reflection configuration can experience a substantial reduction, sometimes as severe as one-tenth of the original waveform, as depicted in Figure 2.11 (a). Such a notable loss in intensity is a common challenge encountered in reflection THz TDS measurements [102]. This issue arises primarily due to limitations in the alignment of the parabolic mirrors and their restricted acceptance apertures. It is essential to clarify that this intensity loss is attributed to the mirrors' acceptance of aperture size limitations rather than misalignment, especially considering that they are 1.5 inch diameter mirrors. Nevertheless, the spectrum obtained after prolonged N_2 purging retains a valid bandwidth spanning from 0.4 to 3 THz. Furthermore, it maintains an acceptable signal-to-noise ratio (SNR) of up to 50 dB.

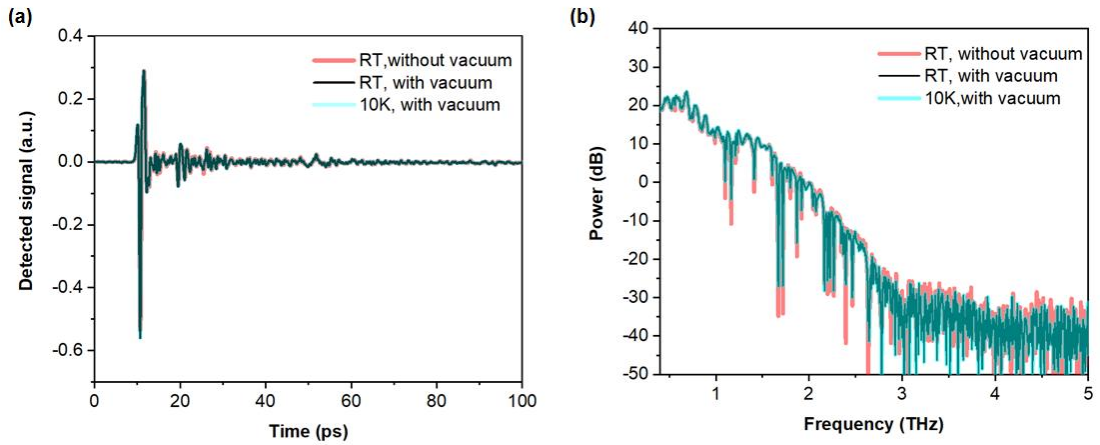

Figure 2.14 Cryogenic THz TDS results of (a) detected time domain current of THz pulse in cryogenic measurement with transmission type Menlo from without vacuum at room temperature (red), with vacuum at room temperature, and with vacuum at 10 K; (b) Spectral power content of the pulse converted by applying a Fourier transformation corresponding to the time domain data shown in (a).

However, N_2 purging is not feasible in cryogenic THz-TDS measurements shown in this thesis due to liquid He transfer tube. To elucidate this limitation, Figure 2.14 comprehensively depicts the time-domain and frequency-domain data obtained from a 420 μm sapphire sample. The data is averaged over a 5-minute interval and is presented under various conditions: without vacuum at room temperature, under vacuum at room temperature, and under vacuum

at 5 K.

In the context of cryogenic THz-TDS measurements, all acquired spectra consistently exhibit a dependable bandwidth extending from 0.4 to 3 THz, with a peak signal-to-noise ratio reaching 60 dB at approximately 0.6 THz. It becomes evident that vacuum pumping has a minor mitigating effect on the spectral absorption lines compared to N_2 purging. However, this reduction is not as pronounced as the effects achieved with N_2 purging. Furthermore, a comparative analysis between the data acquired at room temperature and those acquired at low temperature reveals virtually no discernible differences. This observation underscores the remarkable stability of the cryogenic THz-TDS system.

2.3.2 THz-TDS transmission modeling

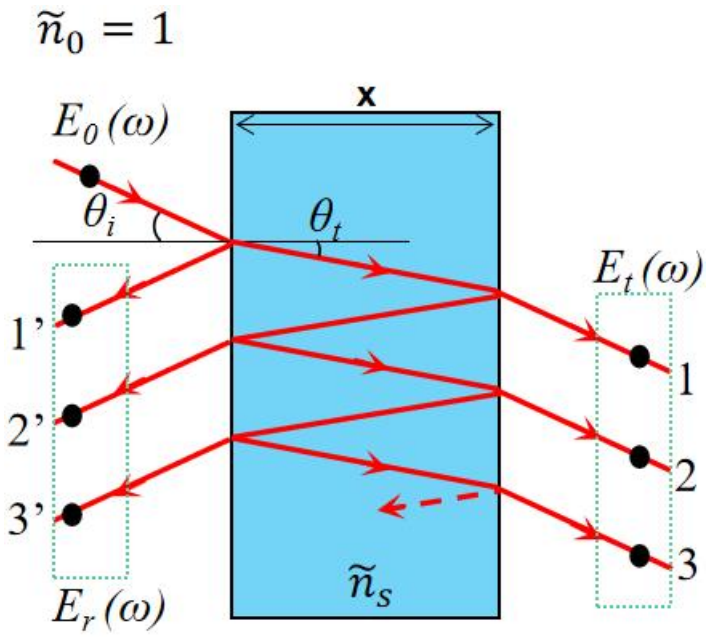

Figure 2.15 The schematic of wave propagation in a homogeneous dielectric slab. $\tilde{n}_0 = 1$ is the refractive index of the free space and $\tilde{n}_s$ is refractive index of the dielectric. $E_0(\omega)$, $E_t(\omega)$ and $E_r(\omega)$ stand for the incident wave, reflected waves and transmitted wave, respectively. θ_i is the incident angle, θ_t is the refraction angle. x is the slab thickness. The red arrow lines show the propagation paths groups of the transmission, 1,2, 3..., and the reflection, 1', 2', 3', ...

Waves passing through a material with a certain thickness have a different performance with free space propagation. Figure 2.15 demonstrates the procedure of a THz wave

propagating through a uniform dielectric slab with a thickness of x and a complex refractive index. Due to the multiple reflection and refraction at each interface between the dielectric and free space, multiple propagation paths appear inside the slab, resulting in multiple transmission and reflection in the time serial of 1', 1, 2', 2, 3', 3...The wave expression of each path is determined by the incident wave $E_0(\omega)$ multiplied by their corresponding factors.

In the case of describing the THz wave propagating through the measured sample with incident angle θ_i=0. The total transmitted wave is expressed by [105]:

$$E_t(\omega) = \tau\tau' * \exp[-j\tilde{n}_s(\omega)\frac{\omega x}{c}] * FP(\omega) * E_0(\omega) \quad (2.4)$$

Similarly, the total reflected wave can be indicated as:

$$E_r(\omega) = \rho E_0(\omega) + \tau\tau'\rho' * \exp[-2j\tilde{n}_s(\omega)\frac{\omega x}{c}] * FP(\omega) * E_0(\omega) \quad (2.5)$$

Where, τ=2/(1+$\tilde{n}_s$) and τ'=2$\tilde{n}_s$/(1+$\tilde{n}_s$) are the complex transmission coefficients incident from free space and in the dielectric, respectively. Similarly, ρ=(1- $\tilde{n}_s$)/(1+ $\tilde{n}_s$) and ρ'=($\tilde{n}_s$ -1)/($\tilde{n}_s$ + 1) are the complex reflection coefficients from the free space and in the dielectric. $FP(\omega)$ encapsulates the intricate nature of the Fabry-Pérot effect, which emerges from the multiple reflections occurring within the sample. It characterises the recurring waveform with a consistent time and diminishing amplitude.

The detailed evaluation of different optical properties by using equations (2.4-2.5) is demonstrated in the next section.

2.3.3 Optical parameters evaluation methods

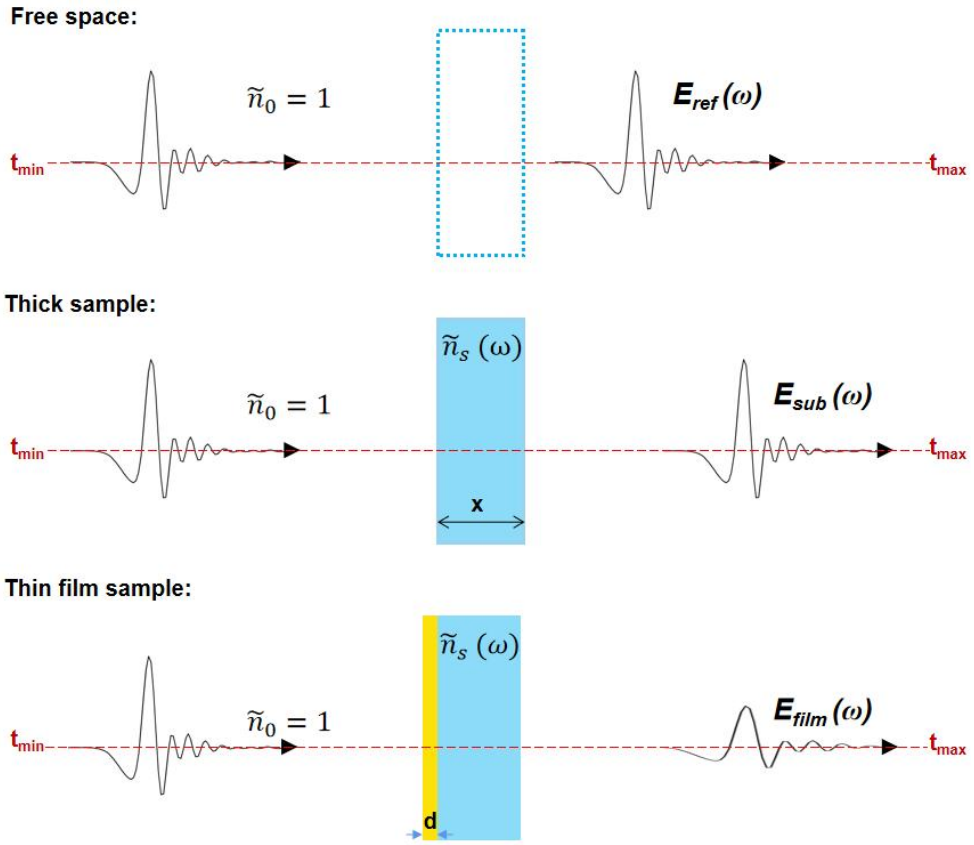

Figure 2.16 Schematic of a terahertz pulse passing through free space, a substrate, and a thin film material.

The post-processing of frequency domain information obtained through THz-TDS is crucial for assessing optical parameters. This post-processing approach can generally be categorized into two groups based on the sample's thickness and wavelength of the THz wave. The first group pertains to thick samples, typically those with thicknesses exceeding tens of micrometers, such as the 500μm Si substrate employed in this thesis. Conversely, the second group deals with thin film samples characterized by thicknesses much smaller than the wavelength of the THz wave. An example is the metamaterial design featuring a 150nm thickness, which will be discussed later in the thesis. Figure 2.16 provides a schematic illustrating the comparison of time-domain waveforms for samples with varying thicknesses.

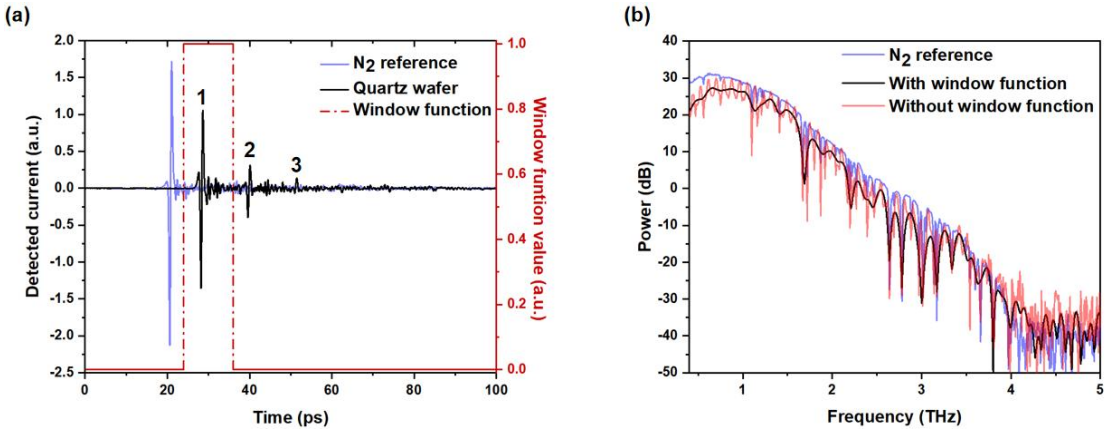

Figure 2.17 THz TDS results evaluation: (a) time domain data from nitrogen reference and through quartz substrate with rectangle window function shown to isolate the first peak. (b) Power spectrum for the nitrogen reference (blue line), full quartz substrate signal containing all pulses (red line), and from the quartz substrate data multiplied by the window function (black line).

Figure 2.17(a) illustrates a typical THz pulse waveform measured by Menlo, transmitted through a 1 mm quartz wafer, compared to a reference waveform of THz pulse propagation in N_2. Notably, the pronounced delay in the arrival time of the primary pulse, attributed to the significantly higher refractive index ($\tilde{n}_s$) and the substantial sample thickness, is a hallmark of THz pulses passing through thick dielectrics. Additionally, the figure's multiple pulses, labelled as 1, 2, and 3, correspond to different transmission paths (1, 2, and 3) induced by the Fabry-Pérot effect, as depicted in Figure 2.15.

In contrast, when observing the converted frequency domain information presented in Figure 2.17 (b), it becomes apparent that, unlike the smooth spectrum of the N_2 reference (depicted by the blue line), the raw spectrum of the quartz sample (illustrated by the red line) exhibits an oscillatory profile throughout the entire range. This behavior arises because the Fourier transformation simultaneously analyzes all the pulses, generating a mathematical periodicity in the calculated results.

There are two possible strategies to address this issue. One approach involves fitting Equation (2-1) with the actual function of FP(ω), thereby enabling the retrieval of the original waveform devoid of multiple reflections. However, this method necessitates the precise determination of the reflection coefficient and the complex refractive index of the sample,

which can be challenging to obtain or require iterative estimation [106]. Hence, an alternative approach employs a window function to selectively extract the first pulse for Fourier transformation. The black line in Figure 2.17 (b) represents the analysis result utilizing the window function depicted in Figure 2.17 (a), yielding a smoothed spectrum devoid of oscillatory characteristics.

Nevertheless, this method does possess a drawback when evaluating sharp spectral features. In such cases, their inverse Fourier transform waveform in the time domain can exhibit prolonged durations akin to classical undamped oscillations. The narrow cropping window selectively omits time domain information beyond the second pulse, crucial for discerning these sharp features' characteristic amplitude and phase.

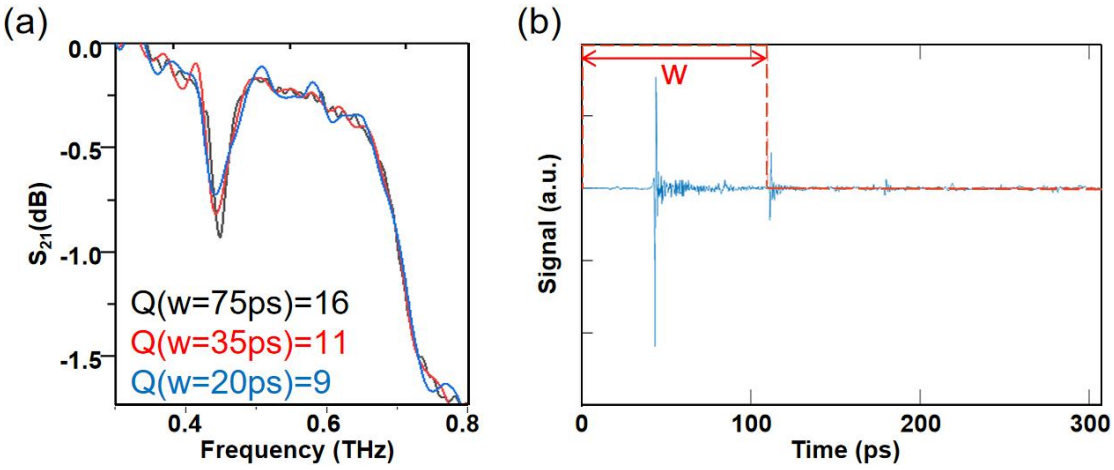

Figure 2.18 (a) An example of analyzing S_{21} experimental spectrum of a metamaterial with using different lengths window function; (b) blue: raw time domain data, red dashed line: window function applied in analysis.

A potential strategy to circumvent analytical aberrations is to augment the thickness of the sample and prolong the temporal window designated for cropping. It is imperative to underscore the significance of this methodology, especially in the measurement of high Q-factor (the details of quality factor are later explained in Chapter 4) resonators. In the analysis, truncation of wave oscillation might transpire due to the window function, culminating in computational values that underrepresent their inherent characteristics. Figure 2.18 (a) furnishes an exemplar, delineating the analysis of the S_{21} experimental spectrum of a metamaterial, employing distinct temporal window lengths **w** as illustrated in Figure 2.18 (b).

The examined metamaterial is constructed on a 3mm-thick Si substrate, delaying the inaugural Fabry-Pérot beyond 80ps. This tactic adeptly sequesters the influence emanating from the secondary pulse within the spectrum, facilitating a comparative evaluation to discern the analytical variances attributed to diverse **w** values. As evidenced in the Figure, the enhancement of ***w*** from 20 ps to 75 ps markedly elevates both the visibility and the Q-factor of the resonance of 0.5 dB and 7 units, respectively.

The transmitted coefficient $\tilde{T}(\omega)$ of the sample, can be expressed by [20, 101 and 105]:

$$\tilde{T}(\omega) = \frac{E_{sub}(\omega)}{E_{ref}(\omega)} = \frac{4\hat{n}_s(\omega)}{\left(1+\hat{n}_s(\omega)\right)^2} * \exp[-j(n_s(\omega)-1)\frac{\omega x}{c}] * \exp[-k_s(\omega)\frac{\omega x}{c}] \quad (2.6)$$

$n_s(\omega)$ and $k_s(\omega)$ are real and imaginary part of the complex refractive index $\tilde{n}_s$, respectively. In analogy to $\tilde{T}(\omega)$, the reflection coefficient $\tilde{R}(\omega)$, can be expressed by reflected electric field measured from the sample, $E_{sub-r}(\omega)$, and from the gold mirror reference, $E_{ref-r}(\omega)$ via reflection THz-TDS:

$$\tilde{R}(\omega) = \frac{E_{sub-r}(\omega)}{E_{ref-r}(\omega)} \quad (2.7)$$

Therefore, assuming the surface scattering is neglectable, the equations of transmission, reflection and absorption parameters of the intermediate material are derived as below:

$$\text{Transmission} = |\tilde{T}(\omega)|^2 \quad (2.8)$$

$$\text{Reflection} = |\tilde{R}(\omega)|^2 \quad (2.9)$$

$$\text{Absorption} = 1 - |\tilde{T}(\omega)|^2 - |\tilde{R}(\omega)|^2 \quad (2.10)$$

In addition, considering the transmitted coefficient can also be written in the form: $\tilde{T}(\omega) = |T(\omega)| * \exp(i\varphi(\omega))$, where $\varphi(\omega)$ is phase value derived from the Fourier transformation., the refractive index $n_s(\omega)$ and absorption coefficient $\alpha(\omega)$ of the measured

material can be expressed as:

$$n_s(\omega) = 1 + \frac{c\varphi(\omega)}{\omega x} \tag{2.11}$$

$$\alpha(\omega) = \frac{2\omega k_s(\omega)}{c} = \frac{2}{x}\ln\frac{4n_s(\omega)}{(1+n_s(\omega))^2}|T(\omega)| \tag{2.12}$$

Chapter 3 Novel Materials Advancement with THz-TDS

The previous chapter provided a concise introduction to the essentials of THz-TDS, the Menlo system, and the methodology used for data analysis in assessing various optical parameters. Building on this foundation, the current chapter presents two experiments that intricately utilize different configurations of THz-TDS for the advancement of materials manufacturing. These experiments involve the development of bio-based nanofiber composites [107] and metallic additive manufacture [108] presented in the published journals.

3.1 THz-TDS analysis of cellulose nano-fiber commingled biocarbon electromagnetic absorber

3.1.1 Introduction of bio-based electromagnetic absorber

As discussed in Chapter 1, THz technologies hold significant promise in various fields, such as the biomedical industry, chemical analysis, security imaging, and high-speed communications. Within these integrated applications, the effective management of electromagnetic interference in compact devices presents a primary challenge, crucial for optimizing performance and ensuring accuracy in THz applications. While substantial progress has been made in developing nanomaterial-based composites for achieving efficient electromagnetic shielding at microwave and millimeter-wave frequencies, the advancement of high-performance electromagnetic absorbers specifically tailored for the THz frequency range has lagged.

Shielding effectiveness (*SE*) plays a critical role in assessing the performance of an electromagnetic absorber. Assuming a propagating wave incident perpendicularly onto the absorber with a smooth surface, the *SE* comprises two main components: SE_R, which quantifies the reduction in shielding intensity due to sample reflection, and SE_A, which accounts for the reduction in shielding intensity attributed to sample absorption. The connection between these *SE* parameters and the conventional optical properties of materials is described by equations (3.1-3.4) [109]:

$$\mathrm{SE_{total}}(\omega) = -10 * \log_{10}(\mathrm{T}(\omega)) \tag{3.1}$$

$$\mathrm{SE_{total}}(\omega) = \mathrm{SE_R}(\omega) + \mathrm{SE_A}(\omega) \tag{3.2}$$

$$\mathrm{SE_R}(\omega) = -10 * \log_{10}(1 - \mathrm{R}(\omega)) \tag{3.3}$$

$$\mathrm{SE_A}(\omega) = -10 * \log_{10}\left(\frac{\mathrm{T}(\omega)}{1 - \mathrm{R}(\omega)}\right) \tag{3.4}$$

A perfect THz absorber should perform a high value of SE_A and almost no SE_R, maximizing wave elimination incident the absorber. It is worth noting that

Conductive nanomaterials like carbon nanotubes, MXene, and graphene [109-119] are the most prevalent for crafting THz absorbers. Typically, they are blended into various matrices to produce films or aerogels, which significantly enhance the shielding performance of these materials. The reported literature showcases a range of *SE* values exceeding 20 dB for film-based absorbers and more than 40 dB for aerogel-based absorbers. While the processing methods may differ across these approaches, the crux of effective THz absorber design lies in creating three-dimensional porous structures with conductive networks, effectively forming a framework that captures and dissipates incident THz waves. A comprehensive overview of diverse methodologies utilizing different materials and structures to fabricate THz absorbers can be found in Table 3-1 at the end of this section.

However, it's worth noting that existing research relies on exotic nanomaterials and complex, resource-intensive, and environmentally impactful nano-fabrication techniques. Hence, there is a growing need to develop bio-friendly materials that offer exceptional shielding performance, produced through straightforward and sustainable processes.

Cellulose nanofiber (CNF) is an eco-friendly biomaterial derived from plant sources. Its remarkable mechanical properties, chemical stability, and environmentally friendly extraction process make it exceptionally well-suited for various applications, including flexible electronics [120] and biomedical scaffolds [121]. Additionally, owing to its low density, high surface-to-volume ratio, and tunable porosity, CNF is extensively employed in developing efficient electromagnetic wave absorbers operating in the GHz range [122].

On the other hand, sustainable bio-carbon (SBC) is another environmentally friendly

material characterized by a graphite-like structure. It forms an effective conduction network when combined with porous materials and is widely utilized in microwave shielding applications [123]. Hence, it is reasonable to expect that a composite material integrating CNF and SBC would represent a fully sustainable solution providing broadband shielding effectiveness, making it an ideal candidate for achieving carbon neutrality goals.

3.1.2 THz SE evaluation of the CNF-SBC thin films and aerogel via THz-TDS

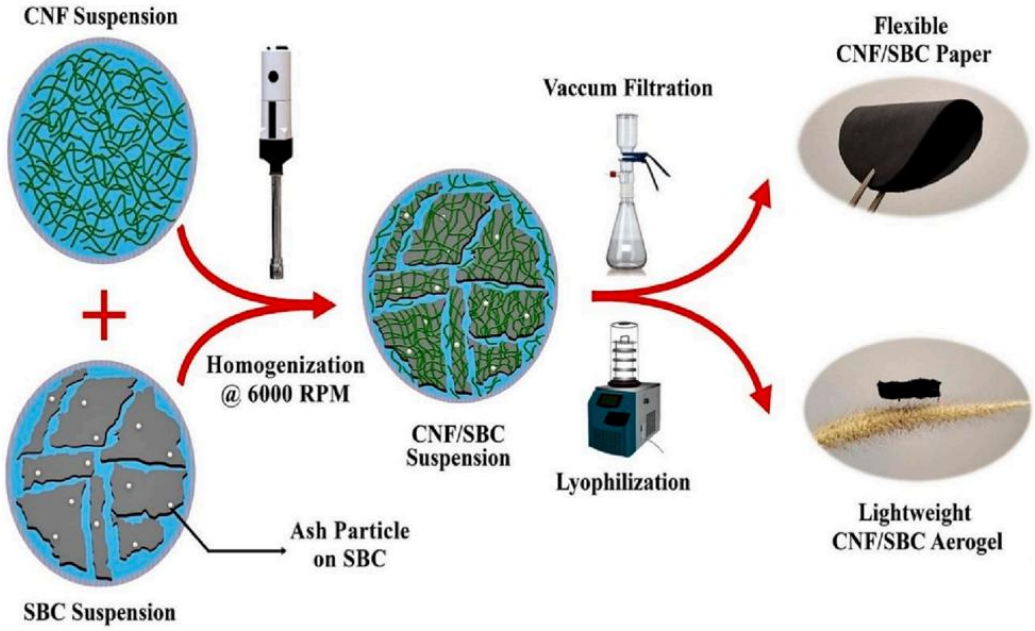

Figure 3.1 Fabrication details and photos of CNF/SBC aerogels and nanopapers [107].

For designing the environmental-friendly THz absorber from CNF and SBC, a series of CNF/SBC nano papers and aerogels are fabricated by Dr Pai Avinash from Mahatma Gandhi University via hasty fabricating techniques, such as vacuum filtration and lyophilization. Figure 3.1 shows the fabricated samples' processing schematic and typical photos [107]. The nanopapers generally have a uniform thickness of 600 μm, and aerogels have an average thickness of 3 mm.

To accurately assess *SE*, it is essential to comprehensively measure the THz waves transmitted through and reflected from the samples. The schematics illustrating the transmission and reflection THz-TDS setups used for characterizing the samples are presented in Figures 2.7 and 2.9 in Chapter 2, respectively. All measurements adhere to the standard analysis procedures previously discussed. It's worth emphasizing that during the reflection

measurements, careful realignment of the pulse positions is performed to ensure that they closely match the original reference position, thereby maintaining a consistent focus on the samples.

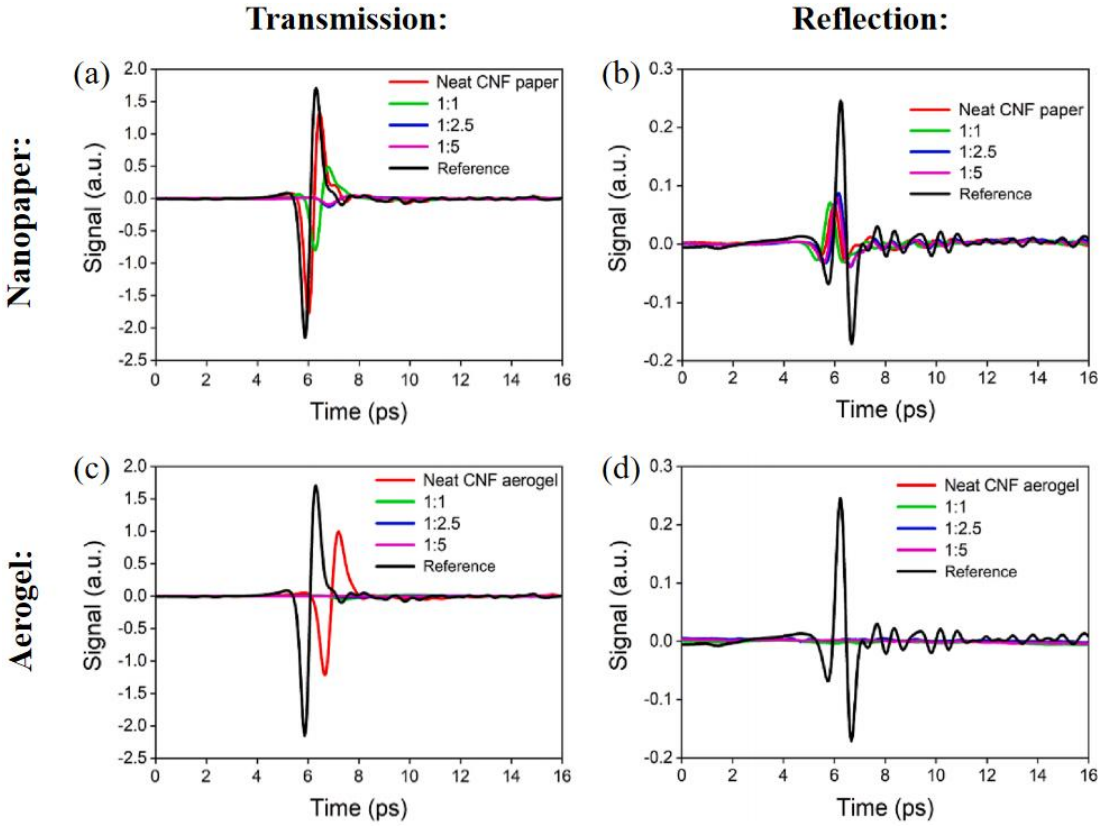

Figure 3.2 Time domain waveform of (a) CNF/SBC nanopapers & (b) CNF/SBC aerogels at different CNF: SBC ratios in transmission mode (c) CNF/SBC nanopapers & (d) CNF/SBC aerogels at different CNF: SBC ratios in reflection mode.

Figure 3.2 (a-d) presents the time-domain waveforms of CNF/SBC nanopapers and aerogels obtained through transmission and reflection THz-TDS measurements with varying CNF:SBC ratios. The term "Neat" designates pure CNF material; "1:1" signifies an equal weight ratio of CNF and SBC, while "1:2.5" denotes a weight ratio of SBC that is 2.5 times that of CNF. Both the neat nano paper and aerogel samples exhibit high transmitted intensities, indicating a low shielding effect. Conversely, the samples containing SBC demonstrate significantly lower transmitted intensities, with the reduction being inversely related to the weight ratio of SBC in the sample. This observation highlights a substantial shielding effect on the THz wave due to the conductive networks formed by SBC. Notably, the aerogel

samples nearly eliminate all transmitted THz waves by adding SBC with a 1:1 weight ratio.

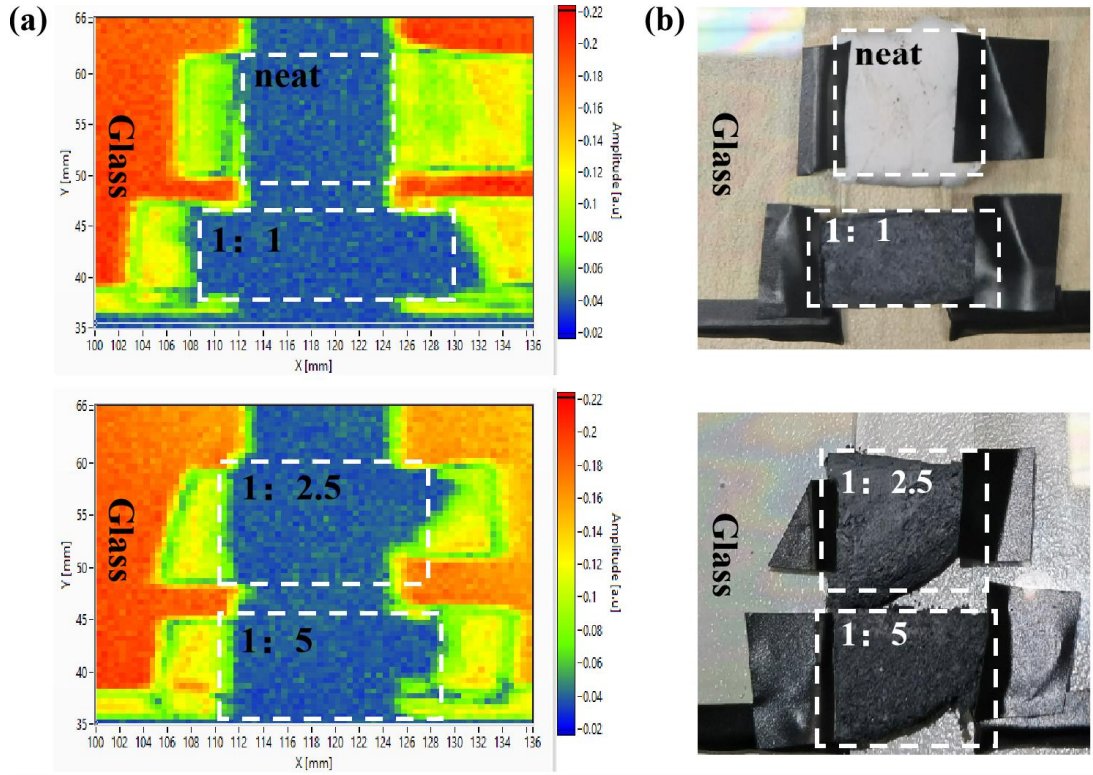

Figure 3.3 (a) illustrates reflection mappings of CNF/SBC aerogels, while (b) provides optical photos of the corresponding measured samples presented in (a). The regions enclosed by white frames in both (a) and (b) indicate the relative locations of the different samples in the mappings and photos.

In the reflection measurement, the nanopapers exhibit a similar reflected intensity in the time domain, with peak values at nearly 20% of the reference. In contrast, the aerogel materials show almost no reflection from the surface. This exceptional performance is further confirmed by the reflection mappings of the aerogel sample presented in Figure 3.3 (a). Additionally, Figure 3.3 (b) depicts the corresponding optical photos of the measured samples in Figure 3.3 (a). The white dashed frames indicate the relative locations of the various samples in both the mapping and photos. Interestingly, there is no discernible difference between the areas containing air and the sample itself, giving the impression that no materials are present within the gap of the glass holder.

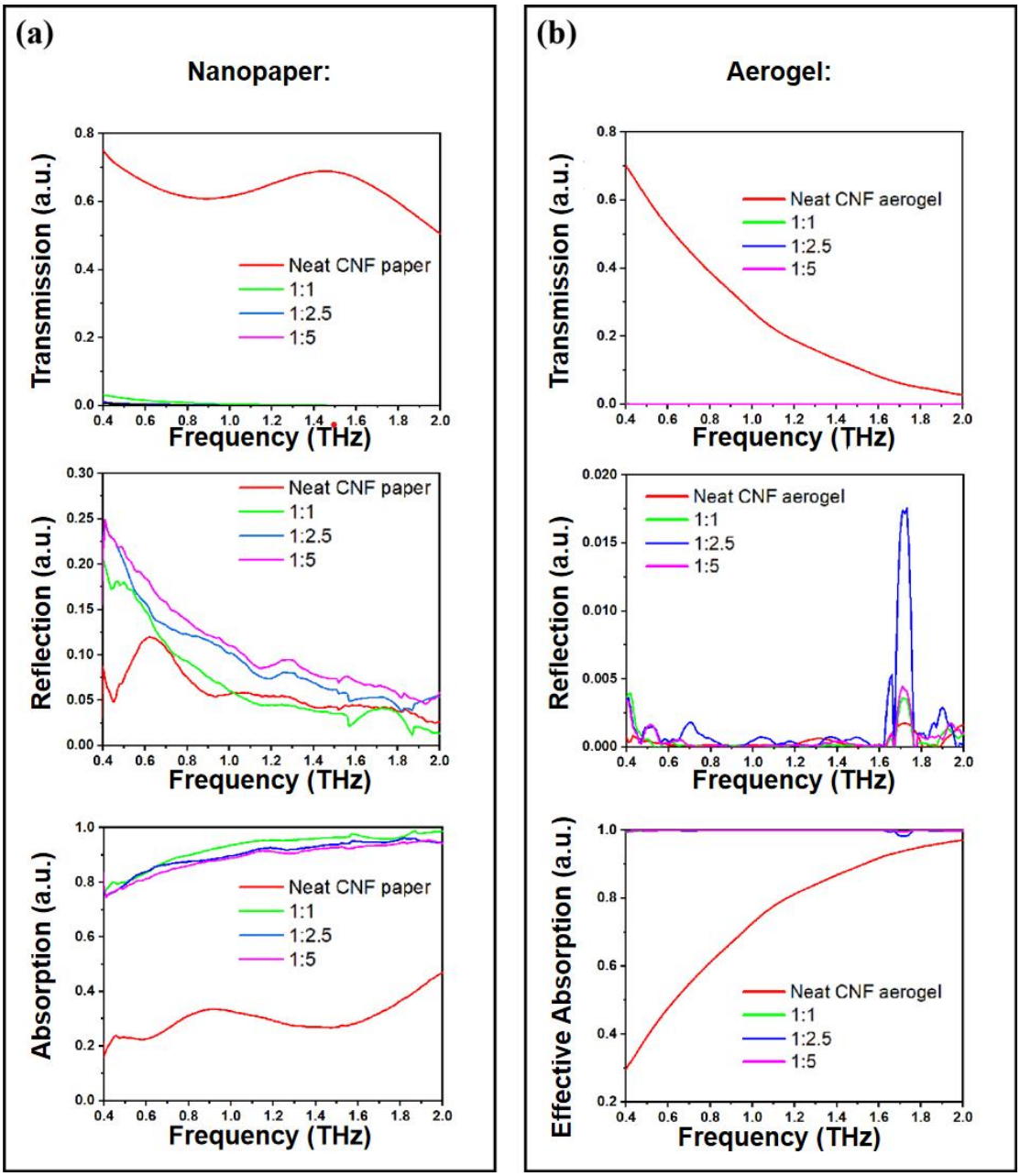

Figure 3.4 (a) Spectral transmission, reflection, and absorption of CNF/SBC nanopapers; (b) Spectral transmission, reflection and effective absorption of CNF/SBC aerogels.

Figures 3.4 (a-b) presents an analysis of various materials' transmission, reflection, and absorption characteristics within the frequency domain, spanning from 0.4 to 2 THz. This analysis is derived from converting time domain waveforms using equations (2.6-2.12). It is worth noting that, the relative uneven surface of the aerogel will induce a considerable wave scattering on the sample surface, which also needs to be considered in the evaluation, changing the equation (2.10) into the new form: $\text{Absorption} = 1 - |\widetilde{T}(\omega)|^2 - |\widetilde{R}(\omega)|^2 -$

$\tilde{S}(\omega)$, where $\tilde{S}(\omega)$ represents the scattering loss. In the domain of ***SE*** evaluation, paramount emphasis is placed on the total propagation loss induced by the absorber, which is attributed to an amalgamation of factors including both structural characteristics and the intrinsic electromagnetic response of the material. While the presence of scattering does not shift the primary evaluative focus in this study, it necessitates a recalibration of the absorption metrics. Specifically, traditional absorption values of aerogels are substituted by "effective absorption" metrics in Figure 3.4 (b), underlining the aggregate loss attributable to both absorption and scattering. For subsequent inquiries into the scattering coefficient of the aerogel surface, methodologies involving radar cross section measurement or diffuse scattering measurement [124]. However, these approaches fall outside the scope of this thesis.

The transmission spectrum of nanopaper and aerogel reaffirms the conclusion that pure CNF samples exhibit high transmission while introducing SBC produces a substantial shielding effect. Notably, although neat aerogel and neat nano paper exhibit approximately 70% transmission at 0.4 THz, the aerogel's transmission diminishes significantly faster with increasing frequency, dropping to 5 % at 2 THz. In contrast, nanopaper maintains a transmission of over 40% at 2 THz. This observation highlights that the 3D porous structure of the aerogel enhances its THz shielding performance at higher frequencies, even without a conductive network.

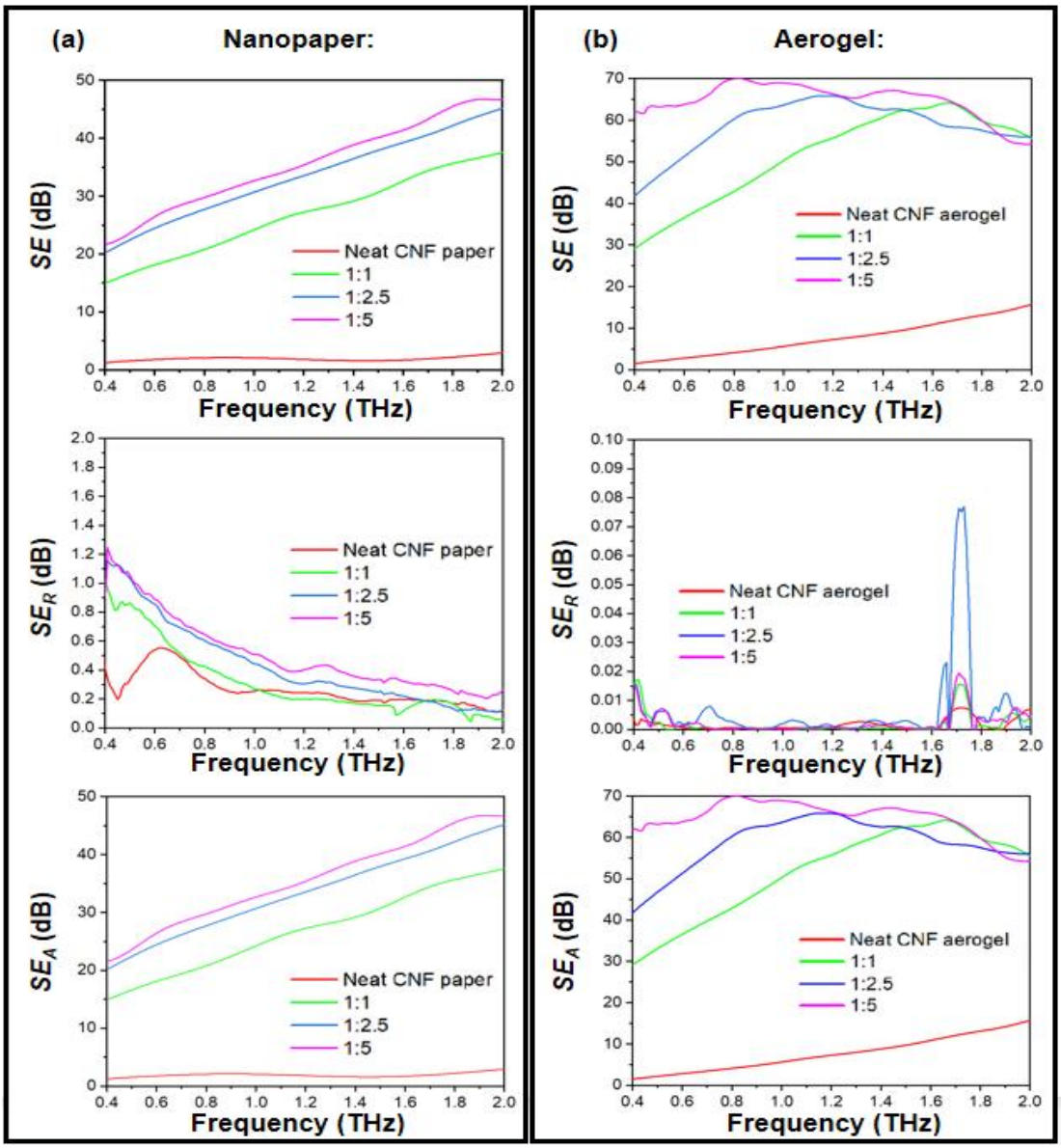

Figure 3.5 (a) Total THz shielding (SE), shielding by reflection (SER) & shielding by absorption (SEA) of CNF/SBC nanopapers; (b) Total THz shielding (SE), shielding by reflection (SER) & shielding by absorption (SEA) of CNF/SBC aerogels.

Regarding the spectral reflection of nanopapers, the values for different weight ratio samples fall within the range of 10-25%, consistent with the findings in the time domain. However, it shows a slight proportionality to the SBC weight ratio. In contrast, the spectral reflection values of the aerogels are mostly below 1 %, effectively matching the noise floor. Consequently, it is challenging to discern any reliable trend related to the SBC weight ratio for aerogels. Both nanopapers and aerogels exhibit low spectral transmission and reflection

values, resulting in absorption levels of over 80 % across the presented frequency range.

Notably, the absorption of nanopapers significantly increases by 60 % when transitioning from pure CNF to a 1:1 CNF: SBC weight ratio, reaching a peak absorption value of 99 % at 2 THz. However, as the SBC ratio increases from 1:1 to 1:5, the maximum absorption value experiences a slight 9 % reduction. This discrepancy arises because an increased SBC weight ratio has virtually no impact on transmission but leads to higher sample reflection, subsequently diminishing absorption.

Figure 3.5 illustrates the assessed shielding effectiveness (*SE*), shielding effectiveness due to reflection (SE_R), and shielding effectiveness due to absorption (SE_A) values for CNF/SBC nanopapers and aerogels with varying CNF:SBC ratios. These assessments are conducted using equations (3.1-3.4). Remarkably, all *SE*, SE_R, and SE_A values presented in the spectrum, except for the noise-affected SE_R in the case of aerogels, demonstrate proportionality to the SBC weight ratio. Consequently, when the CNF:SBC ratio reaches its maximum at 1:5, the nanopaper exhibits a peak THz SE_A of 46 dB, while the aerogel, which possesses a similar SBC content, achieves a THz SE_A increase to 70dB. The SE value of the aerogel is approximately 1.5 times greater than that of the nanopaper, underscoring the potential of porous CNF structures in enhancing terahertz shielding performance.

Significantly, there is a difference in the absorption and SE_A values trend as the SBC ratio increases. This discrepancy arises because a 7 % change in reflection has a more substantial impact on the absorption, which begins at 80 %, compared to the relatively small 0.4 dB reduction in SE_R. This difference is much smaller than the 10 dB disparity in SE resulting from increased SBC ratio.

For a more comprehensive understanding of the fabrication process, materials morphology characterization, and first-principal calculations explaining the absorption mechanism, please refer to the published journal [107].

Table 3-1 Test frequency, THz shielding performance and shield thickness of various THz shielding materials reported in the literature.

No	Material Composition	Frequency Range (THz)	Max THz *SE* value(dB)	Thickness	Specific Max THz *SE* value (dB/mm)
previous works:					
1	Borophene film	0.1-2.7	50	1mm [109]	50
2	MXene film	0.25-2.25	2.5/46.7	25nm [110] / 10μm [111]	10000/250
3	MXene foam	0.2-2	51	85μm [111]	600
4	MXene coated Nanoslot antenna array	1.0	20	500nm [112]	40000
5	MWCNT-/Graphene foam	0.1-1.6	61/74	3mm [113]	20.3/24.6
6	Kapton derived carbon foam	0.2-0.5	60	125μm [114]	480
7	SWCNT/PVA foam	0.3-2.1	29	300μm [115]	96.7
8	PANI/PU film	0.1-4.0	40	0.15mm [116]	266.7
9	GaN aerogel	0.1-1.3	40	1.3mm [117]	30.8
10	PMMA/carbon nanofiber (CNF) film	0.2-1.2	56.8	0.94mm [118]	60.4
11	CNF/PMMA/PVDF coating on cellulose	0.15-1.2	20	24-32μm [119]	625-833
this work:					
12	**CNF/SBC Aerogel**	**0.4-2.0**	**70**	**3mm**	**23.3**
13	**CNF/SBC Nanopaper**	**0.4-2.0**	**46**	**600μm**	**76.7**

3.2 THz-TDS evaluation of additive manufactured metallic components

3.2.1 Introduction of additive manufactured metal

Additive Manufacturing (AM) is a state-of-the-art technique that has gained popularity for simplifying the fabrication of complex geometric designs in modern manufacturing. One of the AM methods, known as selective laser melting (SLM), is employed to produce metal components with high density and exceptional properties by using a laser to melt metal powder [125] selectively. However, components manufactured using SLM often exhibit poor surface uniformity because of the laser on the surface. This limitation hinders their applications in industries such as aerospace and biomedicine, where precise control of surface profiles is crucial [126–128].

To address this issue, researchers like Mohammad et al. and Han et al. have proposed electrochemical polishing (EP) as a practical additional step to eliminate surface imperfections, using an environmentally friendly solvent [129-130]. Several techniques have been suggested for measuring average surface roughness (***Ra***), including contact scanning profilometry [131-132], X-ray micro-CT [133], atomic force microscopy (AFM) [134], and laser scanning microscopy [135], among others. However, many of these methods are time-consuming and require comprehensive scanning across the entire surface. They also face challenges in capturing data from the peak and valley regions on highly rough surfaces, as they often fall outside the measurement limits of these techniques.

Typically, the ***Ra*** values of as-fabricated SLM samples fall within the range of 25-100 μm, which is beyond the measurement capabilities of most conventional techniques. Therefore, there is a need for a more effective method designed to evaluate surfaces with ***Ra*** values in the tens of μm range.

In recent years, the utilization of THz radiation for examining the surface roughness on AM alloy components synthesized via SLM has not been explored. In this research, we leverage THz radiation's inherent sensitivity to scattering phenomena to elucidate the surface roughness distribution and height levelling (***HL***) allocation pertinent to the samples associated with EP (the standard EP procedure will be demonstrated in section 3.2.2).

Notably, the THz analytical method showcases several advantages, including employing more significant analytical spots compared to conventional laser microscopy and offering

higher precision within the relevant roughness parameters. Furthermore, this technique is congruent with in- situ direct measurements during the EP process, enhancing the practicality and accuracy of the analysis.

The present investigation delineates a progressive route towards the non-destructive evaluation of AM-derived devices and products. It facilitates analysis across expansive sample areas, simultaneously adhering to the safety norms pertinent to industrial environments. Concurrently, this research contributes a valuable instrument for scrutinizing the appropriateness of AM-manufactured THz components, potentially spearheading advancements in the respective field.

3.2.2 Samples preparation and electrochemical polishing process

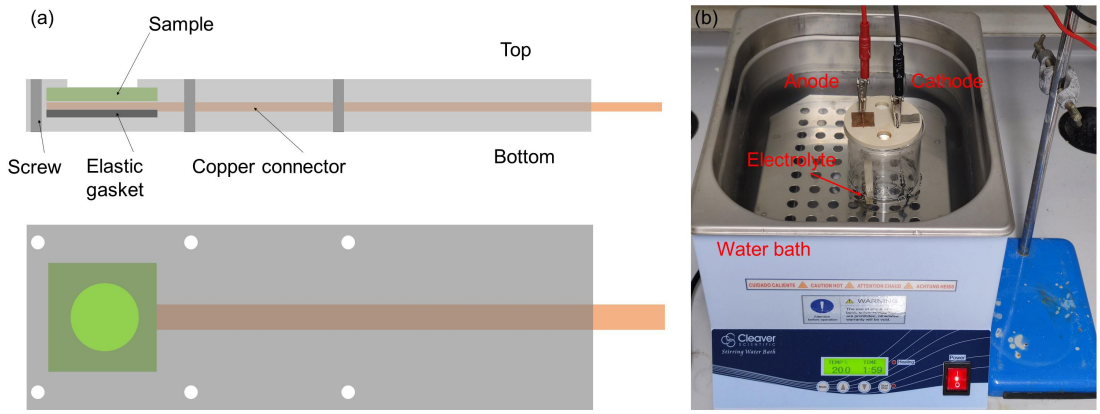

Figure 3.6 (a) The affixed holder of polished SLM sample and (b) the photo of the EP cell.

The experiment's initial stage involved preparing unpolished samples within a bidimensional square region spanning approximately 2.25 cm², complemented by a thickness of 0.2 cm. This was achieved utilizing SLM AM technology. Subsequently, 316 L-grade stainless steel plates were securely affixed to the holder in the electrolytic environment. This securement was facilitated by the mechanical assistance of a resilient gasket coupled with screws, thereby offering stability throughout the polishing phase.

The refinement process was conducted within an electrochemical cell, the detailed imagery of which can be consulted in Figure 3.6. The chosen electrolyte for this procedure was a solution comprising 1 mol/L NaCl, a predominant volume of Ethylene Glycol (accounting for 90%), and a minor volume of ethanol (constituting the remaining 10%). A

notable enhancement in the surface smoothness of the metal was observed following a standardized EP procedure.

To maintain optimal conditions, the reaction was sustained at ambient temperature, facilitated by a water bath. Moreover, applying current intensities ranging from 250 mA/cm² to 1000 mA/cm² during the polishing operations allowed for precise control over the polished specimens' surface roughness average (***Ra***). Consequently, the Ra values could be meticulously regulated within three distinct ranges, 8-10 µm, 5-8 µm, and 1-5 µm, as corroborated by the referenced literature [136].

3.2.3 Samples preparation and electrochemical polishing process

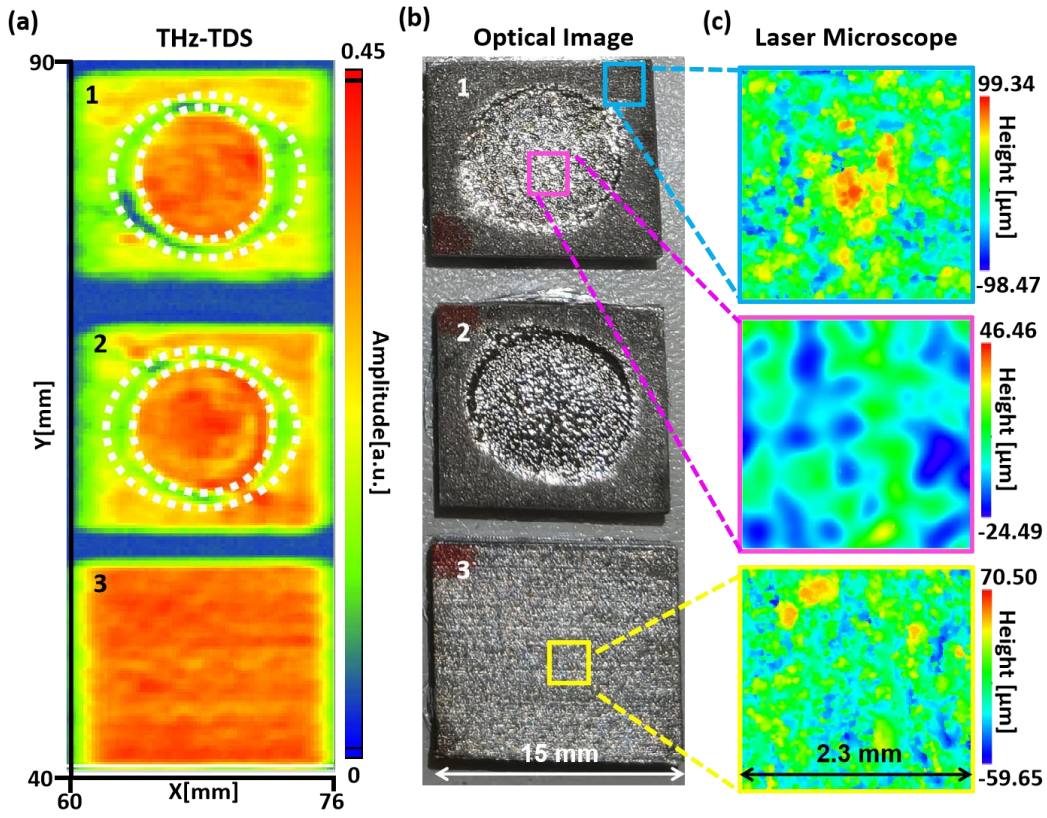

Figure 3.7 (a) THz intensity maps of three distinctive samples captured via reflection THz-TDS. The color bar indicates the peak reflected E-field within the time waveform. Regions a-1 and a-2 depict AM-printed samples undergoing electrochemical polishing with different current densities for 56 minutes, resulting in central polished regions with different Ra values. Area a-3 highlights an unpolished commercial metal plate with partially polished ring areas indicated by white dashed circles. (b) Features optical microscopic images of the

samples identified in part (a), represented as regions b-1, b-2, and b-3. The colored squares (blue, pink, and yellow) mark the areas chosen for ***Ra*** evaluation via laser microscopy, including an unpolished section, a polished portion of sample 1, and a random segment in sample 3, respectively. (c) displays height distribution images acquired from laser microscopy of the selected regions, corresponding with the areas delineated in part (b), allowing for a detailed analysis and comparison of surface topographies captured through different methods.

In this research, the Menlo THz-TDS was deployed and arranged in a reflection geometry configuration to facilitate the acquisition of THz measurements. Through a meticulous raster scanning process of the specimen coupled with the documentation of the THz signals perceived, it was feasible to formulate a map delineating the reflected terahertz waveforms. As mentioned in the last section, one of the predominant challenges in accurately extracting optical parameters utilizing reflection THz-TDS stems from the pronounced susceptibility to phase misalignments between the sample and the reference measurements. Consequently, it was imperative to employ acute precision in realigning the optical setup to maintain the focal plane congruence between the reference and the sample surfaces.

The evaporated gold film demonstrated in Chapter 2 was utilized for the reference measurements. Moreover, this study investigated two samples prepared via SLM AM technology and an additional commercial specimen, as illustrated in Figure 3.7 (a). The AM samples, labelled as samples 1 and 2, underwent refinement through an electrochemical polishing cell (Figure 3.6 (a)), exhibiting central, shiny circular regions corresponding harmoniously with the polishing holder delineated in the supplementary information.

Figure 1 (a) depicts the intensity image retrieved from the THz-TDS, which enumerates the maximal reflected electric field as documented by Menlo. The scrutinized area dimensions were 16mm (x) by 50mm (y), procured with a step size of 0.25 mm in both the x and y axes. Notably, each pixel within the image encompassed digitized THz time-domain data spanning 100ps, averaging 10s, offering substantial contrast in reflection amplitude between the polished and unpolished regions in samples 1 and 2. Remarkably, two central regions in samples 1 and 2 exhibited elevated reflectivity, attributable to surface smoothing processes. Conversely, the third sample area presented a more homogenous reflection profile than its counterparts, with a heightened mean reflection further substantiating the coarse surface

texture of the as-fabricated AM component. Generally, the reflection mapping resembled the roughness distribution discerned in the optical imagery.

This study scrutinized three distinct square regions, each spanning an area of 5.29 mm². These regions, selected from unpolished and electrochemically polished sections of the sample and a random area from sample 3, are delineated in Figure 1(b) as blue, pink, and yellow squares, respectively. Figure 1(c) exhibits laser microscopy-derived height distribution images of these areas, as outlined in the methods section. Notably, the electrochemically polished region showcased reduced relative heights and improved uniformity compared to the unpolished section within the same sample, illustrating the intended polishing effects.

Time-domain data from approximately 81 pixels (arranged in a 9×9grid) were averaged and normalized using the reference derived from the gold film to align with the laser microscope's scanning area dimensions. Additional details, including the captured waveforms and spectra in the THz-TDS analysis, are documented in the supplementary information.

3.2.4 Evaluating RMS roughness and height levelling of metal surface

In the aforementioned THz-TDS acquired images, the interrelation between the incident and the reflected THz waves in the specular direction is delineated as per Equation (3.5) [137-139]:

$$E_r(\omega) = E_i(\omega) \cdot \tilde{f}(w; x, y) = E_i(\omega) \cdot r(\omega; x, y) = E_i(\omega) \cdot \exp\frac{-i\omega\Delta H(x, y)}{c} \quad (3.5)$$

In this equation, $E_i(\omega)$ and $E_r(\omega)$ represent the frequency-dependent electric fields of the incident and reflected waves, respectively. The function $\tilde{f}(w; x, y)$ embodies a complex representation that describes the alterations imposed upon the incident wave upon interacting with the reflective surface. This function integrates the normalized reflective coefficient $r(\omega; x, y)$ and an exponential phase term given by $\exp(-i\omega\Delta H(x, y)/c)$. Here, the phase involvement is attributed to the height discrepancy, denoted as $\Delta H(x, y)/c$ on the surface of the sample relative to a reference point. Keeping in mind that the height distribution on the surface of the sample exhibits randomness and that the correlation distance pertaining to the surface roughness surpasses the wavelength, one can reasonably negate any phase delay instigated by the height leveling (**HL**) of the surface [140].

Within this context, the reflective coefficient denoted as $r(k)$, and the reflectance $R(k)$ represented as concerning the rough surface in the specular direction can be theoretically represented utilizing the Kirchhoff Approximation (KA), as articulated in equations (3.6) and (3.7) as referenced in literature [141-142]:

$$r(k) = \exp(-4\pi\sigma k \cos\theta) \tag{3.6}$$

$$R(k) = (E_i / E_r)^2 = \exp(-4\pi\sigma \cos\theta)^2 \tag{3.7}$$

In the specified equations, σ signifies the root-mean-squared (RMS) roughness, k denotes the wavenumber of the incident wave, and θ indicates the angle of incidence in relation to the normal vector of the metallic surface. Through an analysis of the electric field in the frequency domain rendered by Fourier transformation, the average roughness (Ra) of the sample surface can be assessed using Equation (2) alongside the formula: ***Ra***=0.8×σ, as cited in reference [143].

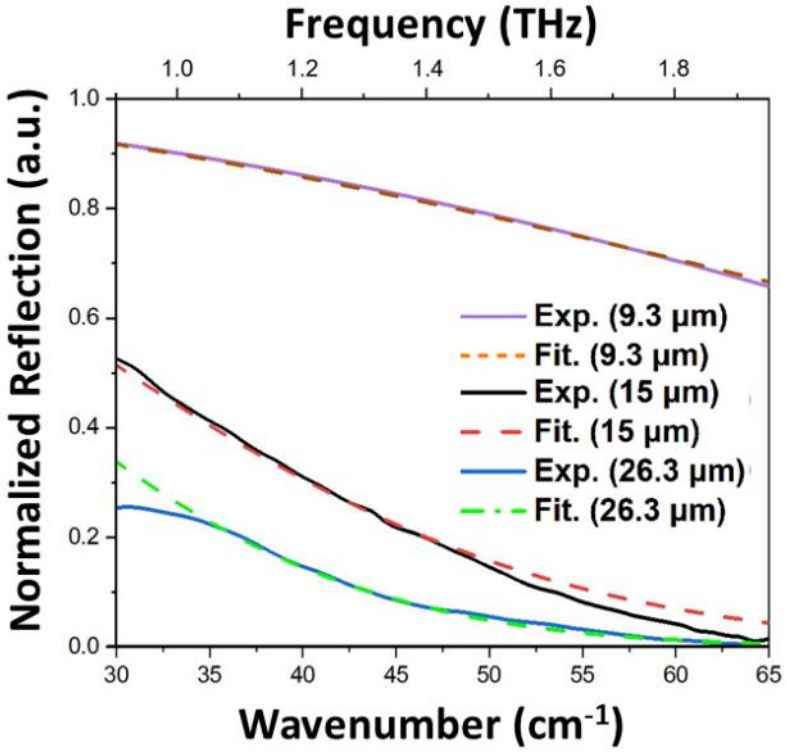

Figure 3.8 Experimental results (Exp.) and fitting models (Fit.) of evaluating the average roughness of selected areas.

It should be noted that the shadowing effect and the occurrence of multiple reflections on the surface due to considerable incident angles have not been incorporated in equations (2) and (3). The *KA* retains its validity only when the RMS height facilitates notable diffuse scattering relative to the incident wavelength. This particular condition is generally ascertained through the application of the Fraunhofer Criterion, detailed in the subsequent inequality as referenced in literature [142, 144]:

$$\sigma \geq \frac{\lambda}{32 \cos \theta} \tag{3.4}$$

Here, λ symbolizes the wavelength of the incident wave. This criterion is essential as it restricts the operative wavelength spectrum for appraising different Ra values. As a case in point, for a rough surface characterized by ***Ra***=40 μm (where σ=50 μm), the Kirchhoff Approximation (*KA*) can typically be employed to extract information using a spectral bandwidth ranging from 0.2 THz to the uppermost discernible frequency (2 THz as shown in Figure 2.13).

Conversely, to assess a smoother surface characterized by ***Ra***=6 μm (where σ=7.5 μm) using the identical methodology, the functional spectrum would be confined to a band ranging from 1.5 THz to the terminal frequency, nearing the operational limit of Menlo deployed in this analysis. Using normalized reflection values, ***Ra*** was determined by aligning the empirical data with Equation (3.7) across the wavenumber range 30-65cm^{-1}. Figure 3.8 delineates the empirical outcomes and their optimum correspondences with *KA* about the selected zones, culminating in the assessment of average roughness values of 26.3±2 μm, 9.3±1 μm, and 15±2 μm respectively. Noteworthy is that all the fit models harmonize well with the experimental trajectories, manifesting correlation coefficients, R, exceeding 95%.

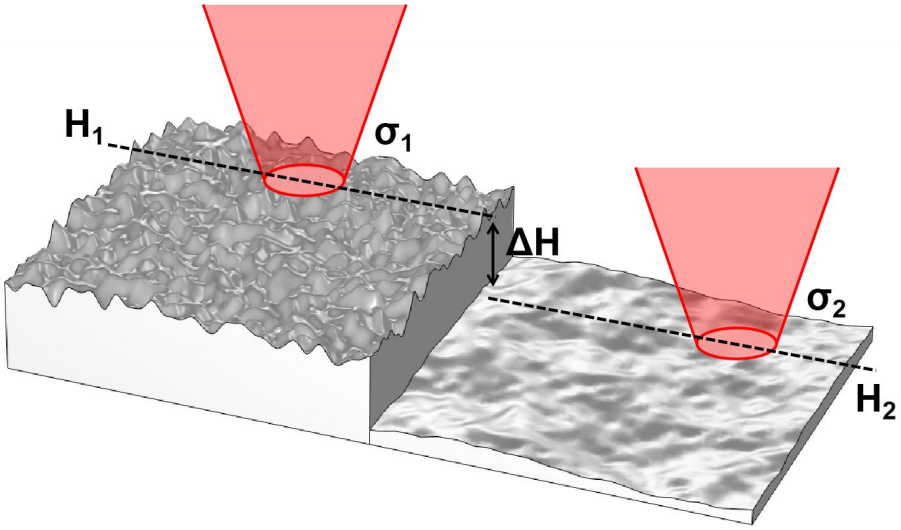

Figure 3.9 Schematic of reflection THz-TDS used to characterize the different RMS roughness (σ) and HL in two identical areas, where H1 > H2 and σ1>σ2. The left region represents the rough as-fabricated metal before EP, the right part represents the area after EP. The red round cones area represents the typical beam form of the incident THz pulse in THz-TDS.

Furthermore, during the EP process, the ***HL*** within the polished zone tends to diminish, attributed to values of $\Delta H(x,y)/c$ resultant of sustained etching. The phase component delineated in Equation (3.5), spurred by the variation in height, serves as an efficacious marker for discerning the authentic etching depth on the surface. Integrating the calculated values of Ra and ***HL*** extracted from the THz-TDS data enables the realization of a three-dimensional mapping that vividly illustrates the impact of the EP process on the 3D-printed 316L stainless steel structure. Figure 3.9 encapsulates a schematic representation of this approach, showcasing the assessment of Ra and ***HL*** in two congruent zones wherein the left segment illustrates the original 3D metal surface (notably rougher and with elevated ***HL***) and the right segment portrays the condition post-EP (markedly smoother with reduced ***HL***).

3.2.5 Laser scanning microscope measurements and comparison

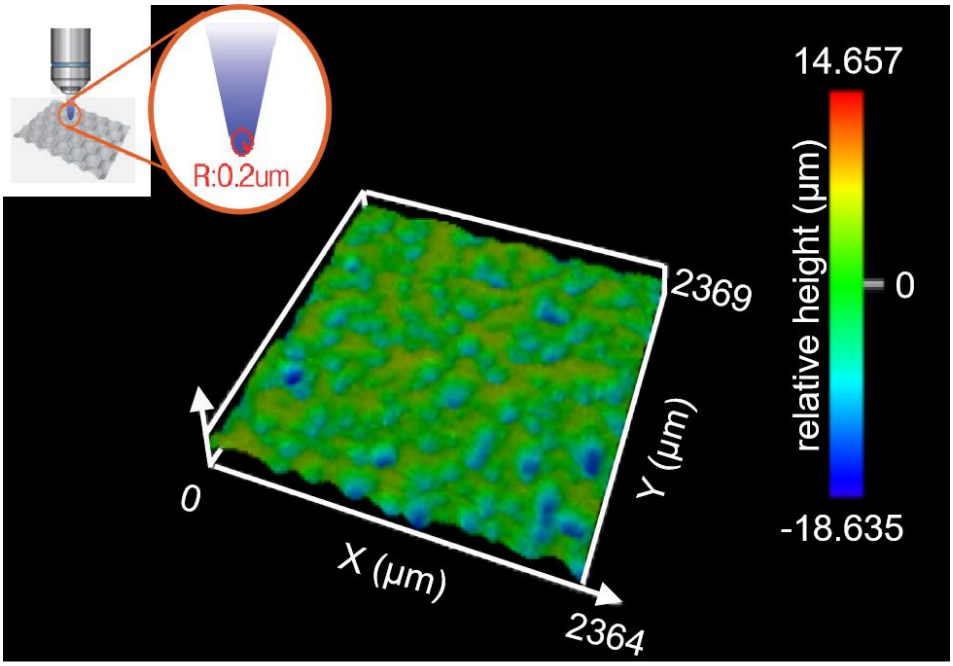

Figure 3.10 Height distribution image measured by the laser microscope. (Inset: schematic of working principle of laser scanning microscope).

The outcomes derived from the Menlo were cross verified through measurements acquired using a laser scanning microscope. The process of gauging the ***Ra*** through the laser scanning methodology was executed utilising an OLYMPUS OLS5000 Laser Scanning Microscope, equipped with a 20X objective lens. This setup achieved a focal spot radius of approximately 0.2μm on the sample surface, as depicted in the inset of Figure 3.10. This figure further illustrates a prototypical mapping of height distribution, which was secured through laser delineation techniques. The calculation of RMS roughness was conducted as per the following equation:

$$R_a = \frac{1}{A}\iint_A |H(x,y)|dxdy \tag{3.5}$$

where *A* is the scanning area, H is the relative height to average leveling.

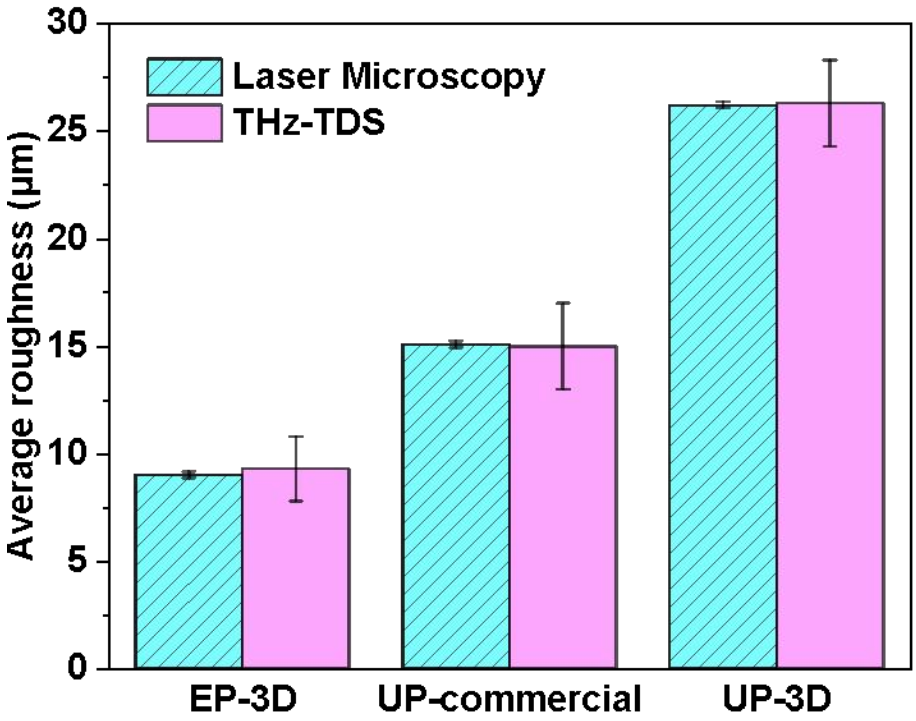

Figure 3.11 Comparison of Ra of selected areas determined from the laser microscope and THz-TDS. EP-3D: electrochemical-polished area on AM fabricated sample, UP-3D: unpolished area on AM fabricated sample, UP-commercial: unpolished area on commercial sample.

Figure 3.11 presents the examined areas' ***Ra*** values, ascertained using laser microscopy and THz-TDS. The precision of the laser microscope adheres to the ISO 25178-2:2012 standards, whereas the accuracy of THz-TDS is determined by a fitting model with R values exceeding 90%.

Figure 3.11 illustrates the ***Ra*** values determined through laser microscopy and THz-TDS techniques. The former meets ISO 25178-2:2012 standards, and the latter's accuracy is verified with R values above 90%. The THz-TDS method exhibits a larger error margin due to the fitting process, but its precision can be heightened by improving the system's SNR, possibly by incorporating more expansive parabolic mirrors or transitioning to a vacuum experimental environment. These adjustments could facilitate the detection of micro or sub-micro roughness levels, showcasing the promising capabilities of THz-TDS in assessing the roughness of additive manufacturing components $\exp(-i\omega\Delta H(x,y)/c)$.

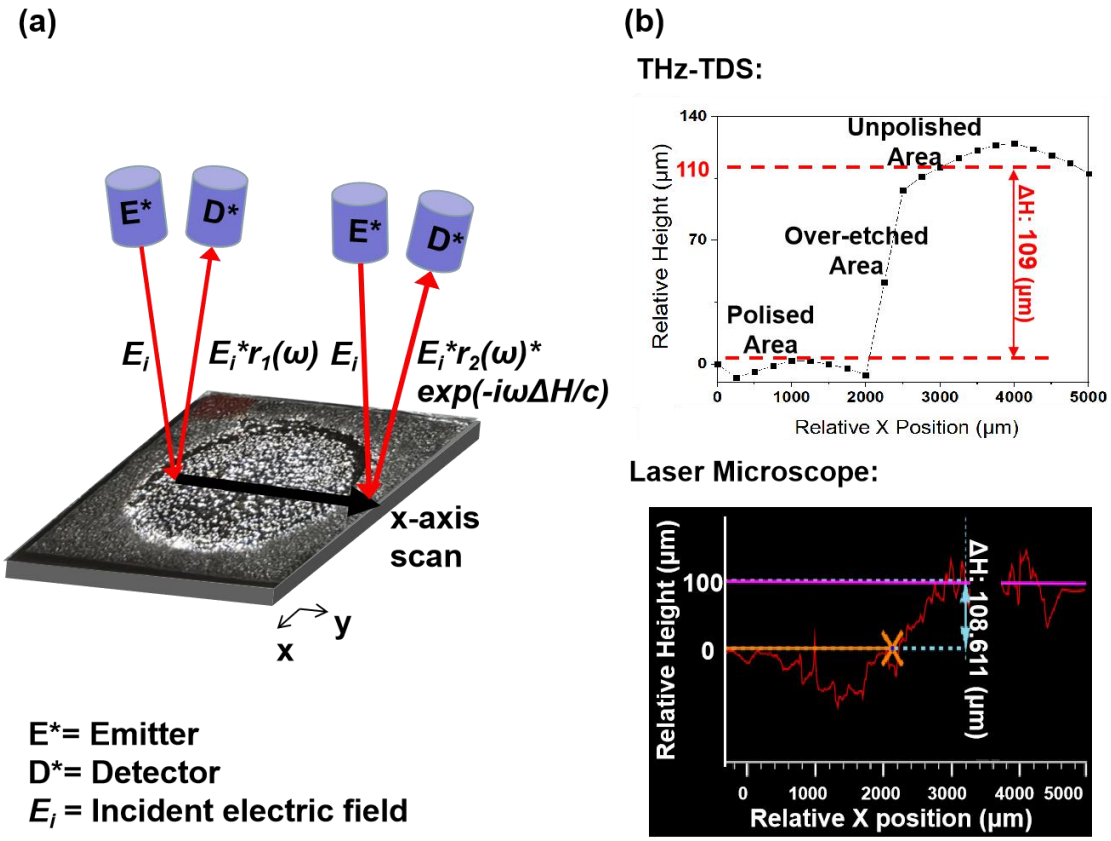

Figure 3.12: (a) Schematic of HL evaluation based on phase change via THz-TDS (b) HL values measured from different techniques (top: THz-TDS, bottom: laser microscope). Three different (polished, over-etched, unpolished) regions can be classified by comparing the ***HL*** variances shown in the THz-TDS results.

The complex phase component $\exp(-i\omega\Delta H(x,y)/c)$ is a critical element that can be segregated to scrutinise the surface profile. Figure 3.12 (a) delineates the schematic of this investigative procedure undertaken through THz-TDS scanning. In the preliminary phase of the acquisition process, the phase value of the initiating point was designated as zero, establishing a benchmark for subsequent measurements. This was followed by cataloguing phase values for successive points, registering them as relative to the inaugural one. The meticulous fitting of these phase disparities makes it feasible to ascertain the distinctions in height, which are contingent on frequency parameters.

In Figure 3.12 (b), a segmental portrayal of the surface profiles of the second sample is presented and analyzed meticulously through dual THz-TDS and laser microscopy methodologies. The topographical analysis via THz-TDS was executed utilizing the phase

values noted at the frequency of 1 THz, as documented in the respective data points. This visual representation underscores a significant congruence in the observations documented through THz-TDS and those registered using the laser microscope, with the ΔH values delineated as 109±2 μm and 108.61±0.15 μm, respectively.

Further, a discernible classification segregates the profile acquired into three distinct sectors. Firstly, the polished sector is characterized as a tiered zone with relative height approximations centered around zero micrometers, as exhibited in the representation. Secondly, the over-etched sector, a consequence of unforeseen diffusion beneath the mechanical holder, manifests as a sloping profile with heights ranging from zero to approximately 110 μm, orchestrated by the diminishing electric field extending from the exposed to the shielded zone. Lastly, the unpolished region, also characterized as a terraced zone, showcases relative height estimates around the 110 μm mark in the graphic representation.

As captured through both analytic avenues, these variations in the surface profile align impeccably, substantiating the efficacy of electrochemical polishing procedures. Consequently, this affirms the application of THz-TDS as a potent tool in the comprehensive evaluation of surface profiles of metals post-electrochemical polishing. It is noteworthy to mention, however, that the resolution of this approach is influenced significantly by a couple of dominant factors.The time-domain data sampling rate, noted at 0.033 ps during this specific measurement, initially correlates to a height approximation of 10 μm. Secondly, the constraints imposed by the diffraction and interactive capacities of the THz pulses notably influence this methodology's resolution.

3.2.6 3D imaging of Ra and HL distribution

Table 3-2 Comparison of Ra and HL of a 4 mm² square metallic area via laser microscopy and THz-TDS

	Laser microscopy	THz-TDS
Scanning time	5~10 mins, (it depends on the absolute roughness difference on the surface).	40 s (4 pixels with 10s averaging)
Data lost	Yes (for out-of-range peaks).	No
Resolution	0.2 μm	>1 mm
Confidence Range	>30 nm	>6 μm

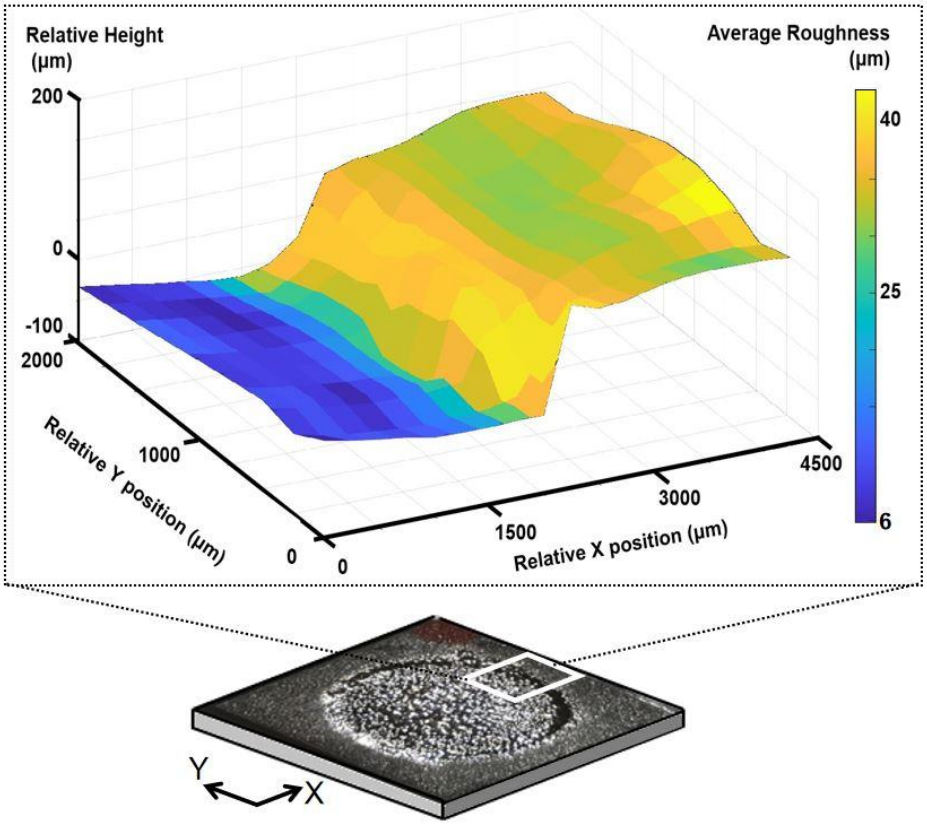

Figure 3.13 3D image of Ra and HL distribution (z-axis) of the partial surface of sample 2.

In this study, the ***HL*** resolution in broadband THz-TDS demonstrated a significant frequency dependence, with potential inaccuracies noted, particularly in components up to 0.75THz. Phase values were selectively chosen within a 0.8-2 THz bandwidth to ensure data consistency. Consequently, a 3D image of a 2×4.5 mm² area was generated using THz-TDS,

illustrating ***Ra*** distribution and surface profiles, as seen in Figure 3.13. The analyzed data revealed a polished region with ***Ra*** values between 6-11 μm, corroborating the data exhibited in Figure 3.8. Adjacent to this, an over-etched region was identified. However, the high ***Ra*** values noted here might not be entirely accurate due to the influence of altered incident angles on the KA fits. Further, an unpolished segment with prominent terraces and ***Ra*** values predominantly within 25-35 μm was discerned, aligning well with earlier observations.

Overall, the 3D imaging data correlated well with laser microscopy findings, underscoring the efficacy of THz-TDS in evaluating surface characteristics and height variations of EP AM fabricated components, specifically 316L stainless steel. The methodology proved promising for extensive scanning operations, especially for samples with ***Ra*** values ranging between 6 and 100 μm and offers potential as an in-situ tool for analyzing underlying processes in the EP cell during the polishing phase, as shown in Table 3-2. It merits reiteration that the minimum R_a value of 6 μm is constrained by Equation (3.4) and the bandwidth limitations of the Menlo system, which spans 0.2-2 THz. Characterization of a lower ***Ra*** value is feasible using the same methodology, provided a more broadband THz TDS system is employed. Fundamentally, the ***KA*** method remains applicable for assessing the surface roughness of non-metallic materials. However, in such instances, it is imperative to account for the multiple reflections occurring within the sample.

3.3 Conclusion

This chapter elucidates two pivotal applications explored during doctoral research presented in this thesis: the utilization of THz TDS for advancing EMI shielding material synthesis and examining surface roughness distribution in electrochemically polished AM components. Experimental findings suggest that THz-TDS is proficient in assessing the EMI attributes of various carbon-based composites. Moreover, it can effectively measure the average roughness and height profiles of AM metal surfaces, yielding results that align closely with measurements from state-of-the-art laser microscopy. Such findings underscore the potential of EMI materials and the AM technique in fabricating essential THz components, such as waveguides and other integrated elements.

Chapter 4 Metamaterial Design and Simulation

The preceding section elucidated applications that deploy THz-TDS for evaluating natural materials and improving industrial manufacturing processes. Concurrently, THz-TDS can be adeptly harnessed to characterize the optical interactions within an array of artificial photonic structures, notable among specific metamaterials endowed with tailored functionalities, such as a high Q-factor and optimal light-capturing capabilities, which conceptualizations are elaborated further within Chapters 6 and 7. Therefore, this Chapter introduces the methodically structured designs that form the bedrock for experimental inquiries and the analytical prognostication of electromagnetic interactions inherent to diverse metamaterial systems.

Embarking on this intricate exploration demands, a series of rigor and orchestrated Finite Element Method (FEM) simulations are also demonstrated in this Chapter, presenting a comprehensive discourse on the underlying mechanism with a pronounced focus on the properties of materials and the foundational unit cell model implemented in the commercial FEM software. This discussion stage serves as a precursor to the subsequent in-depth analysis, where simulations are engineered meticulously to model the high-Q asymmetric metamaterial alongside the active graphene-based metamaterial. Navigating this structured pathway is anticipated to forge a deeper understanding of the nuanced aspects governing the interaction of light with these complex metamaterial structures. The insights garnered through this approach are pivotal in paving the way for advancements in the field, fostering a new era of innovation and discovery in light-harvesting technologies.

4.1 Finite element method simulations

In the quest to create adaptable metamaterial, including the high Q-factor resonators and active graphene modulators highlighted in this dissertation, a series of FEM simulations were conducted using the commercial software COMSOL Multiphysics 5.6 (henceforth referred to as "COMSOL"). This tool facilitates the modelling of electromagnetic responses of metamaterial with varying geometries about simulated incident waves. Consequently, it empowers researchers to assess their spectral performance in far and near fields quantitatively. This segment intends to succinctly delineate the theoretical underpinnings of the FEM while

also elucidating the basic steps involved in executing simulations via COMSOL.

The Finite Element Method (FEM) is a robust numerical technique for transforming an extensive system within an infinite dimensional space into a collection of smaller, manageable systems occupying a finite-dimensional space. This is facilitated by creating a mesh grid encompassing the area of interest. This mesh effectively discretizes the overarching system into distinct domains guided by specified numerical functions.

Within these domains, each segment encapsulates a series of straightforward functions representing a specific portion of the more intricate functions targeted for study. These individualized, more straightforward functions make it feasible to navigate the complexity of the larger system, offering a more accessible avenue for analysis and understanding.

Upon the completion of the analysis within each domain, the gathered sets of solutions are then amalgamated to formulate an approximate solution to the complex functions under scrutiny. This assembled solution is a valuable approximation, offering insights and understandings that facilitate further exploration and study in metamaterial research. This method not only streamlines the process but also enhances the accuracy and reliability of the findings, fostering advancements in the field.

In modelling a photonic system encompassing diverse optical functions within a 3D structure, COMSOL becomes indispensable, given its capacity to resolve a variety of sets of Maxwell's wave equations meticulously. Within a particular simulated analysis, each discretized mesh region delineated in COMSOL is perceived as an actual physical domain, bearing its intrinsic material properties within a three-dimensional space. The exact Maxwell equations stand for a domain in COMSOL are:

$$\nabla \times (\mu_r^{-1} \nabla \times E) - \omega^2 \varepsilon_{rc} E = 0 \tag{4.1}$$

$$\varepsilon_{rc} = \varepsilon_r - j\frac{\sigma}{\omega} = \varepsilon_0(\varepsilon' - j\varepsilon'') \tag{4.2}$$

E is electric field vector, J is the current density, σ is the complex conductivity, ω is the angular frequency, C_0 is the speed of light in vacuum, ε_{rc} is complex permittivity; ε_0, ε'and ε'' are vacuum permittivity, the real part of ε_{rc}, and imaginary part of ε_{rc}, respectively.

To simplify the simulation procedure, all the materials simulated by COMSOL in this

thesis are considered homogeneous, meaning the polarization loss caused by crystal orientations is negligible. Therefore, in equations (4.1~4.2), the real part of conductivity and the ε'' are equivalent, because they both physically represent the surface current induced by free charge oscillations. Thus, to avoid counting the same current twice in simulations, σ is the only parameter used to model for the induced current effect, while ε'' is kept empty in COMSOL in this thesis.

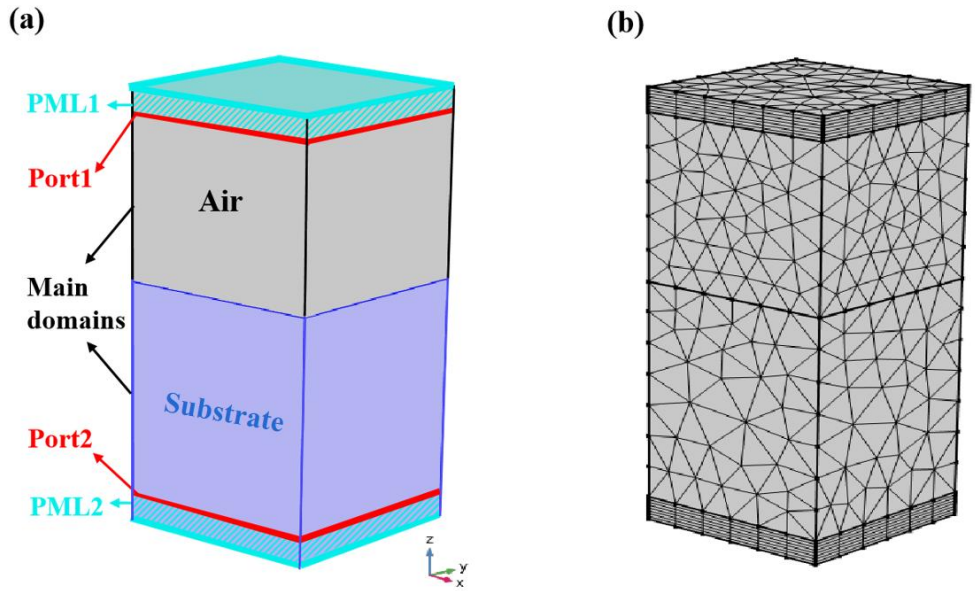

Figure 4.1 (a) A standard unit cell geometry set in COMSOL, including 5 parts of PML1, Port1, Main domains, Port 2 and PML2. (b) the corresponding meshes of blocks shown in (a).

Figure 4.1 (a) illustrates the standard geometry of a simulated unit cell applied in COMSOL. Within the designated unit cell, ports 1 and 2 function analogously to the source and detector encountered in TDS experiments. The initiation site, port 1, can instigate a x- or y-polarized plane wave, subject to a predetermined angular frequency and a typical power output of 1 W. This incites wave propagation in the direction of the z-axis, culminating at the receiving end, port 2. During this progression, the wave functions interact with diverse materials delineated either as elementary blocks or as distinct metamaterial geometries within the primary domains. These interactions significantly shape the wave characteristics and culminate in data registration at port 2.

It is essential to note that waves that permeate beyond port 2 do not undergo

instantaneous attenuation. Instead, there is a distinct possibility of their re-detection by port 2, following multiple reflections within the unit cell, potentially influencing the final simulation outputs. To obviate the ramifications of multiple reflections, Perfect Matching Layers (PML) 1 and 2 are strategically configured to absorb any incident waves, effectively neutralizing the multi-reflection phenomenon. Moreover, periodic Floquet boundary conditions have been instituted across the x and y axes to simulate the coupling effects observed within periodic metamaterials. This procedure facilitates the creation of an infinite repetitive structural framework along the specified axes, offering a nuanced and expansive analytical perspective on the intrinsic properties and behaviors exhibited by the metamaterial under scrutiny.

As elucidated in the preceding segment, the meshing process serves as a quintessential procedure in the FEM, facilitating the decomposition of a comprehensive system into more manageable, smaller subdivisions. Figure 4.1 (b) presents a panoramic view of the customary mesh configurations adopted ubiquitously throughout this dissertation. Within the primary domains, the mesh structures are deliberately designed in triangular or quadrilateral configurations across two-dimensional planes, fostering the formation of continuous tetrahedrons or hexahedrons in three-dimensional spaces. This configuration facilitates a more precise assembly and convergence towards intricate structures. Concurrently, the meshes in the perfect-matched layers (PML) are typically fabricated through the accumulation of repetitive layers, a strategy that simplifies the computations associated with signal decay.

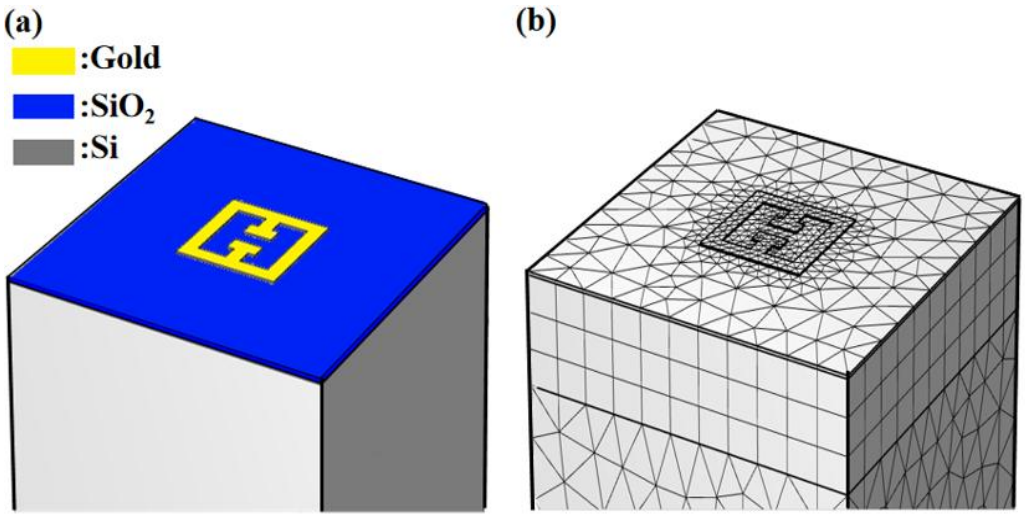

Figure 4.2 (a) The 3D geometry and the allocated materials of a simulated metamaterial unit cell. (b) the corresponding meshes of the unit cell shown in (a).

It is imperative to underscore that the dimension of each domain should ideally not exceed roughly one-tenth of the incident wavelength, as this criterion enhances the convergence of the computational solution. Upon completion of the meshing procedure, the electric field distribution throughout the architecture can be ascertained by resolving the partial differential equation (4.1) at all computational nodes situated at the vertices within all domains. The granularity of these nodal points is directly proportional to the accuracy of the electric field distribution in the resultant simulation.

However, deploying an exceedingly dense mesh topology demands substantial RAM capacity, potentially decelerating the computational processes considerably. Consequently, a prevalent strategy involves intensifying the mesh resolution in regions anticipating elevated electric field gradients, such as the surface vicinity of plasmonic structures, while adopting coarser meshes in uniform regions. This tactic aims to yield precise simulation outcomes while optimizing computational efficiency. Figure 4.2 (a-b) depicts a quintessential metamaterial unit cell, distinguished by a metallic formation affixed upon a SiO_2/Si substrate, undergoing a meticulous mesh generation procedure in alignment with the previously delineated strategy. The electrical field is anticipated to exhibit concentrated localization near the metamaterial, attributed to the plasmonic oscillations induced by gold.

Subsequently, the ascertained electric fields facilitate the extraction of other critical parameters such as surface currents, magnetic flux distributions, energy dissipation rates, and the scattering parameters (S-parameters) between port 1 and port 2 within the COMSOL environment. These S-parameters encapsulate S_{21} and S_{11} in a two-port configuration, signifying electric fields' transmissive and reflective coefficients migrating from port 1 to port 2 and reverting to port 1, respectively. The transmission, reflection, and absorption metrics of the excited wave traversing between port 1 and port 2 are respectively depicted by the equations $|S_{21}|^2$, $|S_{11}|^2$, and $1-|S_{21}|^2-|S_{11}|^2$. These metrics are pivotal in predicting the spectral characteristics of various samples subjected to far-field measurement analyses.

The established methodology for cultivating innovative metamaterial endowed with advanced functionalities entails conducting a series of simulations wherein a range of geometrical parameters are systematically varied and analyzed. In the forthcoming sections, a comprehensive series of detailed simulations are performed, which focus on the design and

analysis of high Q-factor metallic passive metamaterial and the development of graphene-based active metamaterial. These simulations support the intricate THz-TDS experiments executed within various configurations such as far-field, near-field, and high-electric field pumping, as explored in Chapters 6 and 7.

4.2 FEM analysis of high Q-factor metallic passive metamaterial

This section performs the comprehensive simulation procedure instrumental in developing a gold-fabricated asymmetric split ring resonator (ASDR) earmarked for THz a-SNOM analyses presented in Chapter 6. Concurrently, the section elaborates on crafting an NbN-constructed ASDR with a high Q-factor of 160, specifically tailored for cryogenic THz-TDS investigations.

4.2.1 Introduction of high Q-factor metamaterial

The metamaterial characterized by a high quality-factor (Q-factor) denotes resonant infrastructures in which electromagnetic oscillations sustain with minimal loss of energy, paving the way for refined control and manipulation of THz waves. The nuanced optical enhancements engendered by high Q-factor metamaterial substantially accentuate photonic systems by substantially reducing the optical field interaction zone or extending the interaction period, thus entrapping photons within specified regions. This localized photonic system emphasizes the augmentation of sensitivity, the promotion of miniaturization, and the advancement of functional attributes, thereby acting as a catalyst for pioneering advancements in fields such as high-speed telecommunications [145], accurate healthcare infrastructures [146], and sensitive spectroscopy arrangements [147].

4.2.2 Metamaterial Q-factor improvement strategies

The Q-factor is an indicator parameter for assessing the damping condition of an oscillation or resonance, as documented in several studies [148-150]. This factor fundamentally represents the ratio of the energy conserved within the resonator to the energy dissipated during a single oscillation cycle, as cited in [148-150].

In the context of a resonator offering a high Q-factor value, it is inferred that the predominant energy loss transpiring during oscillation predominantly occurs at the

narrow-band resonance. Consequently, this allows for the reconfiguration of the Q-factor definition to embody the normalized frequency-to-bandwidth ratio associated with the resonance, thereby delineated as follows [150]:

$$Q \stackrel{\text{def}}{=} 2\pi \times \frac{E_s}{E_d} = 2\pi f_r \times \frac{E_s}{E_l} \stackrel{\text{def}}{=} \frac{\omega_r}{\Delta\omega} \tag{4.3}$$

E_s is the initial energy stored inside the resonator, E_d is dissipated energy within each cycle of oscillation, and E_l is the total lost power per cycle consumed by work done driven by external force, such as the resistive loss of an electrical system. $\omega_r = 2\pi f_r$ is the central angular frequency of the resonance, and $\Delta\omega$ is the angular half-power bandwidth of the resonance.

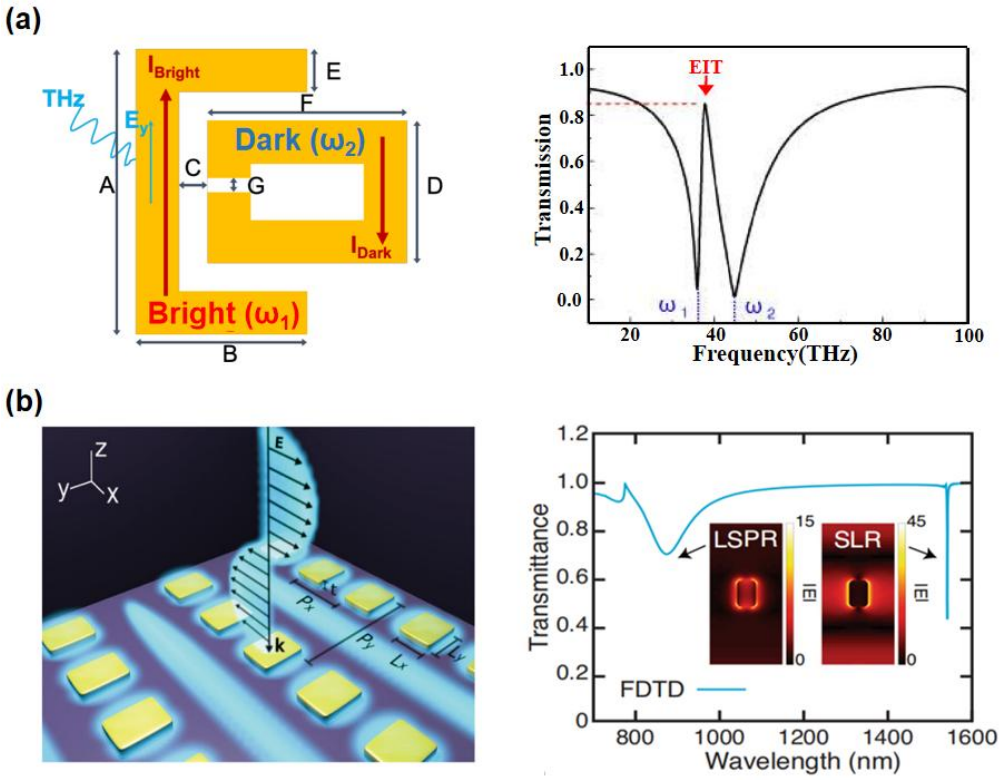

Figure 4.3 (a) The schematic of the EIT metamaterials and its simulated spectra [151]; (b) the schematic of the SLR modes existing in extensive metallic rectangles array and its simulated spectra [152].

The most pragmatic strategy for fabricating a resonator with a high Q-factor involves

minimizing energy leaks. Two primary pathways facilitate power loss in a photonic resonator, such as metamaterial: radiative and dissipative (non-radiative) loss.

The intrinsic oscillatory properties of the system predominantly govern the degree of radiative leakage. Figure 4.3 (a-b) elucidates two exemplary metamaterial design strategies to foster a high Q-factor. On one hand, the inaugural example leverages the phenomena of electromagnetically induced transparency (EIT) coupling effect, delineated in Figure 4.3 (a) [151]. This methodology necessitates the close positioning of a duo of resonators with delicately orchestrated operating frequencies that are not identical but narrowly proximate, distinguishing one as the "bright" mode and the other as the "dark" mode during the oscillation process. The "bright" resonator, directly stimulated by the incident light, engages in capacitive coupling with the "dark" mode resonator, characterized by a closely aligned resonant frequency. This interaction originates from the EIT phenomenon witnessed in atomic physics, arising due to destructive interference among excitation states within atomic systems, and is analogously articulated by coupled resonant oscillators in classical mechanics, initiating a transparency window in the transmission spectrum.

On the other hand, Figure 4.3 (b) unveils an alternative methodology that capitalizes on the collective influence of localized surface plasmon resonances, also denominated as "surface lattice resonance" (SLR) [152]. This paradigm exhibits a Q-factor escalating up to an order of magnitude of 10^3 at the predetermined wavelength defined by the equation $\lambda = nP$ [153], where 'n' denotes the effective refractive index of the enclosed environment, and 'P' represents the periodicity of the metamaterial unit. Nonetheless, this collective mode necessitates the synchronous excitation of numerous metamaterial units and manifests a heightened susceptibility to environmental fluctuations occurring at the surface.

It is imperative to acknowledge that a myriad of alternative high Q-factor metamaterial designs, predicated on diverse mechanisms including photonic crystals [154-155], Fano resonances [156-157], Boundary States in Continuum (BIC) [158-159], and dark-dark mode coupling [160] are not explored in this thesis. This persistent diversity in high Q-factor metamaterial design stems fundamentally from the limited comprehension of the intrinsic high Q-factor resonances manifested within metamaterial structures. This leads to a primary reliance on incessant simulation trials with variable parameter adjustments or analytical fitting. The high Q-factor metamaterial simulations delineated in this chapter are expressly crafted to

serve as a prototype for leveraging THz near-field TDS measurements, fostering a deeper understanding of the underlying nature of high Q-factor resonances beyond mere phenomenological observations.

In parallel, it is to be noted that the intrinsic Ohmic losses largely govern dissipative losses within metamaterial entailed with the metallic constituents, which typically curtail these resonances, consequently diminishing the resonance visibility. In stark contrast, using materials characterized by a predominantly imaginary conductivity, such as superconductors, emerges as a direct and effective approach to curb dissipation substantially [78-79, 161]. An extensive discourse on this phenomenon of superconductors is elucidated in subsequent simulation sections.

4.2.3 Simulations of high Q-factor Au ADSR

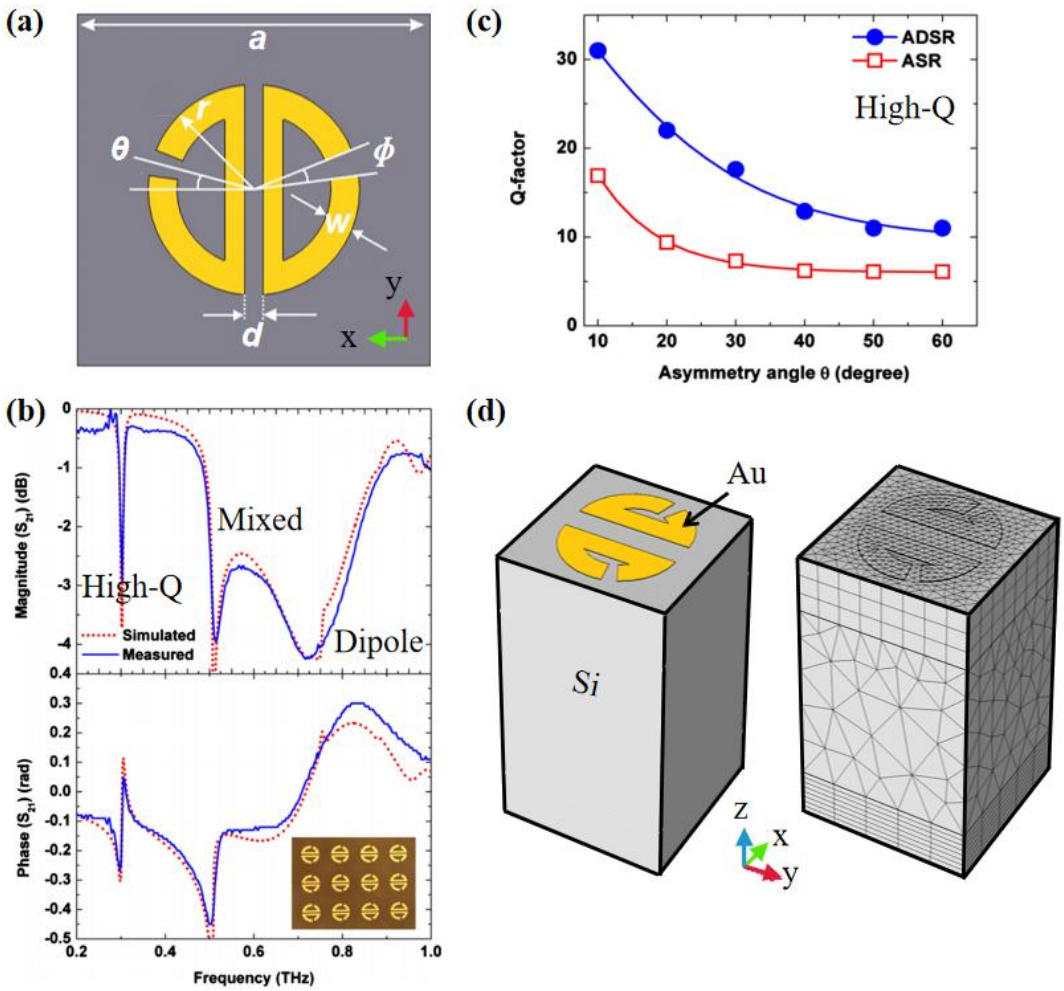

Figure 4.4 (a) The schematic of the ADSR unit cell; (b) the comparison of simulated and experimental results within magnitude and phase spectra acquired from [162]; (c) the Q-factor

increment of High-Q mode in ASDR by subsiding the asymmetry angle [162]; (d) the standard materials and meshing models of ADSR set in COMSOL.

The high Q-factor metamaterial delineated in this thesis adapts the asymmetric split ring resonator (ASDR) blueprint. As illustrated in Figure 4.4 (a), a single-unit ASDR scheme was initially introduced by Christian J. et al [162]. This configuration encompasses two bifurcated ring-shaped resonators organized to display y-axis symmetry, exhibiting asymmetric gaps in a x-axis symmetric configuration. The resonance phenomenon of the ASDR is chiefly orchestrated by a series of parameters: the radius $\boldsymbol{r}$ of the split ring, the width $\boldsymbol{w}$ of the semi-circular segments, the intervening distance $\boldsymbol{d}$ between the two semi-circular segments, the open gap angle denoted as $\boldsymbol{\Phi}$, the sweep angle $\boldsymbol{\theta}$ measured from the y-axis to the midpoint of the gap, and the periodicity $\boldsymbol{a}$ of the structure.

Figure 4.4 (b) illustrates the x-axis excited magnitude alongside phase spectra derived from simulated and empirical S_{21} results of an ASDR array fabricated from 200 nm thick gold layers on a 720 μm fused silica substrate characterized by a refractive index 1.997. As delineated in [162], the various parameters are defined as $\boldsymbol{r}$ = 90 μm, $\boldsymbol{w}$ = 25 μm, $\boldsymbol{d}$= 15 μm, $\boldsymbol{\Phi}$=14°, $\boldsymbol{\theta}$=15°, and $\boldsymbol{a}$=300 μm. Notably, a distinct, sharp resonance characteristic is discernible around the 0.3 THz mark on the spectra, reflecting a high Q-factor approximated at 27. Contrarily, the spectra reveal a broader dipole resonance near the 0.7THz region and another relatively diffuse resonance at 0.5THz, indicative of a mixed modality encompassing high Q-factor and dipole resonances, predominantly manifested in the elevated frequency domain. Furthermore, Figure 4.4 (c) exemplifies the augmentation of the Q-factor about this mode as a direct consequence of diminishing asymmetry angles, mirroring a similar trend observed in a BIC based metamaterial as shown in [159].

To deepen the comprehension of the inherent high-Q mode dynamics and optimize the Q-factor within the gold ASDR structure, we delineate the specified material distribution and meshing conditions implemented in COMSOL simulations in Figure 4.4 (d). To maintain uniformity with experimental conditions, the simulated thickness of the gold layer is held at 150 nm. The refractive index of Silicon (Si) is ascertained to be 3.44, while the electrical conductivity of the gold component adheres to the Drude model as:

$$\tilde{\sigma}_{AC-Au} = \frac{\sigma_{DC-Au}}{1 + i2\pi f\tau} \tag{4.4}$$

Table 4-1 Simulated Q-factor changes of high-Q resonance of ADSR with different substrate.

Substrate materials:	Fused silica (n=1.94)	MgO (n=2.99)	Si (n=3.44)
Q-factor:	27	20	16

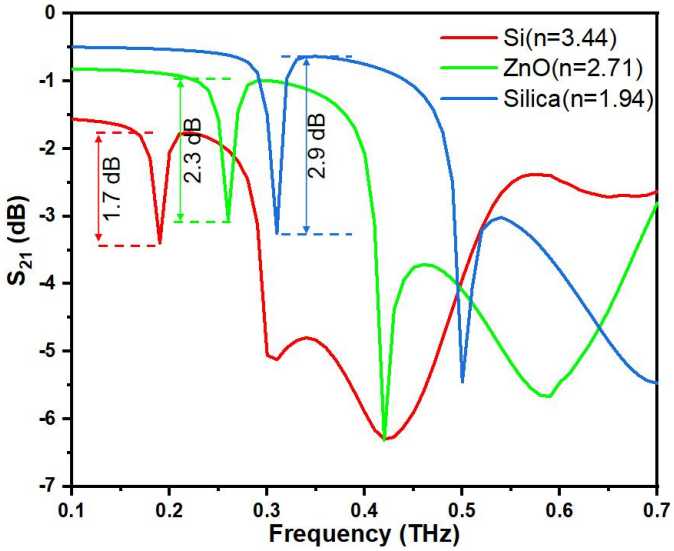

Figure 4.5 Simulated S_{21} spectra of the original ADSR design on different substrate.

Figure 4.5 illustrates the initial series of simulations with x-axis excitation conducted at a frequency sweep step of 0.01 THz, engineered to both replicate the original results depicted in [162] (denoted by the blue line), and to analyze the repercussions of substituting substrates with differing refractive indices (Silica:1.94, ZnO:2.71, and Si:3.44). The replicated simulation meticulously aligns with the primary spectra elucidated in Figure 4.4 (b), thus corroborating the efficacy of employing COMSOL in modelling the ADSR structure. Notably, integrating substrates with elevated refractive index induces a conspicuous red shift in the high-Q mode frequency and attenuates the resonance depth, reducing it from 2.9 dB to 1.7 dB. This modification consequently diminishes the Q-factors of the high-Q mode from 27 (silica) to 16 (Si), as delineated in Table 4-1. The assessment of the Q-factor within COMSOL is predicated upon the subsequent equation:

$$Q = \frac{\omega_0}{\Delta\delta} \tag{4.5}$$

ω_0 is the eigenfrequency of resonance acquired from the eigenvalue scan in COMSOL, δ is the damping of the solution.

Nevertheless, as elucidated in Chapter 2, the authentic far-field spectrum ascertained through THz-TDS analyses predominantly gravitates around 0.8 THz. Consequently, to align the high-Q mode with a frequency of 0.6 THz—where the signal-to-noise ratio is substantially augmented in the Menlo system mentioned in Chapter 2 and is further removed from the influence of gas absorption lines—the dimensions of the ADSR situated on the Si substrate have been meticulously recalibrated. The revised parameters are delineated in Table 4.2.

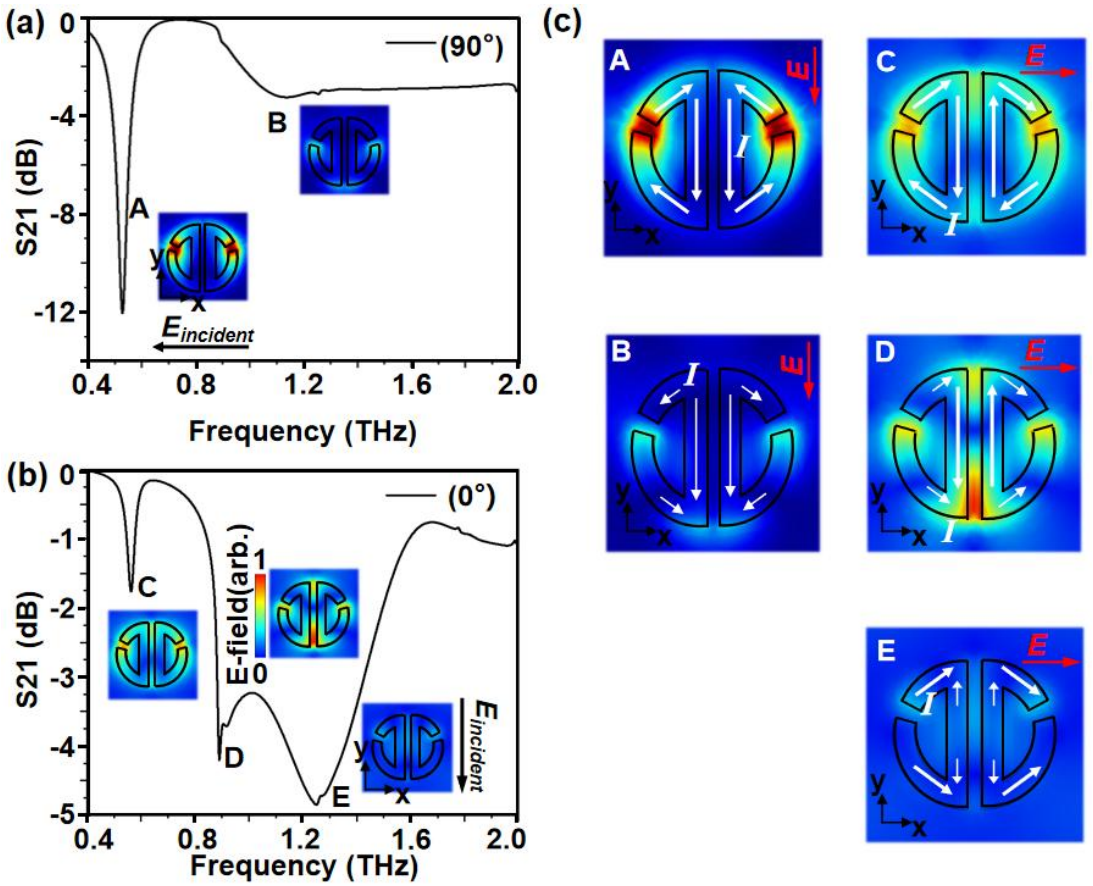

Figure 4.6 (a-b) Simulated spectra and field distribution of modes **A**, **B** excited by 90° , and modes of **C**, **D**, **E** excited by 0° excitation, respectively; (c) Simulated electric field and induced current distribution of different modes on the ASDR surface.

Table 4-2 Simulated parameters of the ASDR arrays used for the THz-TDS far field measurement.

r(μm)	w(μm)	d(μm)	φ(°)	θ(°)	a(μm)
30μm	8.3	5	14	15	100

To illuminate the disparities between the high-Q mode and non-high-Q mode in far-field and near-field assessments, a further simulation, as performed in Figure 4.6 (a), delineating the revised ADSR design stimulated by light in the y-direction with a frequency increment of 0.01 THz in conjunction, which manifests clear non-high-Q modes, becomes indispensable. Within the scope of a 90° polarized incidence, Mode **A**, embodying a robust dipole-like resonance, emerges prominently around the 0.5 THz region, accompanied by substantial visibility. In contrast, a feeble dipole Mode **B**, marked by considerably diminished visibility, pervades from 0.8 THz to 2 THz. In contrast, Figure 4.6 (b) illustrates the refined simulation spectra employing the mapped normalized electric field distribution during the activation of the ADSR by polarized stimulation at 0° angle. The high-Q, mixed, and dipole modes previously delineated in Figure 4.4 have been henceforth reclassified as Modes **C**, **D**, and **E** to facilitate a more streamlined discourse.

Furthermore, Figure 4.6 (c) showcases the distinctive current distributions of these five modes at the ADSR surface, as computed by COMSOL, unveiling their inherent variances. Under the influence of 90° stimulation, Mode **A** exhibits a dipole-like resonance characterized by intense bi-directional circular currents within each ring semi-section. At the same time, Mode **B** typifies a classic dipole current. When subjected to 0° polarized illumination, clockwise circular currents are executed within each semi-ring of the ADSR during Mode **C**'s activation, mirroring a pure magnetic resonance in the plane of light propagation. Mode **D** embodies a composite characteristic, integrating the circular current prevalent in Mode **C** within the central bar region with the dipole current flow observed in Mode **E** at the peripheral zone. Mode **E** represents a classical dipole current distribution like mode **B**.

To delve deeper into the roles of parameters θ, φ, d and w in the ADSR structure, a series of simulations, considered the standard optimization procedure for different simulated designs, have been conducted, as illustrated in the Figures 4.7 (a-d).

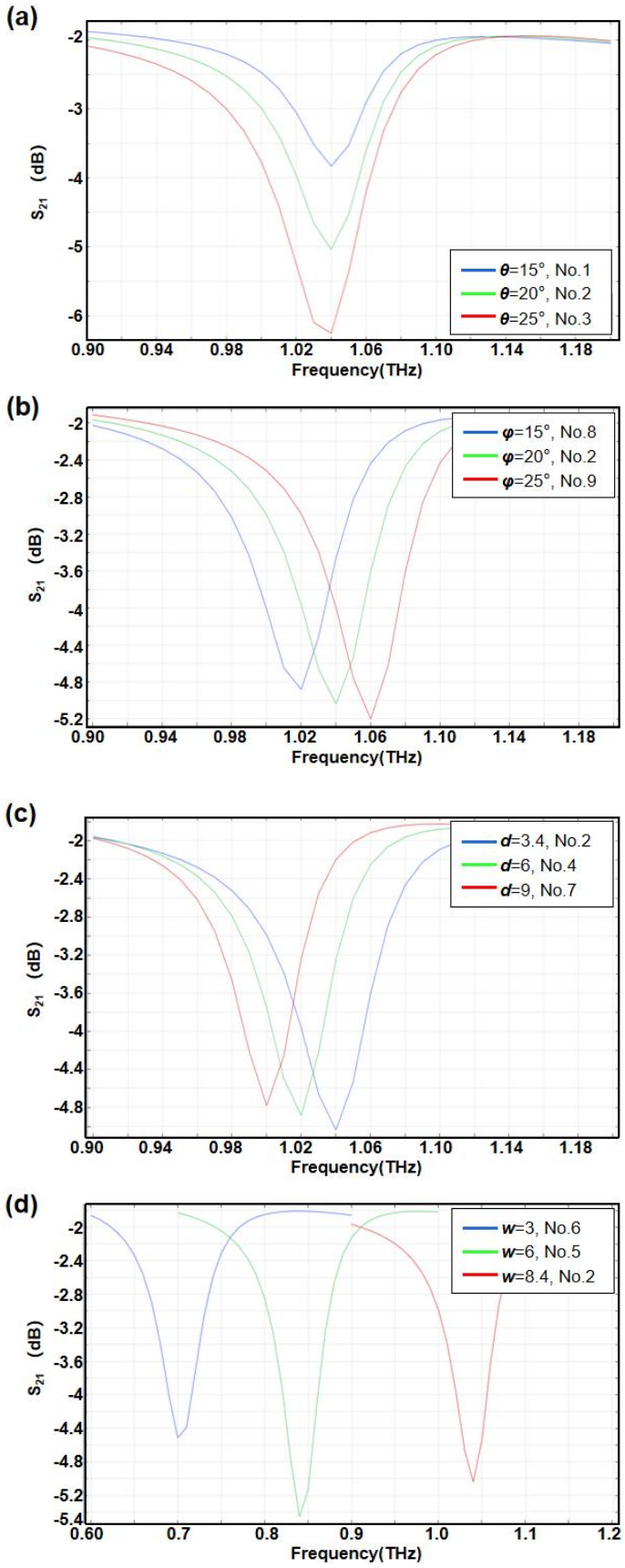

Figure 4.7 Simulated S_{21} spectra showing the effects by changing different parameters of (a) ,

$\boldsymbol{\theta}$, (b) $\boldsymbol{\varphi}$, (c) $\boldsymbol{d}$ and (d) $\boldsymbol{w}$.

As delineated in Figure 4.7 (a), an escalation of $\boldsymbol{\theta}$ from 15° to 25° precipitates a substantial augmentation in resonance visibility, increasing from 1.9 dB to 4.4 dB, whilst maintaining a constant central frequency. Nonetheless, as posited in Figure 3.5 (c), the amplification of $\boldsymbol{\theta}$ concurrently diminishes the Q-factor of Mode **C**, thereby indicating an inherent trade-off in the conceptualization of an efficacious high Q-factor ASDR. Contrastingly, the resonance efficacy exhibits diminished sensitivity to alterations in parameters $\boldsymbol{\varphi}$ and $\boldsymbol{d}$, as depicted in Figures 4.7 (b-c). A decrement of 5° in parameter $\boldsymbol{\varphi}$ or an increment of 3 μm in parameter $\boldsymbol{d}$ culminates in a minor red shift of approximately 0.02 THz and an estimated visibility loss of roughly 0.2 dB. The chosen $\boldsymbol{d}$ value of 3.4 μm is a downscaled from the original 5 μm in Table 4.2, which is indicative of the initial ASDR configuration.

It is worth noting that although the modulations in parameters $\boldsymbol{\varphi}$ and $\boldsymbol{d}$ bear semblance in terms of frequency shift and visibility alteration, an increase in parameter $\boldsymbol{d}$ concurrently contracts the resonance bandwidth, thereby manifesting a propensity towards Q-factor amplification. Pertinently, the modifications in parameter $\boldsymbol{d}$ exert a pronounced influence on radiation loss which will be expounded upon in the succeeding section, given that the elevated dissipation loss intrinsic to gold limits the strength of resonance.

Figure 4.7 (d) delineates the simulated spectra under varying values of parameter $\boldsymbol{w}$, which manifests the most substantial alteration in the resonance frequency. The fluctuation of parameter $\boldsymbol{w}$, ranging from 3 μm to 8.4 μm, induces a notable shift in the central frequency of mode **C**, transitioning it from 0.7 THz to 1.04 THz, a change that is nearly a decade more significant than the effect induced by parameter $\boldsymbol{d}$, as documented in Figure 4.7 (c). Moreover, the variations in parameter $\boldsymbol{w}$ exert a notable influence on the resonance visibility. Initially, the visibility of mode **C** varies from 2.6 dB to a peak of 3.5 dB when $\boldsymbol{w}$ is augmented from 3 μm to 6 μm, only to later recede from 3.3 dB to 3 dB upon a decrement in $\boldsymbol{w}$ from 6 μm to 8.4 μm. Remarkably, mode **C** ceases when the value of $\boldsymbol{w}$ surpasses 8.4 μm, consequent to the closure of the hollow space within each half, thereby morphing the ring's form into a disc.

4.2.4 Simulations of high Q-factor NbN ADSR

The preceding section succinctly elucidated the simulation model and delineated the spectral alterations engendered by the variations in the parameters of the Au ASDR array. Nonetheless, to facilitate a more unambiguous examination of the radiative loss characteristics inherent to mode **C**, ASDRs fabricated from Niobium Nitride (NbN) serve as an optimal platform, largely impervious to direct implications from Ohmic losses. Consequently, this section is poised to present simulations of NbN ASDR, primed for evaluation through cryogenic THz TDS (c-TDS) measurements.

4.2.4.1 Physical property and simulation model of NbN

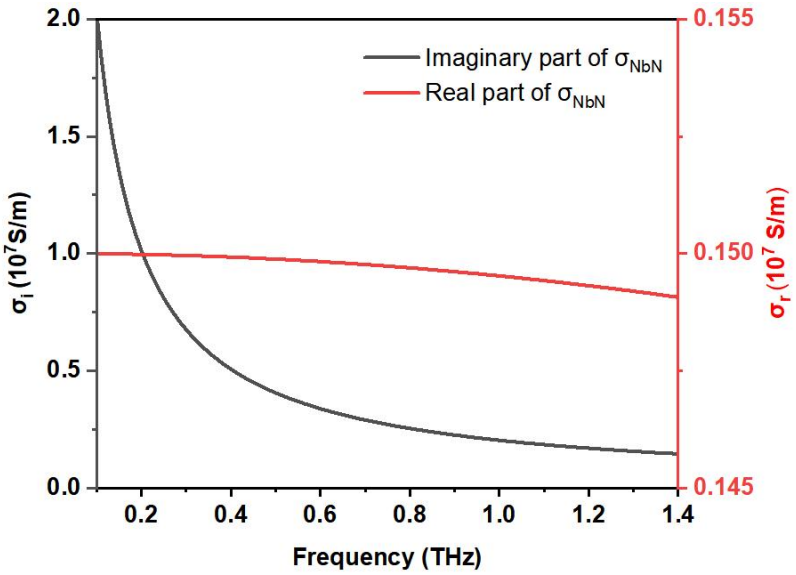

Figure 4.8 Imaginary part (black line) and real part (red line) of NbN's complex conductivity used in COMOSL.

NbN characterized as a type-II superconductor with multidirectional crystalline [163-164], stands as a prevalent choice in the formulation of high Q-factor metamaterials, as delineated in this thesis. Exhibiting superior superconducting attributes with a critical temperature (T_c) positioned beyond 15 K and a notable high operational optical frequency threshold reaching up to 1.4 THz [161], surpassing that of Nb, NbN has carved its niche in facilitating ultra-sensitive functionalities within the THz band. This is exemplified in its application in susceptible devices such as the superconducting hot electron bolometer (HEB)

[165] and the superconducting tunnel junction (SIS) [166]. Furthermore, NbN emerges as a preferred material for realising metamaterial THz resonators, owing to its facilitative properties in fabrication and processing, underscored by its adaptability to sputtering and reactive ion etching (RIE) techniques.

Delving into the phenomenon of superconductivity and its underlying physical model proves vital in accurately simulating the electromagnetic response of NbN within the THz band in COMSOL. Exhibiting the characteristics of a type-II superconductor, NbN operates within a mixed state, displaying both traditional and superconducting properties when subjected to intermediate temperatures or incident electromagnetic fields. This unique behaviour finds a comprehensive explanation within the framework of the two-fluid model, a widely accepted theoretical approach that delineates NbN's electrical and optical behaviour with precision [161].

According to this model, in its superconducting phase, NbN houses two distinct categories of electrons co-existing harmoniously - the superconducting and the conventional. It is crucial to note that these two electron cohorts exist independently of one another, devoid of mutual interactions. Therefore, the total conductivity of NbN under Tc, $\sigma_{NbN}(\omega)$, consists of superconducting electrons' conductivity, $\sigma_s(\omega)$, and the normal the electrons' conductivity, $\sigma_n(\omega)$, :

$$\sigma_{NbN}(\omega) = \sigma_s(\omega) + \sigma_n(\omega) \tag{4.6}$$

$\sigma_n(\omega)$ is a complex value described by the Drude model [161]:

$$\sigma_n(\omega) = \frac{\sigma_{DC-NbN}}{1 - i\omega\tau} \tag{4.7}$$

Where σ_{DC-NbN} is the sheet conductance of the NbN thin film, ω is the angular frequency of the incident electric field, τ is the normal electrons' scattering time. While $\sigma_s(\omega)$ can be written as:

$$\sigma_s(\omega) = i\frac{N_s e^2}{m\omega} = \frac{i}{\mu_0 \omega {\lambda_L}^2} \tag{4.8}$$

In the first expression, N_s is the electron density of the superconducting electrons, e is the electron charge, m is the mass of electron. As a direct measurement of density N_s is arduous, it is commonly to use the alternative form in the second expression, where λ_L is the London penetration depth, a measurable characteristic of type-II superconductors.

The NbN's model in COMSOL is based on a real sample made of 200 nm NbN thin film deposited on a 420 μm sapphire substrate. According to the measurement in [161], the values of σ_{DC-NbN}, τ and λ_L are arbitrarily set as $1.5*10^6$ S/m, 9fs and $2.5*10^{-7}$ m, respectively. Therefore, the real and imaginary part of $\sigma_{NbN}(\omega)$ in the range of 0.1-1.4 THz is performed in Figure 4.8.

4.2.4.2 Simulations of NbN ASDR

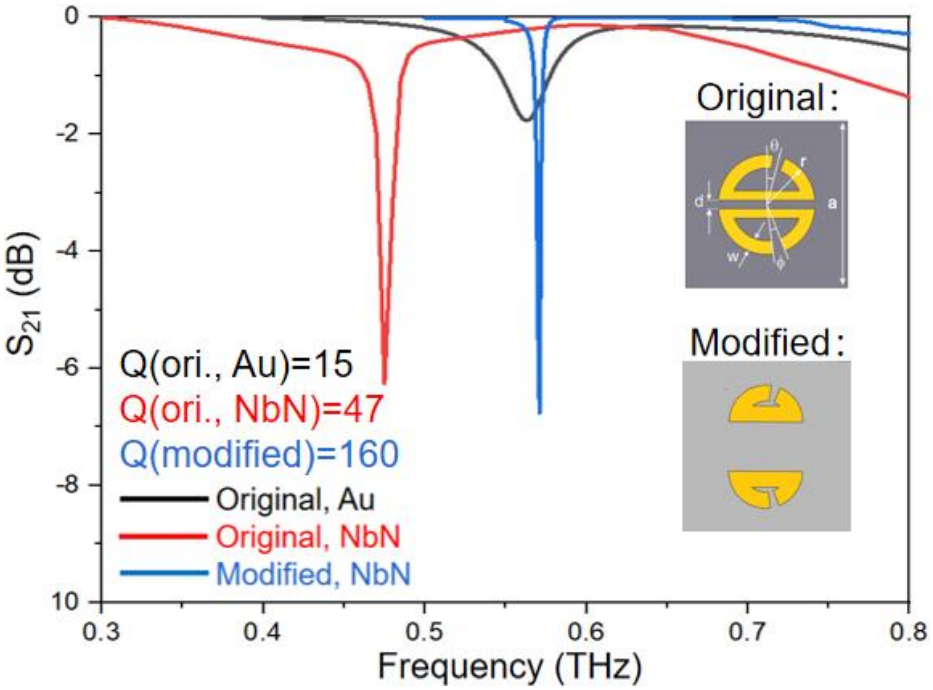

Figure 4.9 Simulated S_{21} spectra of mode C of the gold-made original ADSR, NbN-made original ADSR and NbN-made modified design.

Table 4-3 Modified parameters of the NbN ASDR array for cryogenic far field measurement.

r(μm)	***w***(μm)	***d***(μm)	***φ***(°)	***θ***(°)	***a***(μm)
30	12	40	14	15	140

According to the cryogenic Menlo system introduced in Chapter 2, the resonance frequency of the ADSRs constructed by NbN must align proximately with 0.6 THz to achieve an optimal signal-to-noise ratio. The NbN ASDR unite cell's geometry still obeys the Au ASDR architecture shown in Figure 4.4. The substrate material is replaced by sapphire (n=3.31), and the Au is substituted by NbN (conductivity following the demonstration in the last section).

To have an intuitive comparison of the Au and NbN ASDRs, Figure 4.9 meticulously delineates the different simulated S_{21} spectra about the mode ***C***, utilizing a 0.01 THz frequency step in the representation of various constructs: the original design implemented with gold (depicted in black), the original incarnation utilizing NbN (portrayed in red), and a refined design leveraging NbN, showcasing the pinnacle of Q-factor of 160 (illustrated in blue). The original Au ADSR design simulations draw upon the parameter data following Table 4-2. In contrast, the modified NbN ADSR design simulation is orchestrated based on the parameter details enumerated in Table 4-3. The insets of Figure 4.9 provide a visual representation, showcasing the schematics of both the original and the modified NbN ADSR design.

A noteworthy observation from the simulations is the pronounced enhancement in the Q-factor caused by using NbN, elevating it from a value of 15 to an impressive 55. This leap is accompanied by an increment in visibility, which escalates from 1.7 dB to a substantial 6.6 dB, a feat unattainable through mere adjustments of the ADSR parameters, as elucidated in preceding discussions. Moreover, it is crucial to highlight the evident red shift in the resonance spectrum, a phenomenon rooted in the reduction of permittivity attributed to the diminished absolute conductivity values exhibited by NbN when compared to gold (with respective conductivity values of approximately 10^6 for NbN and approximately 10^7 S/m for Au). This comparison not only underscores the distinctive electrical properties of NbN but also illuminates the potential avenues for achieving superior metamaterial performance through strategic material selection and design refinement.

Consequently, modifications in the geometric structure of the original ASDR are instigated to amplify the Q-factor to its utmost potential. In this regard, as shown in Table 4-3, ***w*** undergoes an enlargement, extending from 8.3 μm to 12 μm; ***d*** undergoes a substantial modification, increasing from 5 μm to 40 μm, while parameter ***a*** is also augmented from 100

μm to 140 μm. In addition, drawing from the insights acquired through the Au ASDR simulations, it can be theoretically postulated that a monumental enhancement in the Q-factor can be achieved through a reduction in $\boldsymbol{\theta}$. However, this modification carries the repercussion of attenuated resonance visibility, thereby erecting substantial challenges in the experimental evaluations. To circumnavigate this predicament, $\boldsymbol{\theta}$ retains a static value, steadfastly held at 15 ° within this design construct. Hence, simulation instances where varying $\boldsymbol{w}$, $\boldsymbol{d}$ and a are implemented, as shown in Appendix A1, illustrating these modifications' influence on the NbN ADSR structure. Notably absent are simulations involving alterations in $\boldsymbol{\varphi}$, as it is markedly inferior compared to its responsiveness to resonances in the other parameters.

4.3 Simulation of graphene-based active metamaterial modulator

In the preceding section, a comprehensive discussion is undertaken regarding the simulations pertinent to modelling high Q-factor passive components fabricated from Au and NbN. Advancing further, this section intends to delineate a sequence of more intricate simulations, which are quintessential for leveraging the adaptable conductivity properties of graphene in the conceptualization and development of graphene-based active modulators, a critical endeavor aimed at augmenting light-harvesting capabilities.

4.3.1 Physical property and simulation model of graphene

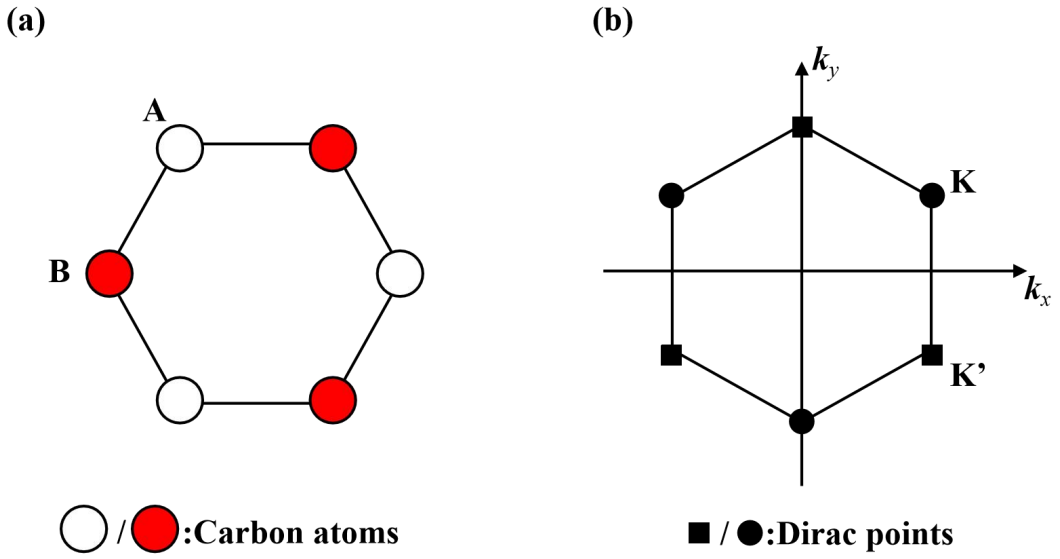

Figure 4.10 (a) Schematic of graphene crystal structure; (b) the corresponding first Brillouin zone in momentum space of the standard cell in (a).

Graphene is sp^2 hybridized 2-dimensional carbon allotrope with a hexagonal lattice. The sp^2 hybridization of carbon atoms in graphene provides interlayer σ bonds and out-of-plane dangling π bonds but without z-axis interaction, resulting in the special linear band structure around the 'Dirac points' in momentum space [167]. This unique property enables modulating the conductive loss of graphene in the THz band by electrical gating [168-170]. The reason is demonstrated below: The crystalline configuration of graphene is characterized by a bifurcated arrangement of non-equivalent atoms, as elucidated in Figure 4.10 (a). Distinctively, the K and K' points delineated in Figure 4.10 (b) represent two Dirac points strategically positioned at the vertices of the primary Brillouin zone within the bidimensional momentum space.

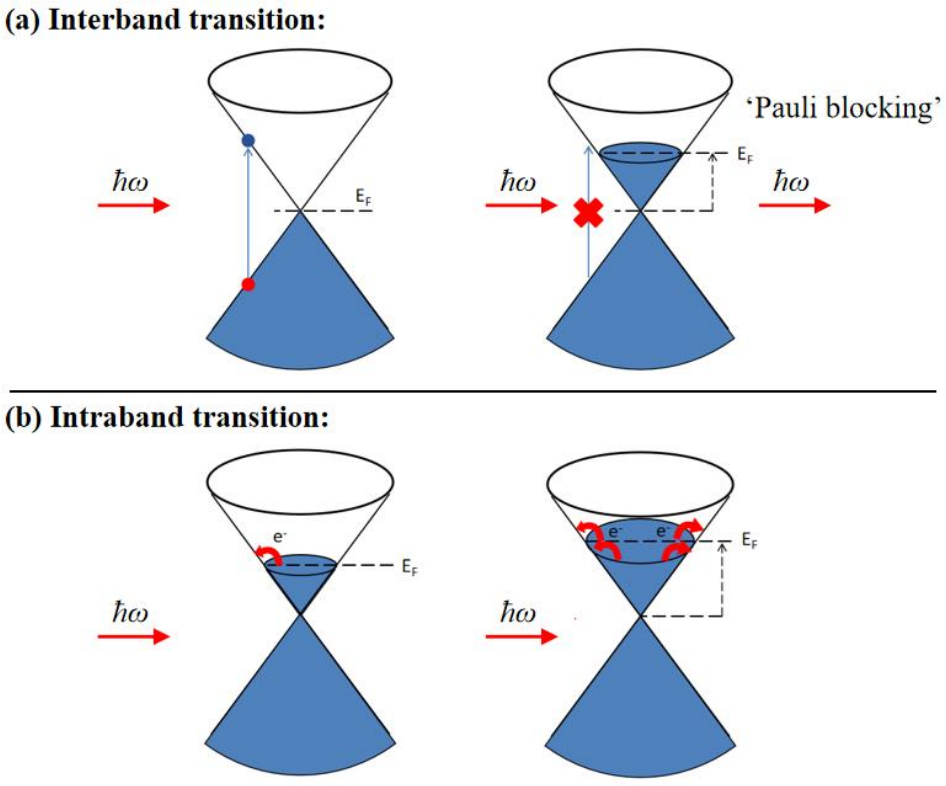

Figure 4.11 Two types of optical interaction within graphene. (a) interband transition. (b) intraband transition.

Within the structural framework of graphene, it is notable that when an electron approximates the vicinity of an atom, it predominantly encounters the influence of the lattice's intrinsic forces, with the atomic field serving as the principal contributor to the electron's

dynamic state. This perspective gives rise to implementing the Tight Binding Approximation (TBA) methodology to describe the derivation of the energy band correlation pertinent to graphene, as expressed in reference [167]:

$$E(k) = \pm \hbar v_F k \tag{4.9}$$

Where $\hbar$ is the normalised Plank constant, v_f is the Fermi velocity of Dirac fermion, $\boldsymbol{k}$ is the relative position in momentum space. The positive sign is used in the upper part beyond the Dirac point while the negative sign is used in the lower part below the Dirac point.

Certainly, the distinct linear band structure of graphene facilitates a remarkable broadband electromagnetic response, spanning from ultraviolet to microwave frequencies. This multifaceted interaction with various frequencies can be fundamentally classified into two mechanisms: the interband and intraband transitions, illustrated vividly in Figures 4.11 (a-b).

To delve into the specifics, Figure 4.11 (a) delineates the interband transition mechanism, which predominantly influences energy conversion across the near infrared to ultraviolet spectrum. This process can be elucidated as the excitation of an exciton pair bridging the conduction and valence bands, a phenomenon that materializes when the energy of incident photons (ω) considerably surpasses twice the Fermi energy ($2\boldsymbol{E_F}$). A noteworthy aspect is that upon saturation of excited energy states, graphene ceases to absorb incident light due to a principle known as Pauli blocking, stabilizing at a consistent absorption rate of approximately 2.3% [167]. Under these conditions, escalating the Fermi energy effectively occupies more vacant states within the conduction band, consequently diminishing the absorption of photons within the lower frequency spectrum.

Contrastingly, when the photon energy satisfies the condition $\omega \leq 2\boldsymbol{E_F}$, generally observed within the microwave to mid-infrared range at ambient temperatures, the absorption of incident light in graphene is mediated through the intraband transition. As depicted in Figure 4.11 (b), this process facilitates the conversion of optical energy to thermal energy, thereby augmenting the momentum of free carriers which subsequently disperse across the lattice until a state of thermal equilibrium is attained. Notably, in scenarios involving the transmission of low-energy photons (typical within the THz domain) into graphene, an

elevation of the Fermi energy (E_F) promotes an increased population of free carriers within the material. This phenomenon substantially heightens the likelihood of scattering incidents with the incoming light, culminating in an enhanced absorption rate. This nuanced understanding of absorption mechanics underpins the potential exploitation of graphene's properties in advanced photonic and optoelectronic applications.

Based on the above discussion, the complex optical conductivity of graphene σ_g can be determined by two parts [167]:

$$\sigma_g = \sigma_{inter} + \sigma_{intra} \tag{4.10}$$

Where σ_{inter} and σ_{intra} are the conductivity contributed by interband and intraband transition, respectively. Assuming the conditions of σ_g is $|\mu_c| >> k_B T$, σ_{inter} can be rewritten from Kubo equation as:

$$\sigma_{inter} = -\frac{ie^2}{4\pi\hbar} \ln\left[\frac{2\mu_c - (\omega + i2\Gamma)}{2\mu_c + (\omega + i2\Gamma)}\right] \tag{4.11}$$

In the case of $\hbar\omega >> 2\mu_c$, $\sigma_{inter} \approx \pi e^2/2\hbar = 2.3\%$ which explains the fixed absorption rate in the high-frequency range. While $\hbar\omega \leq 2\,\mathbf{E_F}$ (for example, incident THz wave at room temperature), $\sigma_g(\text{THz})$ is dominated by σ_{intra} which can be solved by the Drude model equation (4.12):

$$\sigma_{g(THz)} = \sigma_{intra} = \frac{\sigma_{DC-g}}{t_g} \frac{1}{1 + i2\pi f\tau} \tag{4.12}$$

t_g is the thickness of graphene, f is the incident frequency, τ is the Drude scattering time, and σ_{DC-g} is the electrical conductivity of graphene, which is related to $\mathbf{E_F}$ as:

$$\sigma_{DC-g} = e^2|E_F|/\hbar^2 \tag{4.13}$$

To ensure compatibility with the CVD (Chemical Vapor Deposition) synthesized graphene utilized in the fabrication process, a detailed discourse presented in Chapter 5, the

actual parameters in equation 4.12 of the graphene used in COMSOL, sourced from the Cavendish Laboratory at the University of Cambridge, necessitates t_g arbitration at 14 nm within the COMSOL to facilitate optimal simulation convergence, and ascertains τ as 50 fs.

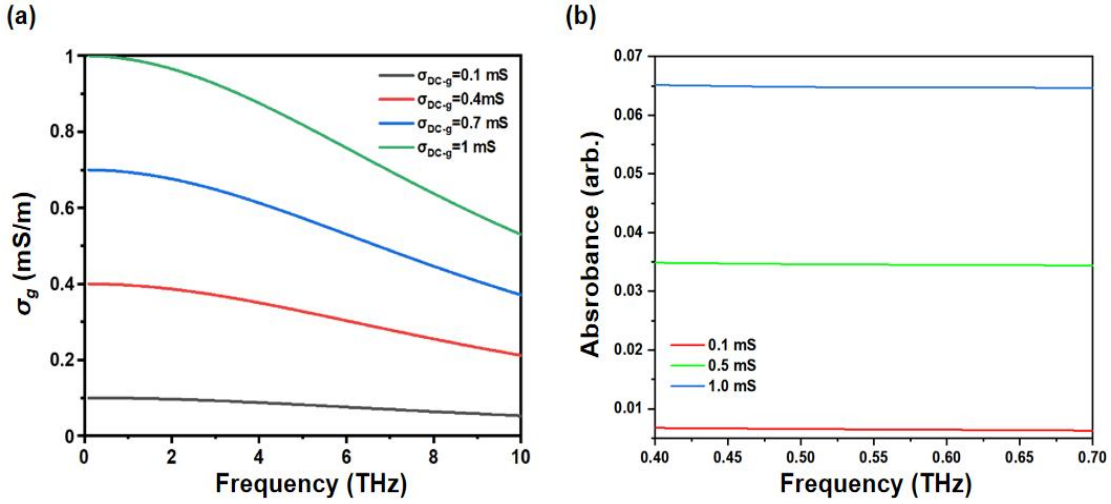

Figure 4.12 (a) Spectral AC conductance σ_g (THz) with different DC sheet conductance σ_{DC-g} of 0.1 mS, 0.4 mS, 0.7 mS and 1 mS; (b)Simulated absorbance of bare graphene with different σ_{DC-g} of 0.1 mS, 0.5 mS and 1 mS.

The values of σ_{DC-g} can be modulated by changing the doping condition of graphene, leading to the variation of σ_g(THz). In this thesis, the doping level of graphene is controlled by the electrical gating from the top-gate or bottom-gate within the sample. Figure 4.12 (a) shows the varied σ_g (THz) with four typical σ_{DC-g} values of 0.1 mS, 0.4 mS, 0.7 mS and 1 mS (determined by the measurement provided by Cavendish Laboratory in the range of 0.1-10 THz). In addition, Figure 4.12 (b) displays the simulated absorbance of bare graphene on the 300 nm SiO_2-doped Si substrate, which is consistent with the actual substrate of the device fabrication shown in Chapter 5, with different σ_{DC-g} of 0.1 mS, 0.5 mS and 1 mS. The conductivity of doped Si is determined by the Drude model form as:

$$\tilde{\sigma}_{AC-Si} = \frac{\sigma_{DC-Si}}{1 + i2\pi f\tau} \tag{4.14}$$

σ_{DC-Si} is the resistivity of p-doped Si, which can be given by its average value of 100Ω/cm, and τ, the Drude scattering time, is 10 ps.

4.3.2 Simulations of single-resonance graphene modulator

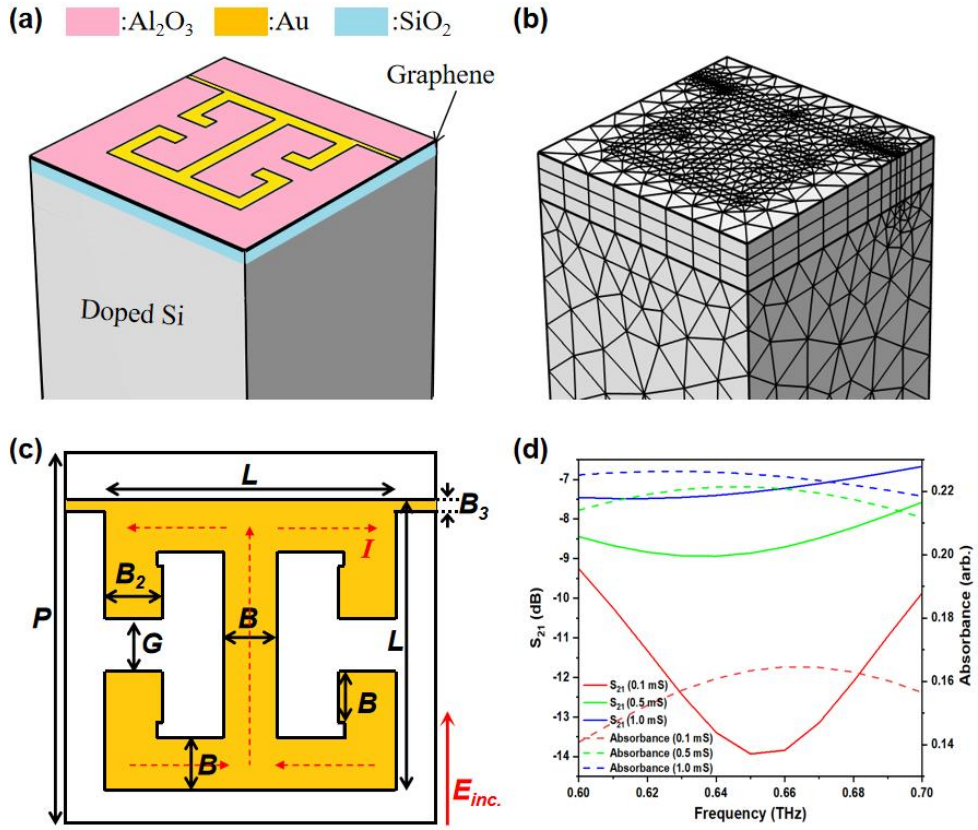

Figure 4.13 (a) The simulated architecture and material models, and (b) the meshing performance of the graphene-based SRR modulator unit cell; (c) the schematic of the single-resonance SRR metamaterials; (d) S_{21} and absorbance simulations of the No.3 graphene-based modulator array with varied $\sigma_{g(THz)}$.

Table 4-4 The modified simulation details of the three single-resonance arrays.

Arrays:	***f*** (THz):	***P***(μm):	***B***(μm):	***B2***(μm):	***L***(μm):	***G***(μm):
No.1	0.4	87.5	11.5	13.5	62.5	9.5
No.2	0.5	70	9	10	50	9
No.3	0.65	56	7.2	9.2	40	7.2

The standard simulated unit cell and its mesh of a typical graphene-based active modulator discussed in this thesis are shown in Figures 4.13 (a-b). Within the modulator, graphene is encapsulated between a 300nm SiO_2 dielectric layer deposited on the doped Si substrate and a 150nm ALD-grown Al_2O_3 layer. The Au film evaporated on the Al_2O_3 layer is

patterned into a particular metamaterial shape to strengthen the interaction and realise the electrical control of graphene by top gating.

Figure 4.13 (c) showcases the metamaterial design integrated on the modulator's surface, which is improved from a Split Ring Resonator (SRR) perfect absorber configuration elucidated in reference [171]. The design embodies a square ring endowed with twin y-axis symmetrical open gaps conjoined to four protruding bars, with a central vertical bar strategically positioned at the x-axis symmetrical nucleus of the square ring. Complementing this structure, an ancillary connection bar affixes itself to the SRR's upper edge, facilitating seamless electrical connection across the entire sample surface. The optical behavior of this structure is governed by five pivotal parameters: the unit cell's periodicity (***P***), the square's side length (***L***), the bar width (***B***), the extended bar's length ($\boldsymbol{B_2}$), and the gap distance (***G***). What's more, a steadfast effort to mitigate parasitic modes, emanating from dipole excitation, dictates the maintenance of the connection bar's width ($\boldsymbol{B_3}$) of 2μm. For fabricating modulators working at separated frequencies, three different modified designs, named as No.1-No.3 with their actual parameters in Table 4-4, are executed in this thesis.

Figure 4.13 (d) performs the typical simulated S_{21} and absorbance spectra of the No.3 array with varied σ_{DC-g} values, showing a S_{21} modulation of 6.5 dB and a absorbance increment of 6.5% by enhancing the graphene's conductance from 0.1 to 1.0 mS at the central resonance frequency. This absorption surge (compared to the pure graphene absorption illustrated in Figure can be attributed to the intensified light-matter interaction facilitated by the metamaterial). At its resonant peak, the metasurface exhibits a pronounced plasmonic response, engendering a coupling with the active electrons present within the graphene, thereby augmenting optical absorption. Nonetheless, this amplification in optical absorption necessitates certain compromises. As evidenced in the absorbance spectra, the ascending trend of absorbance with increasing σ_{DC-g} deviates from the linear progression observed in Figure 4.12 (b) (the increase becomes ineffective in the highly doping condition). This deviation can be attributed to the elevated conductivity of graphene, leading to pronounced Ohmic losses which considerably dampen the resonator's oscillation, diminishing the resonance intensity.

To ascertain the maximum absorbance of each array, a series of simulations adjusting the metamaterial geometry, which are like the procedure performed in the Au/NbN ASDR designs, are undertaken. The clear discussions delineate the standard procedure employed to optimize

the No.2 array centered at 0.5 THz are demonstrated in Appendix A2. Emphasis in these simulations is placed on the modification of parameters ***G***, ***B***, and $\boldsymbol{B_2}$, as outlined in Table S-5.

4.3.3 Simulations of double-resonance graphene modulator

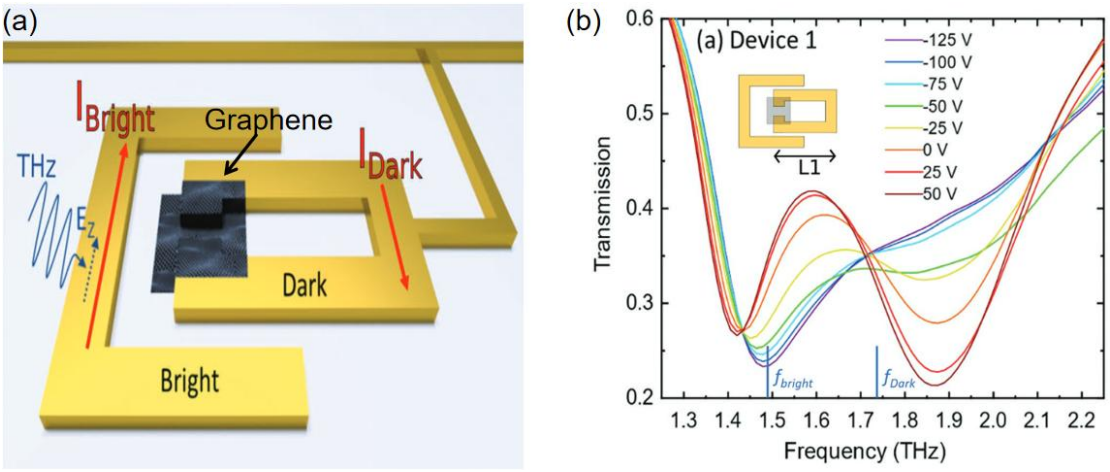

Figure 4.14 (a) Representation of coupled resonator structure. The red arrows indicate the direction of current flow for the bonding mode; (b) transmission data of the device implemented with design shown in (a) using TDS system at different back-gate voltages [172].

As depicted in Figure 4.3 (a), the EIT effect emanates from the interplay between two resonances with proximate yet distinct frequencies. By adjusting the coupling strength between these resonators, one can alter the resonance conditions of the interlinked geometry. To materialize an adaptable design, Figure 4.14 (a) showcases an active metamaterial configuration incorporating CVD-grown graphene, which aims to attenuate the dark resonator within the schema variably, as illustrated in reference [172]. Subsequently, Figure 4.14 (b) elucidates the transmission spectra, revealing alterations in the resonance spectrum corresponding to varying bias voltages applied between the substrate and graphene. This results in a modulation span of approximately 100 GHz, centered at 1.5 THz. Such capabilities hint at its potential deployment as a fast, optoelectronic, tunable band pass/reject filter.

Table 4-5 Simulated details of the two-resonance array.

f (THz):	***P***(μm):	***B***(μm):	***B*$_2$**(μm):	***L***(μm):	***G***(μm):	***D***(μm):
0.35 (No.1)	80	11.5	13.5	62.5	9.5	5
0.45 (No.3)	80	7.2	9.2	40	7.2	

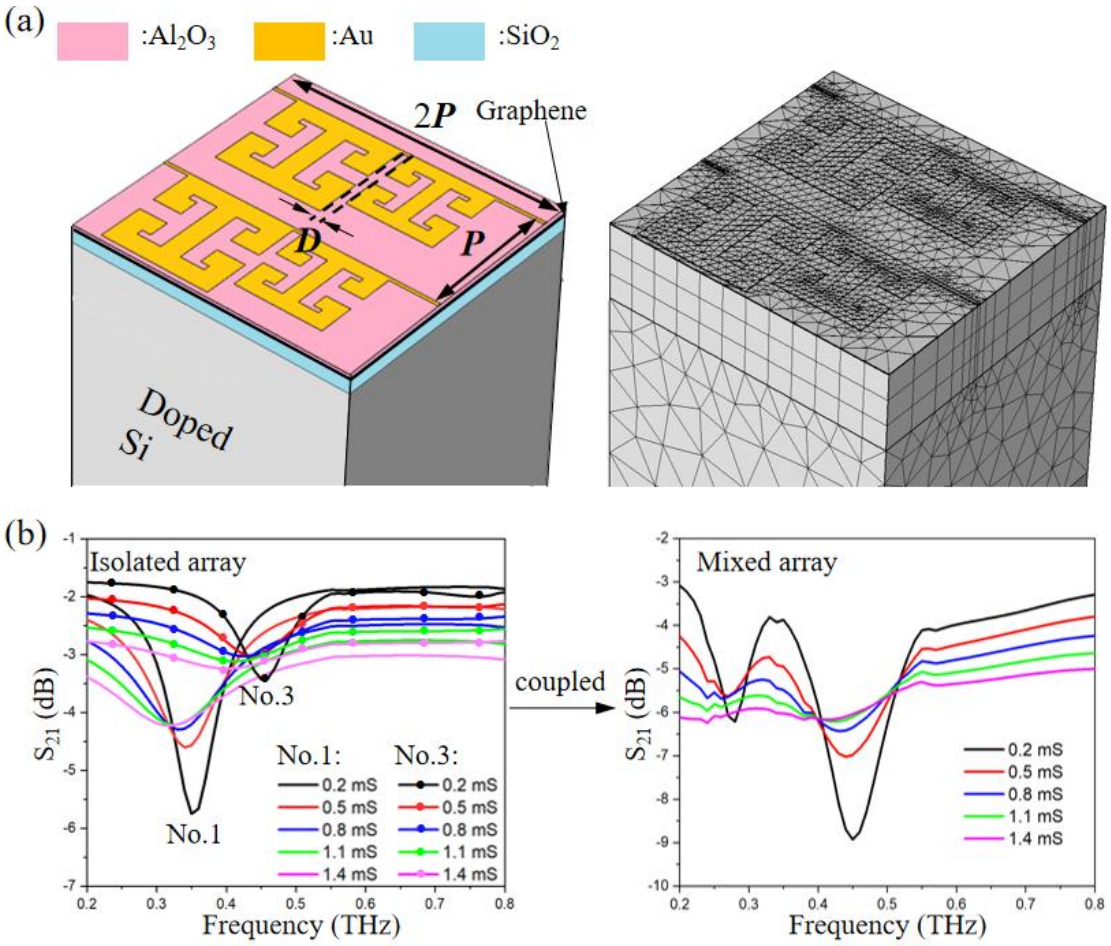

Figure 4.15 (a) The simulated architecture, material allocation and meshes distribution of the two-resonance graphene-based modulator; (b) The S_{21} simulation comparison between the isolated arrays of No.1 and No.3 within the new unit cell and the mixed array involved two types of resonators.

Drawing from the discourse, the single resonance modulator delineated in section 4.3.3 can be repurposed within an EIT configuration to effectuate frequency modulation. Figure 4.15 (a) portrays the specific EIT modulator configuration subjected to simulation in this thesis. This composite structure amalgamates the No.1 and No.3 arrays delineated in the preceding section but with different periodicity. The width of the electrical connection bars

among all resonators remains at 2μm to prevent the parasitic mode. Therefore, the simplest repeated unit cell can be regarded as the rectangle with a length of 2***L*** and a width of ***L*** displayed in Figure 4.13 (a), where it is filled by a pair of different size resonators arbitrarily placed with a certain distance ***D***. Although the incident wave is defined as an uniform planar wave at port 1, the simulated unit cell is constructed in a square shape to keep the uniform spatial field distribution, which is attributed to the paraxial-approximate Gaussian beam based background field in COMSOL. The unequal size of the x- and y-axis boundaries could lead to an unwanted standing wave resonance presented in the result. The detailed parameters for simulating the mixed array are displayed in Table 4-5.

It is worth noting that, diverging from the design in Figure 4.14 (a), graphene extends across the entirety of the substrate and beneath the metamaterial top gate in this configuration. This is not only because the coupling effect manifested by the two SRR designs is not strictly localized at their interstitial gap. This arises because the incident light induces two distinct current flow orientations concurrently, culminating in a 3D interaction that hinges on the electric dipole (directly excited) and toroidal dipole (arising from the two closes but opposite magnetic fluxes induced by the circular currents [173]). In addition, this configuration is beneficial to the multi-wave mixing interaction caused by the graphene nonlinear effect in the THz band, which is further discussed in Chapter 7.

As depicted in Figure 4.15 (b), the simulated S_{21} spectra, when simulating the two differently sized arrays individually within their new periodicity ***P*** (as delineated in Table 4-5), stand juxtaposed against the refreshed S_{21} simulation resulting from the amalgamation of both resonators within a singular unit cell. In the isolated array simulations, there are manifest redshifts in the resonance frequencies compared to their predecessors (shown in Table 4-4) due to the employment of a diminished ***P*** value. Specifically, the No.1 resonator exhibits a frequency descent from 0.4 THz to 0.35 THz upon the augmentation of ***P*** from 87.5 μm to 160 μm, while the No.3 resonator's principal frequency wanes from 0.6 THz to 0.45 THz with an ascension in ***P*** from 56 μm to 160 μm. Moreover, the visibility of the No.1 resonator surpasses that of the No.3 resonator when subjected to an identical ***P***=160 μm.The more pronounced redshift and reduced visibility of No.3 array can be attributed to the positioning of the individual resonator in a relatively larger spatial domain compared to previous simulated dimension.

However, the S_{21} spectra for the coupled array indicate that planar coupling between the No.1 and No.3 resonators can induce a redistribution of energy, chiefly enhancing the resonance strength of the No.3 array under conditions of low graphene conductance. Remarkably, this coupling effect does not alter the resonant frequency of the No.3 array but elevates its visibility from 1.8 dB to 6 dB. In contrast, the No.1 resonators experience a redshift of 0.08 THz and a reduction in visibility by 0.8 dB after the coupling. When heavily doped graphene, the coupling effects between the two sets of resonators are effectively decoupled, thereby reverting the spectral features to broad, dipole-like resonances.

Chapter 5 Fabrication

The execution of micro-fabrication techniques epitomizes the actualization of the metamaterial designs elaborated in Chapter 5. These technologies, pivotal in modern integrated circuitry, embody a spectrum of material processing strategies meticulously devised to craft complex structures at both nano and micro scales. These strategies incorporate established techniques such as lithography, thin film deposition, and materials etching.

This chapter briefly explores the fundamental principles and procedural protocols, outlining the various micro-fabrication approaches utilized in developing passive and active metamaterials, as detailed in Chapters 6 and 7. This section aims to give readers a robust understanding of the intricate processes underpinning the fabrication of state-of-the-art metamaterials, thereby laying a solid foundation for subsequent explorations in this evolving field.

5.1. Mask aligner, thermal evaporation, and lift-off

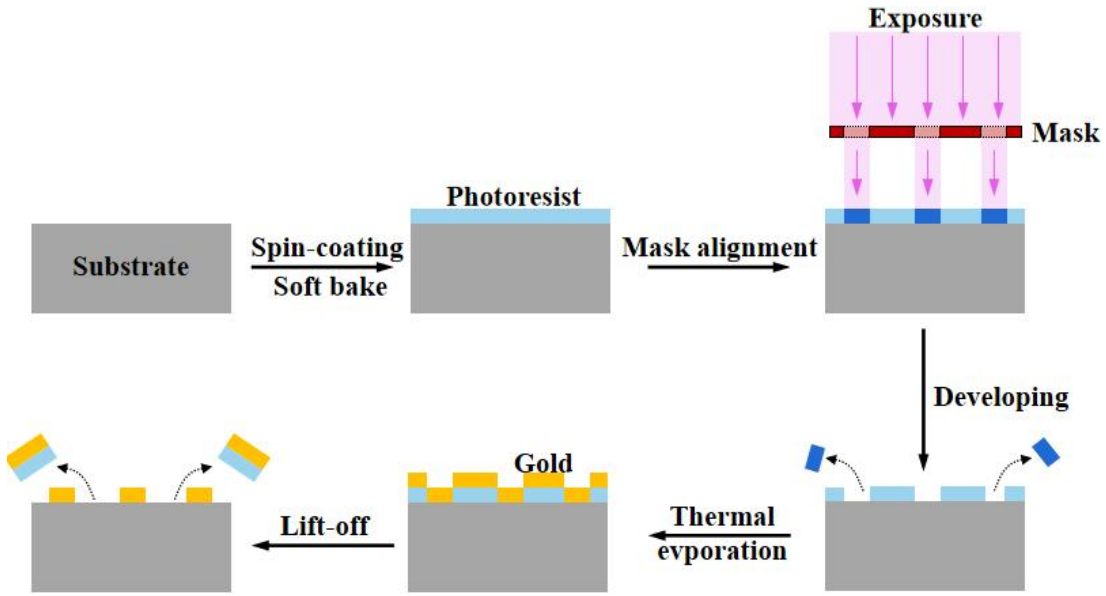

Figure 5.1 The standard procedure of fabricating a metamaterial on a substrate using positive-type photoresist.

Photolithography, a well-established integrated circuit fabrication method, is a conventional means for replicating intricate patterns. This technique entails the utilization of a

mask that is structured with specific configurations of apertures corresponding to the intended patterns. The actual patterning of the substrate occurs through the exposure of optical beams, which pass through the preconfigured mask and onto a specialized polymer layer overlaying the substrate. The specialized polymers employed are called "photoresists (PR)". These photo-sensitive chemicals can alter their solubility in specific solvents, typically known as "developers" when subjected to incident light within a restricted spectrum of wavelengths. Typically, this illumination occurs within the blue to the ultraviolet (UV) band. Classified according to their distinct crosslinking performance, photoresists can be categorized into positive and negative photoresists. Positive photoresists enable dissolution in the developer after activation, while negative photoresists exhibit the opposite behavior, with the activated film persisting on the substrate even in the developer's presence [174].

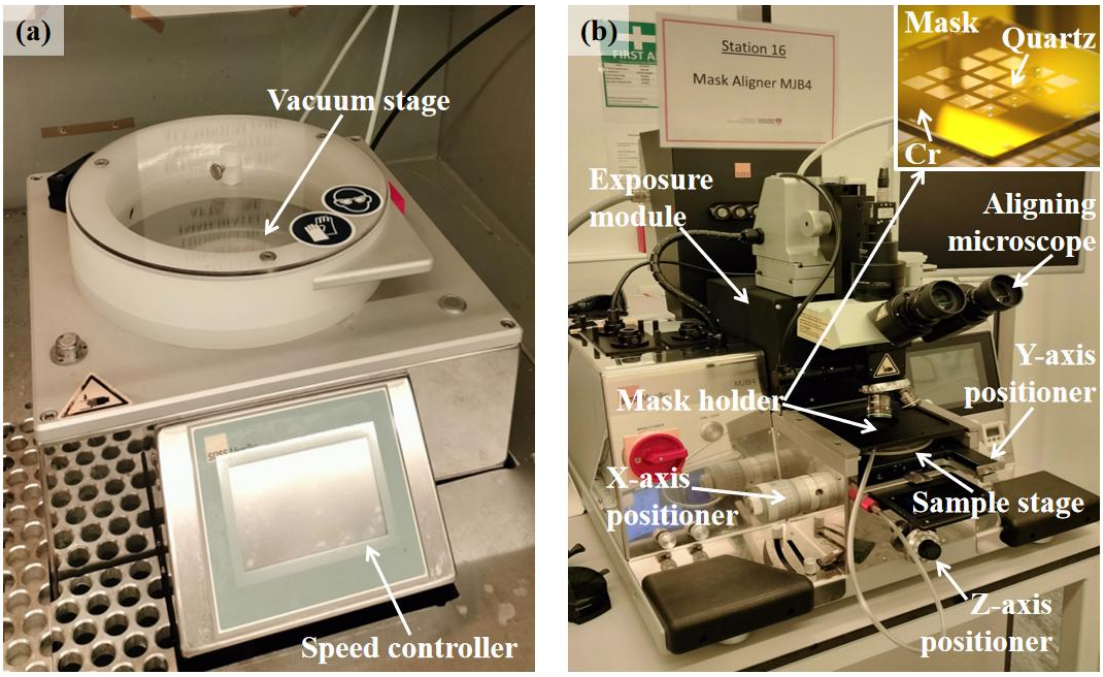

Figure 5.2 Optical pictures of (a) “Suss Labspin” spin-coater and (b) mask aligner “MJB5”. The inset in (b) is the demonstration of a metallic mask used in mask aligner.

Figure 5.1 presents a representative process for producing metamaterials employing a positive-type photoresist through standard lithography. The procedure begins with applying a thin layer of spin-coated PR onto a substrate that has undergone prior cleaning using acetone and isopropyl alcohol. Figure 5.2 (a) depicts an image of the utilized spin-coater, denoted as

"Suss Labspin," as employed within this thesis. The sample is securely positioned on the vacuum stage and rotates at a precise speed established by the controller. The thickness of PR is controlled by adjusting the spin speed, measured in rounds per minute (rpm). Commonly falling within the range of 3000-7000 rpm, this adjustment facilitates the attainment of either thicker or thinner substrate layers. The specific thickness achieved is contingent upon the viscosity inherent to each type of PR, resulting in PR thickness spanning from hundreds of nanometers to several tens of micrometers [175]. Subsequently, the spin-coated substrate undergoes baking before exposure, a stage called the "pre-bake" or "soft bake" step. This pre-exposure baking facilitates the preparation of cross-linked molecules, priming them for subsequent optical reactions.

Following the "pre-bake" stage, the sample is placed into a mask aligner to initiate the subsequent lithographic procedures. The photograph of the employed "MJB5" mask aligner utilized in this thesis is exhibited in Figure 5.2 (b). The mask aligner encompasses a comprehensive assembly that includes an X-Y-Z motion stage, a mask holder, a sample stage, a 505nm light exposure module, and an alignment microscope. At the beginning of lithography, the sample and mask need to be placed at the sample stage and mask holder to finish the masking aligning. As previously mentioned, the requisite mask is fashioned through processes involving laser writing and metallic evaporation (the principles of which will be detailed later) onto a quartz substrate with precision of 0.5μm, as illustrated in the inset of Figure 5.2 (b). The designated area of evaporated chromium effectively obstructs light exposure, thus facilitating the precise transfer of patterns onto the sample. Achieving alignment between the sample and the mask is executed by manipulating the X-Y-Z stage while monitored through a microscope. Ensuring accurate alignment necessitates bringing the appropriately positioned mask into proximity to the sample surface. This proximity aids in meticulously shaping the exposed area for subsequent stages. Once alignment has been established, the exposure module generates and delivers light radiation onto the mask through an optical fiber with determined power and exposed time.

As depicted in Figure 5.1, the filtered light radiation activates the PR on the sample's surface. Subsequently, the sample is immersed in a developer solution, facilitating the removal of the areas exposed to light. Once the developer has effectively established the pattern gap, the sample becomes prepared for the ensuing thermal evaporation process, which

entails transferring metal patterns onto the sample. Thermal evaporation, classified as a prevalent technique in physical vapour deposition (PVD), involves evaporating metal sources within a vacuum to deposit a continuous thin film onto the substrate. Notably, the residual layer of unexposed photoresist on the designated areas prevents the growth of metallic film on the substrate's surface (schematic can be found in Figure 5.1). This vital distinction underscores the necessity for a final step, wherein the metalized sample undergoes immersion in a specialized liquid solution called "remover." This solution effectively eliminates the lingering polymer layer, leaving behind the metallic architecture on the surface, thus culminating in the completion of the metamaterial fabrication process.

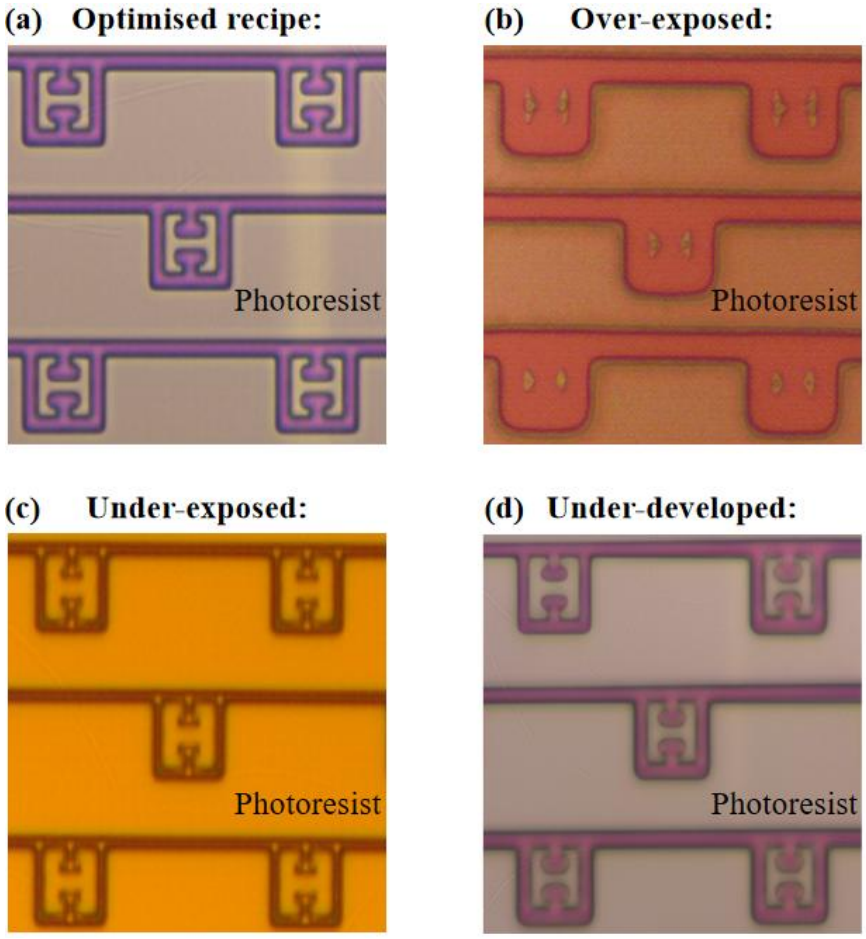

Figure 5.3 Optical images of transferred patterns within S1813 with different conditions of (a) perfect status; (b) over-exposed; (c) under-exposed; (d) under-developed.

The successful fabrication of a high-quality metamaterial is chiefly contingent upon several key factors, including exposure energy, developing time, and lift-off conditions.

Exposure energy is the foundational parameter that dictates both the transferred pattern's size and integrity. A meticulously calibrated light dosage is required to imprint the photoresist according to the intended design dimensions accurately. Moreover, following a comprehensive developing procedure, this process should ensure the absence of any residual polymer within the pattern gaps.

Figures 5.3 (a-d) depict optical images illustrating diverse shaping outcomes obtained through distinct process conditions applied to positive-type single-layer photoresist S1813 (Shipley 1800 series PR, thickness of 1.3 μm achieved at 5000 rpm for 1 minute) in alignment. Figure 5.3 (a) elegantly showcases the successful realization of efficient metamaterial design on the substrate, characterized by well-defined geometry and impeccably cleared pathways (for comprehensive parameters, refer to Tables 5-1~5-3). In contrast, Figure 5.3 (b) exemplifies an erroneous lithography attempt under an over-exposed condition (exposure time: 3 seconds). This outcome exhibits a more extensive and less distinct shape stemming from extended exposure. Conversely, Figure 5.3 (c) captures the optical image of the under-exposed sample (exposure time: 1.5 seconds), with dimensions falling short due to insufficient incident radiation, leading to polymer inactivity on its surface.

Furthermore, the duration of the developing process plays a pivotal role in lithographic precision. An over-developed sample, subjected to extended immersion in the developer, presents a coarse edge profile attributed to prolonged chemical erosion from the solution. Conversely, an under-developed sample (developing time: 50 seconds) showcases incomplete removal of the photoresist in the exposed region, as depicted in Figure 5.3 (d).

Several iterations have established an optimised procedure for single-layer photoresist lithography pertinent to this thesis:

Table 5-1 Single-layer photoresist preparation.

Photoresist:	S1813 (positive type)
Spin-coating:	6000rpm/min for 60s
Soft baking:	115°C for 60s
Acquired thickness：	1.1-1.2μm

Table 5-2 Lithography operation of single-layer photoresist.

Radiation source:	Mercury lamp

Radiated wavelength:	405nm
Power:	22W
Exposed time:	2.2s
Developer:	MF-319
Developing time:	60s

Table 5-3 Thermal evaporation and lift-off setting of single-layer photoresist.

Evaporation environment:	Pressure ≤ 5×10^{-7} Pa
Evaporated metal 1:	10nm Ti
Evaporated metal 2:	150nm Au
Remover:	Acetone
Lift-off time:	>10mins

Of notable standard is the choice of a Ti-Au bi-layer metal film for constructing the metamaterials via thermal evaporation. In this bi-layer configuration, the Ti layer serves as an adhesive intermediary between the substrate surface and the Au layer, forming a robust and enduring architectural structure. It is pertinent to mention that, while Ti is characterized by higher loss characteristics in the THz band compared to Au, a thickness of 10nm has been judiciously selected to achieve a balance between ensuring uniform layer deposition and not introducing excessive optical losses within the optical resonance.

In this design, Au is the preferred material for supporting plasmonic s to the metamaterial, in contrast to alternative metals such as Al or Cu. This selection is based on Au's ease of evaporation and relatively moderate loss characteristics. To strike an optimal equilibrium between supporting plasmonic and minimizing losses within the air (requires thickness ≧ 100nm), as well as providing a robust platform for wire bonding (requires thickness ≧ 100nm) and facilitating successful lift-off (requires thickness < 100nm after multiple attempts), a Au layer thickness of 150 nm has been determined. This meticulous selection process ensures the metamaterial's performance is aligned with its intended functionalities while mitigating potential drawbacks from material properties and deposition processes.

Though the concluding step in manufacturing, the lift-off process is paramount in executing the metamaterial design as shown in the following Figures 5.4 (a-b).

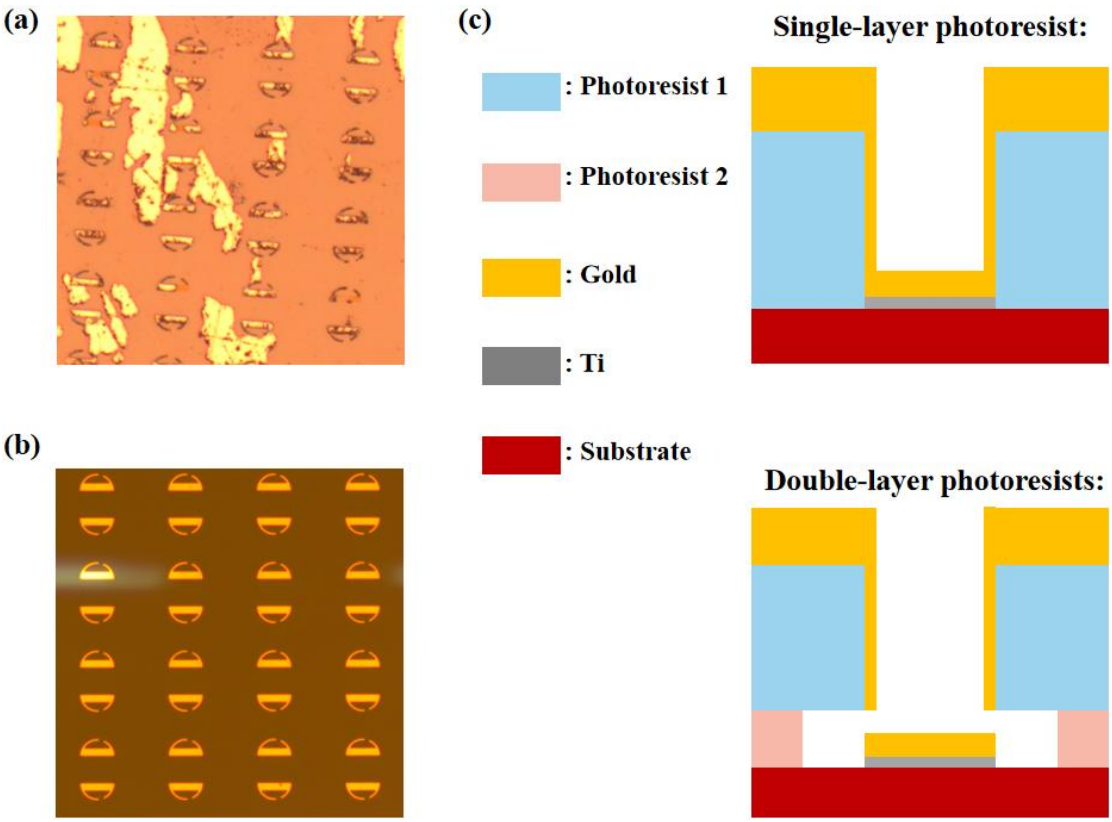

Figure 5.4 (a-b) Optical pictures of the samples with the same design under the unsuccessful and decent lift-offs, respectively; (c) The schematics of different side-wall profiles of the single-layer and double-layer photoresist configuration, explaining the benefit of using an additional photoresist layer.

Figure 5.4 (a) showcases an optical depiction of a sample post a faulty lift-off by using an unoptimized recipe with the implementation of single-layer photoresist and excessive soft baking time, substantially damaging the resonators. Conversely, meticulous execution of the lift-off process following the precise design yields a metamaterial array with exact geometry according to the preconfigured pattern, exemplified in Figure 5.4 (b).

The attainment of a successful lift-off hinges on several considerations, including the photoresist's solubility, the soft-baking stage's duration and temperature, and the metal transfer quality during evaporation. Resolving these issues typically involves pragmatic adjustments tailored to the specific equipment and facilities employed. However, a more systematic enhancement in lift-off performance can be realized by adopting a double-layer photoresist architecture instead of a single-layer configuration. This approach represents a feasible pathway to consistently improve the lift-off procedure's efficacy.

Figure 5.4 (c) elucidates the operational mechanism of this approach. Throughout the process of thermal evaporation, the developed photoresist functions as a soft mask, safeguarding the metal particles from coalescing onto the substrate. This action exclusively permits the deposition of the metal film in the exposed regions. In a single-layer configuration, an excess of metal clusters can adhere to the metal-coated photoresist and the substrate, enveloping the photoresist and impeding its dissolution in the remover solution. Conversely, the double-layer architecture introduces an additional thin layer of photoresist, labelled "photoresist 2," positioned between "photoresist 1" and the substrate. This supplemental photoresist layer exhibits a swifter developing rate than "photoresist 1," thereby engendering an over-developed side-wall profile about other "photoresist 1" regions upon immersion in the developer solution. This strategic integration of a double-layer photoresist architecture optimizes the lift-off process, preventing undesired metal accumulation and ensuring more efficient removal of the photoresist, thereby enhancing the precision of the fabricated metamaterial structure. The updated recipes for completing the metamaterial fabrication are shown in the following tables:

Table 5-4 Double-layer photoresist preparation.

Photoresist 1:	S1813 (positive type)
Spin-coating:	6000 rpm/min for 60s
Soft baking:	115°C for 60s
Thickness:	1.1-1.2μm
Photoresist 2:	LOR 3A (positive type)
Spin-coating:	3000 rpm/min for 30 s
Soft baking:	180°C for 3 mins
Thickness:	350-450 nm (depending on the size of wafer)

Table 5-5 Lithography operation of double-layer photoresist.

Radiation source:	Mercury lamp
Radiated wavelength:	405nm
Power:	22W
Exposed time:	2.5s
Developer:	MF-319
Developing time:	Two-step developing of 50s and 30s

Table 5-6 Thermal evaporation and lift-off setting of double-layer photoresist.

Evaporation environment:	Pressure ≤ 5×10^{-7} Pa
Evaporated metal 1:	10nm Ti
Evaporated metal 2:	150nm Au
Remover:	Remover-1165
Lift-off time:	25mins at 60°C

5.2 Laser writing

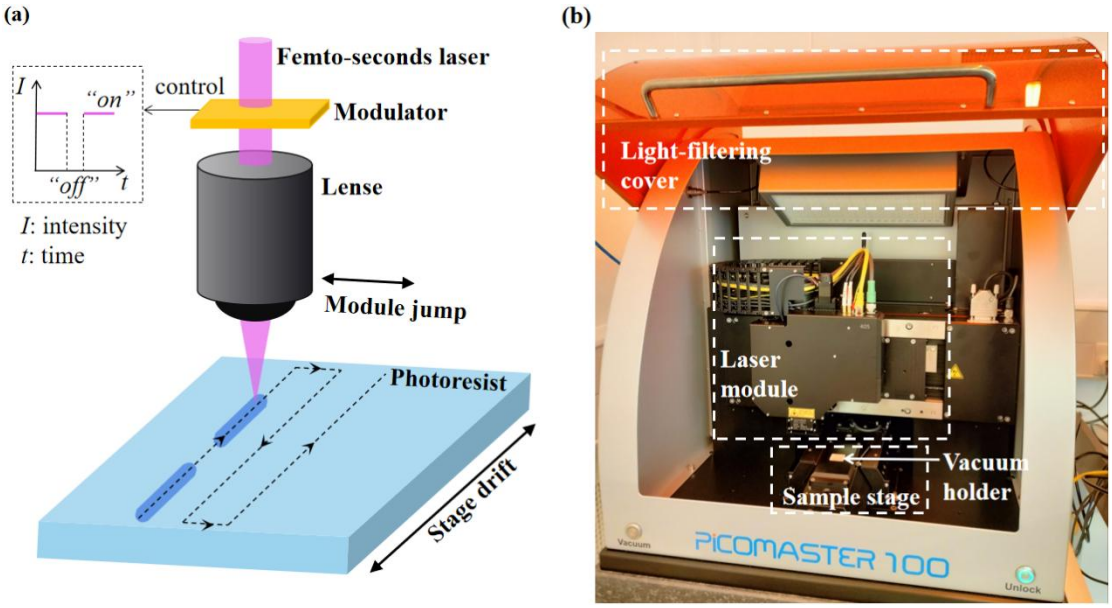

Figure 5.5 (a) The schematic of using a laser writer to implement pattern transfer on the sample; (b) optical image of the laser writer "PICOMASTER 100" used for fabricating samples shown in this thesis.

Laser writing, also called "multiphoton lithography" or "direct laser lithography", is an alternative photolithography method that can transfer the preconfigured pattern onto the sample without using a mask. Figure 5.5 (a) shows the schematic of using a laser writer to activate by moving the relative position of the substrate and laser source [175]. The clear procedure of applying a laser writing is illustrated as below:

Figure 5.5 (b) presents the schematic representation of the "PICOMASTER 100" laser writer employed in producing the samples showcased within this thesis. The laser writer comprises three primary components: the laser exposure module, the sample stage, and a

vacuum system. The laser exposure module is designed to emit two distinct types of lasers. Firstly, the "blue laser" (405 nm) serves to activate the photoresist (PR), featuring an adjustable power of up to 3mW within the spot region, as illustrated by the laser beam depicted in Figure 5.5(a). Secondly, the "red laser" (680 nm) is employed to measure the surface profile of the sample, devoid of triggering PR activation. This dual-laser functionality equips the laser writer with versatility for PR activation and non-destructive sample surface profiling.

At the initiation of the writing process, the sample coated with PR is affixed to the sample stage by vacuum. Subsequently, lens-focused laser beams are directed to carry out a two-step laser exposure onto the sample's surface. In the initial exposure step, the laser module generates the red laser at a predetermined height, pinpointing the optimal focus distance for the subsequent scanning phase. Given the stationary nature of the laser module, the laser writer orchestrates the motion of the sample stage to achieve the raster scanning.

Within the system, two distinct modes of valid motion come into play. During vertical scanning, the stage undergoes rapid movement along a track propelled by a compressed air motor. Conversely, horizontal stepping involves a slower and step-by-step shift of the laser module on an electrically controlled holder. Combining these two motion operations facilitates the achievement of a planar radiation exposure onto the sample. Following the preparation of the scanned surface profile, the laser module commences the generation of the blue laser with the desired power, modulating its height following the scanned surface profile. This meticulous adjustment results in a minimum resolution less than 0.3 μm. Ultimately, the pattern transfer is executed through a bi-dimensional movement mechanism, with the assistance of a light modulator that regulates blue laser exposure duration (as illustrated in Figure 5.5 (a)). This comprehensive orchestration of actions culminates in completing the pattern transfer process.

The post-lithography procedures outlined in tables 5-1~5-6, as introduced in section 5.1, remain applicable to the laser writing process. In contrast, the performance optimization of the Picomaster primarily hinges on the manipulation of exposure dosage, movement compensation, and threshold voltage settings. Notably, exposure dosage operates analogously to the exposure time utilized in conventional lithography, serving as the parameter that influences alterations in pattern shapes, as illustrated in Figure 5.2. Movement compensation

entails the incorporation of a length reduction in the motion operation. This adjustment is introduced to counterbalance the enlarged spot size illuminated on the sample due to imperfect focusing. Concurrently, the threshold voltage setting assumes the role of fine-tuning. It calibrates the recorded background voltage of the detector, a pivotal metric employed for pinpointing the focus point on the sample's surface. The intricate details of the configuration settings for running standard laser lithography can be found in the table 5-7 provided below:

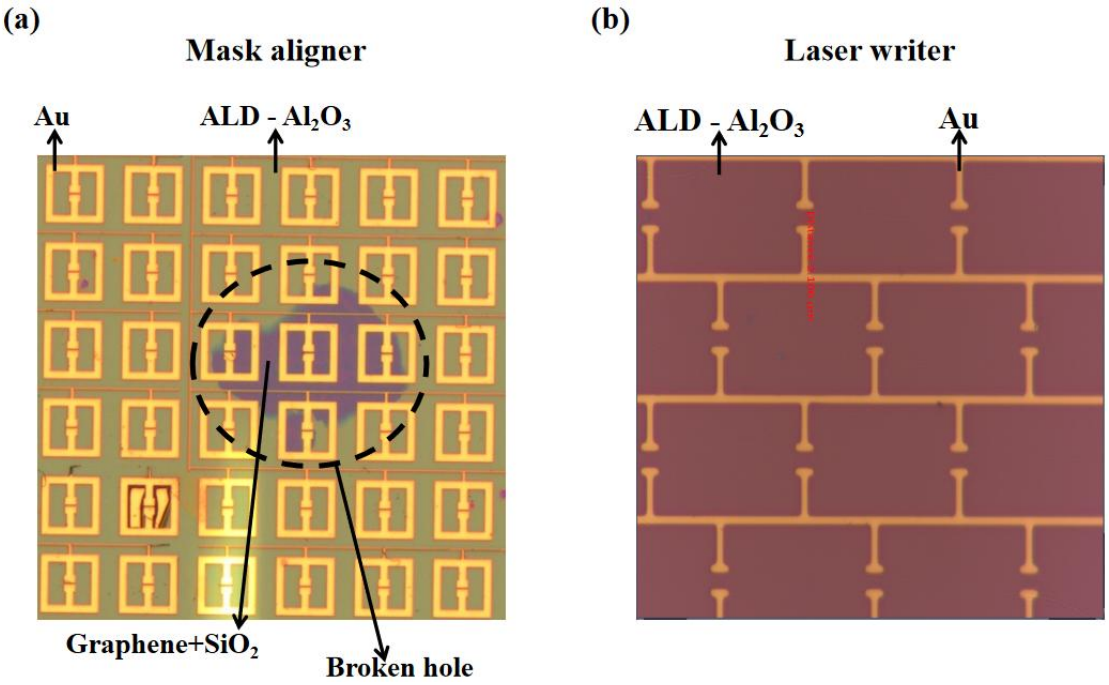

Figure 5.6 Optical images of (a) a broken active metamaterial array affected by the mask contact during the standard lithography; (b) an unharmed active metamaterial array acquired by laser writing.

Table 5-7 Parameters setting in standard writing process on "PICOMASTER 100".

Spot size:	550nm	Dosage:	160mJ/cm^2
Step resolution:	100nm	Scan speed:	200mm/s
Movement compensation:	400nm for standard substrate (such as Si and SiO_2), and 200nm for highly reflective substrate (such as gold and NbN)	Threshold voltage:	1 V

As introduced in section 5.1, the mask must approach the sample's surface during

exposure to reduce over exposure. In this approach, the mask keeps stressing the materials beneath it and can break them within a certain period. Figure 5.6 (a) visually presents an optical depiction of an active metamaterial array that suffered damage from this pressure. The image shows a conspicuous aperture on the continuous ALD-Al_2O_3 film that overlays the graphene-SiO_2 substrate. This aperture exposes the underlying sample surface beneath the gold-constructed metamaterial. The resultant configuration directly connects the graphene to the array, creating an electrical short circuit and thus negating the top-gating effect on graphene.

Conversely, Figure 5.6 (b) presents an optical representation of another active modulator, similarly realized via laser writing and encompassing the same configuration but with a different preconfigured design. This image showcases an intact appearance of the Al_2O_3 film, indicating the absence of material rupture or damage. The variations in colors observed in the ALD-Al_2O_3 films depicted in the images are attributed to alterations in the microscope's illumination conditions.

Nevertheless, due to limitations in moving speed, the laser writer requires significantly more time (typically around an hour) to complete the process of shape profiling for a 2×2 mm^2 metamaterial, in stark contrast to the mask aligner's rapid execution (mere seconds). The minimal spatial resolution achievable with the laser writer mirrors that of standard lithography, contingent upon the incident wavelength. However, the likelihood of overexposure arising from insufficient mask contact can be substantially mitigated.

5.3 Reactive ion etching, atomic layer deposition and graphene fabrication.

5.3.1 Reactive ion etching

Plasma etching (PE) is a critical process of microfabrication and nanotechnology, serving as a fundamental technique for precision material removal and surface modification at the micro- and nanoscale. PE harnesses the controlled interaction between a reactive plasma and a substrate to selectively remove or alter specific layers of materials. Reactive plasma is an ionised gas containing ions, electrons, and neutral particles, which can physically or chemically interact with the substrate, enabling PE as a versatile method of achieving high-resolution patterning and intricate feature definition in various materials, ranging from

metals to organic and inorganic dielectrics. For instance, O_2 plasma is a convenient chemical etcher capable of removing most organic compounds from a substrate. This process involves converting chain molecules into gaseous oxides, facilitating their removal. However, materials with robust chemical resistance, such as gold or aluminum, pose a challenge for O_2 plasma etching [176]. In such cases, a more aggressive approach involves using an Ar plasma to remove metal molecules through collisions with accelerated ions physically.

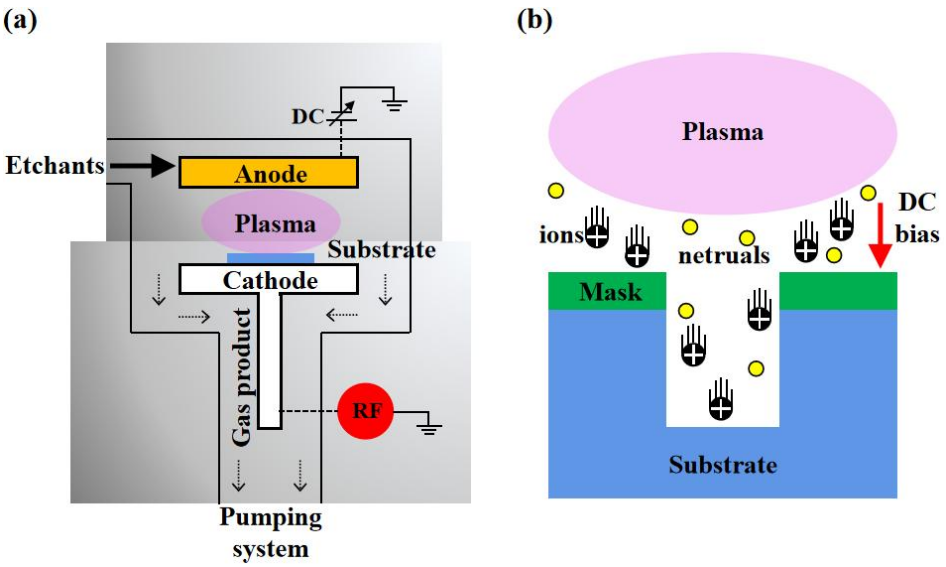

Figure 5.7 (a) The schematic of an RIE machine in operation; (b) the mechanism for patterning substrate surface.

Nevertheless, while effective, pure Argon plasma etching tends to be slow and isotropic. An advanced ion-assisted PE technique known as reactive ion etching (RIE) has been developed to address these limitations. RIE aims to synergize both physical and chemical interactions, thereby accelerating the etching process and enhancing the selectivity of directional etching. The inception of RIE can be attributed to the pioneering work of Hosokawa et al., who introduced the concept of using fluorine and chlorine-based carbon molecules to dramatically enhance etching rates for a wide spectrum of materials [177]. These materials span the gamut from "soft" substances like photoresist, silicon, and quartz to "hard" materials such as aluminum, cobalt, and stainless steel.

Figure 5.7 (a) illustrates the schematic of etching material within a typical RIE machine. During the process, the substrate is placed on the cathode carrier inside the reaction chamber

and kept in a low-pressure environment to provide an ideal atmosphere for forming plasma. The etchants are later precisely controlled with a specific ratio to fill the chamber. Once the target gas pressure of the chamber is reached, the RF module connected to the cathode generates an electromagnetic field (usually in a frequency of 13.56 MHz) with a particular power ranging from tens to hundreds of watts. The powerful oscillated fields split electrons from the corrosive gases, generating plasma between the electrodes. As a result, the uncovered substrate spontaneously reacts with activated radicals by advancing the etchants species (such as F and Cl-based gases). Simultaneously, the DC power attached to the anode forwards the positive charges flow into the etched gap, bombarding the surface to create a deep and anisotropic etching path, as shown in Figure 5.7 (b).

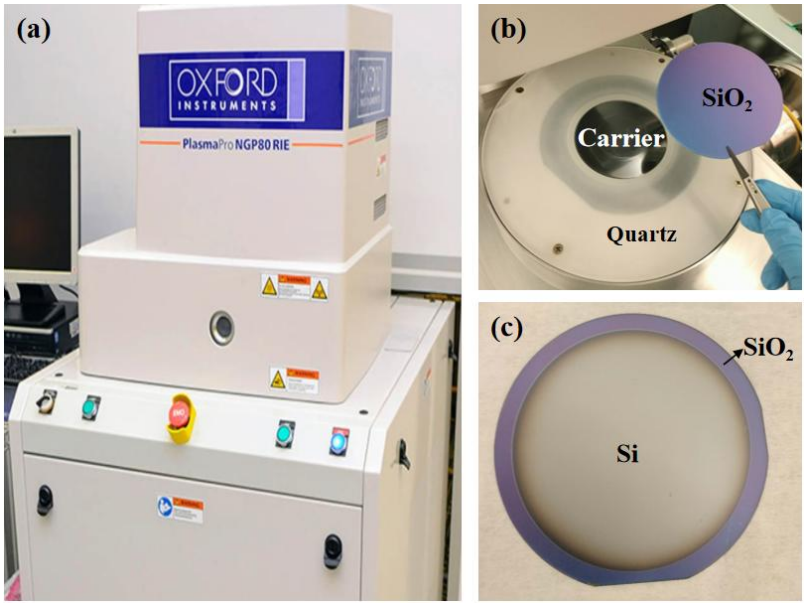

Figure 5.8 Optical pictures of (a) Oxford PlasmaPro NGP80 RIE; (b) RIE reaction chamber and a Si wafer coated by SiO_2; (c) the Si wafer shown in (b) after etching by the RIE.

Figure 5.8 (a) shows a photo of the RIE machine "Oxford PlasmaPro NGP80 RIE" (hereafter called "NGP80") used to pattern all film materials mentioned in this thesis. A representative recipe example for etching 300 nm SiO_2 film on a 500 μm Si substrate can be described as follows: the wafer was initially placed on the carrier inside the reaction chamber where a 5 mm-thick quartz ring was used not only as the holding lid to fix the wafer's position but also as the hard mask during the etching, as shown in Figure 5.8 (b). In a

particular etching procedure, four parameters could modify the etching effects: chamber pressure, etchants flow ratio, etchants flow rate and RF power [178]. Furthermore, NGP80 would automatically adjust the DC bias voltages according to the plasma status to eliminate the reflected RF power. In this experiment, the etching was completed by the mixed gaseous chemicals of CHF_3, O_2 and Ar, which were excited by a 150 W RF power, in a constant flow of 100 sccm, 5 sccm and 5 sccm, respectively, within the chamber pressure of 55 mT. Then, the stimulated plasma etched down SiO_2 at a rate around 45~50 nms/min calibrated by a surface profiler, following the chemical reaction:

$$5CHF_3(g) + 3SiO_2 + 2O_2(g) \rightarrow 3SiF_5(g) + 5CO_2(g) + 2H_2O(g)$$

The additive Ar in the recipe aims to accelerate the procedure via physical etching. The stimulated customized plasma removed all SiO_2 film after a 7 mins reaction, exposing the Si used to be beneath the top layer, as shown in Figure 5.8 (c).

Further, recipes for etching graphene and NbN discussed in this thesis are shown in tables 5-8~5-9:

Table 5-8 Graphene RIE etching recipe.

O_2 flow rate	50sccm
RF power	50W
Pressure	200mT
Etching rate	Remove monolayer CVD-grown graphene with 2 mins etching

Table 5-9 NbN RIE etching recipe:

CHF_3 flow rate	50sccm
O_2 flow rate	1sccm
Ar flow rate	5sccm
RF power	150W
Pressure	50mT
Etching rate	65-70nm/min

5.3.2 Atomic layer deposition

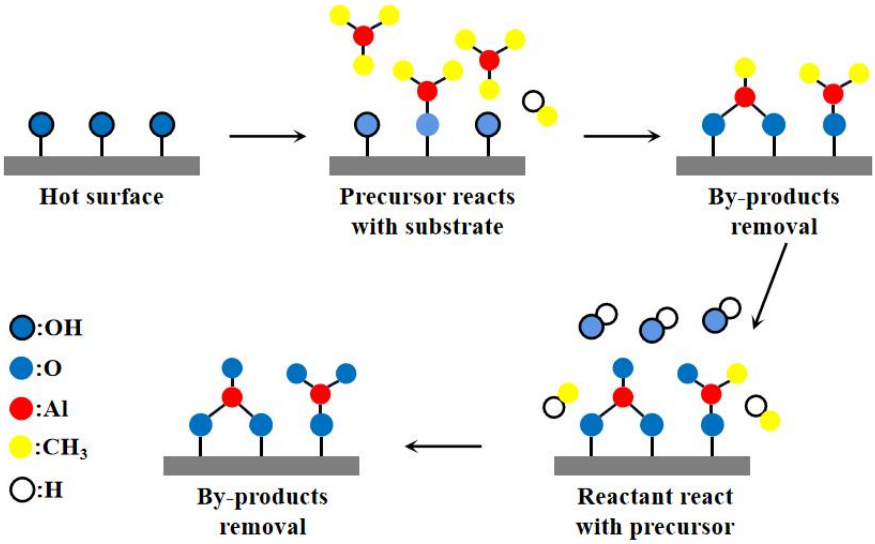

Figure 5.9 Schematic diagram of the formation mechanism of ALD grown Al_2O_3.

The concept of Atomic Layer Deposition (ALD), also recognized as "atomic layer epitaxy," emerged as an evolution of the conventional chemical vapor deposition (CVD) technique and was pioneered by Tuomo Suntola in the 1970s [179]. ALD represents a chemical interfacial reaction that distinguishes itself from CVD by introducing precursor and reactant separately into the reaction chamber within a single reaction cycle. This separation facilitates meticulous control over film thickness, achievable through the precise enumeration of cycles employed.

In the customary cycle, the activated precursor engages with the substrate via surface absorption, which eliminates surplus by-products through either pumping or purging with an inert gas. Subsequently, the adsorbed precursor undertakes chemical reactions with incoming reactants, culminating in a final surface cleaning step to eliminate excess co-reactants. ALD's reliance on self-limiting saturated adsorption reactions makes it well-suited for generating thin film materials characterized by a compact structure, minimal defect ratio, and consistent thickness distribution [180]. Nonetheless, it should be noted that ALD is incompatible for depositing materials exceeding several hundred nanometers in thickness due to its prolonged time requirement. For instance, the 150nm Al_2O_3 film deposition demonstrated in this thesis requires up to 7 hours to complete the procedure.

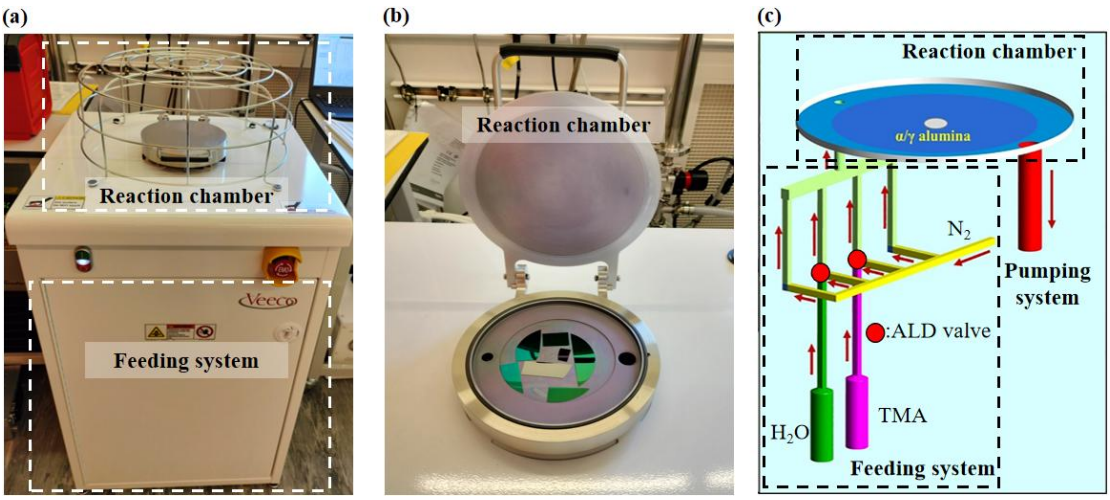

Figure 5.10 (a-b) Optical pictures of Veeco Nanotech Atomic Layer Deposition System and its reaction chamber, respectively; (C) detailed configuration of the ALD reactor showing the feeding system with ALD valves, reaction chamber and the pumping system.

ALD-grown aluminum oxide (Al_2O_3) film is an ideal dielectric material with excellent chemical stability, high transparency, and low loss rate to encapsulate 2D materials in optoelectronics applied within the THz range, preventing the migration of ions, gases, and water vapor at the interface [181]. The two-step irreversible gas-solid reactions can explain the deposition of Al_2O_3 by ALD. Figure 5.9 illustrates the schematic of the reaction process using trimethylaluminum (Al $(CH3)_3$, TMA) and O_2 as precursors and reactants, respectively. In the first half-reaction, the -CH3 group of TMA (precursor) is absorbed by the -OH group on the substrate surface, generating the gas by-product CH_4. When inert gas Ar or N_2 is introduced, excess precursor and reaction by-products can be removed; In the second half reaction, the -OH group from H_2O reacts with the surface CH_3 group to form a layer of Al-O and gas side-product CH_3. Like the previous step, by-products are later cleaned by the inert gas purge, leaving a layer of Al-O. An Al_2O_3 with a precise-controlled thickness is obtained by repeating the reaction cycles. The half and total reactions can be written as:

$$\text{First half reaction : } |||\text{-OH} + Al(CH_3)_3\,(g) \rightarrow |||\text{-O-}Al(CH_3)_2 + CH_4\,(g)$$

$$\text{Second half reaction : } |||\text{-O-}Al(CH_3)_2 + H_2O\,(g) \rightarrow |||\text{-Al-OH} + CH_4\,(g)$$

$$\text{Total reaction: } 2Al(CH_3)_3\,(g) + 3H_2O\,(g) \rightarrow Al_2O_3 + 6CH_4\,(g)$$

Where |||- represents the substrate surface. All the ALD processes mentioned in this

thesis are finished by the "Veeco Nanotech Atomic Layer Deposition System" (hereafter called "Veeco"), as shown in Figure 5.10 (a). Figures 5.10 (b-c) show Veeco's deposition chamber and the schematic of the Veeco system, respectively. During the ALD-Al_2O_3 process, target samples are initially placed in the middle of the chamber and heated up to 150°C in vacuum condition. Before the reaction cycles, a singular step of depositing a thin layer of water on the graphene surfaces reduces the carriers trapped at the interface and enhances the connection of Al atoms [182]. A standard ALD-Al_2O_3 cycle begins with injecting a pulse of TMA inside the reaction chamber for grafting the Al atoms. Then the system waits 5 seconds to pump out the by-products before introducing an H_2O pulse to complete a reaction cycle. Once a deposition cycle is finished, the system stops for 5s to reclean the chamber. The precise control of the gas release time of 0.015 seconds from the sources tank standardizes each pulse's dosage. Every 10-cycle reaction generates a roughly 1nm Al_2O_3 thin film. By repeating cycles 1500 times, an approximately 150nm Al_2O_3 protective layer for the bare graphene is realized. The detailed ALD recipe used to deposit Al_2O_3 on the graphene surface in this thesis can be viewed in Table 5-10.

Table 5-10 The recipe for depositing a 150nm ALD-Al_2O_3 in Veeco.

Steps:	Operations:
1st	Vacuuming the reaction chamber to a pressure below 100mT.
2nd	Baking the sample at 150°C for 10 mins.
3rd	Injecting 5 H_2O pulses with intervals of 5s.
4th	Starting the first cycle. The system first injects a TMA pulse and waits for 5s. Then injects a H_2O pulse to conclude the cycle.
5th	Repeating the cycle 1500 times with the internals of 5s.
6th	Stopping the whole procedure and releasing 5sccm N_2 flow for 2 mins to clean the chamber.

5.3.3 Deposition and transfer of monolayer graphene

The integration of graphene into the metamaterial devices explored in this thesis necessitates the utilization of Metal-Organic Chemical Vapor Deposition (MOCVD) as a growth technique. The MOCVD process is finished by Wadood Tadbier, under the supervision of Stephan Hoffmann's research group within the electrical engineering at the University of Cambridge. Their focus revolves around the intricacies of this specialized growth method.

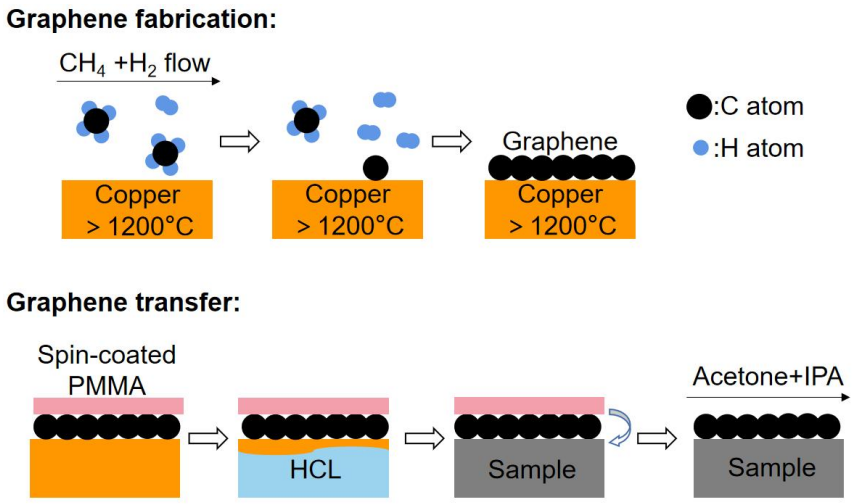

Figure 5.11 Schematic of graphene MOCVD procedure and graphene transfer.

Figure 5.11 illustrates the procedure of the farbrication and transfer of the CVD-grown monolayer graphene. The growth process is initiated by directing a gas mixture of CH_4 and H_2 over a heated copper catalyst (usually temperature >1200°C [183]). The continuity of catalytic reaction prompts the self-assembly of separated graphene atoms into continuous monolayer graphene. Following this, the cooled-down Cu-graphene composite undergoes a spin-coating process involving the application of a thin layer of PMMA, creating a distinctive sandwich-like structure. Subsequently, with precision, the composite sandwich is positioned copper face down atop a hydrochloric acid (HCl) liquid bath. This strategic arrangement prompts the selective etching of the copper component, ultimately leaving behind a PMMA-graphene bilayer composite that remains afloat on the HCl medium. After this etching procedure, the PMMA-graphene composite, duly cleansed with deionized (DI) water, is positioned onto the substrate. The graphene component is situated between the substrate and the PMMA layer in this configuration. The final step involves the gentle application of

acetone, effectively removing the uppermost PMMA layer. This meticulous process culminates in forming a continuous graphene film affixed to the substrate through physical absorption.

5.5 Fabrication procedure of asymmetric split ring resonator

Au arrays:

NbN arrays:

Figure 5.12 Schematics of the standard procedures of manufacturing asymmetric split ring resonator made of gold and NbN, respectively.

Figure 5.12 provides a visual representation of the established protocols employed in the creation of asymmetric split ring resonator arrays, utilizing either gold (Au) or niobium nitride (NbN), subjects that will be further explored in Chapter 6. The fabrication of complete Au arrays follows the conventional procedure of the double-layer photoresist lithography, as delineated in Section 5.1.1, and is implemented on a 3mm silicon (Si) substrate. In contrast, the production of NbN arrays involves the application of the standard single-layer photoresist lithography process. The use of S1813, distinguished by its continuous vertical wall profile, facilitates the anisotropic etching process applied to NbN.

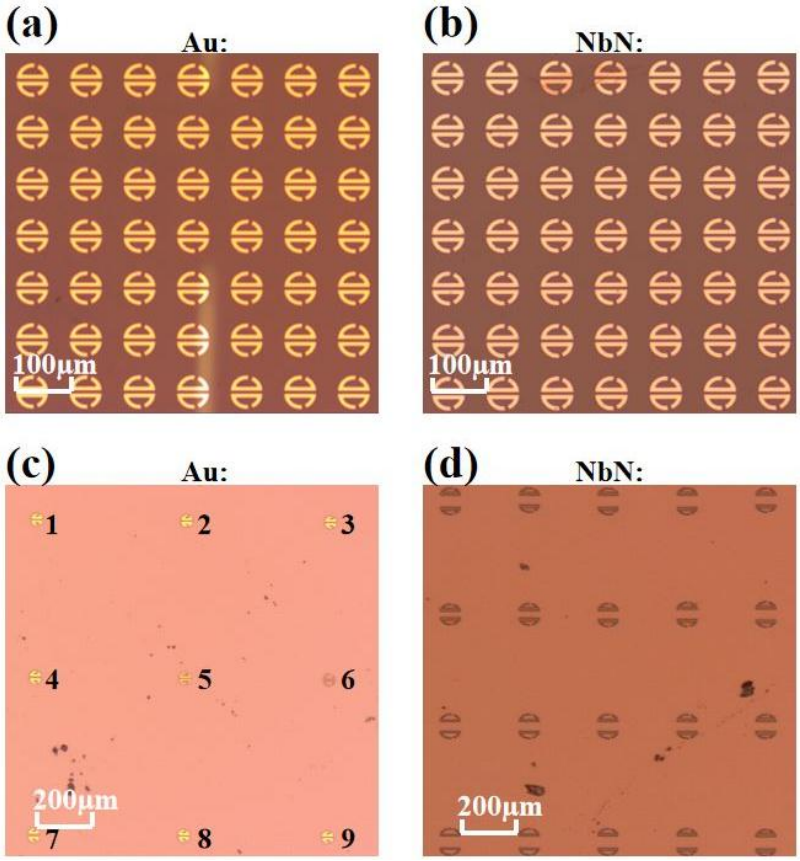

Figure 5.13 Optical images of (a) a standard ASDR array made of gold; (b) a standard ASDR array made of NbN; (c) the THz a-SNOM scanned sample with nine single ASDR; (d) a special sample consisting of various separated individual ADSR prepared for cryogenic THz SNOM.

Figure 5.13 showcases optical representations of four distinctive arrays of Asymmetric Split Ring Resonators (ASDRs) as discussed within this thesis. These include (a) the original ASDR array design, rendered in gold; (b) the same design as (a), yet fabricated from niobium nitride (NbN); (c) a specific sample hosting nine distinct individual ASDRs made from Au, specifically prepared for the THz aperture Scanning Near-Field Optical Microscopy (a-SNOM) study outlined in Chapter 6. The numerals 1-9 within the image correspond to the arbitrary designs later introduced in Chapter 6, and (d) another specialized sample containing multiple uniquely designed ASDRs composed of NbN, prepared for the cryogenic THz SNOM investigation. As depicted in the figures, all samples exhibit precise shape control, reflecting a fabrication tolerance of under 0.2μm (measured via a ZEISS Lab1 optical microscope equipped with a fifty-times magnified lens).

5.6 Fabrication procedure of graphene-based active modulator

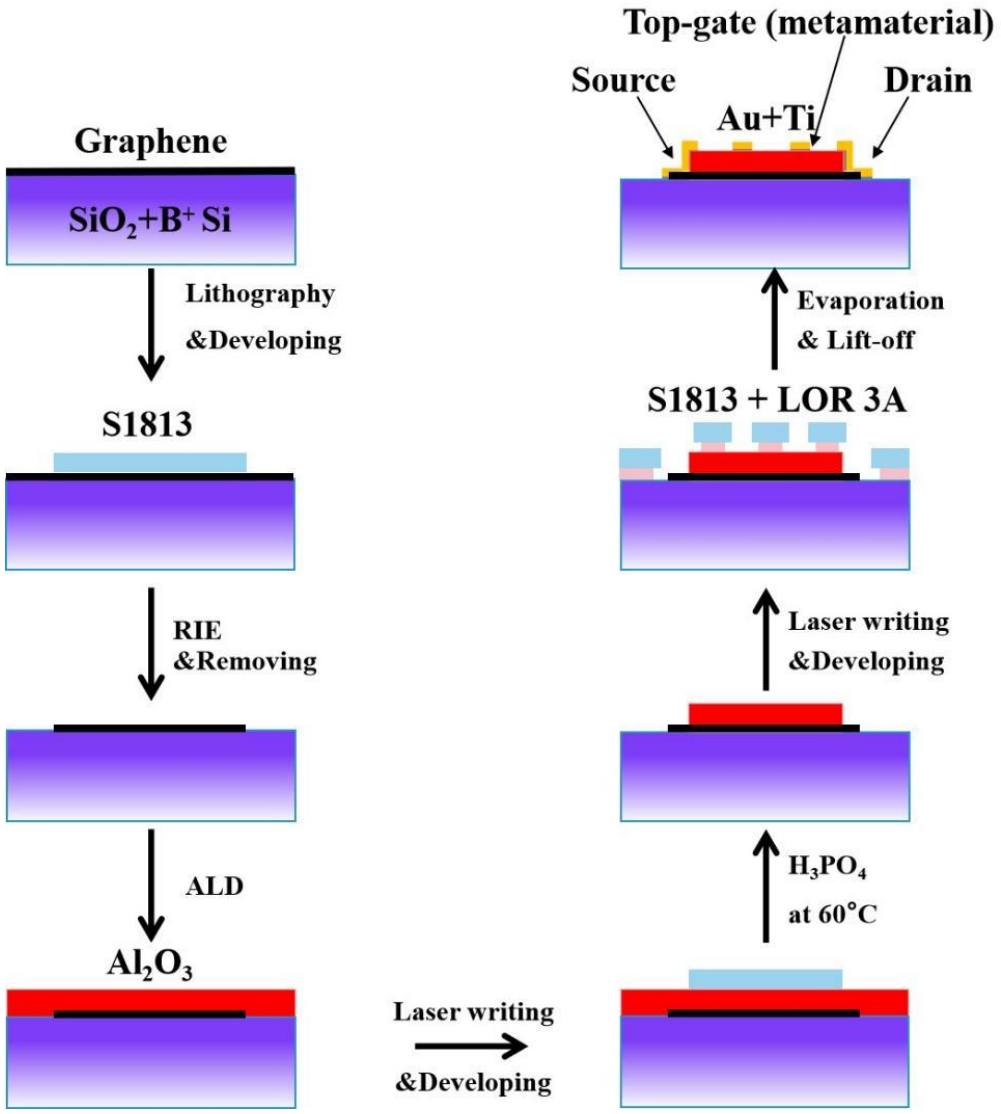

Figure 5.14 The standard procedure for fabricating a graphene-based terahertz modulator.

In continuation, Chapter 7 provides a detailed exploration of high-field THz pumping experiments conducted on a sample housing four identical arrays of graphene-based integrated THz modulators. These arrays are distinguished by unique top-gate geometries, each corresponding to a meticulously characterized metamaterial design. A comprehensive schematic outlining the introduction of the modulator's fabrication is presented in Figure 5.14.

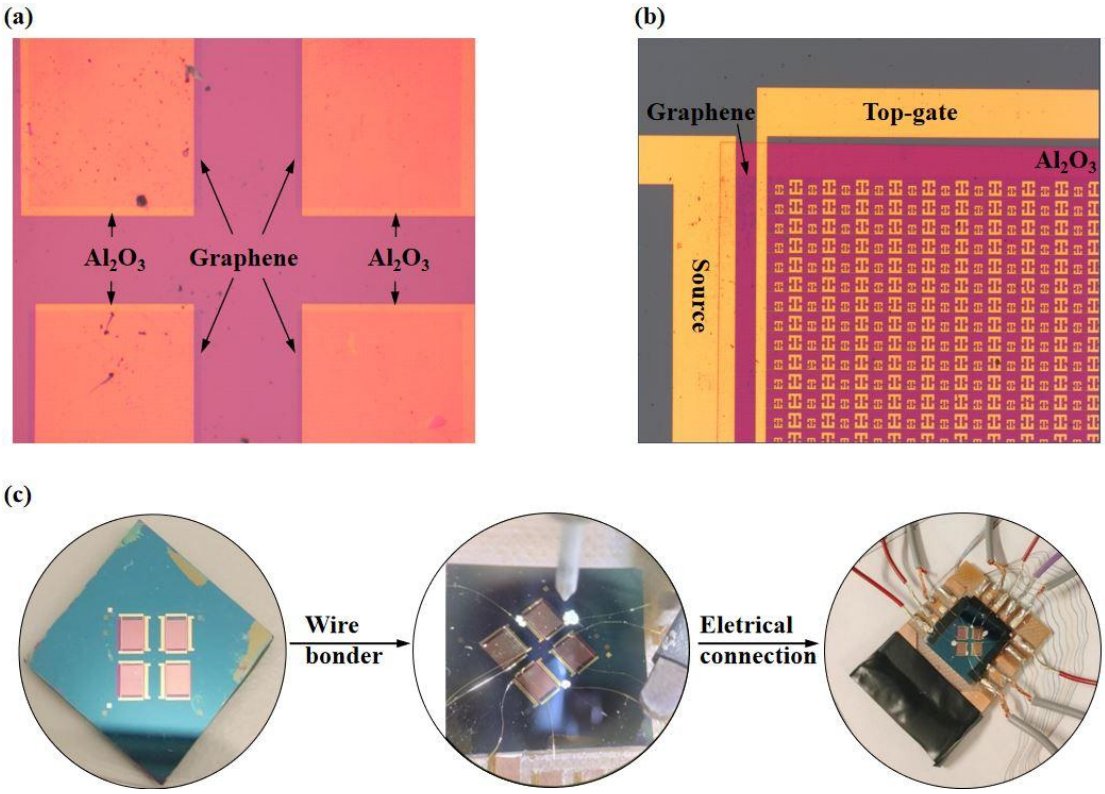

Figure 5.15 (a) The optical image of the four individual areas on the sample surface made of patterned graphene squares and their etched shielding layers of Al_2O_3 ; (b) the optical picture of the mixed-resonator array within the accomplished sample. (c) operations applied to connect the fabricated sample with external electrical systems.

The fabrication procedure unfolds as follows: Initially, a CVD-grown monolayer graphene is meticulously transferred onto a 1.2×1.2 cm² large, 500μm thick Boron-doped Si substrate, coated with a 300nm SiO_2 dielectric film (the Engineering Department of Cambridge University executes this transfer process). Subsequently, the S1813 PR is uniformly coated onto the sample's surface via the standard lithography method expounded in section 5.1.1. This PR is patterned into four distinct squares, each measuring 2.2×2.2 mm² . During the subsequent RIE process, the PR masks safeguard the underlying graphene. The RIE process adheres to the parameters outlined in Table 3-8.

After the cleaning procedure involving acetone and IPA, the removal of the S1813 layer results in square-shaped graphene patches being exposed on the substrate's surface. Given the vulnerability of graphene patches to environmental factors and the potential for damage, a prudent course of action involves depositing a 150 nm ALD-Al_2O_3 layer onto the graphene surface, following the parameters outlined in Table 5-10.

Subsequently, the uniform ALD-Al_2O_3 layer is shaped into four identical squares, each strategically positioned beyond the periphery of the graphene patches. This design exposes edge areas that facilitate the establishment of ground connections. The patterning process involves applying a single-layer PR coating and laser writing, a methodology chosen to avert the risk of damaging the ALD-Al_2O_3 layer during the alignment of the mask. In addition, the wet etching technique, which entails immersing the sample in orthophosphoric acid liquid at 60 °C for 12 minutes, achieves the desired patterning for ALD-Al_2O_3. The choice of wet etching over RIE in this scenario arises because the plasma-based RIE process can potentially inflict serious damage upon the exposed graphene, particularly if over-etching occurs. On the contrary, being considerably less aggressive, orthophosphoric acid offers a safer alternative.

In Figure 5.15 (a), the outcome of this process is visually depicted. The optical image showcases the etched areas of ALD-Al_2O_3 (highlighted in orange), the graphene squares that are partially shielded by the ALD-Al_2O_3 patches (evidenced by shadowed domains within the ALD-Al_2O_3 patches), and specific bare graphene regions, purposefully designated for electrical connections. Finally, the manufacturing process proceeds with the standard double-layer photoresist laser writing procedure, followed by thermal evaporation and the lift-off technique. These consecutive steps culminate in the establishment of ground-connection pads and top gates. A visual representation of the successful two-resonator array completion on the sample is depicted in Figure 5.15 (b). The image conveys the meticulous spatial alignment of key components, such as the source, top gate, ALD-Al_2O_3 layer (highlighted in red), and graphene (dim red).

Figure 5.15 (c) elucidates the steps to establish the necessary electrical connections linking the sample to external systems. Before wire bonding, the precisely prepared sample is affixed onto a PCB board, with the arrays' region occupying a roughly 6×7 mm^2 space at the centre. This arrangement accommodates the essential transmission configuration for THz-TDS measurements, facilitated through an 8×8 mm^2 aperture in the board. Subsequently, the sample affixed to the PCB board is situated within the wire bonder to connect the contact pads on the sample and the pins on the board. Upon the successful execution of the wire bonding process, the sample is transferred to a soldering station to solder additional wires onto the pins, ultimately completing the intricate electrical framework.

Chapter 6 THz a-SNOM Investigation of Individual Asymmetric Split-Ring Terahertz Resonators

As introduced in Chapter 1, metamaterial resonators have emerged as a potent and adaptable tool in the THz domain, widely implemented in integrated optical devices like active modulators [64-66] and detectors [184-185] and in foundational research such as ultra strong light–matter [186-187] interaction studies. However, a persistent challenge remains in precisely characterizing the modes facilitated by these subwavelength components, mainly dependent on the indirect scrutiny of the collective far-field transmission or reflection attributes of resonator arrays.

This Chapter introduces a groundbreaking approach, which is already published in the journal [188], using a broadband TDS analysis of solitary metamaterial resonators facilitated through a THz a-SNOM. The experiments were finished in the THz nearfield lab at UCL in collaboration with Dr Lucy Hale. This innovative technique enables the delineation and the quantitative evaluation of the highly restricted modes sustained by the resonators. Implementing a cross-polarized configuration in this setup significantly unveils an avenue for probing weakly radiative modes, often elusive in conventional methods. This development signifies a monumental stride in metamaterial research, potentially spearheading the next wave of advancements in optoelectronic platforms rooted in THz photonics, paving the way for unprecedented discoveries and innovations in the field.

6.1 Introduction

Extended from the brief discussion in Chapter 1, the recent advancement in metamaterial resonators enhances the device efficiency. It contributes to the progress of compact THz sources such as resonant tunnelling diodes [189-190], quantum cascade lasers [191-193], and spintronic emitters [194-196] by refining their photonic emission and operational efficiency. Notably, high Q-factor resonators have been instrumental in elevating the sensitivity of THz sensing applications [197].

Despite these achievements, the integration of metamaterial resonators presents a unique set of challenges, mainly attributed to their subwavelength dimensions and intense mode confinement which fosters augmented light–matter interactions [198-202]. The intense mode

confinement, however, creates a barrier in directly deciphering the modal attributes through conventional experimental approaches. Current methodologies primarily rely on evaluating extensive arrays of these resonators [152], yet such indirect far-field assessments are often influenced by inter-element coupling within the array, limiting the visibility of certain modes such as the "dark" modes [203].

In this Chapter, a THz broadband a-SNOM is introduced as a potent tool to delve deeper into the complexities of individual metallic ASDRs (as demonstrated in Chapter 4). This setup, complemented with THz-TDS, empowers us to stimulate all observable modes concurrently and selectively scrutinize them, leveraging the superior spatial resolution afforded by near-field techniques. A significant innovation in our approach is the implementation of a cross-polarized excitation and detection configuration, which significantly enhances the visibility of previously elusive "dark" modes, thus facilitating detailed imaging of deeply subwavelength resonators.

Furthermore, this methodology permits the direct measurement of the Q-factors of singular resonators of varying geometrical dimensions, offering a temporal glimpse into the progression of excited modes. These near-field experimental findings align exceptionally well with anticipated outcomes and parallel data obtained through conventional far-field THz-TDS systems. This breakthrough holds the promise of unveiling "dark" modes and associating spectral elements with distinct spatial distributions of highly confined modes, potentially spearheading a new era of research and development in the application of metamaterial resonators in the THz domain.

6.2 Metamaterial resonator design

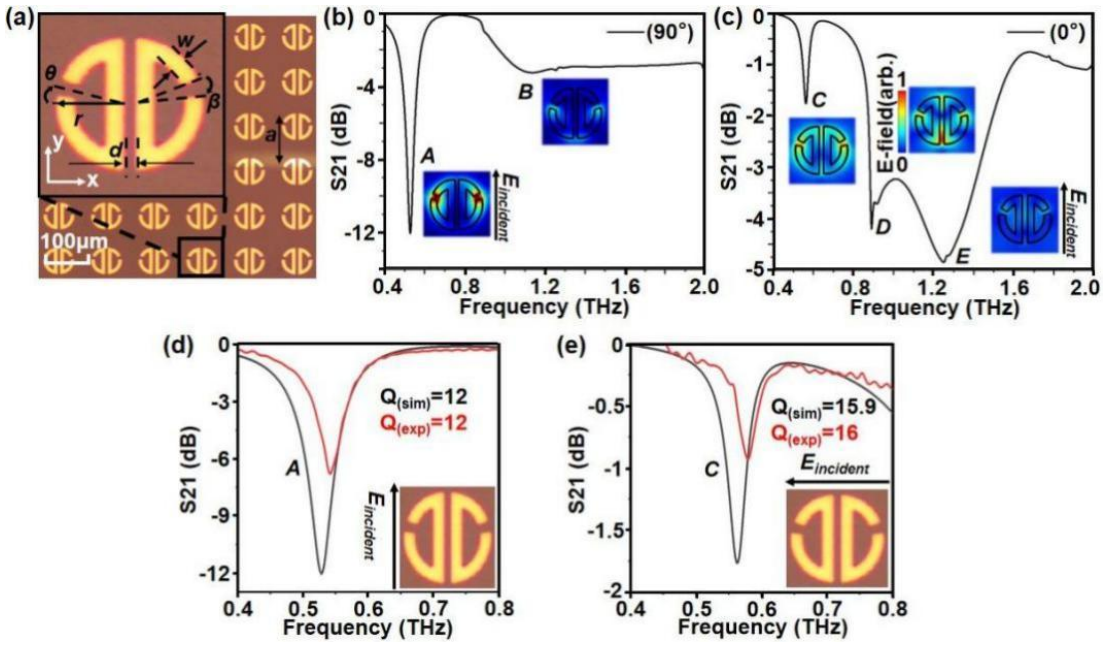

Figure 6.1 (a) Optical picture of the ADSR metamaterial array resonator, inset: a unit cell illustrating resonator parameters. (b, c) Simulated far-field spectra for the 90° and 0° incoming E-field polarization, respectively. Insets: Simulated spatial profiles of the supported modes (normalized E-field at 2μm above the ADSR surface). (d, e) Simulated and measured far-field spectra for modes **A** and **C**. Note the different vertical scales for each mode, which highlight the different mode visibility.

The resonator schematic, depicted in Figure 6.1 (a), adopts the ADSR structure delineated in Figure 4.5 in Chapter 4. It is important to underscore once more that this specific design engenders the emergence of several modes when stimulated by light that is polarized either along the y-axis (henceforth termed as 90°) or the x-axis (hereinafter denoted as 0°). This includes the generation of dark modes, a phenomenon birthed from the asymmetric excitation of electric currents within the linear sections of both the upper and lower segments of the resonator.

The intricate amalgamation of dark and bright modes intrinsic to this design not only engenders control over the Q-factor values but also paves the way for the cultivation of varied functionalities, encompassing phenomena akin to electromagnetic-induced transparency (45,46) as well as the formulation of polarization modulators (47). Nonetheless, the intricate

interplay of dark and bright modes renders the ADSR a complex subject for far-field spectroscopic analysis, establishing it as a prime candidate for meticulous investigation through near-field spectroscopic methodologies.

Figures 6.1 (b) and (c) illustrate the simulated broadband transmission spectra and normalized electric field profiles at the 5 different resonances **A**-**E** of an ADSR under two distinct orthogonal incident polarization excitations (detailed simulation and explanations can be found in Chapter 4).

6.3 Far-field measurement

Initial measurements were conducted in the far field using the Menlo system in a transmission setup to validate the capability of the fabricated resonator arrays to facilitate these modes. These measurements afford a robust experimental mapping of modes, harmonizing well with the numerical simulations, and are vital for deciphering the results obtained in the near-field experiments. Additional fabrication of metamaterial sample is shown in Chapter 5.

Figures 6.1 (d) and (e) showcase the transmission curves of the resonances around 0.54 THz and 0.58 THz for 90° and 0° polarization, which correspond to modes **A** and **C**, respectively. These figures depict the measured (red traces) and simulated (black traces) data. The congruence between the far-field experimental data and the simulation curves is notably high. Regarding visibility, defined here as the absolute value of the S_{21} parameter at resonance, mode **A** exhibits substantially larger visibility (~6 dB) in both simulations and experimental observations compared to dark mode **C** (~2 dB). Moreover, mode **C**'s quality factor, or Q-factor, is greater (Q~16) than mode A's (Q~12). The Q-factor in the experiments was determined by dividing the central frequency of resonance by the full width at half maximum (FWHM). In contrast, the simulated Q-factor was directly extracted using COMSOL Multiphysics software.

6.4 Near-field copolarized measurement

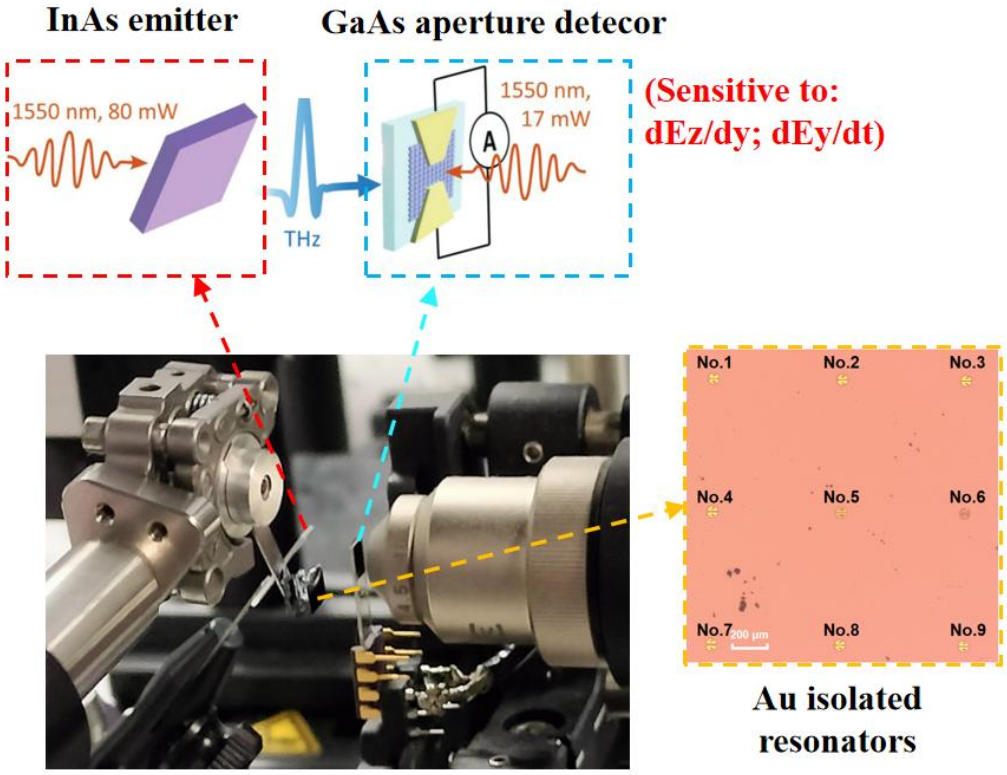

Figure 6.2 Schematic of the THz a-SNOM measurement.

Table 6-1 Parameters of the 9 different resonators prepared for THz a-SNOM measurement.

Resonator	r (μm)	d (μm)	θ (deg)	w (μm)	β (deg)
No.1	20.2	3.4	15	8.4	15
No.2		3.4	20	8.4	15
No.3		3.4	25	8.4	15
No.4		6	20	8.4	15
No.5		3.4	20	6	15
No.6		3.4	20	3	15
No.7		9	20	8.4	15
No.8		3.4	20	8.4	10
No.9		3.4	20	8.4	20

After the far-field experiments, a subsequent sample with 9 individual resonators was created on an identical substrate, each spaced 600μm apart and varying in size (refer to Figure

5.12 for more fabrication details). A slight adjustment to the lithographic parameters, as shown in table 6-1, was made to align the resonators' designs with the peak sensitivity of the near-field setup. This tuning process enables us to alter the resonance frequency and Q-factor of the resonators, circumventing the necessity of producing multiple arrays for each design. Despite showing different far-field transmission spectra compared to those seen in Figure 1, these resonators retain the characteristic distribution of the mode E-field.

In Figure 6.2, the THz a-SNOM measurement schematic is depicted. The resonators were spaced sufficiently to allow individual near-field response measurements without neighboring interference. The setup used an Indium Arsenide (InAs) source to generate THz pulses, powered by an 80mW femtosecond pulsed 1550nm light from a Titanium: Sapphire laser. This illuminated the sample perpendicularly from the substrate side. Throughout all measurements, the aperture probe remained stationary, positioned roughly 5μm from the sample's front surface.

The detection of the THz field was executed in a standard TDS system, pumped by a 15mW 1550nm laser from the source mentioned above. The probe incorporated a gold planar surface featuring a $10\times10\mu m^2$ aperture, integrated directly atop a photoconductive antenna detector (PCA). Consequently, the PCA behind the aperture instantly detected fields channeling through the aperture plane.

The sensitive field components of the aperture probe are contingent on the PCA antenna's orientation. In this experiment, the antenna was aligned with the y-direction (analogous to the central bars seen in Figure 6.1 (a)), making it receptive to the electric field polarized in the y-direction (more precisely, its time derivative, dEy/dt) and the out-of-plane electric field (specifically its spatial derivative along the y-direction, dEz/dy).

Contrary to the far-field transmission spectra where a decrease in amplitude is noted at resonance, the near-field probe discerns the evanescent field located at the surface, resulting in a pronounced amplitude at the resonance point.

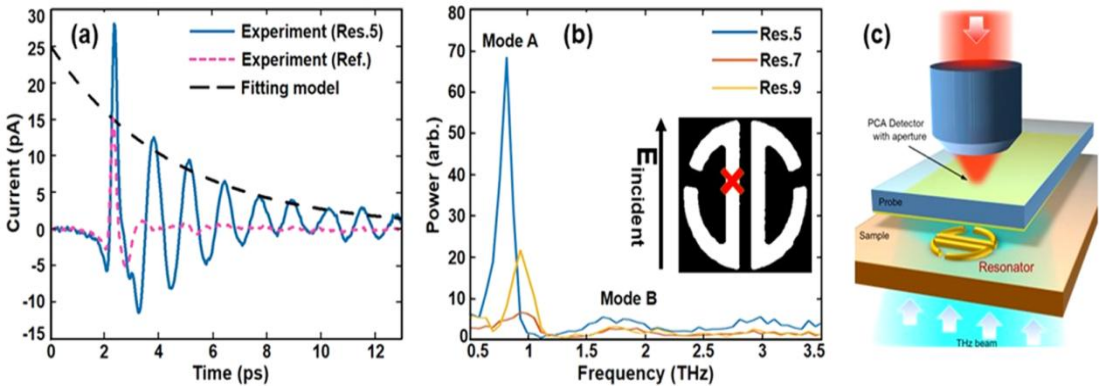

Figure 6.3 THz a-SNOM popularized configuration results of: (a) Solid line: time-domain near-field waveform acquired at the center of resonator 5 with a-SNOM. Dashed purple line: reference time-domain waveform of the incident THz pulse, acquired in the substrate area (without the resonator). Dashed black line: best fitting curve for the evaluation of the Q-value [further information about the evaluation is shown in Appendix A3]. (b) Spectral amplitude of three isolated resonators (Res. 5, Res. 7, Res. 9), normalized to the spectrum measured in a region with no resonator present (pink dashed waveform in panel (a)). The inset shows a resonator sketch, indicating the position where all the waveforms were acquired. (c) Schematic of the near-field setup.

The first measurements examined the resonator's response to 90° polarized excitation, a straightforward setup allowing direct detection of the incident THz pulse by the aperture probe. Simulations indicated a prominent spectral feature of mode **A** in the 0.8-1.0 THz range, where the system has peak sensitivity.

Figure 6.3 (a) shows a typical time-domain pulse waveform near a sample resonator (resonator 5) alongside a reference waveform taken from the substrate area with no resonator. The stage step size of the time delay was 5μm, equivalent to 0.033 ps. The spectral resolution, dictated by the time scan duration, was set to about 12 ps, avoiding Fabry–Perot fringes in the spectra and allowing a 30 GHz resolution. Clear post-main pulse oscillations in the waveform signify the activation of the bright mode (mode **A**). Figure 6.3 (b) presents normalized spectra from three different resonators (No 5,7 and 9), varied by values as defined in Table 6-1 (a). From the simulations as detailed in Appendix A3.2, an increase in the parameters "d" or "β" is directly associated with an elevation in both the resonance frequency and linewidth, concurrently leading to a decrease in the peak spectral amplitude, while a reduction in the "w"

parameter results in an enhancement of the Q-factor and visibility. Importantly, the observed resonance frequencies corroborate the predictions made by the simulations. More attractively, as the intensity of mode ***B*** is more insignificant than the mode ***A*** in frequency domain, enabling the time-domain based Q-factor evaluation as dedicated in Appendix A3.

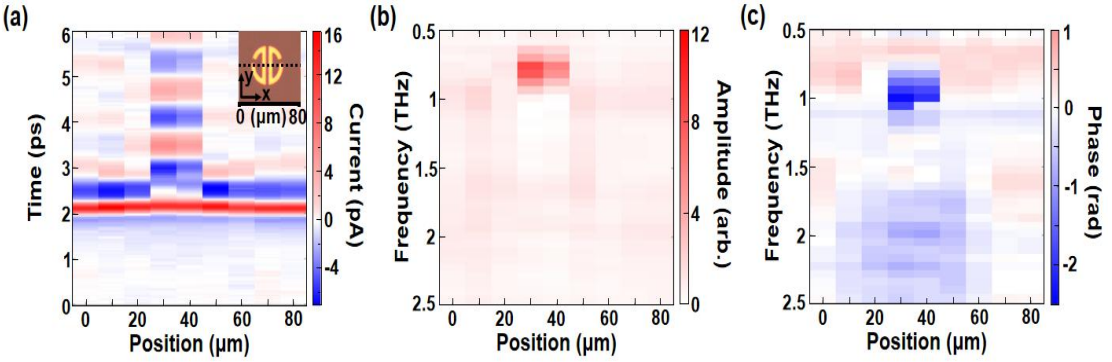

Figure 6.4 (a) Space–time scan across a single resonator (res. 5), with resonant oscillations observed at the resonator center. (b) Spectral amplitude at respective scan positions in panel (a). (c) Spectral phase at different probe positions, as illustrated in the inset, where the dashed line shows the probe position along the X-direction.

In this experiment series, the signal sensitivity significantly fluctuated based on the probe's position relative to the resonator. As depicted in Figure 6.4 (a), a space-time analysis was conducted across a single resonator, traversing through the split-ring gaps (illustrated in the inset of Figure 6.4 (a)). The waveform manifests almost as a single-cycle pulse devoid of detectable resonance excitation at a marginal distance from the resonator's central bars. Conversely, in proximity to the central bars, the THz waveform undergoes a significant transformation, recording oscillations of the highest amplitude at the resonance. Figures 6.4 (b) and (c) delineate the power and phase spectra as functions of the near-field probe's position. Notably, a distinct spectral power peak is accompanied by a swift phase alteration, observable at approximately 0.8THz when the x values range between 30 and 40 μm (as presented in Figures 6.4 (b) and (c)).

These spectral characteristics' dependence on the probe location vividly underscores the superiority of the near-field technique. This approach allows the near-field probe to confine the THz signal within a 10×10μm² region, where the resonant field achieves its maximum intensity, thereby markedly enhancing the mode visibility compared to the far-field

measurements. This highlights the capacity of the near-field technique to offer a granular and detailed insight into the resonant behaviors within such small domains, a feature not accessible with far-field methodologies.

6.5 Near-field cross-polarized measurement

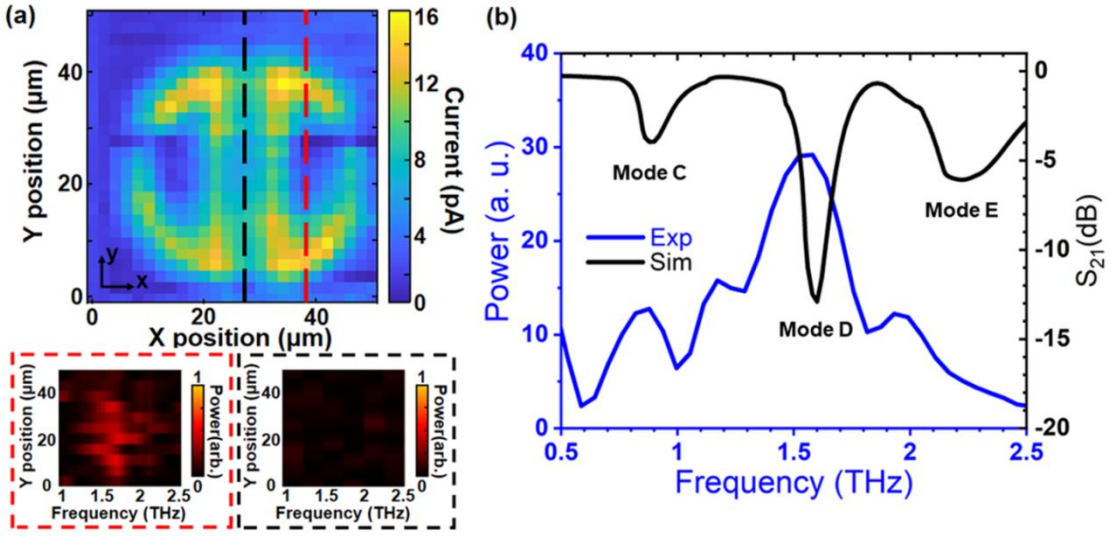

Figure 6.5 THz a-SNOM cross-polarized measurement results of (a) spatial map taken across resonator 5 at a time corresponding to a peak in resonant time-domain waveform. Red and black dash-framed insets: spectra of mode **D** in the frequency domain corresponding to the Y-axis scan at the yellow and black dashed lines in the spatial map, respectively. (b) Comparison between the averaged signal acquired through the whole resonator in the near-field experiment and the simulation results of the S_{21} parameter in the far field.

This passage describes a set of experiments that examined the response of the resonators in a cross-polarized configuration, enhancing the understanding of the response characteristics of different modes and emphasizing the superiority of the a-SNOM technique in detecting and differentiating between “dark” and “bright” modes. In this setup, space-time maps recorded along the y-direction (as highlighted in Figure 6.5(a)) illustrated that the clearest resonance signatures were found at the centers of the resonator rings, as opposed to the center of the resonator, which was the case in the co-polarized experiment. This led to the recording of time-domain waveforms at the center of one of the rings, as delineated by the red dashed line in Figure 6.5 (a).

The power spectrum, depicted in Figure 6.5 (b) (blue trace), is normalized to that of the 0° polarized incident field, showing distinctive peaks at frequencies corresponding to the modes **C**, **D**, and **E**, as simulated in Figure 6.1. This result, particularly the clear presence of modes **C** and **D** at the identified frequencies, underscores the capability of the aperture probe to detect all three modes at the ring center, even with their antiparallel field profiles making them less conducive to far-field radiation.

Notably, the ratios of the mode amplitudes are different in the near-field spectra when compared to the far-field spectra. This discrepancy arises from the various modes contributing to the electric field detected at a specific probe location, with the contribution of each mode dependent on the probe's positioning due to the differing spatial distributions of these modes. The insets in Figure 6.5 (a) substantiate this, illustrating the varying responses based on the probe's traversal over different sections of the resonator.

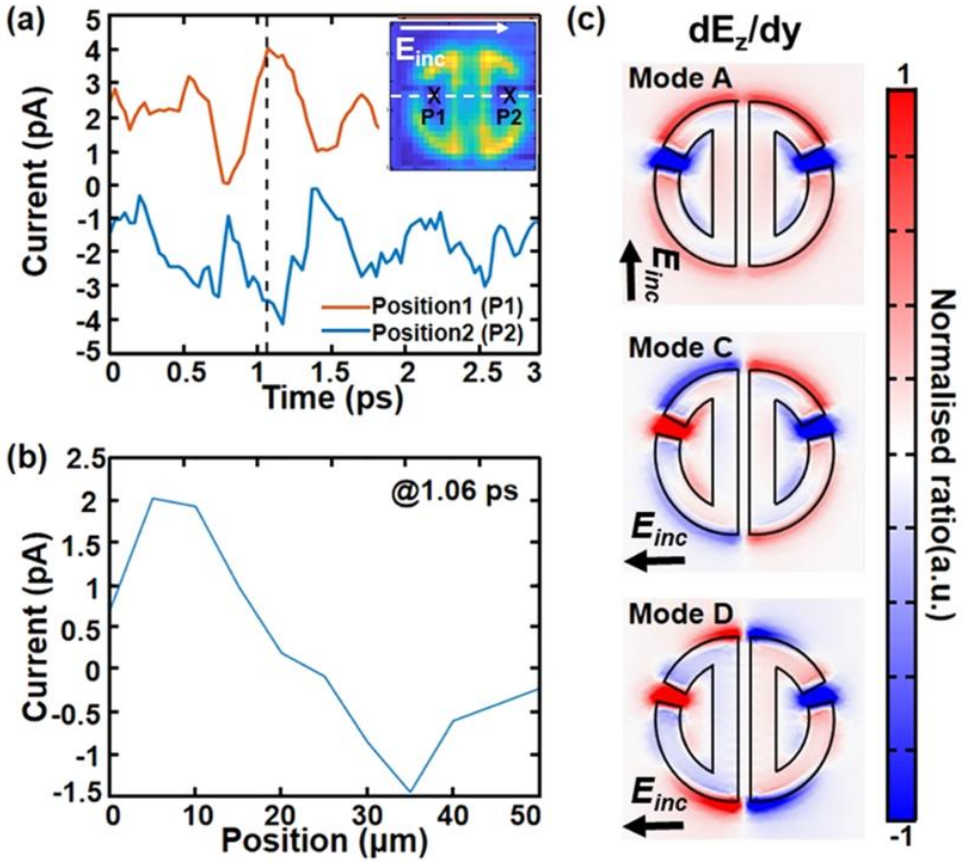

Figure 6.6 (a) Time-domain waveforms at different positions in resonator 5. Inset: Experimental map showing the scanning trace (white dashed line), position 1 and position 2 as described in the main text. (b) Amplitude changes of the waveforms at 1.06 ps according to

the scanned positions in the resonator 5. (c) Simulations of dEz/dy in the ADSR for different modes. Clear signal flips can be found between the upper and the lower halves in modes **C** and mode **D**, while mode A does not show a phase change.

Further, the phase of the near-field signal, dependent on the probe position, serves as a tool in distinguishing "dark" from "bright" modes. Despite challenges in calculating the phase due to low signal amplitude in the cross configuration, distinctive π phase changes were observed at two rings of the resonator, predominantly attributed to the **D** mode, as visualized in Figures 6.6 (a) and (b). The simulations validate this antisymmetric field distribution between the two rings, a hallmark of "dark" modes in ADSR, contrasting sharply with the symmetric distribution observed for mode A, the "bright mode".

In conclusion, these observations underscore the robust capability of the a-SNOM technique, not only in obtaining clear spectra of "dark" modes within individual resonators, as shown in Figure 6.5 (b) but also in pinpointing key features that differentiate them from the standard dipole or radiative modes. It unveils a nuanced level of detail about the resonator responses, highlighting the a-SNOM's potential in further studies into these complex systems.

6.6 Conclusion

The present investigation highlights THz a-SNOM's unparalleled potential and functionalities for spectroscopic analyses of resonant modes facilitated by individual metallic ADSRs. Precise Q-factors were ascertained by meticulously examining singular metamaterial resonators within the THz frequency spectrum, effectively avoiding the inter-resonator coupling phenomena commonly observed in the far-field analysis of extensive arrays.

The evidence indicates that the a-SNOM methodology is exceptionally proficient in detecting the intricate features of all supported resonant modes, encompassing the highly localized, low-loss dark modes. This represents a significant departure from conventional techniques employed in far-field THz-TDS. Furthermore, the adaptation of a cross-polarization measurement strategy has enabled the high-contrast, high-resolution mapping of the metallic components of the resonator, surpassing expectations based on the dimensions of the probe aperture.

Moreover, this research vividly delineates the intrinsic differences between dark and

bright modes regarding the spatial distribution of their respective field amplitude and phase attributes. It is affirmed that the near-field THz-TDS technique manifests as a singularly potent tool in advancing research domains, ranging from creating novel THz optoelectronic platforms to exploring unprecedented photonic phenomena. These phenomena notably encompass investigations into bound state-in-continuum (BIC) resonances, a realm that stands to gain substantially from advancements in the design and understanding of THz metamaterial resonators.

As a prospective avenue of exploration, the utilization of a monochromatic source is suggested, which would facilitate the mapping of pure individual modes supported by the resonators, circumventing the inherent mode superposition typically encountered with the excitation by broadband THz pulses observed in this study. Such a methodological shift promises to impart deeper insights into these sophisticated devices' operational principles, potentially fostering groundbreaking advancements in this burgeoning field of study.

Chapter 7 Conclusion and Future work

7.1 Conclusion

In the present thesis, a multifaceted exploration of THz time-domain spectroscopy (THz-TDS) has been undertaken, manifesting its applications across various investigations into the optical characteristics of naturally occurring materials and artificial photonic architectures. These investigations span industrial manufacturing, materials science, and advanced photonics research. Central to these inquiries is the evolution of THz-TDS into a preeminent and adaptable technique uniquely positioned to decipher optical interactions derived from time-resolved electromagnetic wave measurements.

Chapter 1 provided a brief overview of THz wave propagation's fundamental principles and elucidated various methods employed in generating THz radiation. Subsequent sections delineated a gamut of applications harnessing THz waves, accentuating their inherent challenges across domains such as communication, spectroscopy, and imaging. To offer potential avenues for the augmentation of THz technologies, sophisticated methodologies, encompassing scanning near-field spectroscopy and active metamaterials, were expounded upon.

In Chapter 2, an in-depth exploration of THz-TDS was undertaken, focusing on its analytical prowess in probing diverse materials. The chapter elucidated prevalent radiation and detection methodologies, highlighting designs like the photoconductive antenna (PCA) and nonlinear crystals. Furthermore, the chapter delineated the conventional data analysis techniques used to ascertain various optical parameters. The capabilities and extensive functionalities of the Menlo THz-TDS, which form a significant part of this thesis, were meticulously presented.

Subsequently, Chapter 3 delved into two experimental studies that adeptly employed varying configurations of the Menlo THz-TDS to further the frontier of materials manufacturing. These investigations were tailored to bolster advancements in bio-based nanofiber composites and the additive manufacturing of metals. The ensuing results, encompassing parameters such as shielding effectiveness, height levelling, and average surface roughness, were derived from the foundational data analysis techniques delineated in Chapter 2. The outcomes from the THz-TDS assessment underscored the viability of a low

carbon footprint nanofiber-based THz absorber, achieving absorption rates nearing a remarkable 100%. Furthermore, this analysis presented a prospective methodology for astutely evaluating the effects of varied polishing techniques in industrial additive manufacturing.

To fully harness the potential of THz-TDS in evaluating photonic structures, particularly metamaterials, Chapter 4 and Chapter 5 elucidated a thorough process of metamaterial design transition from theoretical concepts to tangible devices. Chapter 4 expounds upon the foundational principles underpinning the design of diverse metamaterials, emphasizing functionalities such as elevated Q-factors and augmented absorption. Moreover, an exhaustive series of Finite Element Method (FEM) simulations, facilitated by the COMSOL software, was executed to refine the optical responses of various metamaterial designs. This included an exploration of the intricacies related to geometry, unit cell definition, meshing conditions, and the ultimate outcomes.

Further in Chapter 5, the discourse delved deeper into the intricate micro-fabrication techniques employed to actualize a metamaterial starting from rudimentary materials. The chapter elucidated the fundamental principles and meticulous protocols associated with diverse techniques, encompassing standard photolithography, laser writing, reactive ion etching (RIE), atomic layer deposition (ALD), and the deposition and transfer of graphene. Exemplary processes and outcomes pertaining to the fabrication of asymmetric split ring resonators (ASRR) made of Au or NbN, and graphene-based active modulators were systematically presented.

In Chapter 6, an avant-garde methodology was articulated, leveraging a broadband TDS analysis of individual resonators, as expounded upon in Chapters 4 and 5, using a THz aperture scanning nearfield optical microscope (a-SNOM). The findings derived from the THz a-SNOM were rigorously compared with data acquired from the far field Menlo THz-TDS measurements. This pioneering THz a-SNOM instrumentation facilitates meticulous mapping and quantitative assessment of the highly localized modes inherent to the resonators. The integration of a cross-polarized configuration within this framework profoundly unearths the potential to interrogate weakly radiative modes, typically obfuscated in traditional TDS techniques. Such an advancement heralds a paradigm shift in metamaterial research, potentially catalyzing transformative breakthroughs in optoelectronic systems

anchored in THz photonics, charting a course for future seminal innovations in the domain.

7.2 Further work

7.2.1 Cryogenic THz far-field and SNOM measurements

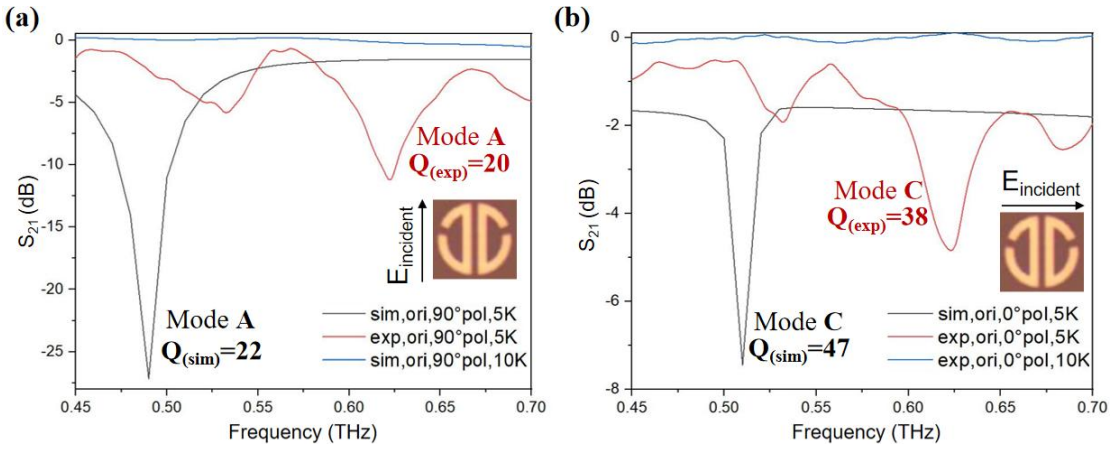

Figure 7.1 Cryogenic far field THz TDS measurement results of (a) the NbN ASDR sample with original design excited by 90° incident light (mode **A** in Figure 6.1); (b) the NbN ASDR sample with original design excited by 0° incident light (mode **C** in Figure 6.1).

In Figure 7.1 (a-b), the results are showcased from experiments utilizing the cryogenic Menlo system as described in Section 2.3.1. These results elucidate the S_{21} spectra of Mode **A** and Mode **C** which denominated in Figure 6.1 of Chapter 6 and pertain to the NbN ASDR sample, illustrated in Figure 5.12 of Chapter 5. Subject to variable temperature conditions and distinct polarizations, the conspicuous variation in the absolute S_{21} values between the two figures accentuates the intrinsic distinctions inherent to the two modes.

For both polarization instances, an evident superconducting transition of NbN is discernible, specifically in the temperature range between 5K (represented by the red line) and 10K (denoted by the blue line). This observation correlates with a marked transformation in the S_{21} spectral profile, aligning seamlessly with the conditions wherein Tc (NbN) is less than 15 K, as outlined in section 4.2.4.

Yet, a factor warranting attention is the fabrication of the NbN sample on a sapphire substrate with a thickness of 380 μm. This arrangement culminates in a pronounced second pulse echo, which is observable around 22 ps in the time domain. Such an occurrence can substantially impede the accurate retrieval of resonance, echoing the mechanism elaborated

upon in Figure 2.18. To circumvent this potential limitation, the S_{21} spectra displayed in Figures 7.1 (a-b) underwent processing with a window function spanning a length of 30ps. This process effectively maximizes each mode's visibility and mitigates the potential obfuscation of resonance arising from pronounced Fabry Perot oscillations within the spectra.

The congruence between experimental outcomes and simulations, particularly concerning visibility and Q-factor across varying polarizations, reaffirms the appropriateness of employing the two-fluid model for simulating NbN ASDR, as elaborated in section 4.2.4. The observed discrepancies of red shift between the experimental and simulation data, can be attributed to factors like the contraction of NbN at cryogenic temperatures and the diminished absolute value of NbN's conductivity compared to the reference provided.

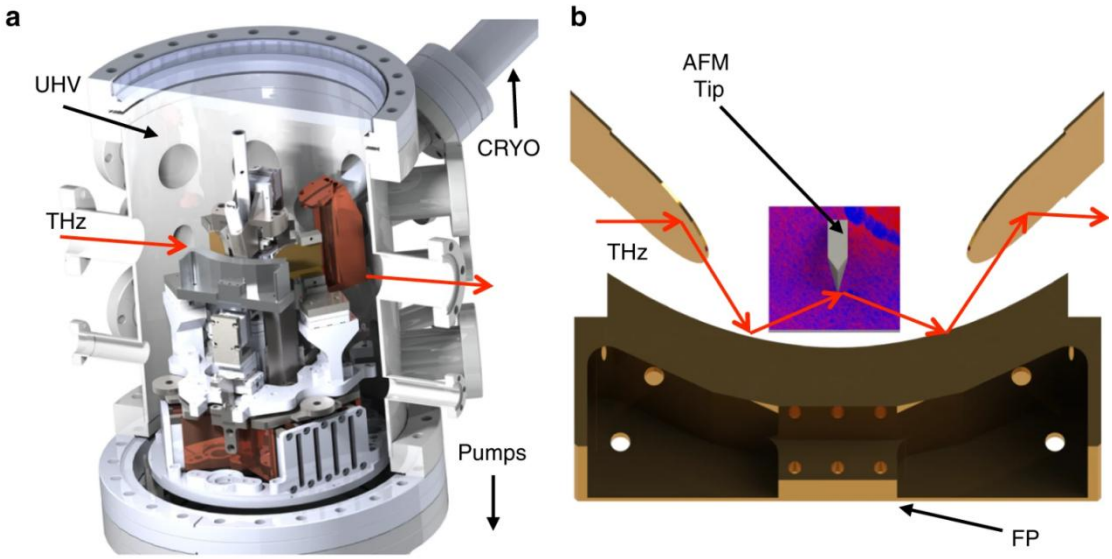

Figure 7.2 (a) Schematic of cryogenic THz s-SNOM; (b) detail view of the SNOM inside the chamber. The same focusing parabola is used to both focus the THz pulse onto the tip (not shown to scale) and collect the tip-scattered light [204].

However, a direct evaluation of the Q-factor of the modes supported by NbN sample is proven difficult. An alternative approach for measuring the resonance strength and Q-factor for Modes **A** and **C**, devoid of the substrate echo effect, can be achieved by integrating cryostat technology with THz near-field spectroscopy. This results in the development of cryogenic THz a/s-SNOM measurements. This methodology parallels the THz a-SNOM procedures conducted at room temperature, as outlined in Chapter 6. It produces distinct

oscillation waveforms by enabling direct assessments of the resonant electric field's intensity adjacent to the metamaterial surface. Such data can subsequently be harnessed to determine the resonance Q-factor utilizing data fitting methodologies, as illustrated in Figure 6.3 (a). This technique has recently been formulated to elucidate low-temperature physics phenomena, such as phase transitions in materials, as referenced in [204], utilizing THz s-SNOM. A representative schematic of the cryogenic THz s-SNOM implementation is depicted in Figure 7.2.

7.2.2 Terahertz high harmonic generation of integrated graphene devices

7.2.2.1 Terahertz high harmonic generation in graphene

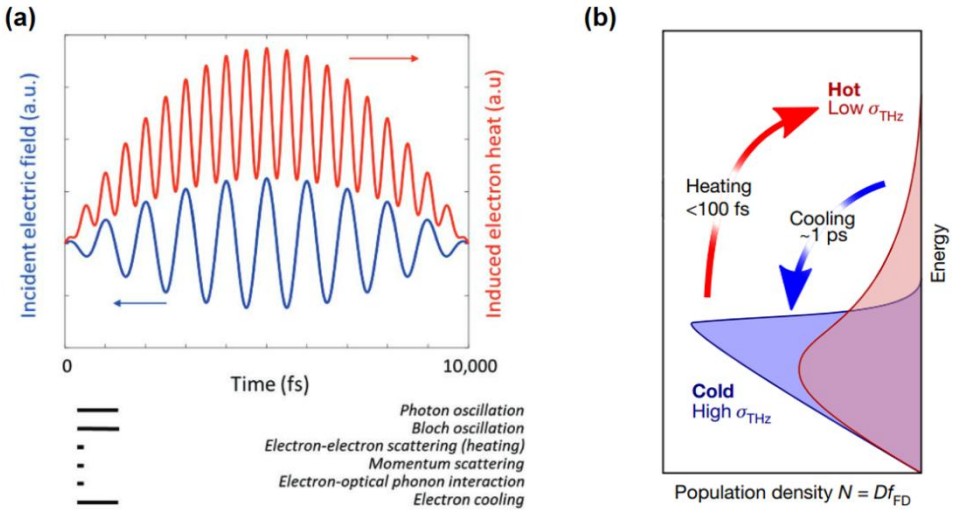

Figure 7.3 (a) Illustration of the nonlinear graphene heat response (red) from incident THz light at 1 THz (blue). The lengths of the black lines under the figure panels indicate the fundamental timescales of the relevant processes, scaling with the corresponding figure above them. [205]; (b) Temporal asymmetry of electron heating and cooling rates in graphene leads to a situation where the application of a THz driving field [206].

As delineated in section 4.3.1, the optical behavior of graphene across the complete electromagnetic spectrum primarily arises from two transitions: the interband transition in the optical-NIR band and the intraband transition in the FIR-THz band. In the THz domain, the energy of THz photons, being a modest few meV (with THz equal to 4.1 meV), is notably less than the thermal energy at room temperature, approximately k_BT_e=26 meV. This ensures that

the intraband transition predominantly governs the optical interaction of graphene within this range.

THz waves exhibit oscillations on a (sub-) picosecond timescale during this intraband transition. This duration is significantly lengthier than the usual electron momentum scattering time observed in graphene, typically ranging from 10–100 fs (as shown in Figure 7.3 (a)) [205]. In addition, Figure 7.3 (b) demonstrates the total carrier concentration changes caused by the momentum scattering and colling procedure [206]. As a result, within the THz domain, carrier transport predominantly unfolds within the diffusive regime. Here, electrons encounter several momentum scattering events during the oscillation period of the THz wave. Consequently, the microscopic movement of these electrons doesn't usually synchronize coherently with the exerted electric field. This diffusive, collective movement of free electrons in the presence of applied THz fields introduces notable nonlinearity in graphene's behavior. Such nonlinearity is strikingly intense, resulting in marked THz saturable absorption [207-210] and exceptionally potent THz high-harmonic generation (HHG). The most attractive part of this nonlinearity mechanism is it only requires incident THz fields of the order of 10s of kV cm^{-1} [211].

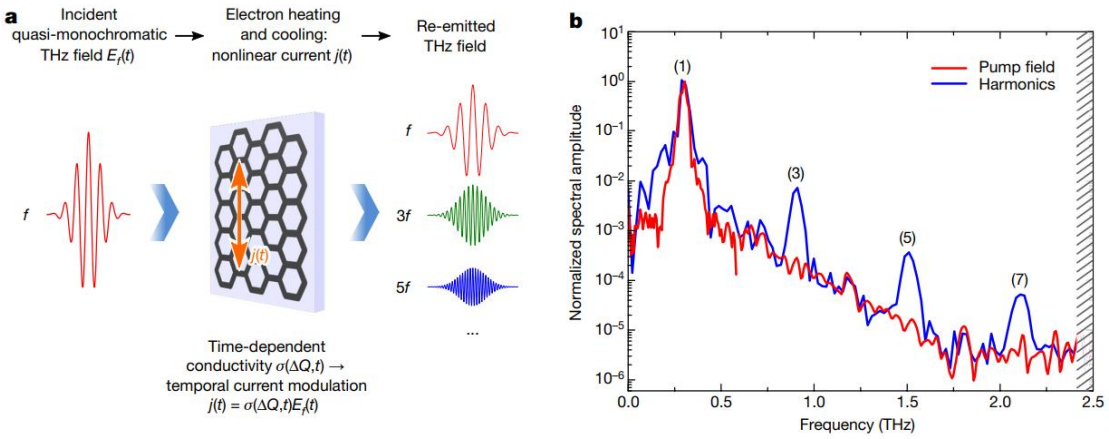

Figure 7.4 (a) Schematic and (b) main results of the graphene THz high-harmonic generation [206].

As a centrosymmetric material, graphene displays a characteristic in which all even-order high harmonic electric fields are nullified by their corresponding fields of opposite vectors. Consequently, the predominant graphene THz HHG is observed primarily at odd harmonics,

particularly at 3***f***, 5***f***, and 7***f***, when the incident frequency is represented by "***f***". The schematic and experimental results depicted in Figures 7.4 (a-b), utilizing an 85 kV/cm THz pump at an incident frequency of 0.3 THz, as presented in [206], corroborate this theoretical assertion.

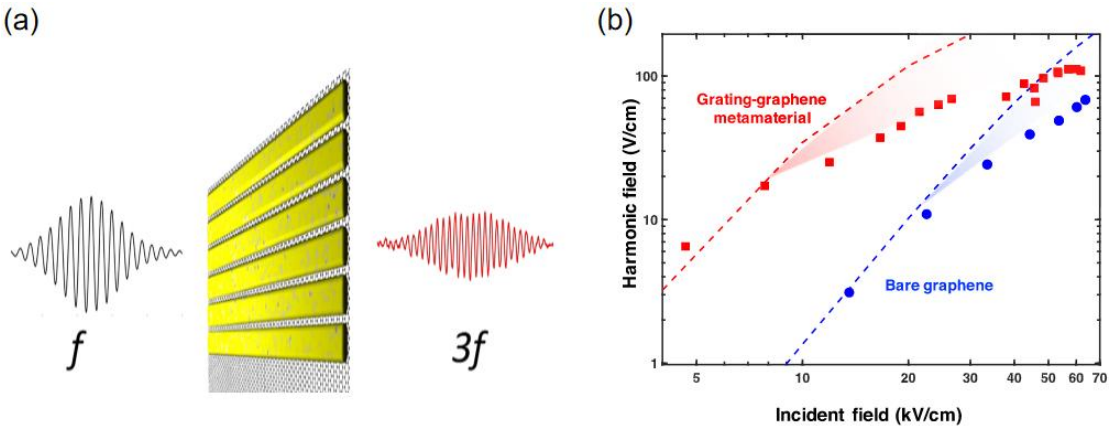

Figure 7.5 (a) Schematic representation of the measurement configuration, with a multicycle THz waveform with fundamental frequency ***f*** incident on a grating-graphene metamaterial sample; (b) comparison of third-harmonic intensity for grating-graphene metamaterial sample (red squares) and bare graphene sample (blue circles), as a function of peak field strength of the incident THz light [216].

Furthermore, numerous studies have indicated that the graphene HHG can be amplified through plasmonic coupling proximate to the graphene surface. Commonly, this enhancement is achieved by patterning the graphene into specific geometries [214-216]. Figure 7.5 (a) illustrates the experimental setup from [216], which utilizes high field THz wave incident on a grating-graphene metamaterial sample. The grating's resonant frequency is designed to match the incident THz wave frequency for maximizing the interaction. The results, presented in Figure 7.5 (b), offer a comparative analysis of the third-harmonic HHG for both the grating-graphene metamaterial sample (represented by red squares) and the bare graphene sample (depicted by blue circles). This juxtaposition effectively underscores the efficacy of employing metamaterial structures to amplify the THz HHG in graphene.

However, most of these experiments have not been conducted within an integrated graphene device, presenting a barrier to their deployment in practical applications. Yet, the effect of coupling has a double resonance structure. As a result, the graphene-based

modulators described in Chapters 4 and 5 emerge as the optimal platforms for examining the THz HHG of graphene within an integrated system.

7.2.2.1 Menlo characterization of the fabricated graphene-based modulators

In line with the details discussed in section 4.3, the modulator's performance is closely associated with the sheet conductance of the graphene. Nonetheless, a homogenous distribution of this conductance across the graphene sample remains elusive, a factor that might result in discernable effects on the modulator's function [217].

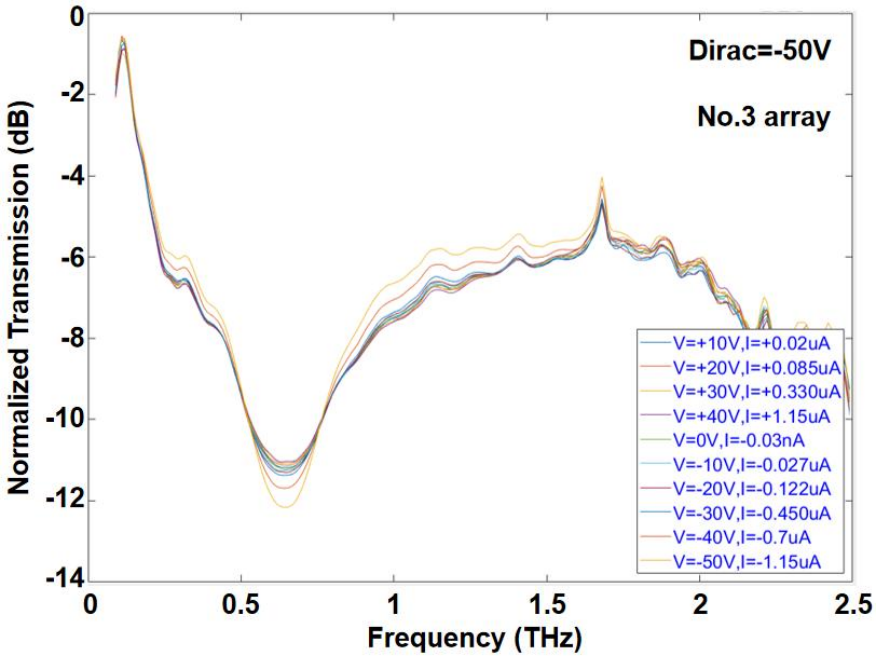

Figure 7.6 THz TDS measured S_{21} spectra of the No.2 array introduced in Chapter 4 with different bias voltages. The term "I" represented in the figure signifies the leakage current, as recorded by the source meter.

For consistency with subsequent discussions on HHG experimental results, Figure 7.6 presents the S_{21} spectra of the single resonance array, specifically the No.3 array (the reason for this selection will be elucidated in the ensuing section), as recorded using the Menlo system across various bias voltages. The measured S_{21} spectra for the other three arrays can be found in Appendix A4. Notably, the resonance in Figure 7.6 prominently appears at 0.65 THz, especially at the Dirac point (-50V). This observation corresponds closely with the

design postulated by the COMSOL simulation, as depicted in Table 4-4. A shift in bias voltages from -50V to 40V reveals a perceptible decline in resonance visibility. Such a phenomenon can be interpreted as an outcome of enhanced absorption caused by the escalating sheet conductance of graphene as depicted by the COMSOL simulations. However, the change in resonance's S_{21} value from -12dB to -11dB, attributed to changes in graphene's conductance, is lower than the difference forecasted by the simulation (-14 dB to -8 dB). This discrepancy can be attributed to a decrease in the Drude scattering time, as represented in equation 4.12. Such an alteration can result from impurities trapped at the interface between the graphene and the substrate. These impurities can introduce higher Ohmic losses, thereby affecting the conductivity of the graphene. This phenomenon is likely to explain the observed disparity between the simulation and the experimental results.

7.2.2.2 High field THz TDS measurement

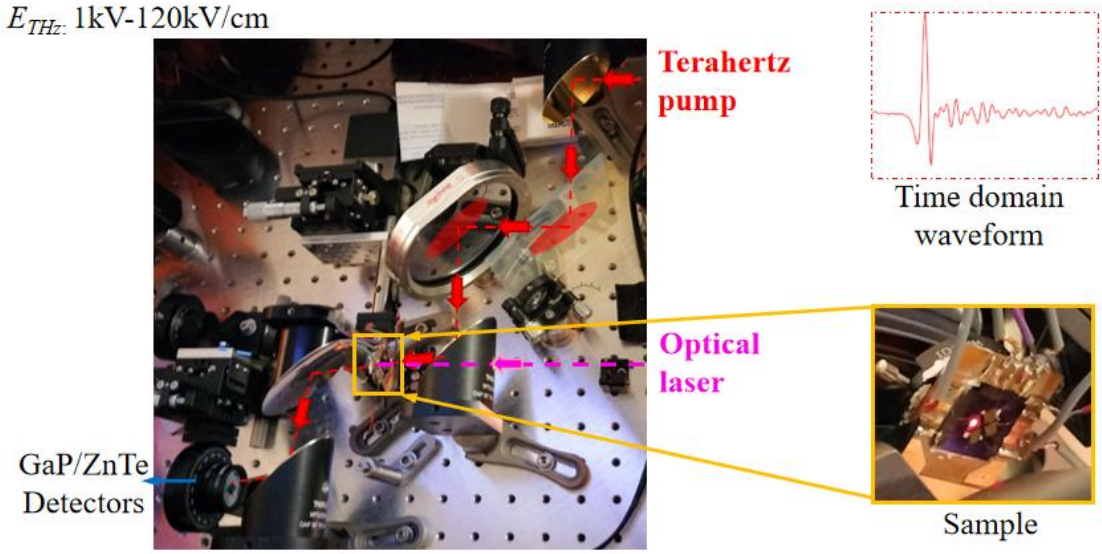

Figure 7.7 Optical picture of the high field THz TDS at Warwick University. Upper inset: typical acquired time domain waveform, lower inset: graphene modulator in alignment.

The high field THz Time-Domain Spectroscopy (TDS) set up at Warwick University offers a robust platform for investigating terahertz high-harmonic generation (HHG) in graphene, as depicted in Figure 7.7. The process begins with the generation of the THz excitation pulse, which is derived from an 800nm radiation focused on a lithium niobate ($LiNbO_3$) crystal by the optical rectification effect, described in section 2.1.3. When aimed at

the sample position, this THz pulse can achieve a peak electric field strength up to 120 kV/cm. Regarding spatial characteristics, the THz pump beam spans a diameter of roughly 1.5mm, and its intensity profile exhibits a Gaussian width of approximately 400μm in both x and y directions. It should be noted that the high field THz TDS at Warwick produces a broadband THz wave, in contrast to the quasi-monochromatic THz wave depicted in Figure 7.4 and 7.5. This broadband wave encompasses a frequency range extending from 0.2 THz to 3 THz.

The setup employs a pair of parabolic mirrors to precisely focus the THz pulse. An auxiliary optical laser is utilized to guarantee the accurate positioning of the incident beam onto the sample. This laser's path is guided through the central axis of the focusing parabolic mirror, an arrangement conveniently illustrated in the figure's inset. Once the THz pulse interacts with the sample, its aftermath is captured using either GaP or ZnTe materials detectors. The detection strategy relies on the free-space sampling method, a technique thoroughly explained in section 2.1.4. The experiments were completed within the N_2 environment to isolate the water molecule absorption. Importantly, this TDS system adopts a mechanical stepper for controlling the time delay, in contrast to the rapid jittering time delay line used in the Menlo system. While this modification offers enhanced flexibility, allowing data collection with finer time resolution, it also significantly prolongs the data acquisition period. Consequently, the average data collection duration in the high field THz TDS extends to tens of minutes which is more than ten times longer than the measurements implemented in Menlo system.

Owing to the deployment of the broadband high-field THz pulse incident upon the fabricated graphene modulators, the data interpretation becomes inherently more intricate than the findings delineated in Figures 7.4 and 7.5, wherein quasimonochromatic THz waves were employed for graphene HHG excitation. This complexity arises from the high harmonic resonance intertwining with modes stimulated by broadband excitation, engendering multifaceted spectral outcomes. Within the confines of this thesis, a representative spectrum derived from the No.3 array, subjected to preliminary detailed analysis, is showcased. A comprehensive data dissection remains in progress.

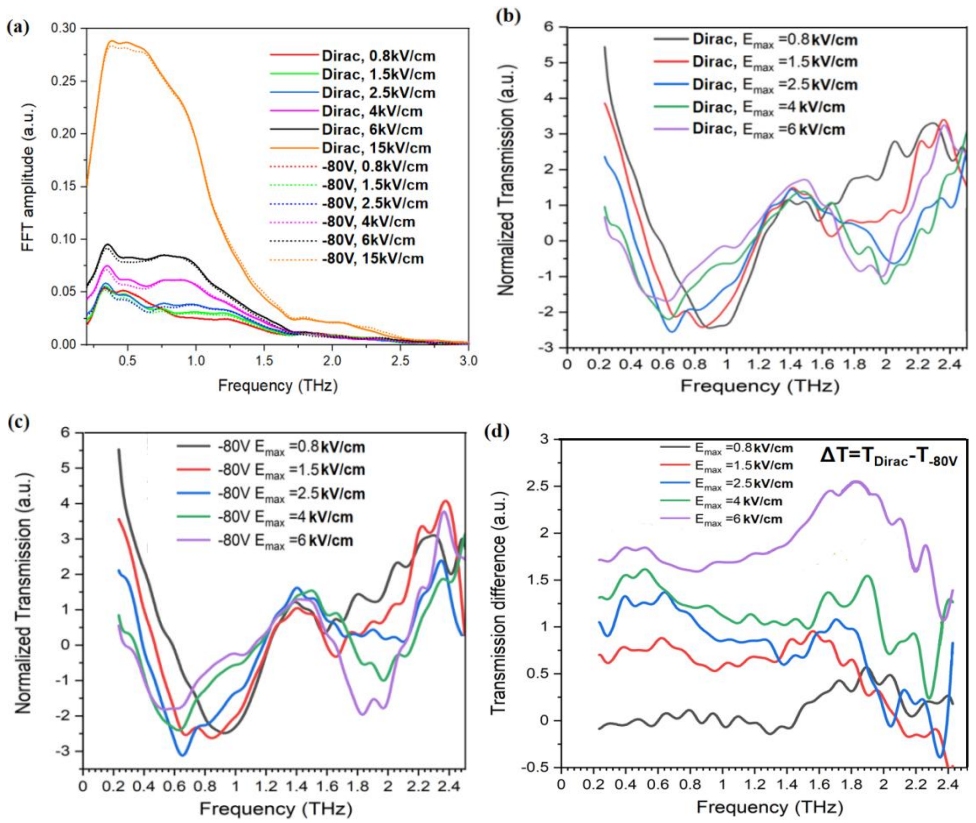

Figure 7.8 Various spectra of No.3 array measured by the high field THz TDS with different maximum electric field (a) FFT amplitude under the bias gating at Dirac point and at -80V away from Dirac point; (b-c) normalized transmission gated at the Dirac point and at -80V away Dirac, respectively; (d) difference of the normalized transmission gated at Dirac point and at -80V away Dirac.

Figures 7.8 (a-d) present the analyzed spectra of the No.3 array, as determined through high-field THz TDS. Figure 7.8 (a) showcases the spectra obtained directly from a fast Fourier transform (FFT) of the preliminary measurement, where the pumping electric field spans between 0.8 and 15kV/cm under two bias conditions: one at the Dirac point and the other offset by -80V from the Dirac point, indicating the valid bandwidth from 0.2 to 2.5 THz. The extensive spectrum modulation induced by the gate voltages attests to the optical interplay originating from the graphene, harmonizing with the results from the Menlo system displayed in Figure 7.6. Moreover, within the 0.8-6 kV/cm results, distinct resonance waveforms centred approximately at 0.65 THz become evident, attributed to the metamaterials' interaction. Yet, when augmenting the peak electric field from 6 to 15kV/cm, the resonance profile's clarity diminishes within the spectra, suggesting that the highly doped

graphene has potentially suppressed the metamaterial resonance.

For a more in-depth exploration of the enhancement of graphene HHG by the metamaterial structure, the amplitude spectra of the electric field from 0.8-6 kV/cm were normalized against the reference recorded on the sample substrate at their respective electric field intensities. Figures 7.8 (b) and (c) display the normalized transmission spectra of the No.3 array under varying gate voltages. These normalized spectra validate the resonance profile discerned in the FFT amplitude spectra. Although the complete spectrum appears more absorptive than emissive, normalized transmission values exceeding 1 post 1.6 THz may hint at the pronounced third harmonic generation mediated by the graphene modulator. An anticrossing phenomenon can also be discerned, corroborating its genuineness, given that the primary frequency resonance and the third harmonic concurrently subsist within the graphene layer, mutually influencing one another. Furthermore, Figure 7.8 (d) presents the transmission difference spectra under Dirac and doped conditions, unambiguously revealing augmented emission at the core frequency 1.8 THz upon intensifying the pumping electric field. A comprehensive wavelet analysis and a meticulous recalibration of the input power as depicted in the prior measurements are underway.

Appendix

A1. NbN ASDR simulations with different adjusted parameters.

Table S-1 The Q-factors of ADSR depending on varied ***d*** value according to Figure S1 (a).

d values (μm):	10	20	25	30
Q-factor:	99.4	118.0	124.1	127.4

Table S-2 The Q-factors of ADSR depending on varied ***a*** value according to Figure S1 (b).

a values (μm):	120	130	140	150
Q-factor:	127.4	147.4	149.3	99.3

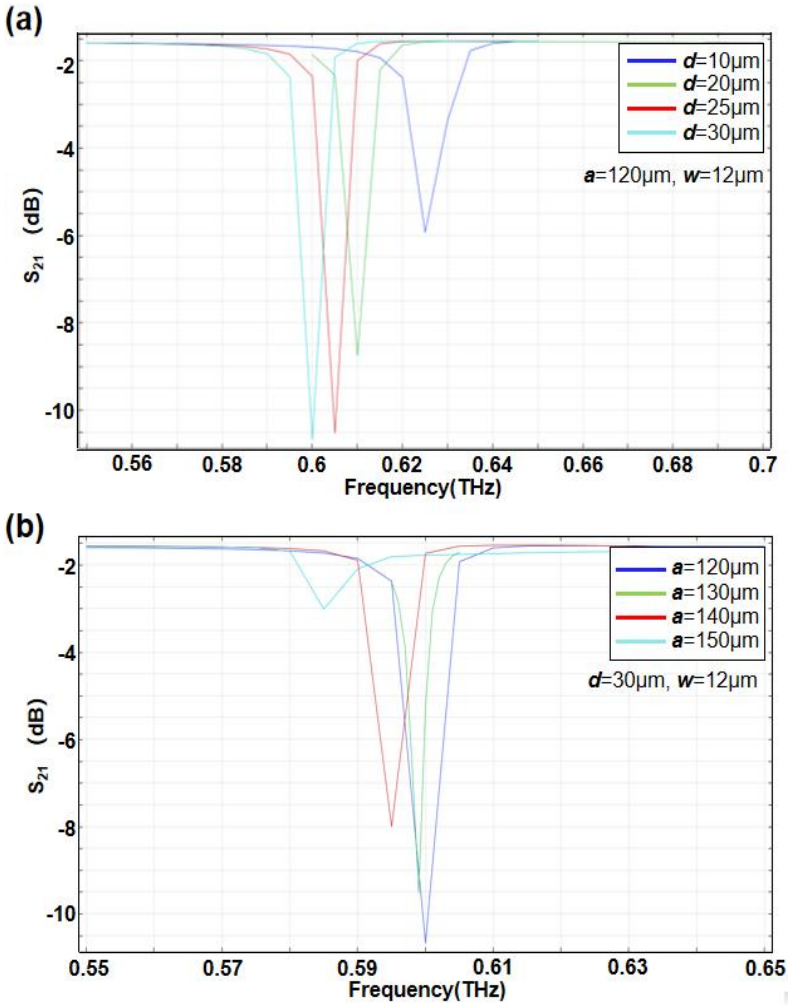

Figure S1 (a-b) Simulated S_{21} spectra of mode **C** with a frequency step of 0.005THz for different ***d*** and ***a*** value, respectively.

Figures S1 (a-b) illustrate the simulated S_{21} spectra of mode ***C*** utilizing a frequency step of 0.01 THz to elucidate the ramifications of modifying parameters ***d*** and ***a***. It is worth noting the frequency step is chosen as 0.005 THz (200 ps in time length) to keep consistent with the minimum resolution provided by the Menlo system.

Figure S1 (a) contrasts with the simulated performances observed in the gold ASDR, as delineated in Figure S1 (c). An increment in the ***d*** value within the NbN ASDR not only augments the resonance visibility, increasing from 4.2 dB to 9.8 dB, but also enhances the Q-factor, elevating it from 99.4 to 127.4, as documented in Table S-1. Notably, in this simulation framework, where ***a*** equals 120 μm, the ***d*** value must remain constrained below 30μm. This precondition is dictated by the requirement to maintain an optimum distance (d_2) between the upper and lower extremities of the ASDR in the current unit cell and the corresponding opposing edges in the subsequent periodic unit cell. This distance can be quantitatively articulated as $d_2=a-d-2r$ This distance must remain inferior to ***d***, to preempt erroneous electric field couplings within the unit cell's edge zone.

Transitioning to Figure S1 (b), it delineates the S_{21} spectra of the alterations in ***a***, whilst holding ***d*** at a steadfast value of 30 μm. An amplification of parameter ***a***, ranging from 120 μm to 140 μm, yields an enhanced Q-factor, which enhances from 127.4 to 149.3, as evidenced in Table S-2 This modification is, however, accompanied by a decrement in visibility, which diminishes from 9.8 dB to 6.9 dB. Furthermore, it is observed that a subsequent expansion of ***a***, extending from 140 μm to 150 μm, precipitates a pronounced decrease in visibility, plummeting from 6.9 dB to a mere 1.8 dB. This alteration concurrently incurs a depreciation in the Q-factor, which regresses from 149.3 to 99.3.

Table S-3 The Q-factors of ADSR depending on different ***a*** values according to Figure S2(a).

a value (μm):	120	140	150
Q-factor:	127.4	160.0	117.3

Table S-4 The Q-factors of ADSR depending on varied ***w*** values according to Figure S2(b).

w value (μm):	11	11.5	12	12.5	13
Q-factor:	127.4	153.6	160.0	155.4	135.5

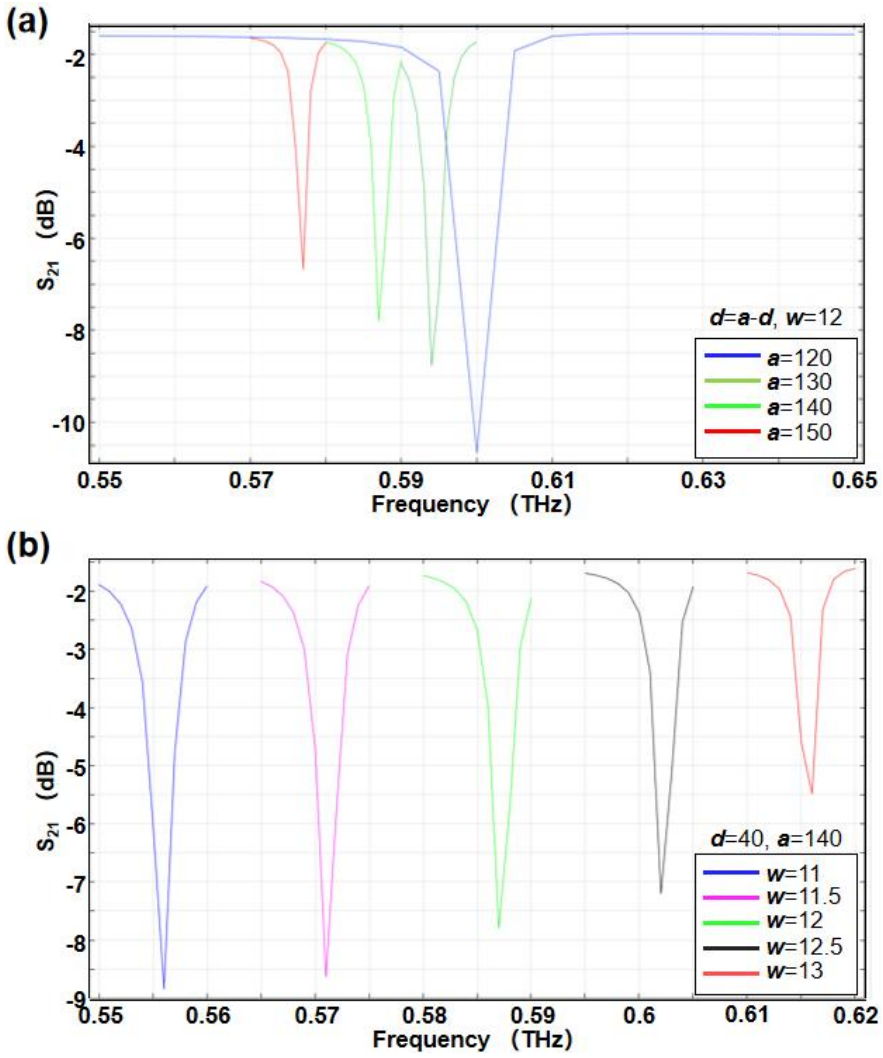

Figure S2 Simulated S_{21} spectra of mode **C** with a frequency step of 0.005 THz (a) of the changes ***a*** by fixing the condition of d_2=***d***; (b) of the changes ***w***.

As previously delineated, the increment of ***d*** can notably enhances in the Q-factor of the NbN ASDR that. Consequently, Figures S2 (a-b) elucidates this phenomenon through a simulation which explores the multi-factorial effects of parameters ***w*** and ***a*** on the NbN ASDR. The value of ***d*** is maintained at parity with d_2 throughout the modelling process and undergoes modifications congruent to alterations in ***a***.

Figure S2 (a) delineates the outcomes of this simulation executed with a frequency step of 0.005 THz. Analogous to the data presented in Figure S1 (a), these multi-factorial simulations demonstrate a resonance frequency redshift of approximately 0.15THz, a consistent decrement in visibility by 3 dB, and a Q-factor amplification of 32, which are manifested because of extending the ***a*** from 120 μm to 140 μm, as corroborated by the data

encapsulated in Table S-3. It is manifest from the comparative analysis between Table S-2 and Table S-3 that maintaining $d=d_2$ significantly contributes to the enhancement of the Q-factor of the mode **C** resonance. A noteworthy Q-factor of 160.0 coupled with a substantial visibility of 6dB is attained when the parameter a is set at 140 μm. While this multi-factor strategy unveils a potent methodology to escalate the Q-factor without a precipitous decline in visibility, it fails to arrest a concomitant decrease in both the Q-factor and visibility once the a surpasses 140 μm. Consequently, the optimal periodicity has been identified as 140 μm.

Moving forward, the final determinant influencing the performance of the NbN ASDR is parameter w. Figure S2 (b) alongside Table S-4 elucidates the simulated S_{21} spectra observed with varying w values and presents the corresponding Q-factors concurrently. As illustrated in the figure, there is a progressive decrease in the visibility of mode **C**, dwindling from 7 dB to 3.7 dB as w transitions from 11 μm to 13 μm. In parallel, an initial uptick in the Q-factor from 127.4 to 160.0 is observed with the expansion of w from 11 μm to 12 μm, followed by a decrement to 135.5 upon further increase to 13μm. Hence, the optimized parameters have been delineated in Table S-4.

A2. Single resonance graphene modulator simulations with different adjusted parameters.

Table S-5 Simulation details for modifying No.2 array with changing different variables.

Variable 1	P (μm):	B (μm):	B_2 (μm):	L (μm):
G	70	8	11	50
Variable 2	P (μm):	B_2 (μm):	L (μm):	G (μm):
B	70	11	50	9
Variable 3	P (μm):	B (μm):	L (μm):	G (μm):
B_2	70	8	50	9

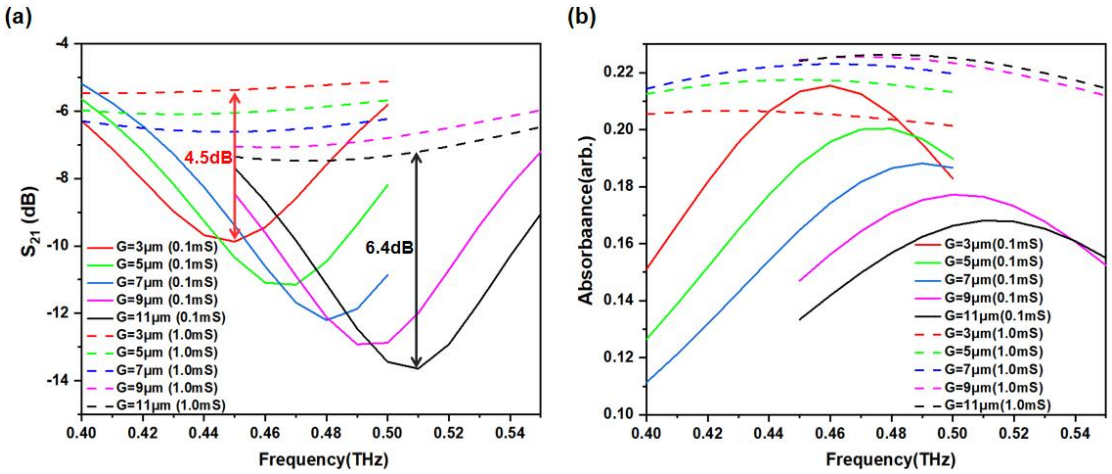

Figure S3 (a) The $S_{21,}$ and (b) absorbance simulations of No.2 array with a frequency step of 0.01THz by changing ***G*** values under the conditions of σ_{DC-g}=0.1 and 1.0mS.

Table S-6 The Q-factors of No.2 SRR array with different ***G*** values.

G (μm):	3	5	7	9	11
Q-factor:	5.0	4.9	4.6	4.4	4.2

Figures S3 (a-b) show the typical S_{21} and absorbance changes of varying ***G*** values from 3 μm to 11 μm with a 2 μm step under graphene conductance of 0.1 and 1 mS, indicating the lowest and highest doping could be achieved in the experiment. As depicted in Figure S3 (a), each incremental step in ***G*** induces a blue shift of approximately 0.015 THz in the resonance dip along with an approximate visibility increase of 1dB. Moreover, the modulation disparities at the central frequencies also expand, ranging from 4.5dB at ***G***=3 μm to 6.4dB at ***G***=11 μm.

As elucidated in Figure S3 (b), the absorbance variations manifest in a complex manner compared to the S_{21} spectra. For **G** set at 3 μm, the modulator exhibits a pronounced absorbance of 21.5 % at its eigenfrequency of 0.46 THz when the σ_{DC-g} is 0.1 mS. However, as **G** is widened from 3 μm to 11 μm, the absorbance of the modulator, with σ_{DC-g} of 0.1 mS, consistently diminishes from 21.5 % down to 16.6 %. On the other hand, the absorbance with a σ_{DC-g} of 1.0 mS exhibits an opposite trajectory, enhancing its peak value from 20.5 % to 22.5 %. This counteractive behavior underscores the inherent trade-off between pronounced light-matter interaction and superior optical absorption by graphene, as previously alluded to.

Moreover, the Q-factors of the resonances, corresponding to various gap distances ***G***, as delineated in Table S-6, further substantiate this hypothesis. As elaborated in Appendix A1, the Q-factor serves as an imperative metric indicative of a resonator's energy dissipation characteristics. A reduction in ***G*** from 11 μm to 3 μm amplifies the Q-factor of the SRR resonance from 4.2 to 5.0, manifesting higher energy retention within the SRR bearing a smaller gap. It's noteworthy that the apex of absorbance enhancement plateaus at ***G***=9 μm. Given that the modulator is tailored for high harmonic generation experiments, which hinge profoundly on the light-matter synergy furnished by the metamaterial, the ultimate ***G*** value is judiciously selected as 9 μm. This optimises a confluence of robust optical absorption and commendable light-matter interaction potency consistently diminishes from 21.5 % down to 16.6 %.

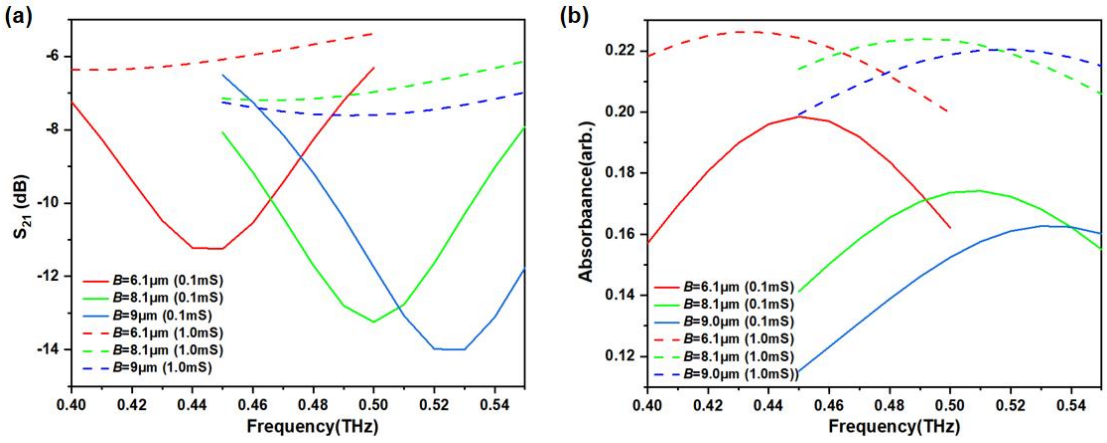

Figure S4 (a) The S_{21}, and (b) absorbance simulations of No.2 SRR array with a frequency step of 0.01 THz by changing ***B*** values under the conditions of σ_{DC-g}=0.1 and 1.0 mS.

Upon finalizing the ***G*** value, further simulations were conducted to discern the implications of altering ***B***. Figures S4 (a-b) elucidate the S_{21} and absorbance spectra, derived from the parameters delineated in the variable 2 sets, as listed in Table S-5, and juxtaposed against varying ***B*** values. An evident blue shift in the central resonance frequency, accompanied by a consistent augmentation in visibility, is discernible as ***B*** values increment from 6 μm to 9 μm, applicable for both 0.1 mS and 1 mS graphene conductance, as revealed in the S_{21} spectra. Concurrently, the utmost differential in S_{21} modulation swells from 5.2 dB to 6.5 dB over this spectrum. This trend can be attributed to the more pronounced absorption disparity, as Figure S4 (b) depicts.

It's noteworthy that at $\sigma_{g(THz)}$ =0.1 mS, the modulator displays an augmented absorbance for reduced **B** values, indicative of the intensified light-matter interplay of the system. Yet, at σ_{DC-g} =1.0 mS, although the minimal **B** value (6.1 μm) still manifests the maximal absorbance, the discrepancies between these metrics are considerably attenuated. In light of the impending high-field THz-TDS evaluations, detailed in Chapter 7, absorbance isn't the sole determinant of the experimental results. The visibility of the S_{21} resonance plays an instrumental role, especially in guiding the THz beam alignment onto the designated array. Thus, a **B** value of 8μm is judiciously chosen to strike an equilibrium, ensuring a confluence of commendable visibility and satisfactory absorbance.

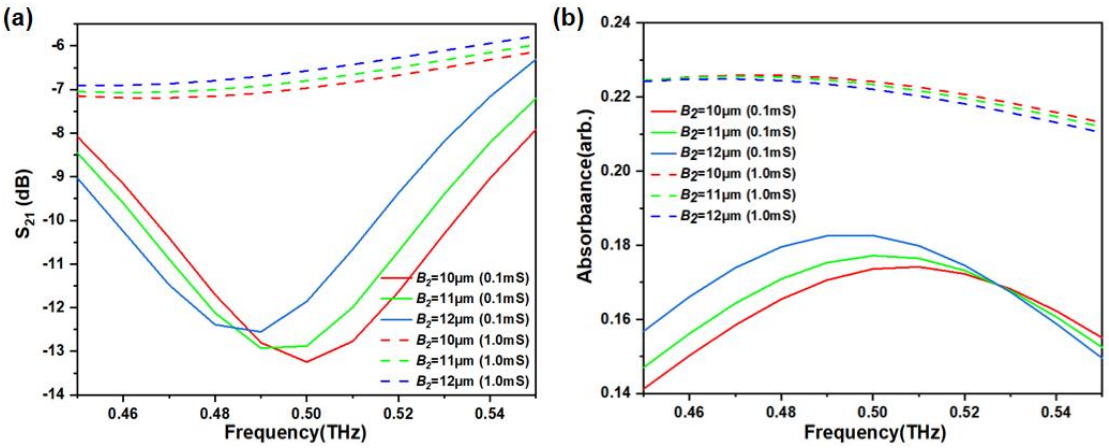

Figure S5 (a) The S_{21}, and (b) absorbance simulations of No.2 SRR array with a frequency step of 0.01 THz by changing $\mathbf{B_2}$ values under the conditions of σ_{DC-g}=0.1 and 1.0 mS.

The final parameter influencing the modulator's performance is denoted as $\mathbf{B_2}$. Figures S5 (a-b) elucidate the S_{21} and absorbance spectra, contingent upon varying $\mathbf{B_2}$ values, utilizing the parameters delineated under variable 3 in Table S-5. An increment in $\mathbf{B_2}$ from 10 μm to 12 μm marginally diminishes the S_{21} visibility by approximately 1dB, concurrently instigating a red shift of 0.015 THz in the resonance's central frequency, given σ_{DC-g}=0.1 mS. This decrement in visibility parallels an augmentation in absorbance by about 1%, as depicted in Figure S5 (b). Interestingly, both the S_{21} and absorbance spectra exhibit diminished sensitivity to variations in $\mathbf{B_2}$ when σ_{DC-g}=1 mS. Within the 0.45-0.55 THz band, alterations in the S_{21} spectrum in response to the modulation in $\mathbf{B_2}$ remain subsumed within 0.5 dB, and the absorbance remains predominantly static. Adhering to the precedent of prioritizing visibility,

as delineated in the preceding section, a value of B_2=10μm is deemed optimal.

A3. Supportive information of Chapter 6

A3.1 Q factor evaluation

There is a clear difference in both the spectral amplitude and Q-factor of the three resonators. The time-domain information from the individual resonances allows us to directly extract the resonance Q- factor using the single harmonic oscillation (SHO) model 1. The classic SHO time domain waveform y(t) is:

$$y(t) = \alpha e^{-\gamma t}\cos(\omega t - \varphi) \tag{S1}$$

Where α is amplitude, γ is decay rate, ω is the natural frequency of the oscillation. The Q-factor of the oscillation can be evaluated by:

$$Q = \frac{1}{2\xi} \tag{S2}$$

Where ξ is the damping ratio, it can be expressed as:

$$\xi = \frac{\gamma}{\omega} \tag{S3}$$

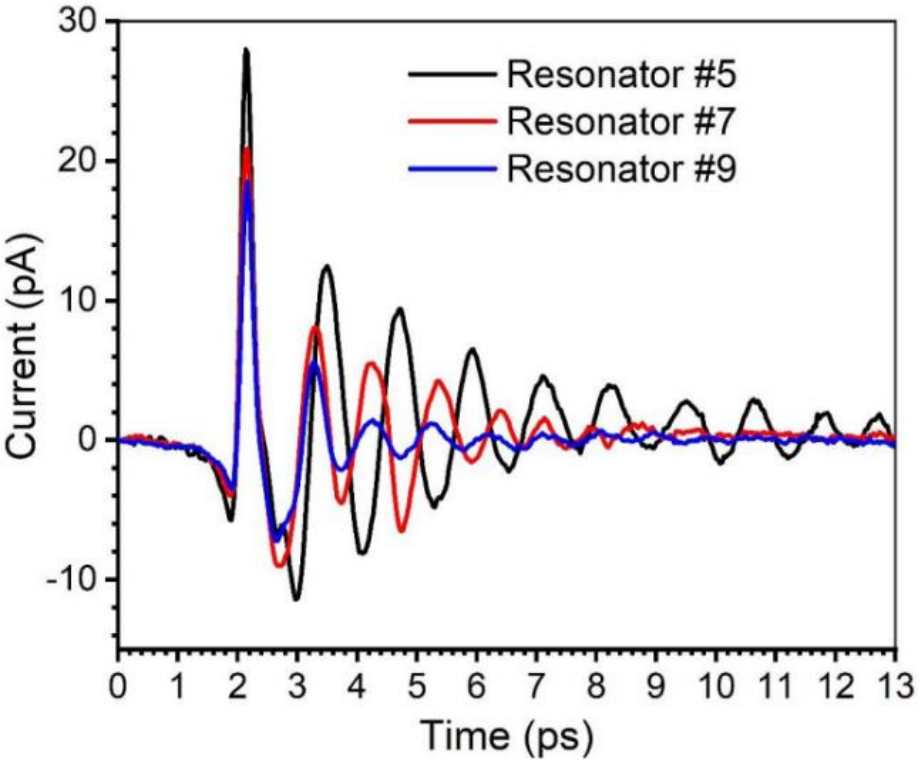

Figure S6 Time-domain near-field waveform acquired at the center of resonator 5, 7 and 9.

The experimental result and its exponential fitting of the resonator 5 are shown in Fig. 2(a), evaluating a Q-value of 11 ± 1 based on equations (S1-S3). The fitting procedure was performed without taking into consideration the first oscillation maximum in the E-field temporal waveform. Time-domain near-field waveforms acquired at the position specified in Figure 6.3 (b) for resonators 5, 7 and 9 are reported in Figure S6 for completeness. The relative Fourier Transformed spectra are shown in the main text in Figure 6.3 (b)).

A3.2 Mode A simulations of Res.5, 7, and 9

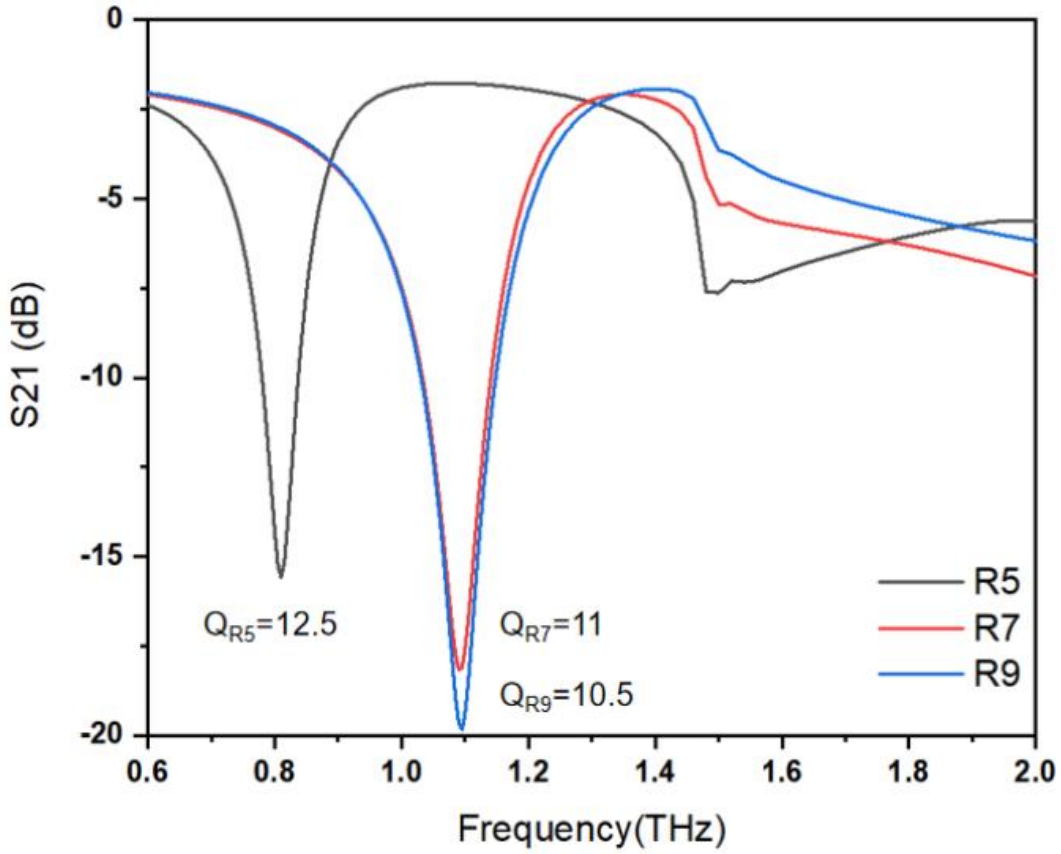

Figure S7 The S_{21} simulation of three different resonators (resonators 5,7 and 9) in the 90° polarized incident. The near-field experimental results show a minimal red shift in the central frequency compared to the simulations.

A4. Supportive information of Chapter 7

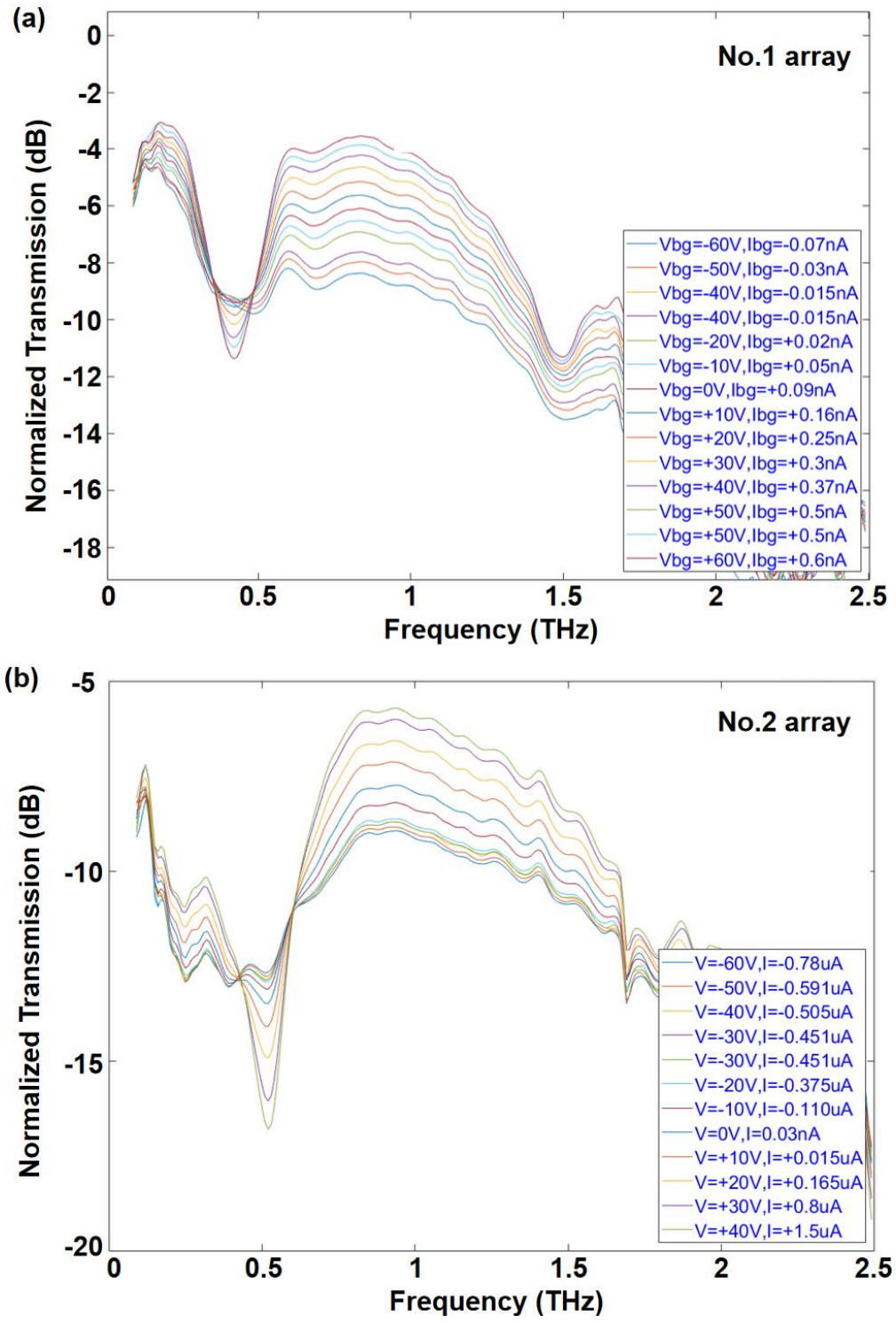

Figure S8 (a-b) THz TDS measured S_{21} spectra of the No.1 and No.2 arrays introduced in Chapter 4 with different bias voltages.

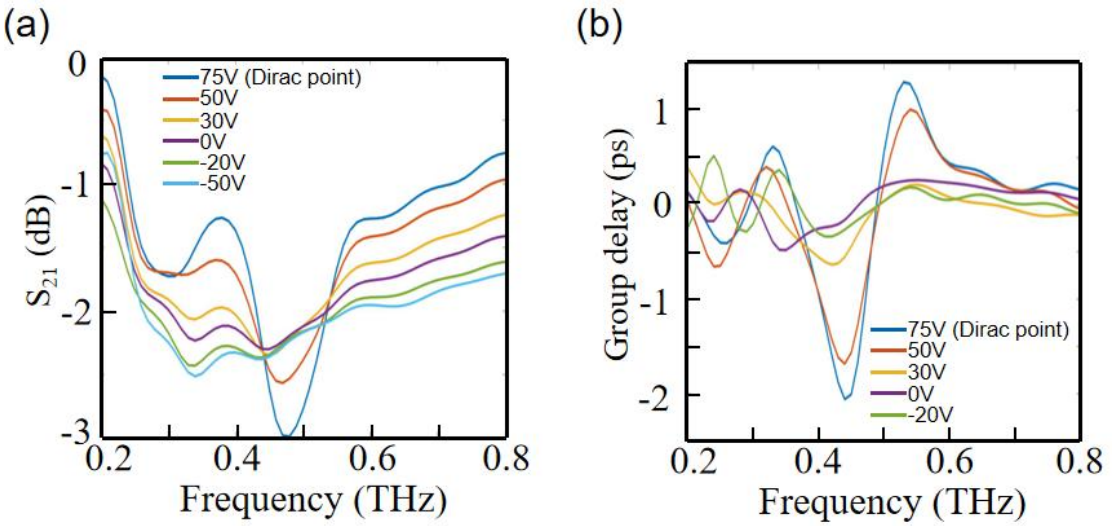

Figure S9 The two-resonance array's (a) S_{21} spectra and (b) time delay evaluated by THz TDS with different applied bias.

Figure S9 (a) presents the S_{21} spectra of the two-resonance array, as examined through the Menlo system, previously introduced in Chapters 4 and 5. While the resonance frequencies from the experimental results align closely with the simulations, there is a discernible reduction in visibility by 3 dB at the Dirac point. This discrepancy can be attributed to a decrease in the Drude scattering time, as represented in equation 4.12. Such an alteration can result from impurities trapped at the interface between the graphene and the substrate. These impurities can introduce higher Ohmic losses, thereby affecting the conductivity of the graphene. This phenomenon is likely to explain the observed disparity between the simulation and the experimental results. Additionally, Figure S9 (b) depicts the adjustable group delay of the two-resonance array under various bias voltages. The group delay, represented as Δt_g, is defined as: $\Delta t_g = \Delta\varphi/\Delta\omega$ [172], where φ is phase, ascertainable from the Menlo measurements and ω is the angular frequency. By modulating the applied voltage within a range of 75 V to -20 V, a shift in the group delay of 1.5 ps at 0.45 THz is observable. This device's tunable dispersion properties surpass the design shown in Figure 4.14 by almost five-fold. Such versatility renders the device well-suited for slow light applications, particularly in the domains of communication and spectroscopy.

References

[1] Tonouchi, M., 2007. Cutting-edge terahertz technology. *Nature photonics*, *1*(2), pp.97-105.

[2] Burford, N.M. and El-Shenawee, M.O., 2017. Review of terahertz photoconductive antenna technology. *Optical Engineering*, *56*(1), pp.010901-010901.

[3] Rice, A., Jin, Y., Ma, X.F., Zhang, X.C., Bliss, D., Larkin, J. and Alexander, M., 1994. Terahertz optical rectification from< 110> zinc-blende crystals. *Applied physics letters*, *64*(11), pp.1324-1326.

[4] Karpowicz, N., Zhong, H., Xu, J., Lin, K.I., Hwang, J.S. and Zhang, X.C., 2005, March. Non-destructive sub-THz CW imaging. In *Terahertz and Gigahertz Electronics and Photonics IV* (Vol. 5727, pp. 132-142). SPIE.

[5] Wietzke, S., Jördens, C., Krumbholz, N., Baudrit, B., Bastian, M. and Koch, M., 2007. Terahertz imaging: a new non-destructive technique for the quality control of plastic weld joints. *Journal of the European Optical Society-Rapid Publications*, *2*.

[6] Zimdars, D., Valdmanis, J.A., White, J.S., Stuk, G., Williamson, S., Winfree, W.P. and Madaras, E.I., 2005, April. Technology and applications of terahertz imaging non-destructive examination: inspection of space shuttle sprayed on foam insulation. In *AIP conference proceedings* (Vol. 760, No. 1, pp. 570-577). American Institute of Physics.

[7] Oyama, Y., Zhen, L., Tanabe, T. and Kagaya, M., 2009. Sub-terahertz imaging of defects in building blocks. *Ndt & E International*, *42*(1), pp.28-33.

[8] Dufour, D., Marchese, L., Terroux, M., Oulachgar, H., Généreux, F., Doucet, M., Mercier, L., Tremblay, B., Alain, C., Beaupré, P. and Blanchard, N., 2015. Review of terahertz technology development at INO. *Journal of Infrared, Millimeter, and Terahertz Waves*, *36*, pp.922-946.

[9] Koch, M., 2003. Bio-medical applications of THz imaging. In *Sensing with terahertz radiation* (pp. 295-316). Berlin, Heidelberg: Springer Berlin Heidelberg.

[10] Kleine-Ostmann, T. and Nagatsuma, T., 2011. A review on terahertz communications research. *Journal of Infrared, Millimeter, and Terahertz Waves*, *32*, pp.143-171.

[11] Cuisset, A., Hindle, F., Mouret, G., Bocquet, R., Bruckhuisen, J., Decker, J., Pienkina, A., Bray, C., Fertein, É. and Boudon, V., 2021. Terahertz rotational spectroscopy of greenhouse gases using long interaction path-lengths. *Applied Sciences*, *11*(3), p.1229.

[12] Crowe, T.W., Globus, T., Woolard, D.L. and Hesler, J.L., 2004. Terahertz sources and detectors and their application to biological sensing. *Philosophical Transactions of the Royal Society of London. Series A: Mathematical, Physical and Engineering Sciences*, *362*(1815), pp.365-377.

[13] Leahy-Hoppa, M.R., Fitch, M.J. and Osiander, R., 2009. Terahertz spectroscopy techniques for explosives detection. *Analytical and bioanalytical chemistry*, *395*, pp.247-257.

[14] Kulesa, C., 2011. Terahertz spectroscopy for astronomy: From comets to cosmology. *IEEE Transactions on Terahertz Science and Technology*, *1*(1), pp.232-240.

[15] Fiorino, S.T., Bartell, R.J., Krizo, M.J., Caylor, G.L., Moore, K.P., Harris, T.R. and Cusumano, S.J., 2008, February. A first principles atmospheric propagation & characterization tool: the laser environmental effects definition and reference (LEEDR).

In *Atmospheric Propagation of Electromagnetic Waves II* (Vol. 6878, pp. 57-68). SPIE.
[16] Armstrong, C.M., 2012. The truth about terahertz. *IEEE Spectrum*, *49*(9), pp.36-41.
[17] Abo-Bakr, M., Feikes, J., Holldack, K., Kuske, P., Peatman, W.B., Schade, U., Wüstefeld, G. and Hübers, H.W., 2003. Brilliant, coherent far-infrared (THz) synchrotron radiation. *Physical Review Letters*, *90*(9), p.094801.
[18] Walowski, J. and Münzenberg, M., 2016. Perspective: Ultrafast magnetism and THz spintronics. *Journal of Applied Physics*, *120*(14).
[19] Wei, B., 2020. *Novel applications of terahertz quantum cascade lasers: gas spectroscopy, active control & nearfield imaging* (Doctoral dissertation, University of Cambridge).
[20] Withayachumnankul, W. and Naftaly, M., 2014. Fundamentals of measurement in terahertz time-domain spectroscopy. *Journal of Infrared, Millimeter, and Terahertz Waves*, *35*, pp.610-637.
[21] Phanindra, V.E., Agarwal, P. and Rana, D.S., 2018. Terahertz spectroscopic evidence of non-Fermi-liquid-like behavior in structurally modulated PrNi O 3 thin films. *Physical Review Materials*, *2*(1), p.015001.
[22] King, M.D., Buchanan, W.D. and Korter, T.M., 2010. Investigating the anharmonicity of lattice vibrations in water-containing molecular crystals through the terahertz spectroscopy of L-serine monohydrate. *The Journal of Physical Chemistry A*, *114*(35), pp.9570-9578.
[23] Naftaly, M. and Miles, R.E., 2007. Terahertz time-domain spectroscopy for material characterization. *Proceedings of the IEEE*, *95*(8), pp.1658-1665.
[24] Zhao, D. and Chia, E.E., 2020. Free carrier, exciton, and phonon dynamics in lead-halide perovskites studied with ultrafast terahertz spectroscopy. *Advanced Optical Materials*, *8*(3), p.1900783.
[25] Ulbricht, R., Hendry, E., Shan, J., Heinz, T.F. and Bonn, M., 2011. Carrier dynamics in semiconductors studied with time-resolved terahertz spectroscopy. *Reviews of Modern Physics*, *83*(2), p.543.
[26] Joyce, H.J., Docherty, C.J., Gao, Q., Tan, H.H., Jagadish, C., Lloyd-Hughes, J., Herz, L.M. and Johnston, M.B., 2013. Electronic properties of GaAs, InAs and InP nanowires studied by terahertz spectroscopy. *Nanotechnology*, *24*(21), p.214006.
[27] Liu, Y., Zhou, T. and Cao, J.C., 2019. Terahertz spectral of enantiomers and racemic amino acids by time-domain-spectroscopy technology. *Infrared Physics & Technology*, *96*, pp.17-21.
[28] Öjefors, E., Lisauskas, A., Glaab, D., Roskos, H.G. and Pfeiffer, U.R., 2009. Terahertz imaging detectors in CMOS technology. *Journal of Infrared, Millimeter, and Terahertz Waves*, *30*, pp.1269-1280.
[29] El-Shenawee, M., Vohra, N., Bowman, T. and Bailey, K., 2019. Cancer detection in excised breast tumors using terahertz imaging and spectroscopy. *Biomedical Spectroscopy and Imaging*, *8*(1-2), pp.1-9.
[30] Zhong, S., 2019. Progress in terahertz nondestructive testing: A review. *Frontiers of Mechanical Engineering*, *14*, pp.273-281.
[31] Wang, J., Xu, T., Zhang, L., Chang, T., Zhang, J., Yan, S. and Cui, H.L., 2022. Nondestructive damage evaluation of composites based on terahertz and X-ray image fusion. *NDT & E International*, *127*, p.102616.

[32] Zimdars, D., White, J., Stuk, G., Chernovsky, A., Fichter, G. and Williamson, S.L., 2006, May. Time domain terahertz detection of concealed threats in luggage and personnel. In *Terahertz for Military and Security Applications IV* (Vol. 6212, pp. 188-192). SPIE.

[33] Liu, J.Y., Huang, T.J. and Liu, P.K., 2018. Terahertz super-resolution imaging using four-wave mixing in graphene. *Optics Letters*, *43*(9), pp.2102-2105.

[34] Wahlstrand, J.K. and Heilweil, E.J., 2018. Contactless THz-based bulk semiconductor mobility measurements using two-photon excitation. *Optics express*, *26*(23), pp.29848-29853.

[35] Chan, W.L., Charan, K., Takhar, D., Kelly, K.F., Baraniuk, R.G. and Mittleman, D.M., 2008. A single-pixel terahertz imaging system based on compressed sensing. *Applied Physics Letters*, *93*(12).

[36] Rong, L., Latychevskaia, T., Wang, D., Zhou, X., Huang, H., Li, Z. and Wang, Y., 2014. Terahertz in-line digital holography of dragonfly hindwing: amplitude and phase reconstruction at enhanced resolution by extrapolation. *Optics Express*, *22*(14), pp.17236-17245.

[37] Long, Z., Wang, T., You, C., Yang, Z., Wang, K. and Liu, J., 2019. Terahertz image super-resolution based on a deep convolutional neural network. *Applied optics*, *58*(10), pp.2731-2735.

[38] Mittleman, D.M., 2018. Twenty years of terahertz imaging. *Optics express*, *26*(8), pp.9417-9431.

[39] Cragg, G.E. and So, P.T., 2000. Lateral resolution enhancement with standing evanescent waves. *Optics letters*, *25*(1), pp.46-48.

[40] Oheim, M., Loerke, D., Chow, R.H. and Stühmer, W., 1999. Evanescent-wave microscopy: a new tool to gain insight into the control of transmitter release. *Philosophical Transactions of the Royal Society of London. Series B: Biological Sciences*, *354*(1381), pp.307-318.

[41] Betzig, E., Isaacson, M. and Lewis, A., 1987. Collection mode near-field scanning optical microscopy. *Applied physics letters*, *51*(25), pp.2088-2090.

[42] Hale, L.L., Wang, Z., Harris, C.T., Brener, I., Law, S. and Mitrofanov, O., 2023. Near-field spectroscopy of Dirac plasmons in Bi2Se3 ribbon arrays. APL Photonics, 8(5).

[43] Degl'Innocenti, R., Wallis, R., Wei, B., Xiao, L., Kindness, S.J., Mitrofanov, O., Braeuninger-Weimer, P., Hofmann, S., Beere, H.E. and Ritchie, D.A., 2017. Terahertz nanoscopy of plasmonic resonances with a quantum cascade laser. *ACS Photonics*, *4*(9), pp.2150-2157.

[44] Lin, H., Fischer, B.M., Mickan, S.P. and Abbott, D., 2007. Review of THz near-field methods. *Smart Structures, Devices, and Systems III*, *6414*, pp.144-151.

[45] Micek, P., Gric, T. and Pudis, D., 2022, December. Near-field probe emission focused by hyperbolic metamaterial. In *22nd Polish-Slovak-Czech Optical Conference on Wave and Quantum Aspects of Contemporary Optics* (Vol. 12502, pp. 126-135). SPIE.

[46] Wang, N., Zhang, X., Liang, J., Chang, T. and Cui, H.L., 2020. Novel configuration of aperture-type terahertz near-field imaging probe. *Journal of Physics D: Applied Physics*, *53*(29), p.295102.

[47] Zenhausern, F., O'boyle, M.P. and Wickramasinghe, H.K., 1994. Apertureless near-field optical microscope. *Applied Physics Letters*, *65*(13), pp.1623-1625.

[48] Schnell, M., Carney, P.S. and Hillenbrand, R., 2014. Synthetic optical holography for

rapid nanoimaging. *Nature communications*, *5*(1), p.3499.
[49] Deutsch, B., Schnell, M., Hillenbrand, R. and Carney, P.S., 2014. Synthetic optical holography with nonlinear-phase reference. *Optics Express*, *22*(22), pp.26621-26634.
[50] Ocelic, N., Huber, A. and Hillenbrand, R., 2006. Pseudoheterodyne detection for background-free near-field spectroscopy. *Applied Physics Letters*, *89*(10).
[51] Smith, D.R., Pendry, J.B. and Wiltshire, M.C., 2004. Metamaterials and negative refractive index. *science*, *305*(5685), pp.788-792.
[52] Fang, N., Lee, H., Sun, C. and Zhang, X., 2005. Sub-diffraction-limited optical imaging with a silver superlens. *science*, *308*(5721), pp.534-537.
[53] Smolyaninov, I.I., Hung, Y.J. and Davis, C.C., 2007. Magnifying superlens in the visible frequency range. *science*, *315*(5819), pp.1699-1701.
[54] Zhang, X. and Liu, Z., 2008. Superlenses to overcome the diffraction limit. *Nature materials*, *7*(6), pp.435-441.
[55] Rogers, E.T., Lindberg, J., Roy, T., Savo, S., Chad, J.E., Dennis, M.R. and Zheludev, N.I., 2012. A super-oscillatory lens optical microscope for subwavelength imaging. *Nature materials*, *11*(5), pp.432-435.
[56] Landy, N.I., Sajuyigbe, S., Mock, J.J., Smith, D.R. and Padilla, W.J., 2008. Perfect metamaterial absorber. *Physical review letters*, *100*(20), p.207402.
[57] Tao, H., Landy, N.I., Bingham, C.M., Zhang, X., Averitt, R.D. and Padilla, W.J., 2008. A metamaterial absorber for the terahertz regime: design, fabrication and characterization. *Optics express*, *16*(10), pp.7181-7188.
[58] Liu, N., Mesch, M., Weiss, T., Hentschel, M. and Giessen, H., 2010. Infrared perfect absorber and its application as plasmonic sensor. *Nano letters*, *10*(7), pp.2342-2348.
[59] Watts, C.M., Liu, X. and Padilla, W.J., 2012. Metamaterial electromagnetic wave absorbers. *Advanced materials*, *24*(23), pp.OP98-OP120.
[60] Pendry, J.B., Schurig, D. and Smith, D.R., 2006. Controlling electromagnetic fields. *science*, *312*(5781), pp.1780-1782.
[61] Schurig, D., Mock, J.J., Justice, 1.B., Cummer, S.A., Pendry, J.B., Starr, A.F. and Smith, D.R., 2006. Metamaterial electromagnetic cloak at microwave frequencies. *Science*, *314*(5801), pp.977-980.
[62] Cai, W., Chettiar, U.K., Kildishev, A.V. and Shalaev, V.M., 2007. Optical cloaking with metamaterials. *Nature photonics*, *1*(4), pp.224-227.
[63] Liu, R., Ji, C., Mock, J.J., Chin, J.Y., Cui, T.J. and Smith, D.R., 2009. Broadband ground-plane cloak. *Science*, *323*(5912), pp.366-369.
[64] Yamada, I., Takano, K., Hangyo, M., Saito, M. and Watanabe, W., 2009. Terahertz wire-grid polarizers with micrometer-pitch Al gratings. *Optics letters*, *34*(3), pp.274-276.
[65] Han, Z., Ohno, S., Tokizane, Y., Nawata, K., Notake, T., Takida, Y. and Minamide, H., 2018. Off-resonance and in-resonance metamaterial design for a high-transmission terahertz-wave quarter-wave plate. *Optics letters*, *43*(12), pp.2977-2980.
[66] Yang, Q., Gu, J., Wang, D., Zhang, X., Tian, Z., Ouyang, C., Singh, R., Han, J. and Zhang, W., 2014. Efficient flat metasurface lens for terahertz imaging. *Optics express*, *22*(21), pp.25931-25939.
[67] Wen, Q.Y., Zhang, H.W., Yang, Q.H., Xie, Y.S., Chen, K. and Liu, Y.L., 2010. Terahertz metamaterials with VO2 cut-wires for thermal tunability. *Applied physics letters*, *97*(2).

[68] Wang, S., Kang, L. and Werner, D.H., 2017. Hybrid resonators and highly tunable terahertz metamaterials enabled by vanadium dioxide (VO2). *Scientific reports*, *7*(1), p.4326.
[69] Savo, S., Shrekenhamer, D. and Padilla, W.J., 2014. Liquid crystal metamaterial absorber spatial light modulator for THz applications. *Advanced optical materials*, *2*(3), pp.275-279.
[70] Yang, L., Fan, F., Chen, M., Zhang, X. and Chang, S.J., 2017. Active terahertz metamaterials based on liquid-crystal induced transparency and absorption. *Optics Communications*, *382*, pp.42-48.
[71] Zaman, A.M., Lu, Y., Romain, X., Almond, N.W., Burton, O.J., Alexander-Webber, J., Hofmann, S., Mitchell, T., Griffiths, J.D., Beere, H.E. and Ritchie, D.A., 2022. Terahertz metamaterial optoelectronic modulators with GHz reconfiguration speed. *IEEE Transactions on Terahertz Science and Technology*, *12*(5), pp.520-526.
[72] Kindness, S.J., Almond, N.W., Michailow, W., Wei, B., Delfanazari, K., Braeuninger-Weimer, P., Hofmann, S., Beere, H.E., Ritchie, D.A. and Degl'Innocenti, R., 2020. A terahertz chiral metamaterial modulator. *Advanced Optical Materials*, *8*(21), p.2000581.
[73] Ju, L., Geng, B., Horng, J., Girit, C., Martin, M., Hao, Z., Bechtel, H.A., Liang, X., Zettl, A., Shen, Y.R. and Wang, F., 2011. Graphene plasmonics for tunable terahertz metamaterials. *Nature nanotechnology*, *6*(10), pp.630-634.
[74] Degl'Innocenti, R., Xiao, L., Jessop, D.S., Kindness, S.J., Ren, Y., Lin, H., Zeitler, J.A., Alexander-Webber, J.A., Joyce, H.J., Braeuninger-Weimer, P. and Hofmann, S., 2016. Fast room-temperature detection of terahertz quantum cascade lasers with graphene-loaded bow-tie plasmonic antenna arrays. *Acs Photonics*, *3*(10), pp.1747-1753.
[75] Wang, X., Jiang, X., You, Q., Guo, J., Dai, X. and Xiang, Y., 2017. Tunable and multichannel terahertz perfect absorber due to Tamm surface plasmons with graphene. *Photonics Research*, *5*(6), pp.536-542.
[76] Rout, S. and Sonkusale, S.R., 2016. A low-voltage high-speed terahertz spatial light modulator using active metamaterial. *Apl Photonics*, *1*(8).
[77] Lee, S.H., Choi, M., Kim, T.T., Lee, S., Liu, M., Yin, X., Choi, H.K., Lee, S.S., Choi, C.G., Choi, S.Y. and Zhang, X., 2012. Switching terahertz waves with gate-controlled active graphene metamaterials. *Nature materials*, *11*(11), pp.936-941.
[78] Chen, H.T., Yang, H., Singh, R., O'Hara, J.F., Azad, A.K., Trugman, S.A., Jia, Q.X. and Taylor, A.J., 2010. Tuning the resonance in high-temperature superconducting terahertz metamaterials. *Physical review letters*, *105*(24), p.247402.
[79] Singh, R., Xiong, J., Azad, A.K., Yang, H., Trugman, S.A., Jia, Q.X., Taylor, A.J. and Chen, H.T., 2012. Optical tuning and ultrafast dynamics of high-temperature superconducting terahertz metamaterials. *Nanophotonics*, *1*(1), pp.117-123.
[80] Beard, M.C., Turner, G.M. and Schmuttenmaer, C.A., 2002. Terahertz spectroscopy. *The Journal of Physical Chemistry B*, *106*(29), pp.7146-7159.
[81] Dexheimer, S.L. ed., 2017. *Terahertz spectroscopy: principles and applications*. CRC press.
[82] Nuss, M.C. and Orenstein, J., 2007. Terahertz time-domain spectroscopy. *Millimeter and submillimeter wave spectroscopy of solids*, pp.7-50.
[83] Burford, N.M. and El-Shenawee, M.O., 2017. Review of terahertz photoconductive

antenna technology. *Optical Engineering*, *56*(1), pp.010901-010901.
[84] Fülöp, J.A., Pálfalvi, L., Klingebiel, S., Almási, G., Krausz, F., Karsch, S. and Hebling, J., 2012. Generation of sub-mJ terahertz pulses by optical rectification. *Optics letters*, *37*(4), pp.557-559.
[85] Benicewicz, P.K., Roberts, J.P. and Taylor, A.J., 1994. Scaling of terahertz radiation from large-aperture biased photoconductors. *JOSA B*, *11*(12), pp.2533-2546.
[86] Zhang, J., Hong, Y., Braunstein, S.L. and Shore, K.A., 2004. Terahertz pulse generation and detection with LT-GaAs photoconductive antenna. *IEE Proceedings-Optoelectronics*, *151*(2), pp.98-101.
[87] Smith, P.R., Auston, D.H. and Nuss, M.C., 1988. Subpicosecond photoconducting dipole antennas. *IEEE Journal of Quantum Electronics*, *24*(2), pp.255-260.
[88] Liu, T.A., Tani, M., Nakajima, M., Hangyo, M., Sakai, K., Nakashima, S.I. and Pan, C.L., 2004. Ultrabroadband terahertz field detection by proton-bombarded InP photoconductive antennas. *Optics express*, *12*(13), pp.2954-2959.
[89] Lee, Y.S., 2009. *Principles of terahertz science and technology* (Vol. 170). Springer Science & Business Media.
[90] Ravi, K., Huang, W.R., Carbajo, S., Nanni, E.A., Schimpf, D.N., Ippen, E.P. and Kärtner, F.X., 2015. Theory of terahertz generation by optical rectification using tilted-pulse-fronts. *Optics express*, *23*(4), pp.5253-5276.
[91] Jin, Y.H. and Zhang, X.C., 1995. Terahertz optical rectification. *Journal of Nonlinear Optical Physics & Materials*, *4*(02), pp.459-495.
[92] Kawase, K., Sato, M., Taniuchi, T. and Ito, H., 1996. Coherent tunable THz-wave generation from LiNbO3 with monolithic grating coupler. *Applied Physics Letters*, *68*(18), pp.2483-2485.
[93] Vidal, S., Degert, J., Tondusson, M., Freysz, E. and Oberlé, J., 2014. Optimized terahertz generation via optical rectification in ZnTe crystals. *JOSA B*, *31*(1), pp.149-153.
[94] Vodopyanov, K.L., Fejer, M.M., Yu, X., Harris, J.S., Lee, Y.S., Hurlbut, W.C., Kozlov, V.G., Bliss, D. and Lynch, C., 2006. Terahertz-wave generation in quasi-phase-matched GaAs. *Applied Physics Letters*, *89*(14).
[95] Tanabe, T., Suto, K., Nishizawa, J.I. and Sasaki, T., 2003. Characteristics of terahertz-wave generation from GaSe crystals. *Journal of Physics D: Applied Physics*, *37*(2), p.155.
[96] Wu, Q. and Zhang, X.C., 1995. Free-space electro-optic sampling of terahertz beams. *Applied Physics Letters*, *67*(24), pp.3523-3525.
[97] Siegel, P.H., Terahertz Pioneer: Daniel R. Grischkowsky.
[98] Neu, J. and Schmuttenmaer, C.A., 2018. Tutorial: An introduction to terahertz time domain spectroscopy (THz-TDS). *Journal of Applied Physics*, *124*(23).
[99] Soref, R.A. and Bennett, B.R., 1987, March. Kramers-Kronig analysis of electro-optical switching in silicon. In *Integrated Optical Circuit Engineering IV* (Vol. 704, pp. 32-37). SPIE.
[100] Shiino, T., Shiba, S., Sakai, N., Yamakura, T., Jiang, L., Uzawa, Y., Maezawa, H. and Yamamoto, S., 2010. Improvement of the critical temperature of superconducting NbTiN and NbN thin films using the AlN buffer layer. *Superconductor Science and Technology*, *23*(4), p.045004.
[101] Dorney, T.D., Baraniuk, R.G. and Mittleman, D.M., 2001. Material parameter

estimation with terahertz time-domain spectroscopy. *JOSA A*, *18*(7), pp.1562-1571.
[102] Van Exter, M., Fattinger, C. and Grischkowsky, D., 1989. Terahertz time-domain spectroscopy of water vapor. *Optics letters*, *14*(20), pp.1128-1130.
[103] Zarepour, E., Hassan, M., Chou, C.T. and Warkiani, M.E., 2016. Characterizing terahertz channels for monitoring human lungs with wireless nanosensor networks. *Nano communication networks*, *9*, pp.43-57.
[104] Araki, M., Tabata, Y., Shimizu, N. and Matsuyama, K., 2019. Terahertz spectroscopy of CO and NO: The first step toward temperature and concentration detection for combustion gases in fire environments. *Journal of Molecular Spectroscopy*, *361*, pp.34-39.
[105] Withayachumnankul, W. and Naftaly, M., 2014. Fundamentals of measurement in terahertz time-domain spectroscopy. *Journal of Infrared, Millimeter, and Terahertz Waves*, *35*, pp.610-637.
[106] Huang, S., Ashworth, P.C., Kan, K.W., Chen, Y., Wallace, V.P., Zhang, Y.T. and Pickwell-MacPherson, E., 2009. Improved sample characterization in terahertz reflection imaging and spectroscopy. *Optics express*, *17*(5), pp.3848-3854.
[107] Pai, A.R., Lu, Y., Joseph, S., Santhosh, N.M., Degl'Innocenti, R., Lin, H., Letizia, R., Paoloni, C. and Thomas, S., 2023. Ultra-broadband shielding of cellulose nanofiber commingled biocarbon functional constructs: a paradigm shift towards sustainable terahertz absorbers. *Chemical Engineering Journal*, *467*, p.143213.
[108] Lu, Y., Zhu, H., Zaman, A.M., Rennie, A.E., Lin, H., Tian, Y. and Degl'Innocenti, R., 2023. Contactless 3D surface characterization of additive manufactured metallic components using terahertz time-domain spectroscopy. *Optical Materials Express*, *13*(9), pp.2513-2525.
[109] Zhang, Z., Zhou, M., Zhang, T., Yang, M., Yang, Q., Yu, J. and Zhang, Y., 2020. Few-layer borophene prepared by mechanical resonance and its application in terahertz shielding. ACS applied materials & interfaces, 12(17), pp.19746-19754.
[110] Li, G., Amer, N., Hafez, H.A., Huang, S., Turchinovich, D., Mochalin, V.N., Hegmann, F.A. and Titova, L.V., 2019. Dynamical control over terahertz electromagnetic interference shielding with 2d ti3c2t y mxene by ultrafast optical pulses. Nano letters, 20(1), pp.636-643.
[111] Lin, Z., Liu, J., Peng, W., Zhu, Y., Zhao, Y., Jiang, K., Peng, M. and Tan, Y., 2020. Highly stable 3D Ti3C2T x MXene-based foam architectures toward high-performance terahertz radiation shielding. ACS nano, 14(2), pp.2109-2117..
[112] Choi, G., Shahzad, F., Bahk, Y.M., Jhon, Y.M., Park, H., Alhabeb, M., Anasori, B., Kim, D.S., Koo, C.M., Gogotsi, Y. and Seo, M., 2018. Enhanced terahertz shielding of MXenes with nano‐metamaterials. Advanced Optical Materials, 6(5), p.1701076.
[113] Huang, Z., Chen, H., Xu, S., Chen, L.Y., Huang, Y., Ge, Z., Ma, W., Liang, J., Fan, F., Chang, S. and Chen, Y., 2018. Graphene‐Based Composites Combining Both Excellent Terahertz Shielding and Stealth Performance. Advanced Optical Materials, 6(23), p.1801165..
[114] Venkatachalam, S., Bertin, D., Ducournau, G., Lampin, J.F. and Hourlier, D., 2016. Kapton-derived carbon as efficient terahertz absorbers. Carbon, 100, pp.158-164.
[115] Polley, D., Barman, A. and Mitra, R.K., 2014. EMI shielding and conductivity of carbon nanotube-polymer composites at terahertz frequency. Optics Letters, 39(6), pp.1541-1544.
[116] Agnandji, E.N., Vigneras, V., Miane, J.L. and Mounaix, P., 2007. Shielding effectiveness in terahertz domain of monolayer-doped polyaniline films. Electronics Letters,

43(23), p.1.
[117] Braniste, T., Zhukov, S., Dragoman, M., Alyabyeva, L., Ciobanu, V., Aldrigo, M., Dragoman, D., Iordanescu, S., Shree, S., Raevschi, S. and Adelung, R., 2019. Terahertz shielding properties of aero-GaN. Semiconductor Science and Technology, 34(12), p.12LT02.
[118] Rubab, N., Mumtaz, M., Zakria, M., Ahmad, I., Khan, S.D., Shahzada, S. and Raffi, M., 2021. Studies on electromagnetic wave absorption characteristics of PMMA-CNF nanocomposite films in terahertz frequency range. Applied Physics A, 127, pp.1-8.
[119] Naseer, A., Mumtaz, M., Raffi, M., Ahmad, I., Khan, S.D., Shakoor, R.I. and Shahzada, S., 2019. Reinforcement of electromagnetic wave absorption characteristics in PVDF-PMMA nanocomposite by intercalation of carbon nanofibers. Electronic Materials Letters, 15, pp.201-207..
[120] Zhao, D., Zhu, Y., Cheng, W., Chen, W., Wu, Y. and Yu, H., 2021. Cellulose-based flexible functional materials for emerging intelligent electronics. *Advanced materials*, *33*(28), p.2000619.
[121] Seddiqi, H., Oliaei, E., Honarkar, H., Jin, J., Geonzon, L.C., Bacabac, R.G. and Klein-Nulend, J., 2021. Cellulose and its derivatives: Towards biomedical applications. *Cellulose*, *28*(4), pp.1893-1931.
[122] Gopakumar, D.A., Pai, A.R., Pottathara, Y.B., Pasquini, D., Carlos de Morais, L., Luke, M., Kalarikkal, N., Grohens, Y. and Thomas, S., 2018. Cellulose nanofiber-based polyaniline flexible papers as sustainable microwave absorbers in the X-band. *ACS applied materials & interfaces*, *10*(23), pp.20032-20043.
[123] Aslam, M.A., Ding, W., ur Rehman, S., Hassan, A., Bian, Y., Liu, Q. and Sheng, Z., 2021. Low cost 3D bio-carbon foams obtained from wheat straw with broadened bandwidth electromagnetic wave absorption performance. *Applied Surface Science*, *543*, p.148785.
[124] Jansen, C., Priebe, S., Moller, C., Jacob, M., Dierke, H., Koch, M. and Kurner, T., 2011. Diffuse scattering from rough surfaces in THz communication channels. IEEE Transactions on Terahertz Science and Technology, 1(2), pp.462-472..
[125] M. Yakout, M. Elbestawi, and S. C. Veldhuis, “Density and mechanical properties in selective laser melting of Invar 36 and stainless steel 316 L,” J. Mater. Process. Technol. 266, 397–420 (2019).
[126] C. M. B. Ho, S. H. Ng, and Y.-J. Yoon, “A review on 3D printed bioimplants,” Int. J. Precis. 16(5), 1035–1046 (2015).
[127] J. Muñoz and M. Pumera, “3D-printed biosensors for electrochemical and optical applications,” Trends Analyt. Chem. 128, 115933 (2020).
[128] C. W. J. Lim, K. Q. Le, Q. Lu, and C. H. Wong, “An overview of 3-D printing in manufacturing, aerospace, and automotive industries,” IEEE Potentials 35(4), 18–22 (2016).
[129] A. E. K. Mohammad and D. Wang, “Electrochemical mechanical polishing technology: recent developments and future research and industrial needs,” Int. J. Adv. Manuf. Technol. 86(5-8), 1909–1924 (2016).
[130] W. Han and F. Fang, “Fundamental aspects and recent developments in electropolishing,” Int. J. Mach. Tools Manuf. 139, 1–23 (2019).
[131] E. Magsipoc, Q. Zhao, and G. Grasselli, “2D and 3D roughness characterization,” Rock Mech. Rock Eng. 53(3), 1495–1519 (2020).
[132] W. Durham and B. Bonner, “PEAK: A new kind of surface microscope,” Int. J. Rock

Mech. Min. 30(7), 699–702 (1993).
[133] G. Kerckhofs, G. Pyka, M. Moesen, S. Van Bael, J. Schrooten, and M. Wevers, “High-resolution microfocus X-ray computed tomography for 3D surface roughness measurements of additive manufactured porous materials,” Adv. Eng. Mater. 15(3), 153–158 (2013).
[134] R. De Oliveira, D. Albuquerque, T. Cruz, F. Yamaji, and F. Leite, Measurement of the Nanoscale Roughness by Atomic Force Microscopy: Basic Principles and Applications. Atomic Force Microscopy-imaging, Measuring and Manipulating Surfaces at the Atomic Scale, (IntechOpen, (2012).
[135] A. Hongru, L. Xiangqin, S. Shuyan, Z. Ying, and L. Tianqing, “Measurement of Wenzel roughness factor by laser scanning confocal microscopy,” RSC Adv. 7(12), 7052–7059 (2017).
[136] H. Zhu, A. Rennie, R. Li, and Y. Tian, “Two-steps electrochemical polishing of laser powder bed fusion 316 L stainless steel,” Surf. Interfaces 35, 102442 (2022).
[137] Y. Ino, J. Heroux, T. Mukaiyama, and M. Kuwata-Gonokami, “Reflection-type pulsed terahertz imaging with a phase-retrieval algorithm,” Appl. Phys. Lett. 88(4), 041114 (2006).
[138] P. U. Jepsen, “Phase retrieval in terahertz time-domain measurements: a “how to” tutorial,” J. Infrared Millim Terahertz Waves 40(4), 395–411 (2019).
[139] S. Van Frank, E. Leiss-Holzinger, M. Pfleger, and C. Rankl, “Terahertz time-domain polarimetry in reflection for film characterization,” Sensors 20(12), 3352 (2020).
[140] N. Vieweg, “Terahertz-time domain spectrometer with 90 dB peak dynamic range,” J. Infrared, Millimeter, Terahertz Waves 35(10), 823–832 (2014).
[141] E. I. Thorsos and D. R. Jackson, “The validity of the perturbation approximation for rough surface scattering using a Gaussian roughness spectrum,” J. Acoust. Soc. Am. 86(1), 261–277 (1989).
[142] P. Beckmann and A. Spizzichino, The Scattering of Electromagnetic Waves from Rough Surfaces (Artech House Publishers, 1987).
[143] R. F. Anastasi and E. I. Madaras, “Terahertz NDE for metallic surface roughness evaluation. nondestructive evaluation and health monitoring of aerospace materials, composites, and civil infrastructure,” Proc. SPIE 61760O, 61760O (2006).
[144] F. T. Ulaby, R. K. Moore, and A. K. Fung, Microwave Remote Sensing: Active and Passive: From Theory to Applications (Artech House Publishers, 1986).
[145] Naghizade, S. and Sattari-Esfahlan, S.M., 2019. Excellent quality factor ultra-compact optical communication filter on ring-shaped cavity. Journal of Optical Communications, 40(1), pp.21-25.
[146] Mohammed, N.A., Hamed, M.M., Khalaf, A.A., Alsayyari, A. and El-Rabaie, S., 2019. High-sensitivity ultra-quality factor and remarkable compact blood components biomedical sensor based on nanocavity coupled photonic crystal. Results in Physics, 14, p.102478.
[147] Tabatabaeian, Z.S., 2022. Developing THz metasurface with array rectangular slot with High Q-factor for early skin cancer detection. Optik, 264, p.169400.
[148] Kajfez, D., 2005. Q-Factor. Encyclopedia of RF and Microwave Engineering.
[149] Selesnick, I.W., 2011. Wavelet transform with tunable Q-factor. IEEE transactions on signal processing, 59(8), pp.3560-3575.
[150] Capek, M., Jelinek, L. and Vandenbosch, G.A., 2016. Stored electromagnetic energy

and quality factor of radiating structures. Proceedings of the Royal Society A: Mathematical, Physical and Engineering Sciences, 472(2188), p.20150870.
[151] Chen, C.Y., Un, I.W., Tai, N.H. and Yen, T.J., 2009. Asymmetric coupling between subradiant and superradiant plasmonic resonances and its enhanced sensing performance. Optics express, 17(17), pp.15372-15380.
[152] Bin-Alam, M.S., Reshef, O., Mamchur, Y., Alam, M.Z., Carlow, G., Upham, J., Sullivan, B.T., Ménard, J.M., Huttunen, M.J., Boyd, R.W. and Dolgaleva, K., 2021. Ultra-high-Q resonances in plasmonic metasurfaces. Nature communications, 12(1), p.974.
[153] Auguié, B. & Barnes, W. L. Collective resonances in gold nanoparticle arrays. Phys. Rev. Lett. 101, 143902 (2008).
[154] Fekete, L., Kadlec, F., Kužel, P. and Němec, H., 2007. Ultrafast opto-terahertz photonic crystal modulator. Optics letters, 32(6), pp.680-682.
[155] Zhang, H., Dunbar, L.A., Scalari, G., Houdré, R. and Faist, J., 2007. Terahertz photonic crystal quantum cascade lasers. Optics Express, 15(25), pp.16818-16827.
[156] Xie, Q., Dong, G.X., Wang, B.X. and Huang, W.Q., 2018. High-Q Fano resonance in terahertz frequency based on an asymmetric metamaterial resonator. Nanoscale research letters, 13, pp.1-7.
[157] Gupta, M. and Singh, R., 2016. Toroidal versus Fano resonances in high Q planar THz metamaterials. Advanced Optical Materials, 4(12), pp.2119-2125.
[158] Li, Z., Xiang, Y., Xu, S. and Dai, X., 2022. Ultrasensitive terahertz sensing in all-dielectric asymmetric metasurfaces based on quasi-BIC. JOSA B, 39(1), pp.286-291.
[159] Zeng, T.Y., Liu, G.D., Wang, L.L. and Lin, Q., 2021. Light-matter interactions enhanced by quasi-bound states in the continuum in a graphene-dielectric metasurface. Optics Express, 29(24), pp.40177-40186..
[160] Khanpour, M.A. and Karimzadeh, R., 2023. Transparency window in the THz frequency based on asymmetric dark-dark modes interaction. Optical Materials Express, 13(7), pp.1895-1909.
[161] Wang, D., Tian, Z., Zhang, C., Jia, X., Jin, B., Gu, J., Han, J. and Zhang, W., 2014. Terahertz superconducting metamaterials for magnetic tunability. Journal of Optics, 16(9), p.094013.
[162] Jansen, C., Al-Naib, I.A., Born, N. and Koch, M., 2011. Terahertz metasurfaces with high Q-factors. Applied Physics Letters, 98(5).
[163] Semenov, A., Günther, B., Böttger, U., Hübers, H.W., Bartolf, H., Engel, A., Schilling, A., Ilin, K., Siegel, M., Schneider, R. and Gerthsen, D., 2009. Optical and transport properties of ultrathin NbN films and nanostructures. Physical Review B, 80(5), p.054510.
[164] Ilin, K., Schneider, R., Gerthsen, D., Engel, A., Bartolf, H., Schilling, A., Semenov, A., Hübers, H.W., Freitag, B. and Siegel, M., 2008, February. Ultra-thin NbN films on Si: crystalline and superconducting properties. In Journal of Physics: Conference Series (Vol. 97, No. 1, p. 012045). IOP Publishing.
[165] Hajenius, M., Baselmans, J.J.A., Gao, J.R., Klapwijk, T.M., De Korte, P.A.J., Voronov, B. and Gol'tsman, G., 2004. Low noise NbN superconducting hot electron bolometer mixers at 1.9 and 2.5 THz. Superconductor Science and Technology, 17(5), p.S224.
[166] McGrath, W.R., Stern, J.A., Javadi, H.H.S., Cypher, S.R. and Hunt, B.D., 1991. Performance of NbN superconductive tunnel junctions as SIS mixers at 205 GHz. IEEE

transactions on magnetics, 27, pp.2650-2653.
[167] Soldano, C., Mahmood, A. and Dujardin, E., 2010. Production, properties and potential of graphene. Carbon, 48(8), pp.2127-2150.
[168] Batrakov, K., Kuzhir, P., Maksimenko, S., Volynets, N., Voronovich, S., Paddubskaya, A., Valusis, G., Kaplas, T., Svirko, Y. and Lambin, P., 2016. Enhanced microwave-to-terahertz absorption in graphene. Applied Physics Letters, 108(12).
[169] Ergoktas, M.S., Bakan, G., Kovalska, E., Le Fevre, L.W., Fields, R.P., Steiner, P., Yu, X., Salihoglu, O., Balci, S., Fal'ko, V.I. and Novoselov, K.S., 2021. Multispectral graphene-based electro-optical surfaces with reversible tunability from visible to microwave wavelengths. Nature photonics, 15(7), pp.493-498.
[170] Degl'Innocenti, R., Kindness, S.J., Beere, H.E. and Ritchie, D.A., 2018. All-integrated terahertz modulators. Nanophotonics, 7(1), pp.127-144.
[171] Landy, N.I., Sajuyigbe, S., Mock, J.J., Smith, D.R. and Padilla, W.J., 2008. Perfect metamaterial absorber. Physical review letters, 100(20), p.207402.
[172] Kindness, S.J., Almond, N.W., Michailow, W., Wei, B., Jakob, L.A., Delfanazari, K., Braeuninger-Weimer, P., Hofmann, S., Beere, H.E., Ritchie, D.A. and Degl'Innocenti, R., 2019. Graphene-integrated metamaterial device for all-electrical polarization control of terahertz quantum cascade lasers. ACS Photonics, 6(6), pp.1547-1555.
[173] Marinov, K., Boardman, A.D., Fedotov, V.A. and Zheludev, N., 2007. Toroidal metamaterial. New Journal of Physics, 9(9), p.324.
[174] Seisyan, R.P., 2011. Nanolithography in microelectronics: A review. Technical Physics, 56, pp.1061-1073.
[175] Selimis, A., Mironov, V. and Farsari, M., 2015. Direct laser writing: Principles and materials for scaffold 3D printing. Microelectronic Engineering, 132, pp.83-89.
[176] Davidse P D. RF sputter etching—a universal etch [J]. Journal of The Electrochemical Society: 1969, 116(1): 100-104.
[177] Hosokawa N, Matsuzaki R, Asamaki T. RF sputter-etching by fluoro-chlorohydrocarbon gases [J]. Japanese Journal of Applied Physics: 1974, 13(1): 435-438.
[178] Henry, M.D., 2010. ICP etching of silicon for micro and nanoscale devices. California Institute of Technology.
[179] Min, K.H., Choi, S., Jeong, M.S., Kang, M.G., Park, S., Song, H.E., Lee, J.I. and Kim, D., 2019. Investigation of interface characteristics of Al2O3/Si under various O2 plasma exposure times during the deposition of Al2O3 by PA-ALD. Current Applied Physics, 19(2), pp.155-161.
[180] Suntola, T., 1989. Atomic layer epitaxy. Materials Science Reports, 4(5), pp.261-312.
[181] Cabrero-Vilatela, A., Alexander-Webber, J.A., Sagade, A.A., Aria, A.I., Braeuninger-Weimer, P., Martin, M.B., Weatherup, R.S. and Hofmann, S., 2017. Atomic layer deposited oxide films as protective interface layers for integrated graphene transfer. Nanotechnology, 28(48), p.485201.
[182] Alexander-Webber, J.A., Sagade, A.A., Aria, A.I., Van Veldhoven, Z.A., Braeuninger-Weimer, P., Wang, R., Cabrero-Vilatela, A., Martin, M.B., Sui, J., Connolly, M.R. and Hofmann, S., 2016. Encapsulation of graphene transistors and vertical device integration by interface engineering with atomic layer deposited oxide. 2D Materials, 4(1), p.011008.

[183] Kim, K.S., Lee, H.J., Lee, C., Lee, S.K., Jang, H., Ahn, J.H., Kim, J.H. and Lee, H.J., 2011. Chemical vapor deposition-grown graphene: the thinnest solid lubricant. ACS nano, 5(6), pp.5107-5114.

[184] Montoya, J.A., Tian, Z.B., Krishna, S. and Padilla, W.J., 2017. Ultra-thin infrared metamaterial detector for multicolor imaging applications. Optics express, 25(19), pp.23343-23355.

[185] Jeannin, M., Bonazzi, T., Gacemi, D., Vasanelli, A., Suffit, S., Li, L., Davies, A.G., Linfield, E., Sirtori, C. and Todorov, Y., 2020. High temperature metamaterial terahertz quantum detector. Applied Physics Letters, 117(25).

[186] Jeannin, M., Mariotti Nesurini, G., Suffit, S., Gacemi, D., Vasanelli, A., Li, L., Davies, A.G., Linfield, E., Sirtori, C. and Todorov, Y., 2019. Ultrastrong light–matter coupling in deeply subwavelength THz LC resonators. ACS photonics, 6(5), pp.1207-1215.

[187] Messelot, S., Symonds, C., Bellessa, J., Tignon, J., Dhillon, S., Brubach, J.B., Roy, P. and Mangeney, J., 2020. Tamm cavity in the terahertz spectral range. ACS photonics, 7(10), pp.2906-2914.

[188] Lu, Y., Hale, L.L., Zaman, A.M., Addamane, S.J., Brener, I., Mitrofanov, O. and Degl'Innocenti, R., 2023. Near-Field Spectroscopy of Individual Asymmetric Split-Ring Terahertz Resonators. ACS photonics, 10(8), pp.2832-2838.

[189] Yu, X., Suzuki, Y., Van Ta, M., Suzuki, S. and Asada, M., 2021. Highly efficient resonant tunneling diode terahertz oscillator with a split ring resonator. IEEE Electron Device Letters, 42(7), pp.982-985.

[190] Cimbri, D., Wang, J., Al-Khalidi, A. and Wasige, E., 2022. Resonant tunneling diodes high-speed terahertz wireless communications-A review. IEEE Transactions on Terahertz Science and Technology, 12(3), pp.226-244.

[191] Xu, L., Curwen, C.A., Chen, D., Reno, J.L., Itoh, T. and Williams, B.S., 2017. Terahertz metasurface quantum-cascade VECSELs: Theory and performance. *IEEE Journal of Selected Topics in Quantum Electronics*, *23*(6), pp.1-12.

[192] Kindness, S.J., Jessop, D.S., Wei, B., Wallis, R., Kamboj, V.S., Xiao, L., Ren, Y., Braeuninger-Weimer, P., Aria, A.I., Hofmann, S. and Beere, H.E., 2017. External amplitude and frequency modulation of a terahertz quantum cascade laser using metamaterial/graphene devices. *Scientific reports*, *7*(1), p.7657.

[193] Almond, N.W., Qi, X., Degl'Innocenti, R., Kindness, S.J., Michailow, W., Wei, B., Braeuninger-Weimer, P., Hofmann, S., Dean, P., Indjin, D. and Linfield, E.H., 2020. External cavity terahertz quantum cascade laser with a metamaterial/graphene optoelectronic mirror. *Applied Physics Letters*, *117*(4).

[194] Liu, Y., Bai, Z., Xu, Y., Wu, X., Sun, Y., Li, H., Sun, T., Kong, R., Pandey, C., Kraft, M. and Song, Q., 2020. Generation of tailored terahertz waves from monolithic integrated metamaterials onto spintronic terahertz emitters. *Nanotechnology*, *32*(10), p.105201.

[195] Lee, S., Baek, S., Kim, T.T., Cho, H., Lee, S., Kang, J.H. and Min, B., 2020. Metamaterials for enhanced optical responses and their application to active control of terahertz waves. *Advanced Materials*, *32*(35), p.2000250.

[196] He, J., Dong, T., Chi, B. and Zhang, Y., 2020. Metasurfaces for terahertz wavefront modulation: a review. *Journal of Infrared, Millimeter, and Terahertz Waves*, *41*(6), pp.607-631.

[197] Shen, S., Liu, X., Shen, Y., Qu, J., Pickwell-MacPherson, E., Wei, X. and Sun, Y., 2022. Recent advances in the development of materials for terahertz metamaterial sensing. Advanced Optical Materials, 10(1), p.2101008.
[198] Bergman, D.J. and Stockman, M.I., 2003. Surface plasmon amplification by stimulated emission of radiation: quantum generation of coherent surface plasmons in nanosystems. *Physical review letters*, *90*(2), p.027402.
[199] Cho, C.H., Aspetti, C.O., Turk, M.E., Kikkawa, J.M., Nam, S.W. and Agarwal, R., 2011. Tailoring hot-exciton emission and lifetimes in semiconducting nanowires via whispering-gallery nanocavity plasmons. *Nature materials*, *10*(9), pp.669-675.
[200] Van Beijnum, F., Van Veldhoven, P.J., Geluk, E.J., de Dood, M.J., Gert, W. and Van Exter, M.P., 2013. Surface plasmon lasing observed in metal hole arrays. *Physical review letters*, *110*(20), p.206802.
[201] Wang, B., Yu, P., Wang, W., Zhang, X., Kuo, H.C., Xu, H. and Wang, Z.M., 2021. High-Q plasmonic resonances: fundamentals and applications. Advanced Optical Materials, 9(7), p.2001520.
[202] Grinblat, G., Li, Y., Nielsen, M.P., Oulton, R.F. and Maier, S.A., 2017. Efficient third harmonic generation and nonlinear subwavelength imaging at a higher-order anapole mode in a single germanium nanodisk. *ACS nano*, *11*(1), pp.953-960.
[203] Al-Naib, I. and Withayachumnankul, W., 2017. Recent progress in terahertz metasurfaces. *Journal of Infrared, Millimeter, and Terahertz Waves*, *38*, pp.1067-1084.
[204] Stinson, H.T., Sternbach, A., Najera, O., Jing, R., Mcleod, A.S., Slusar, T.V., Mueller, A., Anderegg, L., Kim, H.T., Rozenberg, M. and Basov, D.N., 2018. Imaging the nanoscale phase separation in vanadium dioxide thin films at terahertz frequencies. Nature communications, 9(1), p.3604.
[205] Hafez, H.A., Kovalev, S., Tielrooij, K.J., Bonn, M., Gensch, M. and Turchinovich, D., 2020. Terahertz nonlinear optics of graphene: from saturable absorption to high-harmonics generation. Advanced Optical Materials, 8(3), p.1900771.
[206] Hafez, H.A., Kovalev, S., Deinert, J.C., Mics, Z., Green, B., Awari, N., Chen, M., Germanskiy, S., Lehnert, U., Teichert, J. and Wang, Z., 2018. Extremely efficient terahertz high-harmonic generation in graphene by hot Dirac fermions. Nature, 561(7724), pp.507-511.
[207] Nair, R.R., Blake, P., Grigorenko, A.N., Novoselov, K.S., Booth, T.J., Stauber, T., Peres, N.M. and Geim, A.K., 2008. Fine structure constant defines visual transparency of graphene. *science*, *320*(5881), pp.1308-1308.
[208] Hwang, H.Y., Brandt, N.C., Farhat, H., Hsu, A.L., Kong, J. and Nelson, K.A., 2013. Nonlinear THz conductivity dynamics in p-type CVD-grown graphene. The Journal of Physical Chemistry B, 117(49), pp.15819-15824.
[209] Hafez, H.A., Al-Naib, I., Oguri, K., Sekine, Y., Dignam, M.M., Ibrahim, A., Cooke, D.G., Tanaka, S., Komori, F., Hibino, H. and Ozaki, T., 2014. Nonlinear transmission of an intense terahertz field through monolayer graphene. AIP Advances, 4(11).
[210] Mics, Z., Tielrooij, K.J., Parvez, K., Jensen, S.A., Ivanov, I., Feng, X., Müllen, K., Bonn, M. and Turchinovich, D., 2015. Thermodynamic picture of ultrafast charge transport in graphene. Nature communications, 6(1), p.7655.
[211] Paul, M.J., Chang, Y.C., Thompson, Z.J., Stickel, A., Wardini, J., Choi, H., Minot, E.D., Hou, B., Nees, J.A., Norris, T.B. and Lee, Y.S., 2013. High-field terahertz response of

graphene. New Journal of Physics, 15(8), p.085019.
[212] Dawlaty, J.M., Shivaraman, S., Strait, J., George, P., Chandrashekhar, M., Rana, F., Spencer, M.G., Veksler, D. and Chen, Y., 2008. Measurement of the optical absorption spectra of epitaxial graphene from terahertz to visible. *Applied Physics Letters*, *93*(13)..
[213] Razavipour, H., Yang, W., Guermoune, A., Hilke, M., Cooke, D.G., Al-Naib, I., Dignam, M.M., Blanchard, F., Hafez, H.A., Chai, X. and Ferachou, D., 2015. High-field response of gated graphene at terahertz frequencies. *Physical Review B*, *92*(24), p.245421.
[214] Jadidi, M.M., Daniels, K.M., Myers-Ward, R.L., Gaskill, D.K., König-Otto, J.C., Winnerl, S., Sushkov, A.B., Drew, H.D., Murphy, T.E. and Mittendorff, M., 2019. Optical control of plasmonic hot carriers in graphene. *ACS Photonics*, *6*(2), pp.302-307..
[215] Cox, J., Marini, A. & de Abajo, F. Plasmon-assisted high-harmonic generation in graphene. Nat Commun 8, 14380 (2017)
[216] Deinert, J.C., Alcaraz Iranzo, D., Pérez, R., Jia, X., Hafez, H.A., Ilyakov, I., Awari, N., Chen, M., Bawatna, M., Ponomaryov, A.N. and Germanskiy, S., 2020. Grating-graphene metamaterial as a platform for terahertz nonlinear photonics. ACS nano, 15(1), pp.1145-1154.
[217] Lin, H., Braeuninger-Weimer, P., Kamboj, V.S., Jessop, D.S., Degl'Innocenti, R., Beere, H.E., Ritchie, D.A., Zeitler, J.A. and Hofmann, S., 2017. Contactless graphene conductivity mapping on a wide range of substrates with terahertz time-domain reflection spectroscopy. Scientific Reports, 7(1), p.10625.